SUPERCONDUCTIVITY, HIGH TEMPERATURE SUPERCONDUCTIVITY

Temperature singularities in reflection spectra of YBaCuO superconducting films in the infrared frequency range

I. Ya. Fugol, V. N. Svishchev, and M. Yu. Libin

B. Verkin Institute for Low Temperature Physics and Engineering, National Academy of Sciences of the Ukraine, 310164 Kharkov, Ukraine

(Submitted March 18, 1997; revised September 8, 1997)
Fiz. Nizk. Temp. **24**, 195–203 (March 1998)

The reflection spectra of YBaCuO superconducting films with moderate and optimal doping are measured in the IR region ($2500-10000\ \mathrm{cm}^{-1}$) by varying temperature in the interval 5–200 K. The experimental results convincingly confirm an optical response to the superconducting transition occurring at the point $T=T_c$ and the sensitivity of optical IR spectra to the phase ordering temperature $T=T^*>T_c$. It is found that samples with optimal doping display reproducible temperature changes at $T^*>T_c$. It is shown that the two-component model of carriers, including light fermions and heavy bosons, is most adequate for a description of the entire body of optical data. Optical data are used for reconstructing the phase diagram for $YBa_2Cu_3O_{6+x}$ in the T vs. x coordinates. © *1998 American Institute of Physics.*
[S1063-777X(98)00103-0]

Optical properties of high-temperature superconductors of the copper oxide type in the near and middle infrared frequency range have not received an unambiguous interpretation so far. This also applies completely to the IR spectrum of $YBa_2Cu_3O_{6+x}$ samples investigated by us. Many experimental results indicate that the classical Drude model cannot be matched with spectral reflection and optical conductivity curves in the case of optimal doping and the more so under moderate doping conditions. The IR optical characteristics are usually described on the basis of extended Drude models in the framework of nesting or marginal Fermi liquid theory.[1–5] The values of the two main parameters in the Drude model, viz., the unscreened plasma frequency ω_p and optical damping Γ, differ considerably in different models. No matching is observed for the third parameter either (the high-frequency dielectric constant ε_∞) for YBaCuO. In a phenomenological description based on the extended Drude model, it is usually assumed that the damping is a function of frequency ($\Gamma=\Gamma(\omega)$) and sometimes that the plasma frequency also depends on frequency ($\omega_p=\omega_p(\omega)$). The reflection coefficient $R(\omega)$ normally decreases upon an increase in frequency less sharply than in the classical Drude model and varies almost linearly near the reflectance minimum in the vicinity of the screened plasma frequency $\omega_{\mathrm{pl}}=\omega_p/\sqrt{\varepsilon_\infty}$.[6] The necessity of using the dependences $\Gamma=\Gamma(\omega)$ and especially $\omega_p=\omega_p(\omega)$ has not received a clear physical substantiation yet.

Another disputable aspect of the optical IR spectroscopy is the origin of the wide absorption band with a peak near 0.6 eV, which emerges in $YBa_2Cu_3O_{6+x}$ samples with $x>0.2$. The intensity and width of this band increases upon a further doping, and the band is displaced simultaneously towards low frequencies. Under optimal doping conditions, it virtually ''merges'' with the Drude component. It remains unclear whether this band makes a noticeable contribution to the reflection from the ab-plane of YBaCuO.[1–5]

Along with these aspects of the IR spectroscopy of HTS materials, which are widely discussed in the literature, it is important to explain the peculiar temperature behavior of IR spectra and their sensitivity to the superconducting transition temperature T_c noted by several authors.[5–9] It should be recalled that the effect of sensitivity of the optical transmission spectra of YBaCuO and BiCaCuO superconducting films to the formation of a superconducting condensate in the visible frequency range was established reliably in Refs. 10 and 11. In the IR frequency range, the very fact of the IR response to T_c as well as the existence of temperature dependence of reflectance at $T>T_c$ remain disputable.

In our previous publications,[8,9] we mainly analyzed the IR transmission spectra for thin YBaCuO films and found that like in the visible range, a response to the superconducting transition (ST) is observed in the IR frequency region. We also noted a peculiar linear temperature dependence of transmittance. It was found that temperature dependences in the IR and visible regions are opposite: the transparency decreases in the IR spectrum and increases in the visible region upon sample cooling. At the same time, it was found[11,12] that the amplitude and type of the optical response to the SC-ity can vary depending on the extent of deviation from thermodynamic equilibrium in the electron and spin–lattice subsystems. In some cases, the kink on optical characteristics at T_c can be masked by the contribution of relaxation changes in the electron-structural state of the sample. This is the reason behind possible irreproducibility of the optical response at T_c as well as the slopes of temperature dependences of optical parameters of the samples for measurements made under different conditions (different cooling or heating rates) The relaxation of the electron-structural state of YBaCuO

 © 1998 American Institute of Physics

after a sharp change in temperature is manifested most clearly in optical spectra under moderate and weak doping ($0.3<x<0.8$). If we take into account the fact that the relative change in the optical transmission signal at T_c is of the order of 0.5–1%, and temperature variation from 200 to 90 K is of the order of several percent, the need for multiple reproduction of results on temperature anomalies in optical spectra becomes obvious.

In this research, we analyzed in detail temperature variations in IR reflection spectra for most stable samples with a doping level near the optimal value. Measurements were made on YBaCuO superconducting epitaxial films. One of the advantages of using such films in reflection experiments is the high quality of their surface. Temperature measurements of $R(\omega)$ confirm (1) the existence of a noticeable temperature dependence of reflectance at $T>T_c$, (2) the emergence of a response in the IR reflection spectrum to the onset of the SC and (3) the existence of a special critical point T^* at $T>T_c$. As regards the critical point T^*, it is assumed that it separates temperature regions with different extents of localization and ordering of charge carriers. Using the optical data obtained here and supplementing them with our previous results, we made an attempt to reproduce the $T-x$ phase diagram and to plot the curves $T_c=T_c(x)$ and $T^*=T^*(x)$ in these coordinates. An analysis of the temperature dependence $R_\omega(T)$ in the region $T>T_c$ leads to the conclusion that optical data can be explained adequately on the basis of the two-band model of optical conductivity in the case when the boson component dominates in the near IR frequency range.

EXPERIMENT

We measured the $R(\omega,T)$ dependences on an optical setup with almost normal incidence of monochromatic radiation on the sample under investigation ($\sim 10°$ relative to the normal to the film surface). The spectral distribution of radiation was analyzed with the help of a monochromator MDR-23 with a set of attachments for the IR region. The radiation source was a globar (SiC), and the receiver was a superconducting helium bolometer with a low noise level. The windows of the bolometer and of a optical helium cryostat were made of zinc selenide (ZnSe). The cryostat made it possible to control the temperature smoothly in the interval from 300 to 5 K and to maintain a given temperature to within 0.3 K. Measurements were made by using a two-beam optical circuit under modulation conditions. The reflectance $R(\omega,T)$ was determined from the ratio of intensity of the luminous flux reflected by the sample to the intensity of flux reflected by a reference silver mirror. The random error in the measurements of $R(T)$ was ~ 0.005.

We made experiments on thin YBaCuO films with different oxygen doping levels. The samples were prepared specially for our optical setup by Dr. M. Lippert at the Institute of Physics, Erlangen University (Germany), at the department headed by Prof. G. Saemann-Ishchenko. The films were prepared by magnetron sputtering of the target from YBaCuO melt on a $SrTiO_3$ epitaxial substrate under a high pressure. The samples were oriented in the ab-plane (001). The conditions of sputtering were optimized for preparing

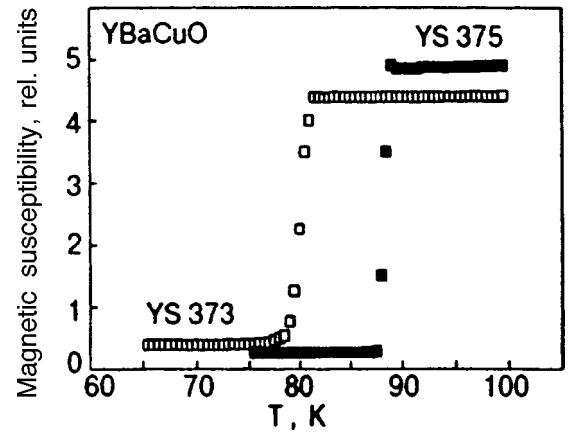

FIG. 1. Characteristics of the superconducting transition for YS 373 and YS 375 samples.

films with doping corresponding to the highest value of T_c (88.2–89.2 K). Oxygen concentration in the films was varied by prolonged holding under the corresponding partial pressure of oxygen (at $T=550$ °C) and quenching (for 5 min) to 300 °C by using liquid nitrogen. In this way, YBaCuO films with $T_c=81.5$; 61.1 K, etc., were prepared.

Figure 1 shows two curves demonstrating the superconducting transition in YBaCuO films YS 375 ($T_c=88.2$ K) and YS 373 ($T_c=81.5$ K) and obtained by using the inductive ac-method. The length of the c-axis was determined by x-ray diffraction technique using 6 (001) reflexes and was found to be $c=11.680$ Å for YS 375 and $c=11.725$ Å for YS 373. According to normalization tables, the parameters of the c-axis correspond to the oxygen index $x=0.9$ for YS 375 and $x=0.75$ for YS 373. The film thickness was controlled from the change in the frequency of standard quartz generator to within 10%: $d=1800$ Å for YS 375 and $d=2100$ Å for YS 373. Since the thickness d of these films exceeds the penetration depth $l(\omega)$ for IR radiation in the sample ($l(\omega)\simeq 1000$ Å for the frequency range 0.3–1.2 eV),[3] the contribution of the reflection from the substrate is negligibly small, although the transmittance $\tilde{t}$ differs from zero.

RESULTS

The reflection spectra $R(\omega)$ for the ab-plane of YS 373 and YS 375 films are shown in Fig. 2 for two temperatures in the frequency range from 2500 to 10000 cm^{-1} (0.3–1.2 eV). In this IR frequency range, the reflection coefficient varies from a nearly metallic value ($R(\omega)=0.8$ for $\hbar\omega=2500$ cm^{-1}) to nearly insulator value ($R(\omega)=0.2$ for $\hbar\omega=10000$ cm^{-1}). A considerable decrease in $R(\omega)$ in the range under investigation, culminating in low values of reflectance for $\omega>1.2$ eV indicates a transition from from the spectral region with a dominating contribution of quasi-Drude free charge carriers to a spectrum with dominating contribution of localized electron excitations. Note that the decrease in $R(\omega)$ with frequency is weakly nonlinear, which does not contradict the Drude model for YS 375. Figure 2 shows that the temperature dependence of the spectrum for the YS 375 sample with optimal doping is manifested less

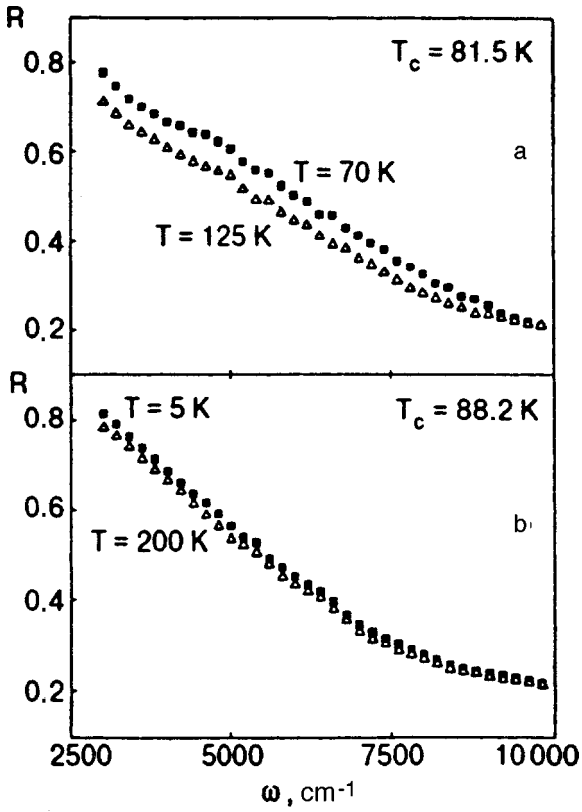

FIG. 2. Reflectance spectra $R(\omega)$ for the YS 373 sample with $T_c = 81.5$ K at $T = 70$ and 125 K (a) and for the YS 375 sample with $T_c = 88.2$ K at $T = 5$ and 200 K (b).

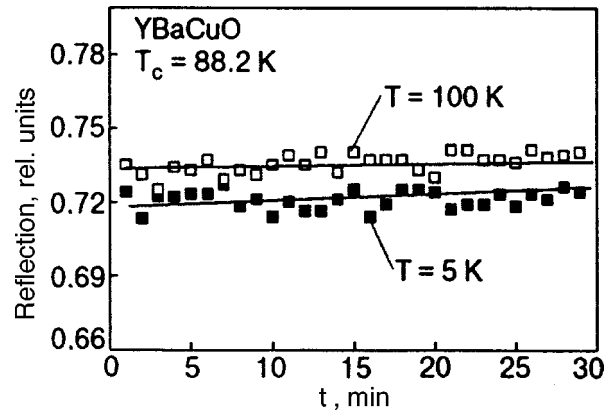

FIG. 3. Temporal stability of reflectance for the energy $h\omega = 0.68$ eV ($\omega = 5500$ cm^{-1}) for a film with optimal doping.

strongly than for the sample with moderate doping. In the spectra of both samples, the strongest temperature changes are observed in the frequency range 5000 cm^{-1} (near the peak of the possible IR absorption band), while the changes near 10000 cm^{-1} are much smaller. If we compare these curves with $R(\omega)$ dependences from Ref. 9, we can note that all the reflection curves converge at the crossover point near 1.2 eV, which almost coincides with the position of the plasma frequency $\omega_{\rm pl}$.

It should be noted that the temperature dependence of $R(\omega)$ is very sensitive to deviations from thermodynamic equilibrium in the electron and lattice subsystems, and hence samples should be held for a long time at each given temperature (especially at low temperatures) to observe the temperature effect in pure form. LT-relaxation processes occur relatively rapidly (during $\sim$30 min) for optimal doping. All measurements of the temperature scanning effect were made at a fixed frequency $\omega = 5500$ cm^{-1}. Experiments were usually started after preliminary holding of the optical cryostat with the sample at $T = 200$ K for one hour. After this, the $R_\omega(T)$ dependence was measured during slow cooling from 200 to 5 K, and then the sample was held at $T = 5$ K (for 30–40 min), and the values of $R_\omega(T)$ were measured again during heating. A similar cycle was repeated once again in the same experiment. The duration of scanning from 200 to 5 K was 30–40 min. The same film was repeatedly investigated during several days.

Figure 3 shows the results of studying the temporal stability of the reflectance $R_\omega(T)$ of the YS 375 sample at $T = 100$ K after cooling from $T = 200$ K and at $T = 5$ K after cooling from 100 K. It can be seen that thermodynamic equilibrium in the $YBa_2Cu_3O_{6.9}$ film sets in $\sim$30 min after cooling from 200 to 5 K, while the maximum relative change $\Delta R_\omega(t)/R_\omega$ during the relaxation process of increasing $R_\omega(T)$ attains the value

$$\frac{R_\omega(5\ \text{K},\ 30\ \text{min}) - R_\omega(100\ \text{K},0)}{R_\omega(5\ \text{K},\ 30\ \text{min})} \sim 1.5\times 10^{-2}.$$

For cooling from 200 to 100 K, the maximum value of $\Delta R_\omega(t)/R_\omega \simeq 3\cdot 10^{-3}$ is attained in about 30 min. A comparison with the results obtained in Ref. 12 in which the parameters of relaxation process for a $YBa_2Cu_3O_{6.7}$ film are presented shows that the film with optimal doping is less labile. Relative changes in the optical signal for a film with $x = 0.7$ were up to 7% for cooling below T_c.

Figure 4 shows the results of two independent measurements of reflectance R_ω for $YBa_2Cu_3O_{6.9}$ under temperature scanning for cooling (below 200 K). In spite of a considerable spread in experimental points, the $R_\omega(T)$ dependence can be described under the assumption concerning the existence of three different temperature regions I, II, and III and two critical temperatures T_c and T^*: region I for $T < T_c$, II for $T_c < T^*$, and III for $T > T^*$. In regions II and III, $R_\omega(T)$ is a linear function of temperature, while in region I (the ST state) the dependence is more complex and seems to revert to a straight line independent of T. In T scanning, a peak of the value of R_ω can be clearly seen at the point $T = T_c$. The point $T = T^*$ is manifested less clearly during cooling, but it can be identified from a kink on the straight lines $R_\omega(T)$ where a change in the slope occurs. Both at T_c and at T^*, a jump in the value of $R_\omega(T)$ can sometimes be observed.

The isolation of three different temperature regions in the course of cooling is not accidental, which is confirmed by the results of independent measurements of $R_\omega(T)$ dependences obtained during scanning under heating. Figure 5 shows the results obtained from three independent experiments for the same film with $T_c = 88.2$ K during a slow heating from 5 K. A comparison of the three dependences

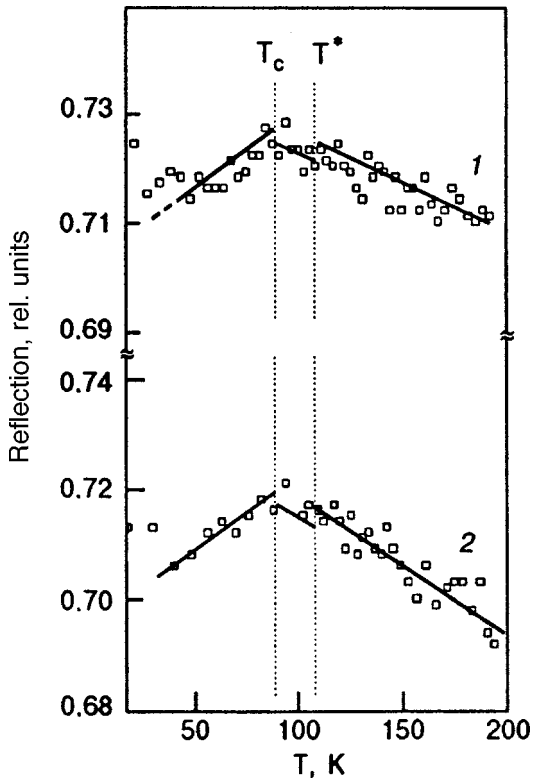

FIG. 4. Temperature dependences of reflection for the energy $h\omega = 0.68$ eV ($\omega = 5500$ cm^{-1}) for a $YBa_2Cu_3O_{6.9}$ film with $T_c = 88.2$ K under cooling. Curves *1* and *2* corresponds to measurements made on different days.

(curves *1–3*) shows general tendencies in variation of R_ω as a function of T and allows us to single out the same three temperature regions as those marked in Fig. 4. In region I ($T < T_c$), the value of R_ω is virtually independent of T. At the point $T = T_c$, a jump in the value of R_ω and a kink on the $R(T)$ curve can be seen simultaneously. In region II ($T_c < T < T^*$), a linear temperature dependence appears, and as we reach the point $T = T^*$, a small jump in the value of $R_\omega(T^*)$ is observed again, followed by a linear dependence for $T > T^*$, but with a different slope. Curves *1* and *2* in Fig. 5 correspond to heating in different experiments, while curves *2* and *3* were obtained during thermal cycling on the same day in different heating cycles. An analysis of the data allows us to single out the points $T_c \sim 88$ K and $T^* \sim 107$ K for YBaCuO with $x = 0.9$. It should be noted that the point T^* can be seen more clearly for heating than for cooling.

Figure 6 shows for comparison the curves of temperature scanning of reflectance for a YS 373 sample with moderate doping for cooling from 200 to 5 K and subsequent heating. The critical points at $T_c = 81.5$ K and $T^* = 125$ K can be seen clearly in the heating cycle and are almost blurred under cooling conditions. A noticeable hysteresis is observed for the entire temperature range (even at $T > T_c$) and is due to stronger deviation from equilibrium for the YS 373 sample at temperature variations than for the YS 375 sample. The variation $\delta R = [R_2(T_1) - R_2(T_2)]/R(T)$ for this sample amounts to ~ 0.07 for temperature variation from 125 to 70 K. Accordingly, the relative temperature reflection coefficient is $\delta R/\Delta T \sim 10^{-3}$ deg^{-1} (see Fig. 2a).

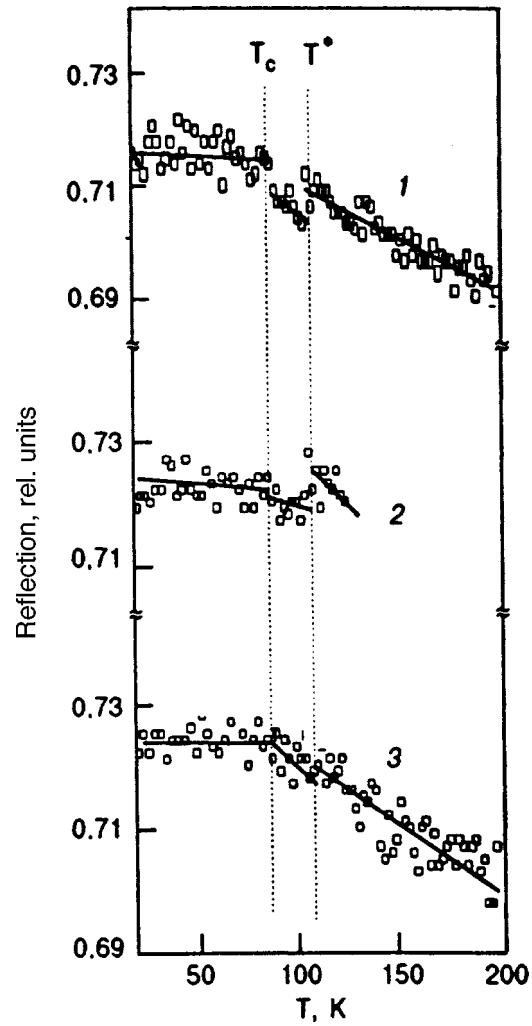

FIG. 5. Temperature dependences of reflection for the energy $h\omega = 0.68$ eV ($\omega = 5500$ cm^{-1}) for a $YBa_2Cu_3O_{6.9}$ film with $T_c = 88.2$ K under heating. Curves *1* and *2* corresponds to measurements made on different days, while curves *2* and *3* were measured on the same day.

DISCUSSION

The above data on temperature behavior of the reflectance of superconducting films concern a number of important aspects: (1) the observation of the temperature dependence $R(\omega,T)$ at $T > T_c, T^*$; (2) the existence of optical response in the IR spectrum to the emergence of superconductivity at $T = T_c$ and a change in the $R_\omega(T)$ dependence at $T < T_c$ in the superconducting phase, and (3) the discovery of temperature singularity on the $R_\omega(T)$ curve near the critical point $T^* > T_c$. Let us analyze these peculiarities for the YS 375 sample with optimal doping.

1. The temperature dependence of the reflection coefficient for $T > T_c$ was observed repeatedly experiments both during frequency scanning of $R(\omega)$ at different temperatures and during selective measurements of reflectance at a fixed frequency $\omega_0 = 5500$ cm^{-1} in the course of temperature scanning. Under moderate doping, the temperature effects are manifested more clearly than in samples with optimal doping. The true nature of the temperature dependence and the exclusion of possible contributions due to temperature variation of lattice parameters and/or due to deviations from ther-

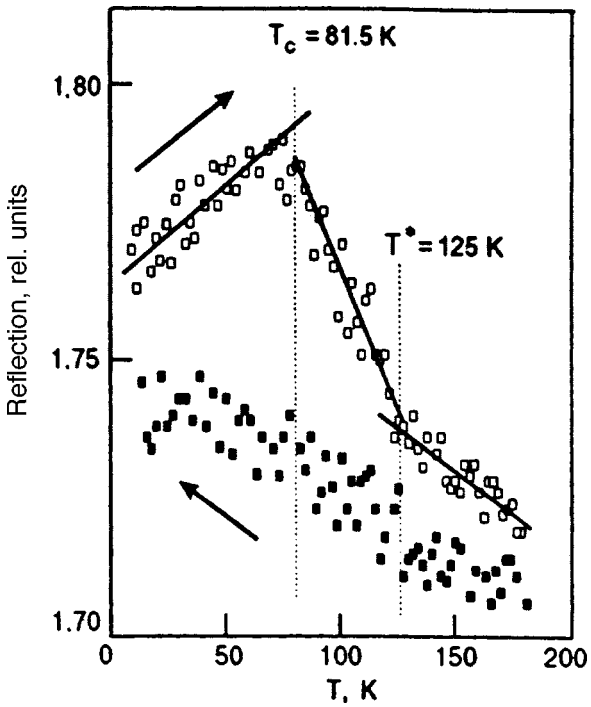

FIG. 6. Temperature dependence of reflection for $h\omega = 0.68$ eV ($\omega = 5500$ cm^{-1}) for a $YBa_2Cu_3O_{6.75}$ film (with moderate doping) under cooling (■) and heating (□).

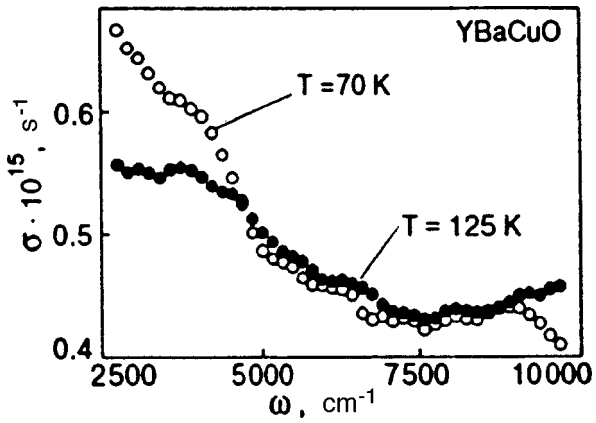

FIG. 7. Optical conductivity $\sigma(\omega)$ at $T = 70$ and 125 K for the YS 373 sample, obtained from calculations based on the Kramers–Kronig relations.

modynamic equilibrium of electronic and structural states are confirmed by measurements for different directions of scanning: cooling and heating at $T > T_c$ lead to virtually the same temperature dependences of reflectance for a sample with optimal doping (see Figs. 4 and 5).

According to the results depicted in Fig. 4, the relative temperature reflection coefficient for a sample with optimal doping ($x = 0.9$) is $|\delta R/\Delta T| \simeq 4 \times 10^{-4}$ deg^{-1} and has negative sign. Almost the same value ($\delta \tilde{t}/\Delta T \simeq (3-5) \times 10^{-4}$ deg^{-1}) was obtained for the relative transmission coefficient $\tilde{t}$ in our earlier experiments,[9,12] which is in accord with the data reported by Yagil *et al.*,[5] the sign of the coefficient being positive. It follows hence that the relative temperature absorption coefficient in the measuring range must be close to zero:

$$\frac{\delta A}{\Delta T} = -\left(\frac{\delta R}{\Delta T} + \frac{\delta \tilde{t}}{\Delta T}\right) \simeq 10^{-4} \ \text{deg}^{-1}, \tag{1}$$

where $A = 1 - (\tilde{t} + R)$ stands for total absorption. It would be expedient to assess the scale of temperature variations of optical conductivity in the near IR region. The quantity $\delta\sigma_\omega/\Delta T$ should be presented by two contributions, i.e., the temperature variation of absorbance $\delta k/\Delta T \sim \delta A/\Delta T$ and the temperature variation of refractive index $\delta n/\Delta T$. The value of $\delta n/\Delta T$ has the same scale as $\delta k/\Delta T$, but the opposite sign. Hence we can draw the conclusion that optical conductivity in the near IR region must be virtually independent of temperature, i.e., $\delta\sigma/\Delta T \sim 0$. The above qualitative considerations are confirmed by the results of calculations of optical conductivity $\sigma(\omega)$ by the Kramers–Kronig relations. The results of these calculations are shown in Fig. 7 for two temperatures (below and above T_c). It will be proved in our next publication that this conclusion is also in accord with the results of calculations of the imaginary component of permittivity $\varepsilon_2(\omega) = 2nk$ as a function of temperature T, indicating that $\varepsilon_2(\omega)$ is virtually independent of T in the frequency range 4500–9000 cm^{-1}.

Is it possible to match the obtained result $\delta\sigma^{\text{IR}}/\Delta T \sim 0$ with the data concerning the signs and magnitudes of $\delta\sigma/\Delta T$ for other frequency regions in the one-band model? Let us write the relations for $\delta\sigma/\Delta T$ for the case of static conductivity $\sigma^0(\omega = 0)$, for the IR region ($\omega < \omega_{\text{pl}}$), and for the visible range ($\omega > \omega_{\text{pl}}$) at $T > T_c$, which were determined experimentally:

$$\omega = 0, \quad \frac{\delta\sigma^0}{\Delta T} < 0, \quad \left|\frac{\delta\sigma^0}{\Delta T}\right| \simeq 7 \times 10^{-2} \ \text{deg}^{-1},$$

$$\omega < \frac{\omega_p}{\sqrt{\varepsilon_\infty}}, \quad \frac{\delta\sigma}{\Delta T} \simeq 0, \quad \frac{\delta\sigma}{\Delta T} \lesssim 10^{-4} \ \text{deg}^{-1},$$

$$\omega > \frac{\omega_p}{\sqrt{\varepsilon_\infty}}, \quad \frac{\delta\sigma}{\Delta T} > 0, \quad \frac{\delta\sigma}{\Delta T} \simeq 5 \times 10^{-4} \ \text{deg}^{-1}. \tag{2}$$

The data for static conductivity were determined from resistive characteristics of YBaCuO films with optimal doping, while the data for the visible region are borrowed from Ref. 12. It is well known that the following two main spectroscopic parameters are used in the one-band model: plasma frequency ω_p and damping Γ. Static conductivity is defined as

$$\sigma^0(T) = \frac{1}{4\pi} \frac{\omega_p^2(T)}{\Gamma(T)}, \tag{3}$$

while optical conductivity at frequency ω for $\omega \gg \Gamma$ has the form

$$\sigma_\omega(T) = \frac{1}{4\pi} \frac{\omega_p^2(T)}{\omega^2} \Gamma(T). \tag{4}$$

It should be noted that the condition $\omega \gg \Gamma$ holds for frequencies $\omega > 2500$ cm^{-1}. It follows from relations (3) and (4) that the damping $\Gamma(T)$ appears in the denominator of the expression for $\sigma^0(T)$ and in the numerator for $\sigma_\omega(T)$. The tem-

perature dependence of damping $\Gamma(T)$ for static conductivity of YBaCuO was determined experimentally by Beschofen *et al.*,[14] who proved that $\Gamma(T)\propto T$ in the case of optimal doping. If we assume that the conductivity of an HTS material is determined by one type of carriers with damping $\Gamma(T)$, it follows from (3) and (4) that the signs of the temperature derivatives for σ^0 and $\sigma_\omega^{\mathrm{IR}}$ must be opposite, and the temperature dependence itself must be as strong as for $\sigma^0(T)$. This contradicts expression (2) and shows that the one-band model cannot explain the temperature behavior of static and optical conductivity.

Along with relations (3) and (4), conditions (2) can be easily satisfied by considering the two-band model with two types of charge carriers with strongly different masses, viz., light and heavy holes that can be put in correspondence with fermions and bosons (bipolarons). The necessity of using two types of carriers was emphasized by us earlier in the interpretation of IR and visible spectra.[8,12] Experimental evidences supporting the boson–fermion model can be found in Refs. 5, 15, and 16, and the theoretical substantiation of this model was given in Refs. 17 and 18. In this model, the total number n_h of hole carriers and corresponding plasma frequencies satisfy the relations

$$n_h=n_F+2n_B,\quad n_F\gg n_B,\quad n_F\leftrightarrow n_B,$$
$$\omega_{PF}^2\simeq 4\pi e^2\frac{n_F}{m_F};\quad \omega_{PB}^2\simeq 4\pi e^2\frac{n_B}{m_B}. \tag{5}$$

It is possible that fermions n_F and bosons n_B are converted into each other since it is assumed that the boson band falls in the fermion band.

The contribution to optical transmittance in the near and middle IR region must come from both band branches with corresponding statistical weights g_F and g_B:

$$\sigma_\omega=g_F\sigma_{\omega,F}+g_B\sigma_{\omega,B}=\frac{1}{4\pi\omega^2}[g_F\omega_{PF}^2(T)\Gamma_F(T)+g_B\omega_{PB}^2(T)\Gamma_B(T)]. \tag{6}$$

Taking account of two terms in (6), we can easily describe the compensation of the temperature dependence of $\sigma_\omega^{\mathrm{IR}}$ due to mutual conversion of two types of charge carriers (which depends on T). It can be assumed that the localization of fermions and an increase in the number of bipolarons (bosons) upon cooling are the effects that actually compensate the decrease in damping Γ_B with temperature in the second term and lead to a temperature balance between the contributions from the two terms in (6). At the same time, the role of the boson component of charge carriers in the visible region ($\omega>\omega_p/\sqrt{\varepsilon_\infty}$) becomes small, and the energy spectrum is determined by the $d-d$ electron transitions and interband transitions involving charge transfer, which are strongly correlated with the fermion subsystem. The observed weak dependence $\sigma_\omega(T)$ in the visible range with the sign of temperature coefficient opposite to that for static conductivity (in accordance with (2)) can be described taking into account the dominating contribution of fermion carriers to $\sigma_\omega(T)$.

The above considerations allow us to choose an optimal model for a quantitative description of dielectric response in YBaCuO and a detailed analysis of basic spectral characteristics (this will be done in our next publication).

2. The proof of the sensitivity of IR reflection spectra to the superconducting transition is one of the most remarkable results of this research. It can be seen from Figs. 4 and 5 that the temperature dependence of reflectance has a kink-type singularity at the point $T=T_c$, but the singularity has different forms for cooling and heating. The difference emerges mainly due to ambiguous behavior of $R_\omega(T)$ in the superconducting phase. We can avoid hysteresis ambiguities in a sample with optimal doping in the region $T>T_c$, but this cannot be done completely in the region $T<T_c$ even for a holding time $t\sim 40$ min at $T=5$ K. Cooling curves are normally characterized by a noticeable decrease in $R_\omega(T)$, while heating curves are on the contrary characterized by a certain increase in the value of this quantity near the superconducting transition at $T<T_c$. It is difficult to say without additional measurements which of the $R_\omega(T)$ curves (for heating or cooling) carry true information on the temperature dependence $R_\omega(T)$ (without a contribution from relaxation effects in the superconducting condensate). Nevertheless, we can see that the optical response to the emergence of superconductivity of the condensate at T_c is manifested clearly for both modes of temperature scanning. In the case of heating, a jump in $R(T_c)$ at the superconducting transition can sometimes be observed upon an increase in R_ω, which corresponds to a positive jump in the number n_h of charge carriers upon a transition from the normal to superconducting phase. According to our data, the magnitude of the reflectance jump amounts to $\delta R=\Delta R(T_c)/R\sim 4\times 10^{-3}$.

Note for comparison that similar jumps were also observed in absorption spectra[12] in the range of higher frequencies ($1.5\ \mathrm{eV}<h\omega<3\ \mathrm{eV}$) due to an increase in the number of free charge carriers at T_c. The existence of optical response to superconducting transition in the range of Drude reflection at frequencies much higher than the superconducting energy gap and temperature ($h\omega\gg\Delta_0,T$) cannot be explained adequately by traditional electron pairing due to the phonon mechanism. It is necessary to consider additional mechanisms of pairing during the formation of superconducting condensate.

3. Another remarkable singularity on the $R_\omega(T)$ curve (which is manifested most clearly for heating) appears at the point $T^*>T_c$. For a sample with $T_c=88.2$ K ($x=0.9$), this singularity lies at $T^*=(107\pm 5)$ K. For a sample with $T_c=81.5$ K, the point T^* corresponds to temperature ~ 130 K. Not only do the slopes of straight lines change at the point T^*, but the jump in reflectance $\Delta R(T^*)/R\sim 10^{-2}$ at this point can also be singled out in many cases. The sign of the jump corresponds to a decrease in the number of free charge carriers (localization effect) as we go over from higher to lower temperatures, i.e., the sign of the jump at T^* is opposite to that of the jump at T_c.

The existence of singularity at the point $T^*>T_c$ was noted earlier in the IR spectra for moderately doped YBaCuO samples.[8,9] In analogy with singularities on resistivity and reciprocal mobility curves,[17] this temperature can

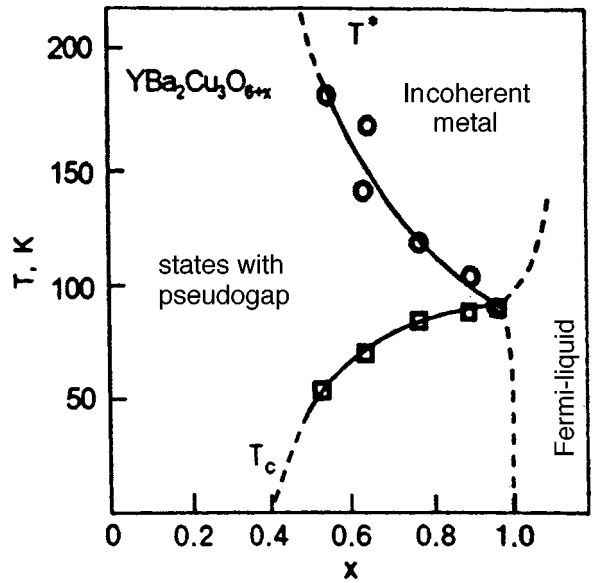

FIG. 8. Superconducting transition temperature T_c (□) and the critical temperature T^* (○) obtained from optical reflection and transmission spectra in the IR and visible regions for $YBa_2Cu_3O_{6+x}$ epitaxial films.

be identified as the point separating two phase regions with different extents of dielectrization. In samples with $T_c = 81$ K ($x = 0.75$–0.8), the singularity is manifested at $T^* \simeq 125$ K, while for those with $T_c = 55$ K ($x = 0.55$), the singularity rises to $T^* \sim 180$ K.[12] The results obtained for IR spectra as well as the data on the visible-range spectra for samples with $T_c = 90$ K ($x = 0.95$) and $T_c = 75$ K ($x = 0.65$) presented in Refs. 11 and 12 are shown in Fig. 8 in the form of phase diagram for YBaCuO. This diagram for YBaCuO is in good agreement with the general phase diagram for cuprate superconductors.[19] According to Puchkov *et al.*,[19] a pseudogap emerges in HTS materials below T^*, and incoherent pairing of charge carriers takes place. Thus, our results confirm that superconducting condensate in the case of optimal (and the more so moderate) doping is formed from insulator-type states as was assumed by Bednorz and Müller in their pioneering works.

CONCLUSIONS

In this work, we have studied temperature singularities in the reflection spectra of $YBa_2Cu_3O_{6+x}$ superconducting films with moderate and optimal doping in the near and middle IR frequency range. The strongest temperature effects are observed in samples with moderate doping ($x = 0.75$). Nevertheless, multiple experiments on a sample with optimal doping ($x = 0.9$) indicate that temperature effects with the same type of singularities are also manifested for these samples (with a higher degree of ordering).

We have analyzed the sign of the temperature coefficient of optical conductivity in the IR ($\omega < \omega_{pl}$) and visible ($\omega > \omega_{pl}$) ranges and for static conductivity ($\omega = 0$) at $T > T_c$. The results of analysis show the expedience of application of the two-liquid model of charge carriers (light fermions and heavy bosons). It is temperature-dependent contribution of the boson component that compensates the temperature effect from the fermion component so that the optical conductivity in the near IR region becomes virtually independent of temperature.

The measurement of reflectance R_ω for $h\omega = 0.68$ eV during temperature scanning (both for cooling and for heating) has made it possible to single out two special points on the temperature scale: the superconducting transition temperature T_c and the temperature $T^* > T_c$ of phase ordering in the normal state.

In analogy with measurements of resistivity, reciprocal mobility, and optical conductivity in the far IR region,[14,19] the point T^* can be interpreted as a point of opening of a pseudogap in the boson subsystem. Optical measurements of reflectance and absorption in the IR and visible regions are used for constructing the T–x phase diagram for $YBa_2Cu_3O_{6+x}$ samples.

The results obtained here confirm the existence of optical response to the superconducting transition in the IR frequency range and the sensitivity of optical spectra to phase ordering at the point T^*.

The authors express their gratitude to Prof. G. Saemann–Ishchenko and his colleagues for supplying samples of thin HTS films, to V. N. Samovarov for fruitful discussions, to A. I. Galuza for his help in calculations based on the Kramers–Kronig method, and to M. Bludov for his assistance in carrying out the experiments.

*E-mail: fugol@ilt.kharkov.ua

[1] D. B. Tanner and T. Timusk, in *Physical Properties of HTS III* (ed. by D. M. Ginsberg), World Scientific, Singapore (1992).
[2] T. Arima, K. Kikuchi, M. Kasuya *et al.*, Phys. Rev. B **44**, 917 (1991).
[3] I. Bozovic, Phys. Rev. B **42**, 1969 (1990).
[4] S. L. Cooper, D. Reznik, A. Kotz *et al.*, Phys. Rev. B **47**, 8233 (1993).
[5] Y. Yagil, F. Baudenbacher, M. Zhang *et al.*, Phys. Rev. B **52**, 15582 (1995).
[6] M. J. Holcomb, L. L. Perry, J. P. Collman, and W. A. Little, Phys. Rev. B **53**, 6734 (1996).
[7] H. L. Dewing and K. Scott, J. Supercond. **7**, 481 (1994).
[8] I. Ya. Fugol', V. N. Samovarov, V. N. Svishchev, and M. Yu. Libin, Fiz. Nizk. Temp. **21**, 878 (1995) [Low Temp. Phys. **21**, 878 (1995)].
[9] V. N. Svishchev and I. Ya. Fugol', Fiz. Nizk. Temp. **22**, 1257 (1996) [Low Temp. Phys. **22**, 956 (1996)].
[10] I. Fugol, G. Saemann-Ishchenko, V. Samovarov *et al.*, Solid State Commun. **80**, 201 (1991).
[11] I. Ya. Fugol, V. N. Samovarov, Yu. I. Rybalko, and V. M. Zhuravlev, in *Series Research Rep. of Physics ''High-T_c Superconductivity''* (ed. by A. S. Davydov and V. M. Loktev), Springer-Verlag (1992).
[12] I. Fugol and V. Samovarov, in *Studies of HTS*, Vol. 22 (ed. by Narlikar), Nova Science Pub., Commack, New York (1997).
[13] V. N. Samovarov, M. Yu. Libin, and I. Ya. Fugol, Fiz. Nizk. Temp. **22**, 1245 (1996) [Low Temp. Phys. **22**, 948 (1996)].
[14] B. Beschofen, S. Sadewasser, and G. Guntherodt, Phys. Rev. Lett. **77**, 1837 (1996).
[15] A. S. Alexandrov, A. M. Bratkovsky, N. F. Mott, and E. K. H. Salje, Physica C **215**, 359 (1993).
[16] N. V. Anshukova, A. N. Golovashkin, L. I. Ivanova, *et al.*, Fiz. Nizk. Temp. **22**, 485 (1996) [Low Temp. Phys. **22**, 372 (1996)].
[17] Yu. B. Gaididei and V. M. Loktev, Fiz. Nizk. Temp. **18**, 135 (1992) [Sov. J. Low Temp. Phys. **18**, 92 (1992)].
[18] J. Ranninger and J. M. Robin, Physica C **253**, 279 (1995).
[19] A. V. Puchkov, D. N. Basov, and T. Timusk, submitted to J. Phys. Condens. Matter (1996).

Translated by R. S. Wadhwa

Analysis of the shift in the superconducting transition under pressure in the Anderson–Hubbard two-orbital model

A. A. Kosov

*Mari State University, Yoshkar-Ola, Mari El, 424001, Russia**

(Submitted August 21, 1997)
Fiz. Nizk. Temp. **24**, 204–214 (March 1998)

The two-orbital Hubbard model is used to obtain formulas for the fermion excitation spectrum in the energy bands hybridized by Anderson's interaction. A transition to the Hubbard operators, which diagonalizes the one-site part of the Hamiltonian, allows us to use the Green's temperature function technique to take into account the interstitial jump term while studying the superconducting properties of the model. An analysis of the lower part of the energy spectrum leads to a formula for the superconducting transition temperature T_c associated with the pairing of quasiparticles in one of the correlated bands. The dependence of T_c on electron concentration and energy parameters determining the intraatomic correlation is studied. Proposing a simple relation between the value of pressure (P) and width of the correlated band, the dependence of T_c on the pressure was defined. Good agreement between the theoretical calculation of the dependence of T_c on the pressure and the experimental results for $Y_{1-x}Pr_xBa_2Cu_3O_{7-\delta}$ is found. Comparison of the theoretical and experimental results for the dependence of T_c and its derivative $d(\ln T_c)/dP$ on Sr and Bi-content (x) in $La_{2-x}Sr_xCuO_4$ has been made. It is concluded that the model under consideration can be used for the description of the shift in T_c under pressure for a number of superconductors.
© *1998 American Institute of Physics.* [S1063-777X(98)00203-5]

1. INTRODUCTION

The theoretical investigation of transition metal compounds is greatly complicated by the need to take into account not only the band effects but also the atom-like behavior of d and f states. Nevertheless, investigations of strongly correlated systems have increased during the last few years.[1,2] The enhanced interest in this problem is due to the conviction of many researches that strong electron correlations in the d (f)-electron subsystem ensure a comparatively high superconducting transition temperature T_c in cuprate compounds like $La_{2-x}Sr_xCuO_4$, $YBa_2Cu_3O_{7-\delta}$, $Tl_2Ba_2CuO_y$, and others. Investigation of the mechanisms of superconductivity of such systems is closely connected with the high-pressure investigation of these substances. One of the advantages of using high pressure technique is to change atomic distance without any substitution of components, which often causes some side effects.[3,4]

One of the popular models, which is used for the description of a strongly correlated system, is the Hubbard model.[5] Recently, Kosov and Shilov showed[6] that Hubbard's two-orbital degenerate model is quite promising for studying the superconducting transition in narrow-band materials. In contrast with Hubbard's classical single-orbit model,[5] the two-orbit modification has a greater potential and can describe the behavior of two groups of strongly interacting electrons, i.e., conduction electrons and electrons localized at crystal lattice sites.

This work is devoted to the theoretical study of the superconducting transition and the high pressure effect in compounds, described by a unified Hamiltonian containing operators of Hubbard's two-orbital model and Anderson's interaction. Such unification considerably enhances the possibilities of Hubbard's two-orbital model and allows a more consistent analysis than, say, that in Refs. 7–9, of the interaction of nonlocalized and localized electrons by proceeding from the mixing of their one-particle states. In order to develop the paper[6] we include here the Coulomb repulsive interaction of conduction electrons on the one site U_1. Taking into account the potential U_1 allows us to compare the results of the investigation of T_c, which were obtained here, with well-known results of others models.

In Sec. 2 we derive the energy spectrum of a system described by the Hubbard–Anderson two-orbit model. In Secs. 3 and 4 we use the Green's temperature functions to study the energy spectrum in disperse bands. We obtained the operator responsible for superconducting pairing in the strong-coupling approximation and analyzed its energy dependence. On the basis of a numerical analysis we show that there exists an optimal range of variation of energy parameters, which corresponds to the maximum value of T_c. Special attention is focused on the dependence of T_c on the potentials U_1 and V_0 (Anderson's hybridization) and on the single-particle energy E. In Sec. 5 we calculate the effect of pressure on the superconducting transition temperature. A comparison of theoretical and experimental results for the dependence of T_c on pressure in $Y_{1-x}Pr_xBa_2Cu_3O_{7-\delta}$, and for the dependence of T_c and its derivative $d(\ln T_c)/dP$ on Sr- and Bi-content x in $La_{2-x}Sr_xCuO_4$ and $BaPb_{1-x}Bi_xO_3$ has been made.

 © 1998 American Institute of Physics

2. WAVE FUNCTIONS

In order to describe the properties of the strongly correlated electron system we start from the Hamiltonian

$$\mathscr{H}=\mathscr{H}_0+\mathscr{H}_{\rm int}=\sum_i \mathscr{H}_{0i}+\sum_{ijs} t_{ij}C_{is}^+C_{is}, \tag{1}$$

$$\begin{aligned}\mathscr{H}_{0i}=&-\mu(n_{ia\uparrow}+n_{ia\downarrow}+n_{ic\uparrow}+n_{ic\downarrow})+E(n_{ia\uparrow}+n_{ia\downarrow})\\&-H(n_{ia\uparrow}-n_{ia\downarrow}+n_{ic\uparrow}-n_{ic\downarrow})+In_{ia\uparrow}n_{ia\downarrow}\\&+U(n_{ia\uparrow}+n_{ia\downarrow})n_{ic\uparrow}+n_{ic\downarrow})+U_1n_{ic\uparrow}n_{ic\downarrow}\\&+V_0(a_{i\uparrow}^+C_{i\uparrow}+a_{i\downarrow}^+C_{i\downarrow}+\text{H.c.}),\end{aligned}$$

where C_{is}^+, C_{is} and a_{is}^+, a_{is} are the field operators corresponding to free and localized electrons at the site i with spin projection s; $n_{ias}=a_{is}^+a_{is}$ and $n_{ics}=C_{is}^+C_{is}$ are the operators of the electrons; μ is the chemical potential; H is the applied magnetic field; E is the one-particle energy of a-electrons; I, U, and U_1 are the energy parameters defining intraatomic correlation; I is Hubbard interaction of localized electrons; U is the interorbital Coulomb interaction of c- and a-electrons; U_1 is the repulsive interaction of c-electrons at one site; V_0 is the matrix element responsible for hybridization of c- and a-electronic states (Anderson constant); and $\mathscr{H}_{\rm int}$ describes the interstitial tunneling of c-electrons with transport integral t_{ij}.

Diagonalization of the single-cell Hamiltonian $\mathscr{H}_{0i}$ and transition to the Hubbard operators X_p^q lead to the following results for the wave function and the energy spectrum:

$$E_0=0,\quad \Psi_0=|0,0\rangle-\text{vacuum state};$$

$$E_{A,B}=-\mu+(E-2H)/2\pm(E^2/4+V_0^2)^{1/2};$$

$$\Psi_{A,B}=\cos\alpha|+,0\rangle\pm\sin\alpha|0,+\rangle;$$

$$E_{C,D}=-\mu+(E+2H)/2\pm(E^2/4+V_0^2)^{1/2};$$

$$\Psi_{C,D}=\cos\alpha|-,0\rangle\pm\sin\alpha|0,-\rangle;$$

$$|s,0\rangle=a_{is}^+|0,0\rangle;|0,+\rangle=C_{is}^+|0,0\rangle;$$

$$\cos\alpha=Z/(Z^2+V_0^2)^{1/2};$$

$$\sin\alpha=V_0/(Z^2+V_0^2)^{1/2};$$

$$Z=\begin{cases}(E^2/4+V_0^2)^{1/2}+E/2 & \text{if } E>0;\\(E^2/4+V_0^2)^{1/2}-E/2 & \text{if } E<0.\end{cases}$$

It was mentioned in the introduction that the one-particle states A, B, C, and D depend on the energy V_0:

$$E_{F,G}=U-2\mu+E\pm 2H;$$

$$\Psi_F=|+,+\rangle;\quad \Psi_G=|-,-\rangle;$$

$$E_T=U-2\mu+E;$$

$$\Psi_s=2^{-1/2}\{|+,-\rangle-|-,+\rangle\};$$

$$|+,+\rangle=a_{i\uparrow}^+\,C_{i\uparrow}^+\,|0,0\rangle;\quad |-,-\rangle=a_{i\downarrow}^+\,C_{i\downarrow}^+\,|0,0\rangle;$$

$$|+,-\rangle=a_{i\uparrow}^+\,C_{i\downarrow}^+\,|0,0\rangle.$$

The energy of the remaining two-particle states, E_K, E_L, and E_M, can be obtained by using the cubic equation

$$X^3+AX^2+BX+C=0; \tag{2}$$

$$A=-(I+U+U_1+3E);$$

$$B=(I+2E)(I+U)+U_1(3E+U+I)-4V_0^2;$$

$$C=2V_0^2(I+2E+U_1)-U_1(E+U)(2E+I).$$

The roots $X=\{X_m\}$ of Eq. (2) define the energy $E_{K,L,M}$; $X_m=2\mu+E_{m,m=K,L,M}$. The wave functions Ψ_K, Ψ_L, and Ψ_M, which correspond to the energy states E_K, E_L, and E_M, are presented in the Appendix. It must be emphasized that a consideration of two-particle states is the most significant aspect of this research, which distinguishes it from the widely discussed calculation of T_c in the t-J model,[10] which does not directly take into consideration the two-particle electron states at a single site.

After exact diagonalization of the single-lattice part of the Hamiltonian (1), it can be represented in terms of Hubbard diagonal operators X_p^q in the following form:[6]

$$\mathscr{H}_{0i}=\sum_P E_PX_P^P,$$

$$P=0,\ A,\ B,\ \ldots,\ K,\ L,\ M. \tag{3}$$

The operator $\mathscr{H}_{\rm int}$ which is responsible for interstitial electron jumps can be represented as the quadratic form of nondiagonal Hubbard operators:

$$\mathscr{H}_{\rm int}=\sum_{ijs} t_{ij}g_{is}^*(X)g_{js}(X). \tag{4}$$

The operators C_{is}^+ and C_{is} in $\mathscr{H}_{\rm int}$ are expressed using the matrix defined in Eq. (A1) in terms of the Hubbard operators, and are given in terms of the operator functions $C_{is}^+=g_{is}^*(X)$ and $C_{is}=g_{is}(X)$, whose explicit form is given in the Appendix by Eqs. (A2) and (A3).

Since it is difficult to analyze operators (3) and (4) directly, we restrict our analysis to certain conditions for preliminary calculations. We assume that I, $U\gg U_1$, $|E|$, $|\mu|$, and V_0. Also, we need to check our results according to two separate conditions: $E>0$ and $E<0$. For this reason, we use the intermediate symbols:

$$Q=\begin{cases}B & \text{if } E>0;\\A & \text{if } E<0;\end{cases}$$

$$S=\begin{cases}D & \text{if } E>0;\\C & \text{if } E<0\end{cases}.$$

This means, for example, that for the value R_K^S we have

$$R_K^S=\begin{cases}R_K^D & \text{if } E>0;\\R_K^C & \text{if } E<0.\end{cases}$$

After the satisfaction of these conditions we need to consider the one-particle states Ψ_Q and Ψ_S, the two-particle state Ψ_K, and the vacuum state Ψ_0 only. Furthermore, based on consideration of the low-lying part of the energy spec-

trum, we will obtain the formula for the superconducting transition temperature T_c resulting from the paired quasiparticles in one of the correlated bands.

3. THE GREEN'S FUNCTIONS

According to Zyubin *et al.*[9] and Plakida *et al.*,[10] who applied and developed the Green's function technique for solving such a problem, the above-mentioned energy levels of single-cell part of the Hamiltonian, correct wave functions, and familiar commutation relations for Hubbard operators can be used for finding the spectrum of elementary excitations of nonlocalized c-electrons in the strong-coupling approximation and for investigating their superconducting properties. Using these assumptions, we define the vector

$$\Psi^+=(X_Q^0,X_S^0,X_K^S,X_K^Q).$$

We then determine the temperature Green's functions[11]

$$G(R_m,\tau;R_n,\tau')=-\langle T_\tau\Psi(R_m,\tau)\Psi^+(R_n,\tau')\rangle. \tag{5}$$

The equations for the components of the Green's function G are determined in the Appendix by Eq. (A4). We obtain these equations by assuming the existence of the order parameter Δ_0^K in the superconducting phase:

$$\Delta_0^K=\langle\Psi_K|X_Q^0(R_m)X_K^Q(R_m)+X_K^S(R_m)X_S^0(R_m)|0,0\rangle$$
$$=\langle\Psi_K|X_K^0(R_m)|0,0\rangle. \tag{6}$$

The origin of the parameter Δ_0^K is closely related to the anomalous mean $\langle 2,0|C_{m\uparrow}^+C_{m\downarrow}^+\|0,0\rangle$, which plays a fundamental role in the classical model of superconductivity of nonlocalized BCS electrons.[12] This can be verified, first using Eq. (A2) for the operators $C_{m\uparrow}^+$ and $C_{m\downarrow}^+$ and, secondly, through a detailed analysis of the symmetry properties of the state Ψ_K. It can be seen from Eq. (A1) that the wave function Ψ_K is a linear combination of the initial functions $|0,2\rangle$, $|2,0\rangle$, $|T\rangle$ and, together with them, corresponds to the spin $S=0$ of the two groups of electrons, while the spin moments described by these states of the two particles are opposite. If $V_0=0$ (hybridization of localized and conduction electrons is absent), we have $\Psi_K=\Psi_K^0=|0,2\rangle$. It can be seen from definition (6) that Δ_0^K can be defined in terms of the anomalous functions $F_{QK}^{0Q}(p,\omega_n)$ and $F_{KS}^{S0}(p,\omega_n)$:

$$\Delta_0^K=T\sum_p\sum_n[F_{QK}^{0Q}(p,\omega_n)+F_{KS}^{S0}(p,\omega_n)]. \tag{7}$$

The main determinant of Eqs. (A4) is

$$D=(\omega_n^2+(\xi_{10}(t_p))^2)(\omega_n^2+(\xi_{20}(t_p))^2)$$
$$+t_p^2\cos^2\alpha(R_K^S)^2(\Delta_0^K)^2[(E_K+E_S-E_Q)^2+4\omega_n^2]; \tag{7a}$$

$$\xi_{20,10}(t_p)=-\mu-\Delta/2-[\cos^2\alpha(n_0+n_Q)+(R_K^S)^2$$
$$\times(n_S+n_K)]t_p/2\pm(1/2)\{[\cos^2\alpha(n_0+n_Q)$$
$$+(R_K^S)^2(n_S+n_K)]t_p+\Delta_1]^2$$
$$+4\cos^2\alpha(R_K^S)^2(n_S+n_K)(n_0+n_Q)t_p^2\}^{1/2},$$

$$\Delta=-(E_K+2\mu);$$

$$\Delta_1=\Delta+E-\mathrm{sign}(E)[E^2+4V_0^2]^{1/2}.$$

The quantity $\xi_{20,10}$ is the energy spectrum of dispersed bands in the normal state, and n_0, n_Q, n_S, and n_K are the population densities of the energy states Ψ_0, Ψ_Q, Ψ_S, and Ψ_K, which satisfy the condition $(n_S+n_K)+(n_0+n_Q)=1$. For numerical calculations we will use one parameter for concentration n, where

$$(n_0+n_Q)=1-n/2 \quad \text{and} \quad (n_K+n_S)=n/2. \tag{7c}$$

The conditions (7c) are convenient for the half-filling of the c-band.

After solving the equation $D=0$, the following expression for the energy spectrum in the Anderson bands at $T<T_c$ can be found:

$$\xi_{2,1}^2=(\xi_{10}^2+\xi_{20}^2)/2\pm\{[(\xi_{10}^2-\xi_{20}^2)/2]^2$$
$$+\cos^2\alpha(R_K^S)^2t_p^2(\Delta_0^K)^2[2(\xi_{10}^2+\xi_{20}^2)$$
$$-(E_K+E_S-E_Q)^2+4\cos^2\alpha(R_K^S)^2t_p^2(\Delta_0^K)^2]\}^{1/2}. \tag{7b}$$

Knowing the Green's function $G(p,\omega_n)$ and the electron concentrations for localized states with zero dispersion and using the completeness condition (A5) for occupation numbers, we can determine the chemical potential μ for $\Delta_0^K=0$. For this purpose, we assume that the density of states in the dispersion region has a rectangular shape:[6,8,9]

$$\rho(\varepsilon)=\frac{1}{2W}\,\theta(W^2-\varepsilon^2),$$

where $2W$ is the width of the c band.

Carrying out calculations similar to those in Refs. 6 and 9, we obtain the expression for the chemical potential

$$\mu=-\frac{\Delta}{2}-\frac{WB_+}{2}+2(n_K+n_S)W(R_K^S)^2-\frac{P_-}{2};$$

$$P_\pm=\{B_+^2W^2\pm2\Delta_1B_-W+\Delta_1^2\}^{1/2}; \tag{8}$$

$$B_\pm=\cos^2\alpha(n_0+n_Q)\pm(R_D^K)^2(n_K+n_S).$$

The chemical potential μ is determined by the concentration of electrons in the dispersed correlated band, which equals $n_c=(R_K^S)^2(n_K+n_S)$. The dependence of n_c and μ on V_0 shows different behavior patterns in the cases $E>0$ and $E<0$. An increase of the hybridizing parameter V_0 leads to a decrease of n_c when $E>0$ and to its increase when $E<0$.

4. TEMPERATURE OF THE SUPERCONDUCTING TRANSITION

Before solving Eq. (7) for T_c, we must determine the Green's functions $F_{QK}^{0Q}(p,\omega_n)$ and $F_{KS}^{S0}(p,\omega_n)$ with the help of Eq. (A4). We write the following expression for these functions:

$$F_{QK}^{0Q}(p,\omega_n)=-t_p\Delta_0^K(R_K^S)^2(n_K+n_S)(i\omega_n-E_Q)\times\frac{i\omega_n-E_Q+E_K-B_-t_p}{\Omega_0};$$

$$F_{KS}^{S0}(p,\omega_n)=-t_p\Delta_0^K\cos^2\alpha(n_0+n_Q)\times(i\omega_n+E_S-E_K)\frac{i\omega_n+E_S+B_-t_p}{\Omega_0};$$

$$\Omega_0=(\xi_2^2+\omega_n^2)(\xi_1^2+\omega_n^2), \tag{9}$$

where ξ_2 and ξ_1 are given in Eq. (7b).

Taking the relation (7) into account and considering that $\Delta_0^K(T_c)=0$, we obtain the equation for the critical temperature T_c

$$1=\int_{-W}^{W}\frac{tJ(t)\tanh[\xi_{10}(t)/2T_c]dt}{4W[\xi_{20}^2(t)-\xi_{10}^2(t)]\xi_{10}(t)}; \tag{10}$$

$$J(t)=\cos^2(\alpha)(n_0+n_Q)(\xi_{10}(t)+E_S-E_K)(\xi_{10}(t)+E_S+B_-t_p)+(R_K^S)^2(n_K+n_S)(\xi_{10}(t)-E_Q)\times(\xi_{10}(t)-E_Q+E_K-B_-t_p);$$

here $\xi_{10}(t)$ and $\xi_{20}(t)$ are determined by Eq. (7a).

In order to solve Eq. (10) approximately, we determine the value of t_0 from the equation $\xi_{10}(t_0)=0(-W<t_0<W)$:

$$t_0=\frac{(2\mu+\Delta)^2-\Delta_1^2}{2[\Delta_1B_-+B_+(2\mu+\Delta)]}.$$

The approximate formula for T_c following from Eq. (10) and $\xi_{10}(t_0)=0$ has the form

$$\frac{T_c}{2W}=0.57\left[-\frac{\xi_{10}(-W)\xi_{10}(W)}{W^2}\right]^{1/2}\exp[-1/A(n,t_0)];$$

$$\xi_{10}(-W)=-2(R_K^S)^2(n_K+n_S)W, \tag{11}$$

$$\xi_{10}(W)=-\mu+\frac{B_+W-P_+-\Delta}{2};$$

$$A(n,t_0)=\Gamma(n,t_0)/\Lambda(n,t_0);$$

$$\Gamma(n,t_0)=t_0[\cos^2\alpha(n_0+n_Q)(E_S-E_K)(E_S+B_-t_0)+(R_K^S)^2(n_K+n_S)E_Q(E_Q-E_K+B_-t_0)];$$

$$\Lambda(n,t_0)=W[B_+(2\mu+\Delta)+B_-\Delta_1](2\mu+\Delta-B_+t_0).$$

The quantity $A(n,t_0)$ plays the role of the quasiparticle scattering amplitude with different spin orientations. The attraction between quasiparticles in a correlated band takes place under the conditions

$$A(n,t_0)>0;\quad -W<t_0<W;\quad \xi_{10}(W)\geqslant 0. \tag{12}$$

The conditions (12) can be used to determine the concentrations $n_{S1}<n<n_{S2}$, for which $T_c\neq 0$. Solving the equation $\xi_{10}(W)=0$ gives the following value for n_{S2}:

$$n_{S2}=2\cos^2\alpha/[\cos^2\alpha+(R_K^S)^2]. \tag{12a}$$

The condition $A(n,t_0)=0$ gives the following result for n_{S1}:

$$n_{S1}=\frac{2\cos^2\alpha}{\cos^2\alpha+2(R_K^S)^2}. \tag{12b}$$

In particular, if we set $V_0=0$ and $E>0$ in (12a) and (12b), we obtain $n_{S1}=2/3$ and $n_{S2}=1$. This result has been obtained in Ref. 7 in the frame of the one-orbit Hubbard model (the so-called ''kinematics mechanism of superconductivity'').

5. PRESSURE EFFECTS

Many investigations of high-T_c superconductors have been performed at high pressure.[3,4,13,14] The application of pressure usually strongly affects the crystal structure of materials. High-pressure investigations of elastic properties often give important information about the relation between T_c and crystal symmetry. Applying the two-orbit Anderson-Hubbard model to describe the pressure dependence of T_c, we chose to study the energy parameters, which more sensitively depend on the pressure P. Since U, I, U_1, V_0, and E are on-site properties, their pressure dependence can be ignored. The transport integral t_p depends on the spatial distribution of atoms and can be changed by the applied pressure. Let us consider the region where W depends linearly on $t_p(W-t_p)$. According to Ref. 15, the transport integral in metal oxides can be expressed in terms of the lattice parameters of the CuO_2 planes a, b, and c by the formulas

$$t_\parallel=h^2/(2m_\parallel a^2);\quad t_\perp=h^2/(2m_\perp c^2),$$

where $m_\parallel$ and $m_\perp$ are the respective effective masses.

Disregarding pressure dependence of the effective masses, we estimate the magnitude of dW/dP:

$$dW/dP\sim dt_p/dP\sim -2W(d\ln a/dP)=2Wk_a. \tag{13}$$

Here k_a, k_b, and k_c are the compressibility components along each crystallographic direction as defined by

$$k_a=-d\ln a/dP;\quad k_b=-d\ln b/dP;$$

and $k_c=-d\ln c/dP$.

In order to simplify the numerical estimation of these quantities, we consider the case $k_a=k_b=k_c$. Using the relations (13), we obtain the expression for the dependence of the band width on the pressure P

$$W(P)=W(P=0)\exp(2k_aP). \tag{14}$$

Equations (11) and (14) allow us to express T_c as a function of pressure. Using the expression (13), it is possible to obtain equations for dT_c/dP and $d\ln T_c\,dP$:

$$dT_c/dP=T_c(d\ln T_c/dP)\sim 2Wk_a(dT_c/dW); \tag{15}$$

$$\frac{dT_c}{dW}=\frac{T_c}{2W}\left\{1+2W[B_-+(B_+^2(P_+-P_-)W-\Delta_1B_-(P_++P_-))/2P_+P_-]+\frac{2W}{A^2(n,t_0)}\frac{dA(n,t_0)}{dW}\right\};$$

$$\frac{dA(n,t_0)}{dW}=-\frac{A(n,t_0)}{W}+\Lambda(n,t_0)^{-1}\left\{\frac{2(2\mu+\Delta)-2B_+t_0}{B_+(2\mu+\Delta)+\Delta_1B_-}\times[\cos^2\alpha(n_0+n_Q)(E_S-E_K)(E_S+2B_-t_0)+(R_K^S)^2(n_K+n_S)E_Q(E_Q-E_K+2B_-t_0)+A(n,t_0)B_+W(B_+(2\mu+\Delta)+\Delta_1B_-)]-2WA(n,t_0)[2B_+(2\mu+\Delta)+\Delta_1B_--B_+^2t_0]\right\}\frac{d\mu}{dW};$$

$$\frac{d\mu}{dW}=2(R_K^S)^2(n_K+n_S)-\frac{B_+}{2}-\frac{WB_+^2-\Delta_1B_-}{2P_-}.$$

6. DISCUSSION

Superconducting transition

Expression (11) has the standard form of the BCS theory. It should be noted that the amplitude $A(n,t_0)$ directly depends on the values $\cos^2\alpha$ and $(R_K^S)^2$ [see (A3)], which determine, according to (A3), the efficiency of the transition between states Ψ_Q, Ψ_S, Ψ_K, and Ψ_0. As was mentioned above, in the cases $V_0=0$ (hybridization of a and c electrons is absent) and $E>0$, Eq. (11) describes the results of the well-known kinematics mechanism of superconductivity.[7] If we insert $U_1=0$ into (11), we obtain the results of Kosov and Shilov.[6] In order to simplify the analysis of the dependence of T_c on the parameters of the problem, we carried out detailed numerical calculations on the basis of Eq. (11). The results are shown in Figs. 1a–1f. As expected, the concentration dependence of $T_c/2W$ shown in Figs. 1a–1f is bell-shaped with two critical concentrations n_{S1} and n_{S2} ($T_c\neq 0$ for $n_{S1}<n<n_{S2}$). As shown in Fig. 1a, an increase in V_0 when $E>0$ leads to a decrease of the superconducting transition temperature and to a decrease of the concentrations n_{S1} and n_{S2}. In this case Anderson's hybridization partly localizes the electrons and decreases the concentration of carriers in the correlated band $n_c=(R_K^S)^2(n_K+n_S)$. It contributes to the decrease of T_c and shifts the curve $T_c=T_c(n_c)$ to the region of small concentration. If $E<0$, Anderson's hybridization partly delocalizes electrons and increases the concentration of carriers in the lower correlated band $n_c=(R_K^S)^2(n_K+n_S)$. In this case (Fig. 1b), the maximum of the curve $T_c=T_c(n_c)$ increases sharply with increasing value of V_0/W. Such behavior of $T_c(n_c)$ is just the opposite when $E>0$.

The dependence of $T_c(n_c)$ on E/W ($E>0$ in Fig. 1c and $E<0$ in Fig. 1d can be seen in Fig. 1c and 1d. Figure 1e and 1f shows the dependence of T_c on U_1 in different cases, $E>0$ (a) and $E<0$ (b).

Pressure effects

To study the capability of the model presented here to describe the pressure effect on T_c, we attempted to explain the results of a high pressure study of $Y_{1-x}Pr_xBa_2Cu_3O_{7-y}$ by Neumeier *et al.*[14] According to Ref. 16, the substitution of Pr^{4+} for Y decreases the number of in-plane holes in $Y_{1-x}Pr_xBa_2Cu_3O_{7-y}$. In order to take into account this argument we therefore must change the population densities in Eq. (7c):

$$(n_K+n_S)=n/2\rightarrow(2(R_K^S)^2)(n_c-x_p),$$

where x_p is the concentration of Pr^{4+} ions.

Using Eqs. (7c), (11), (14), and (15), we obtain an expression which allows us to find the dependence of $T_c=T_c(P,x_p)$. Initial compressibility data for polycrystalline $YBa_2Cu_3O_{6.93}$ and $YBa_2Cu_3O_{6.6}$ of orthorhombic symmetry were obtained by using a hydrostatic He-gas pressure cell in a neutron diffractometer. According to Ref. 17, the values of k_a and k_b for these compounds are respectively $k_a=2.22\times10^{-3}$ GPa^{-1}, 2.40×10^{-3} GPa^{-1}, $k_b=1.65\times10^{-3}$ GPa^{-1}, and 2.14×10^{-3} GPa^{-1}. In the present numerical calculations we used the value $k_a=k_b=2.42\times10^{-3}$ GPa^{-1}. Figure 2 shows the dependence of $T_c=T_c(P,x_p)$ and the results of a high pressure study by Neumeier *et al.*[14] on $Y_{1-x}Pr_xBa_2Cu_3O_{7-y}$ for a different Pr concentration. We found that the best agreement between this model and experimental data takes place when the intra-atomic parameters of energies are $U=3$ eV, $U_1=2$ eV, $I=8$ eV, $E=-2$ eV, $V_0=1.4$ eV, and $W(P=0)=1$ eV. These values are typical of metal oxides.[18] In Figs. 3 and 4 we compare the theoretical and experimental results[19–21] for the dependence of T_c and its derivative $d(\ln T_c)/dP$ [by using expression (15)] on Sr and Bi-content x in $La_{2-x}Sr_xCuO_4$ and in $BaPb_{1-x}Bi_xO_3$. An analysis of the dependence of $d(\ln T_c)/dP$ on the concentration of carriers n_c based on the results presented in Figs. 3 and 4, indicates that an increase in the band width W leads to a change of sign of the derivative $d(\ln T_c)/dP$ from positive at small values of W (Fig. 3b) to negative at large values of W (Fig. 4b). The results shown in Figs. 3 and 4 are basically in accordance with the experimental results regarding the pressure dependence of the superconducting transition of many metal oxides. The dependence of T_c on the width W of the correlated band, shown in Fig. 5, also indicates that the Anderson-Hubbard two-orbital model, in principle, is able to describe the pressure dependence of T_c for various high-temperature superconductors[22] ($Tl_2Ba_2CaCu_2O_8$, $YBa_2Cu_4O_8$, and others).

This research has been done under the auspices of the Junior Faculty Development Program and was supported by the U.S. Information Agency and Office of Sponsored Programs and Research of Bowling Green State University (BGSU), Ohio.

I am grateful to Ms. C. Crow, Dr. A. M. Boccanfuso, and Dr. D. D. Gehring for their encouragement to carry out scientific and educational research at BGSU. I thank Dr. R. Boughton for interesting discussions.

APPENDIX

1. The wave functions of the two-particle states K,L,M can be determined by the standard procedure after calculating the roots of the cubic Eq. (3):

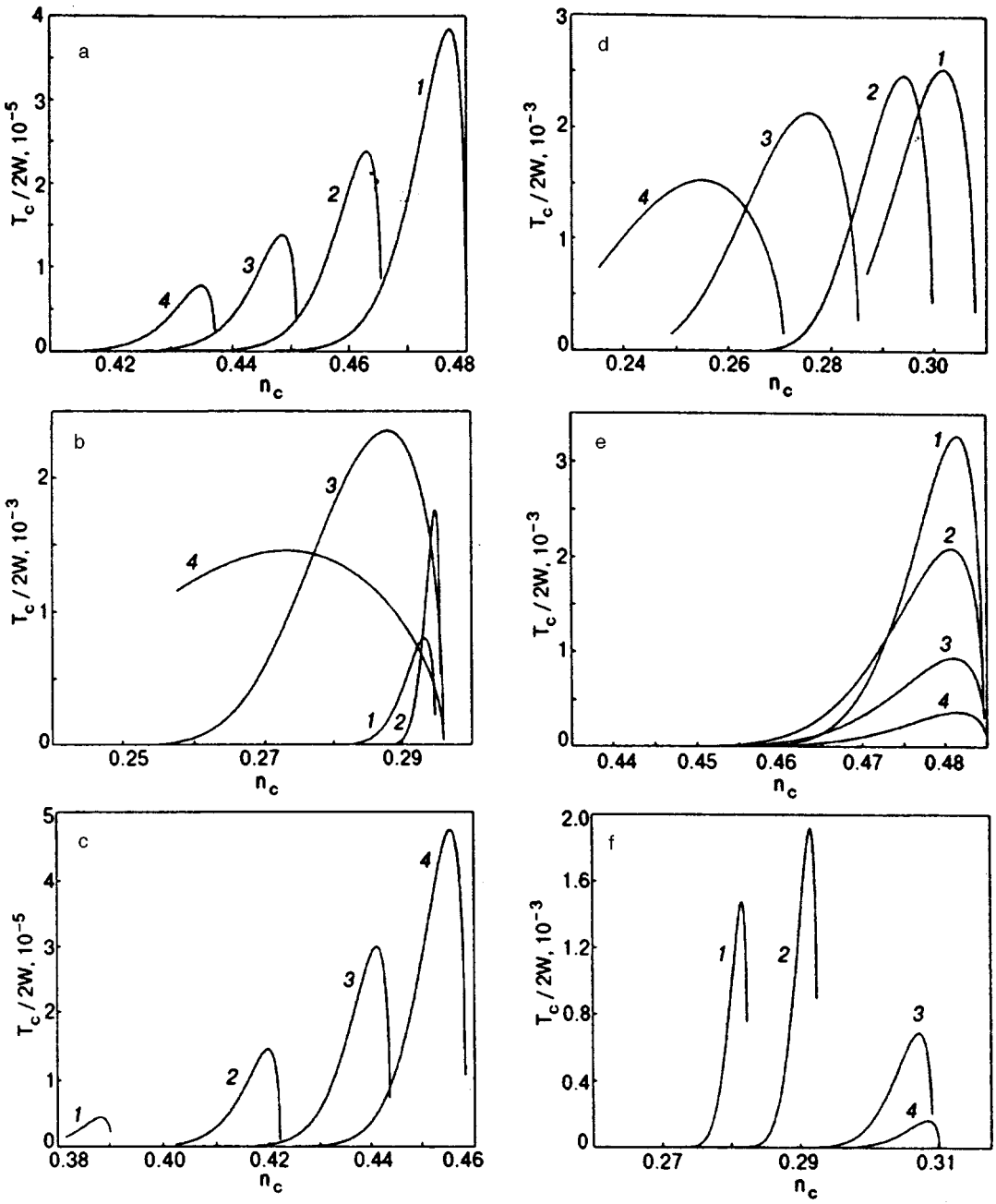

FIG. 1. Dependence of the function $T_c/2W$ on the carriers concentration n_c for the following values of the parameters: $E/W=2.0$, $U/W=6.0$, $U_1/W=3.0$, $I/W=10.0$ at different values of V_0/W: 0.5 (*1*), 0.7 (*2*), 0.9 (*3*), 1.1 (*4*) (a); $E/W=-3.0$, $U/W=6.0$, $U_1/W=4.0$, $I/W=10.0$ at different values of V_0/W: 1.0 (*1*), 1.2 (*2*), 1.4 (*3*), 1.5 (*4*) (b); $V_0/W=1.0$, $U/W=6.0$, $U_1/W=2.5$, $I/W=10.0$ at different values of E/W: 1.0 (*1*), 1.5 (*2*), 2.0 (*3*), 2.5 (*4*) (c); $V_0/W=1.2$, $U/W=6.0$, $U_1/W=2.0$, $I/W=8.0$ at different values of E/W: -1.5 (*1*), -2.0 (*2*), -2.5 (*3*), -2.8 (*4*) (d); $E/W=1.0$, $V_0/W=0.2$, $U/W=6.0$, $I/W=10.0$ at different values of U_1/W: 0.5 (*1*), 1.0 (*2*), 1.5 (*3*), 2.0 (*4*) (e); $E/W=-1.5$, $V_0/W=1.0$, $U/W=6.0$, $I/W=8.0$ at different values of U_1/W: 1.5 (*1*), 2.0 (*2*), 3.0 (*3*), (4.0) (*4*) (f).

$$\begin{pmatrix}\Psi_L\\ \Psi_M\\ \Psi_K\end{pmatrix}=\begin{pmatrix}A_1 & A_2 & A_3\\ B_1 & B_2 & B_3\\ C_1 & C_2 & C_3\end{pmatrix}\begin{pmatrix}|2,0\rangle\\ |T\rangle\\ |0,2\rangle\end{pmatrix}, \tag{A1}$$

$$A_1=(1+A_{21}^2+A_{31}^2)^{-1/2};\quad A_2=A_{21}A_1;$$

$$A_3=A_{31}A_1;$$

$$A_{21}=(E_L-2E-I)^2/2V_0^2;$$

$$A_{31}=(E_L-2E-I)^2/(E_L-U_1)^2;$$

$$B_2=(1+B_{12}^2+B_{32}^2)^{-1/2};\quad B_1=B_{12}B_2;$$

$$B_3=B_{32}B_2;$$

$$B_{12}=\frac{(E_M+2E-U)(E_M-U_1)-2V_0^2}{\sqrt{2}V_0(E_M-U_1)};$$

$$B_{32}=\sqrt{2}V_0/(E_M-U_1);$$

$$C_3=(1+C_{13}^2+C_{23}^2)^{-1/2};\quad C_1=C_{13}C_3;$$

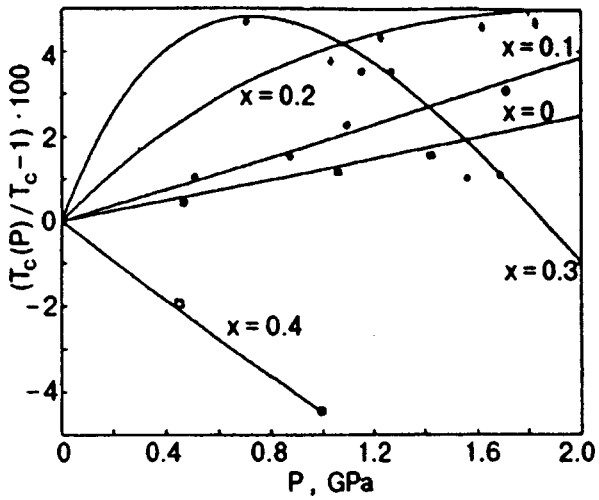

FIG. 2. Experimental data from Ref. 14 and theoretical curves for the percentage shift in the superconducting transition temperature T_c under pressure for $Y_{1-x}Pr_xBa_2Cu_3O_{7-y}$ compounds. The solid lines show the results of numerical calculations using Eq. (15) for the following values of the parameters: $E/W=-2.0$, $V_0/W=1.4$, $U/W=3.0$, $I/W=8.0$, $U_1/W=2.0$, $n_c=x$, $k_a=2.4\times10^{-3}$ GPa^{-1}.

$$C_2=C_{23}C_3;$$

$$C_{13}=[(E_K-E-U)(E_K-U_1)-2V_0^2]/[2V_0^2];$$

$$C_{23}=(E_K-U_1)/\sqrt{2}V_0;$$

$$|T\rangle=2^{-1/2}\{|+,-\rangle+|-,+\rangle\};\quad |2,0\rangle=a_{i\uparrow}^{+}\,a_{i\downarrow}^{+}\,|0,0\rangle;$$

$$|0,2\rangle=C_{i\uparrow}^{+}\,C_{i\downarrow}^{+}\,|0,0\rangle.$$

2. Having determined the reciprocal matrix $\{a_{ij}\}^{-1}$ [the matrix $\{a_{ij}\}$ was written in Eq. (A1)] and using the expressions for the functions $\Psi_{Q,S}$, we can express the field operators C_{is}^{+} in terms of Hubbard's operators:

a. $E>0$;

$$C_{i\uparrow}^{+}=\cos\,\alpha X_B^0+R_D^K X_K^D=g_{i\uparrow}^{*}(X);$$

$$C_{i\downarrow}^{+}=\cos\,\alpha X_D^0+R_B^K X_K^B=g_{i\downarrow}^{*}(X);$$

$$R_D^K=R_B^K=\cos\,\alpha(A_1B_2-A_2B_1)+\sin\,\alpha(A_1B_3-A_3B_1)/\sqrt{2}. \tag{A2}$$

b. $E<0$;

$$C_{i\uparrow}^{+}=\cos\,\alpha X_A^0+R_C^K X_K^D=g_{i\uparrow}^{*}(X);$$

$$C_{i\downarrow}^{+}=\cos\,\alpha X_C^0+R_A^K X_K^B=g_{i\downarrow}^{*}(X);$$

$$R_C^K=R_A^K=\cos\,\alpha(C_1A_3-A_1C_3)/\sqrt{2}+\sin\,\alpha(C_1A_2-C_2A_1). \tag{A3}$$

3. After writing the equation of motion for function (6) using the Hamiltonian expressed by Eqs. (3) and (4), we obtain the following expressions for the components of the Green's function $[G_{qs}^{pr}(\tau,\tau')=-\langle T_\tau X_q^p(\tau)X_s^r(\tau')\rangle=-F_{qs}^{pr}(\tau,\tau')]$ in the momentum-frequency representation:

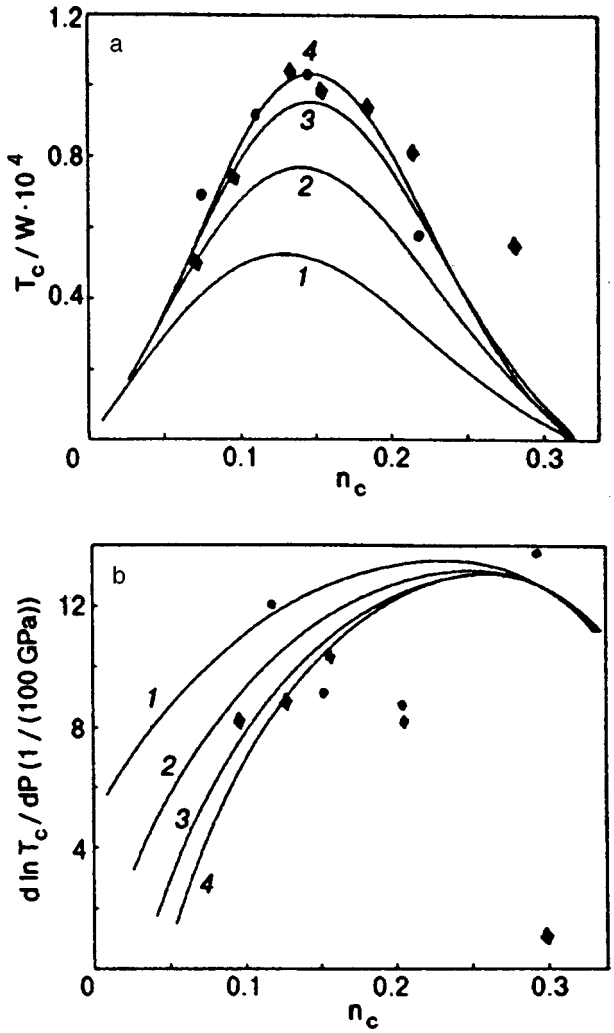

FIG. 3. Experimental data and theoretical curves for the dependence of T_c (a) and its derivative $d(\ln T_c)/dP$ (b) on Sr content x in $La_{2-x}Sr_xCuO_4$ (electron concentration n) (●—Ref. 19; ♦—Ref. 20). Solid lines show the results of numerical calculations using Eq. (15) for the following values of the parameters: $V_0/W=1.25$, $U/W=3.0$, $I/W=5.0$, $U_1/W=1.0$, $n_c=x$, $k_a=8.0\times10^{-3}$ GPa^{-1}, $P=2$ GPa at different E/W: -0.5 (*1*), -0.75 (*2*), -1.0 (*3*), -1.25 (*4*).

$$\begin{pmatrix} n_d+n_k \\ 0 \\ 0 \\ 0 \end{pmatrix}=\begin{pmatrix} b_{11} & b_{12} & b_{13} & b_{14} \\ b_{21} & b_{22} & b_{23} & b_{24} \\ b_{31} & b_{32} & b_{33} & b_{34} \\ b_{41} & b_{42} & b_{43} & b_{44} \end{pmatrix}\begin{pmatrix} G_{DK}^{KD}(p,\omega_n) \\ G_{OK}^{BD}(p,\omega_n) \\ F_{KK}^{BD}(p,\omega_n) \\ F_{DK}^{OD}(p,\omega_n) \end{pmatrix}, \tag{A4}$$

$$\begin{pmatrix} n_b+n_0 \\ 0 \\ 0 \\ 0 \end{pmatrix}=\begin{pmatrix} c_{11} & c_{12} & c_{13} & c_{14} \\ c_{21} & c_{22} & c_{23} & c_{24} \\ c_{31} & c_{32} & c_{33} & c_{34} \\ c_{41} & c_{42} & c_{43} & c_{44} \end{pmatrix}\begin{pmatrix} G_{OB}^{BO}(p,\omega_n) \\ G_{DB}^{KO}(p,\omega_n) \\ F_{KB}^{BO}(p,\omega_n) \\ F_{DB}^{OO}(p,\omega_n) \end{pmatrix},$$

$$b_{11}=i\omega_n+E_D-E_K-(R_D^K)^2(n_d+n_k)t_p;$$

$$b_{22}=i\omega_n-E_B-\cos^2\,\alpha(n_0+n_b)t_p;$$

$$b_{33}=i\omega_n-E_B+E_K+(R_D^K)^2(n_d+n_k)t_p;$$

$$b_{44}=i\omega_n+E_D+\cos^2\,\alpha(n_0+n_b)t_p;$$

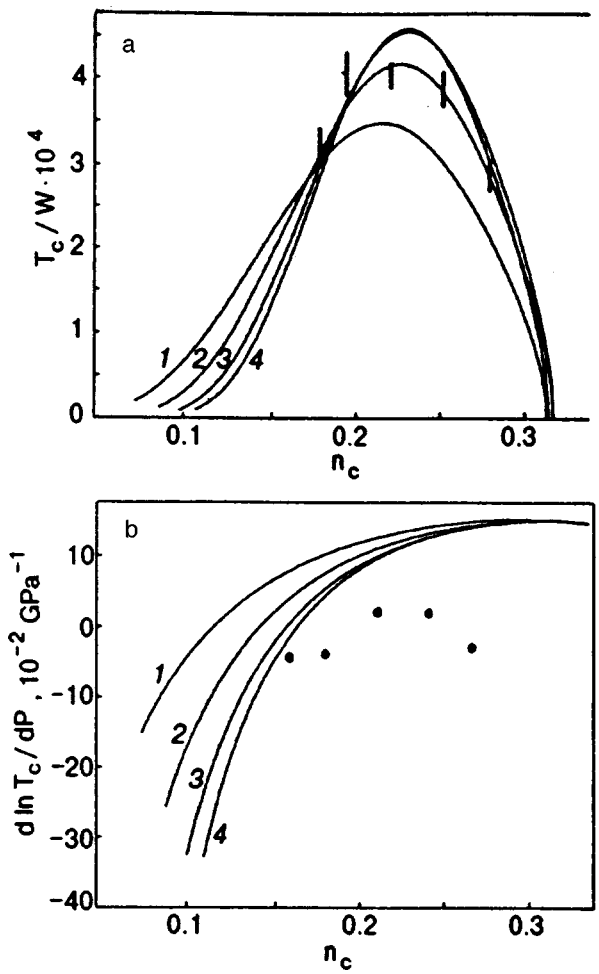

FIG. 4. Experimental data and theoretical curves for the dependence of T_c (a) and its derivative $d(\ln T_c)/dP$ (b) on Bi content x in $BaPb_{1-x}Bi_xO_3$ (electron concentration n) (●—Ref. 21). Solid lines show the results of numerical calculations using Eq. (15) for the following values of the parameters: $V_0/W=1.0$, $U/W=2.4$, $I/W=4.0$, $U_1/W=0.8$, $n_c=x$, $k_a=2.29\times10^{-3}$ GPa^{-1}, $P=2$ GPa at different E/W: -0.4 (*1*), -0.6 (*2*), -0.8 (*3*), -1.0 (*4*).

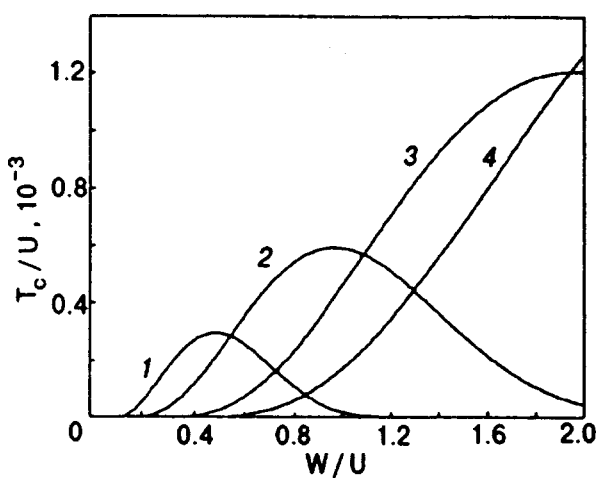

FIG. 5. Dependence of the function $T_c/2W$ on the width of the band for the following values of the parameters: $E/W=-1.5$, $V_0/W=1.0$, $U/W=6.0$, $I/W=8.0$ at different U_1/W: 1.5 (*1*), 2.0 (*2*), 3.0 (*3*), 4.0 (*4*).

$$b_{12}=\cos\alpha R_D^K(n_d+n_k)t_p;$$

$$b_{21}=\cos\alpha R_D^K(n_0+n_b)t_p;$$

$$b_{32}=b_{14}=-c_{31}=c_{24}=-\cos^2\alpha\Delta_0^k t_p;$$

$$b_{23}=b_{41}=-c_{42}=-c_{13}=(R_D^K)^2\Delta_0^k t_p;$$

$$b_{31}=-b_{43}=b_{24}=-b_{13}=c_{23}=-c_{14}=c_{41}=-c_{32}=\cos\alpha R_D^K\Delta_0^k t_p;$$

$$b_{34}=b_{12}=c_{21}=c_{34}=\cos\alpha R_D^K(n_d+n_k)t_p;$$

$$b_{43}=b_{21}=c_{12}=c_{43}=\cos\alpha R_D^K(n_b+n_0)t_p;$$

$$c_{11}=i\omega_n-E_B-\cos^2\alpha(n_0+n_b)t_p;$$

$$c_{22}=i\omega_n-E_K+E_D-(R_D^K)^2(n_d+n_k)t_p;$$

$$c_{33}=i\omega_n-E_B+E_K+(R_D^K)^2(n_d+n_k)t_p;$$

$$c_{44}=i\omega_n+E_D+\cos^2\alpha(n_0+n_b)t_p,$$

where n_b, n_0, n_d, and n_k are the population densities of the energy states under investigation, which satisfy the condition

$$n_b+n_0+n_d+n_k=1, \tag{A5}$$

$\omega_n=(2n+1)\pi T$; T is the absolute temperature; $n=0$, ±1, ±2, ...; and t_p is the momentum representation of the transport integral t_{ij}.

In the case $E<0$ we obtained the same equations for the Green's function as (A4), in which we should make the exchange: $E_B\to E_A$, $E_D\to E_C$, and $R_D^K\to R_C^K$.

*E-mail: kosov@margu.mari.su

[1] Yu. A. Izyumov, M. I. Katsnel'son, and Yu. N. Skryabin, *Magnetism of Collectivized Electrons* [in Russian], Nauka, Moscow (1994).
[2] J. J. Neumeier, Physica C **233**, 354 (1994).
[3] J. S. Schilling and S. Klotz, *Physical Properties of High Temperature Superconductors*, Vol. III, D. M. Ginsberg (Ed.), World Scientific, Singapore (1992).
[4] H. Takahashi and N. Mori, *Studies of High Temperature Superconductors*, vol. 16, Anant Narlikar (Ed.), Nova Science Publishers, INC (1996).
[5] J. Hubbard, Proc. Roy. Soc **A276**, 238 (1963).
[6] A. A. Kosov and V. E. Shilov, Fiz. Nizk, Temp. **22**, 1032 (1996) [Low Temp. Phys. **22**(9), 787 (1996)].
[7] R. O. Zaitsev and V. A. Ivanov, Fiz. Tverd. Tela (Leningrad) **29**, 2554 (1987) [Sov. Phys. Solid State **29**, 1475 (1987)].
[8] D. M. Newns, P. Pattnaik, M. Rasolt, and D. A. Papaconstantopoulos, Physica C **153–155**, 1287 (1988).
[9] P. B. Zyubin, V. A. Ivanov, and E. A. Ugolkova, Teor. Mat. Fiz. **101**, 304 (1994).
[10] N. M. Plakida, V. Yu. Yushankhai, and I. V. Stasyuk, Physica C **160**, 80 (1989).
[11] A. A. Abrikosov, L. P. Gor'kov, and I. E. Dzyaloshinsky, *Methods of Quantum Field Theory in Statistical Physics*, Prentice Hall, Englewood Cliffs, NJ (1963).
[12] J. Schriffer, Superconductivity, Nauka, Moscow (1970).
[13] M. B. Maple, L. M. Paulius, and J. J. Neumeier, Physica C **195**, 64 (1992).
[14] J. J. Neumeier, M. B. Maple, and M. S. Torikachvili, Physica C **156**, 574 (1988).
[15] Marsiglo and J. E. Hirsh, Phys. Rev. B **41**, 6435 (1990).
[16] J. J. Neumeier, T. Bjoernholm, M. B. Maple, and Iv. K. Schuller, Phys. Rev. Lett. **63**, 2516 (1992).
[17] J. D. Jorgensen, S. Pei, D. Lightfoot, D. G. Hinks, B. W. Veal, B. Dabrowski, A. D. Daulikas, R. Kleb, and I. D. Brown, Physica C **171**, 93 (1990).
[18] J. Yu and A. F. Freeman, Phys. Rev. Lett. **58**, 1035 (1987).

[19] N. Tanahashi, I. Ye, T. Tamegai, C. Murayama, N. Mori, S. Yomo, N. Okazaki, and K. Kitazawa, Jpn. J. Appl. Phys. Lett. **28**, L762 (1989).
[20] J. E. Schirber, E. L. Venturini, J. F. Kwak, D. S. Ginley, and B. Morosin, J. Mater. Res. **2**, 421 (1987).
[21] H. Uwe, T. Osada, A. Iyo, K. Murata, and T. Sakudo, Physica C **162–164**, 743 (1989).
[22] N. Mori, C. Murayama, H. Takahashi, H. Kaneko, K. Kawabata, I. Ye, S. Uchida, H. Takagi, M. Tokura, T. Kubo, H. Sasakura, and K. Yamaya, Physica C **185–189**, 743 (1991).

This article was published in English in the original Russian journal. It was edited by S. J. Amoretty.

Hall effect studies in YBCO films

A. L. Solovjov

*B. Verkin Institute for Low Temperature Physics and Engineering, National Academy of Sciences of Ukraine, 47 Lenin Ave., 310164 Kharkov, Ukraine**

(Submitted September 2, 1997)
Fiz. Nizk. Temp. **24**, 215–218 (March 1998)

The longitudinal, $\rho_{xx}(T)$, transverse, $\rho_{xy}(T)$, and Hall, $\rho_H(T)$ resistivities have been measured for $YBa_2Cu_3O_x$ (YBCO) films, showing positive resistivity buckling and those with usual linear $\rho_{xx}(T)$ dependence. In the former case unexpected peak on $\rho_{xy}(T)$ and unusual $\rho_H(T)$ dependence with double sign change just above transition temperature T_c have been revealed. The data are analyzed using recent theory for the sign of the Hall conductivity in strongly correlated systems. © *1998 American Institute of Physics.* [S1063-777X(98)00303-X]

1. INTRODUCTION

Investigation of the Hall effect is known as a useful method in getting reliable information about specific normal-state properties of high-T_c superconductors (HTS's),[1] which are believed to be of primary importance in deciphering their behavior in the superconducting-state. Despite a huge amount of papers published on this problem, unusual temperature dependence of the Hall resistivity with sign reversal (SR) at the resistive transition[2] still remains controversial. Besides, there is an evident dependence of the properties of HTS's on the carrier density in the CuO_2 planes, n_h, which is determined by oxygen doping and which leads to spin gap opening[3] in the underdoped regime. Another phenomenon in HTS's, which also depends on doping, is the enhanced electron-electron correlation.[4,5] In slightly underdoped regime ($80\ \mathrm{K} < T_c < 90\ \mathrm{K}$), where the features of the spin scattering are not so pronounced, effects due to electron-electron correlation are believed to be observable, both in the resistivity and Hall effect measurements. However, the role of both mechanisms in superconducting coupling in HTS's is still questionable.

2. RESULTS AND DISCUSSION

To further investigate this point, we carried out resistivity and Hall effect measurements of YBCO films with different oxygen content. In this paper we report the results obtained on two YBCO films, designated below as samples S1 and S2, and on a reference film (S3). The films were epitaxially grown by pulsed laser deposition on $SrTiO_3$ (100) substrates and patterned into well-defined $4\times 02.$ mm Hall-bar structures by standard lithography and chemical etching techniques.[6] The Hall-bar geometry consists of current leads and three pairs of transverse voltage contacts. To exclude uncertainties due to geometric effect, the Hall data reported here have been acquired using both the first and the third pair.

The reference film with $T_c = 90$ K shows a typical dependence for such YBCO systems, which is almost linear $\rho_{xx}(T)$ dependence in the normal state. But S1 ($T_c = 86$ K) and S2 ($T_c = 84$ K) demonstrate enhanced resistivity and slightly positive resistivity buckling just above 120 K (S1) and 110 K (S2), respectively. Here T_c is defined as the temperature at which the approximated $\rho_{xx}(T)$ drops to zero. The enhancement of the resistivity and lowering of T_c suggest that the films are in a slightly underdoped regime. On the other hand unusual buckling can be attributed to the changes in spin-fluctuation parameters, as it has been studied extensively by Stojkovich and Pines.[7]

The longitudinal resistivity $\rho_{xx}(T)$ was measured and the transverse resistivity $\rho_{xy}(T) \sim V_{xy}/I_{xx}$, which simultaneously has been observed on the transverse pairs of contacts even in the absence of magnetic field, was investigated. Simple algebra yields (2–4) μm misalignment of opposite transverse strips is enough to produce $R_{xy}(100\ \mathrm{K}) = (0.5 - 1)\Omega$, which is usually observed experimentally. To avoid a suspicion of thermo-emf origin of the transverse signal, we performed measurements with a very small transport current, $I_{xx} = 10^{-7}$ A. No transverse voltage has been observed in this case. Any other intrinsic reasons that may cause the transverse signal have not yet been identified.

No unexpected peculiarities are revealed on the $\rho_{xx}(T)$ dependences of the reference film and S1, whereas S2 exhibits a pronounced ρ_{xy}-vs-T peak at the beginning of the resistive transition (Fig. 1, squares). The peak starts to grow at $T_{c0} > T_c$, which is the temperature at which the magnetic field begins to broaden the resistive transition (Fig. 2, solid and dashed lines). The peak is clearly seen on both pairs of contacts, suggesting its intrinsic nature. The magnetic field B_z, of opposite directions, along the c axis and vice versa, noticeably suppresses the peak and shifts it slightly towards low temperatures (Fig. 1, dots and circles).

There are several theoretical models[8,9] to describe the appearance of the transverse voltage in HTS's. According to Glazman,[8] vortices and antivortices produced by the transport current can attract each other at a relatively small current, when the number of vortices is not too large. The interaction gives rise to deformation of the vortex trajectories. As a result, a nonzero transverse voltage should appear on the film since the trajectories intersect the measurement contour. Unfortunately, no dependence on the external magnetic field is analyzed. The effect must disappear with increasing trans-

 © 1998 American Institute of Physics

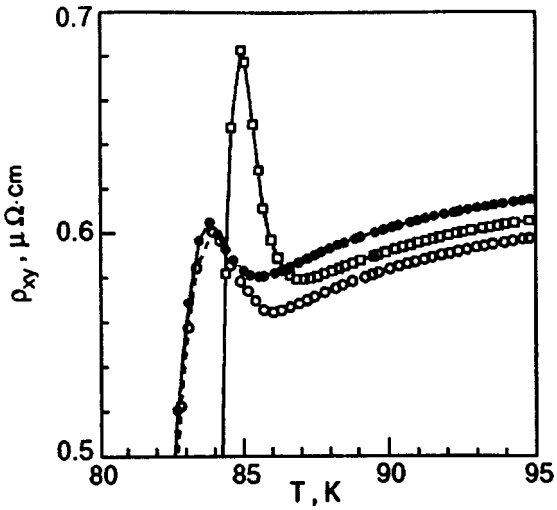

FIG. 1. Effect of magnetic field, $B_z = 600$ mT, applied parallel to the c axis in opposite directions, in the ab plane transverse resistivity, $\rho_{xy}(T)$, for sample S2 (dots and circles). Squares correspond to $\rho_{xy}(T)$ without a magnetic field.

port current, which leads to the enhancement of the number of vortices. However, no expected dependence on current has been observed in our experiments.

Another theoretical approach to the problem has been proposed by Doornbos *et al.*[9] They have shown that inhomogeneity of oxygen impurity concentration in high-T_c oxides leads to spatial fluctuation in the charge carrier density and, consequently, to fluctuation in T_c. Because of the very short coherence length in HTS's, different inhomogeneities, even with very small characteristic lengths, may deeply affect the superconducting properties. To model an inhomogeneous high-T_c superconductor they considered a square, two-dimentional, random resistor network (RRN). Because the resistivities and $T_c's$ of the resistors are expected to be different, there must be a transverse component of the transport current producing the peak just at the beginning of the resistive transition. When activation energy U is considered to be constant, but T_c is randomly distributed, the anomalous peak

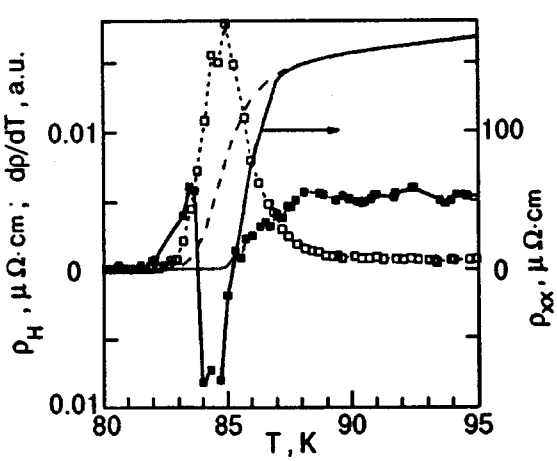

FIG. 2. ρ_H (solid squares), ρ_{xx} (solid line—$B_z = 0$, dashed line—$B_z = 600$ mT) and $d\rho_{xx}/dT$ (squares—$B_z = 600$ mT) vs T dependences for sample S2.

must decrease with increasing magnetic field, as we observed in our experiments. It has been shown[10] that very moderate T_c difference, of the order of 1 K or less, is large enough to produce the effect.

Mosqueria *et al.*[10] used a model[11] similar to RRN to account for their results obtained in measuring the longitudinal resistivity, $\rho_{xx}(T)$, in YBCO single crystals. The oxygen-deficient crystals, with T_c between 85 K and 90 K, showed a similar resistivity peak being quenched by a magnetic field in the same manner as in our measurements. The only difference is that the value of the transverse voltage measured in our experiments is much smaller. In the framework of the RRN model this suggests the fact that a transverse component of the transport current, I_{xx}, which produces the transverse voltage, is rather small, approximately (1–5) $\times 10^{-4} I_{xx}$, which seems to be a reasonable value. Thus the RRN model[9] enables us to physically reasonably explain the appearance of the transverse resistivity peak. We also think that observation of the peak may be viewed as additional evidence that the sample is underdoped. No peaks have been observed on films with $T_c = 90$ K. Moreover, as has been demonstrated by Mosqueira *et al.*[10], after re-oxygenation the crystals showed $T_c \geqslant 90$ K and all peaks disappeared.

As Fig. 1 shows, magnetic field of both opposite directions noticeably affects the resistivity curve in the normal state (Fig. 1, dots and circles). One-half of the distance between these two curves determines the Hall-resistivity,

$$\rho_H(T) \sim (V_{xy}/I_{xx}) = R_H(T) d^{-1} B_z, \tag{1}$$

where d is the sample thickness. Thus, the Hall coefficient R_H can be easily determined. In high-T_c oxides R_H turns out to be temperature dependent[12]. Usually measured experimentally, $\rho_H(T) \sim R_H(T)$ starts to noticeably grow at about 240 K and reaches its maximum level just above T_{co}, as the temperature is lowered. Below T_{co}, $\rho_H(T)$ rapidly decreases, becomes negative, and then comes to zero at $T_c(H)$, thus giving rise to the sign reversal (SR) of the Hall resistivity. Both S1 and S3 show the usual $\rho_H(T)$ dependence with the SR effect. But S2 exhibits unusual, almost linear, $\rho_H(T)$ dependence with a positive slope and unexpected double sign reversal (Fig. 2, solid squares), which was observed experimentally on YBCO films for the first time. As has recently been shown[13], the linear $\rho_H(T)$ dependence can be considered as additional evidence for enhanced electron-electron correlation in the sample.

To account for the SR effect different flux-flow-based models (see, for example, Hagen *et al.*[2] and the bibliography cited there), are commonly used. The authors[2] have concluded that due to the specific interplay between the Magnus force and the drag force, vortex velocity v_L should generate a Hall voltage, whose sign is opposite to that of the normal state. But the double sign reversal effect does not seem to be explained by the models. Moreover, recent theory concerning the Hall effect in strongly correlated (SC) systems[14] is believed to be more appropriate. Using the Hubbard $t-J$ model, Rojo *et al.*[14] have analyzed the Hall current as a function of the filling fraction, $n = N_p/N_s$, where N_p and N_s are the total particle number and the number of sites in the con-

sidered lattice, respectively. In the framework of this approach, the $t-J$ Hamiltonian have to include the Hubbard repulsion,

$$H' = G\sum_{\langle i,j\rangle} (n_i - \langle n\rangle)(n_j - \langle n\rangle), \tag{2}$$

which suggests a clear dependence on n_h with $\langle n\rangle$ being the mean particle number. Finally, the result was found to be strongly dependent on the correlation parameter G/t. When $G/t=0$, the equilibrium Hall current changes sign at half filling as the Fermi surface changes its shape from electron-like to hole-like shape. As a result, the usual SR effect is observed. In the strongly correlated limit ($G/t \gg 1$) an additional sign change should occur below half filling, which is entirely due to the correlation, as we have observed experimentally. The results are found to be the same for fermionic and bosonic systems.

To see the applicability of the SC theory to real samples, we should remember that there are many Cooper pairs, which are bosons, in the superconducting state, whereas there are no Cooper pairs in the normal state. Thus, a strong rearrangement of the filling fraction of bosons is expected at the resistive transition, which gives rise to the SR effect. As Fig. 2 illustrates, the Hall resistivity always changes sign at the mean-field transition temperature T_c^{mf}, which is defined as the temperature at which $d\rho_{xx}/dT$ vs T (Fig. 2, hollow squares) has a maximum or $\rho_{xx}(T)$ has the inflection point. This result suggests a half filling of the bosonic lattice at T_c^{mf}, which seems reasonable. In accordance with the SC theory, the observation of the double sign reversal with an additional positive peak below half filling (Fig. 2) should be considered as an indication of enhanced electron-electron correlation in the sample with $G/t \sim 2-3$. Moreover, we consider the other observed peculiarities demonstrated by S2 as additional clear signs of enhanced electron correlation in the sample.

In conclusion, the observed phenomena were found to be in good agreement with the RRN and SC theories. Consequently, the enhanced electron correlations[1,5] should definitely be taken into account in the consideration of scattering and coupling mechanisms in high-T_c superconductors.

The author thanks the staff of MPI-Stuttgart, where the experimental part of this work was done, for their hospitality. He also thanks H.-U. Habermeier for a critical reading of the manuscript, M. Indenbom for computer assistance, B. Leibold for the film preparation, and V. N. Morgun for fruitful discussions.

*E-mail: solovjov@ilt.kharkov.ua

[1] Y. Iye, in Physical Properties of High-Temperature Superconductors III, D. M. Ginsberg (Ed.), World Scientific, Singapore (1992), p. 285.
[2] S. J. Hagen, A. W. Smith, M. Rajeswari, J. L. Peng, Z. J. Li, R. L. Greene, S. N. Mao, X. X. Xi, S. Bhattacharya, Qi Li, and C. J. Lobb, Phys. Rev. B **47**, 1064 (1993).
[3] T. Ito, K. Takenaka, and S. Uchida, Phys. Rev. Lett. **70**, 3995 (1993).
[4] G. M. Ellashberg, J. Supercond. **7**, 525 (1994).
[5] A. L. Solovjov, V. M. Dmitriev, H.-U. Habermeier, and I. E. Trofimov, Phys. Rev. B **55**, 8551 (1997).
[6] H.-U. Habermeler, Appl. Surf. Sci. **69**, 204 (1993).
[7] B. P. Stojkovic and D. Pines, Phys. Rev. B **55**, 8576 (1997).
[8] L. I. Glazman, Sov. J. Low Temp. Phys. **12**, 389 (1986).
[9] G. Doornbos, R. J. Wijngaarden, and R. Griessen, Physica C **235–240**, 1371 (1994).
[10] J. Mosqueira, A. Pomar, A. Diaz, J. A. Veira, and F. Vidal, Physica C **225**, 34 (1994).
[11] R. Vagio, C. Attanasio, L. Maritato, and A. Ruosi, Phys. Rev. B **47**, 15302 (1993).
[12] R. Hopfengartner, M. Leghissa, G. Kreiselmeyer, B. Holzapfel, P. Schmitt, and G. Saemann-Ischenko, Phys. Rev. B **47**, 5992 (1993).
[13] V. P. Galaiko (to be published).
[14] A. G. Rojo, G. Kotliar, and G. S. Canright, Phys. Rev. B **47**, 9140 (1993).

This article was published in English in the original Russian journal. It was edited by S. J. Amoretty.

LOW-TEMPERATURE MAGNETISM

Generalized surface nuclear spin wave induced by external magnetic field

S. V. Tarasenko

A. Galkin Physicotechnical Institute, National Academy of Sciences of the Ukraine, 340114 Donetsk, Ukraine

(Submitted July 22, 1997; revised October 29, 1997)
Fiz. Nizk. Temp. **24**, 219–224 (March 1998)

The two-sublattice model of an easy-axis antiferromagnet is used to show that an additional rhombic anisotropy induced by an external magnetic field can lead to the formation of a generalized nuclear spin wave near the surface of the magnet. The criterion for the existence of a generalized surface spin wave is formulated. © *1998 American Institute of Physics.* [S1063-777X(98)00403-4]

INTRODUCTION

It is well known that a nonzero nuclear spin of magnetic atoms of a crystal leads to the emergence of a hyperfine interaction. The existence of such an interaction leads to the following two main effects in the nuclear spin subsystem of a magnetically ordered crystal: (1) the presence of a strong effective magnetic field at the nucleus, which is responsible for the unshifted NMR frequency ω_n, and (2) the emergence of a special type of one-particle excitations, viz., nuclear spin waves (NSW) in the paramagnetic subsystem of nuclear spins.[1–4] The physical mechanism responsible for the emergence of NSW is the Suhl–Nakamura exchange, i.e., indirect spin–spin interaction of nuclear spins through the subsystem of electron spin waves. In this case, spatial dispersion of NSW is completely determined by the nonlocal nature of the Heisenberg exchange in the electron spin subsystem. Taking into account the finite size of a real magnetic sample, we also obtain the following additional mechanisms of formation of spatial dispersion of NSW disregarding nonuniform exchange (''exchange-free approximation''): the magnetostatic[5,6] and electrostatic[7–11] mechanisms. In the former case, spatial dispersion of NSW is formed owing to indirect interaction of spins in the electron subsystem of the crystal through the magnetic dipole field; the relevant type of nuclear magnons is referred to as magnetostatic NSW. The other ''exchange-free'' mechanism of formation of spatial dispersion of nuclear spin waves in magnetically ordered crystals is the indirect interaction of nuclear spin through the long-range field of quasi-static magnetoelastic deformations. In this case, the NMR frequency ω_n and the minimum phase velocity s of propagation of elastic waves in an unbounded magnetic crystal must satisfy the elastostatic criterion[12]

$$\omega_n \ll sk. \tag{1}$$

Accordingly, the class of nuclear magnons induced by this type of spin–spin exchange was called[7–11] elastostatic NSW. Naturally, the above mechanisms of formation of dispersion properties of NSW in a real crystal are observed simultaneously. It should be noted, however, that most of the crystals in which the dispersion properties of NSW were investigated were exchange-collinear antiferromagnets. It is well known that these materials display, along with exchange enhancement of magnetoelastic effects, also the exchange-induced suppression of magnetic-dipole effects in the spectrum of electron spin waves.[13] Thus, an analysis of nuclear spin dynamics of exchange-limited collinear antiferromagnets in the range of wave vectors **k** satisfying criterion (1) can be confined to simultaneous inclusion of only the ''phonon'' and ''exchange'' mechanisms of formation of NSW dispersion. Such an approach was developed in Ref. 7 for an easy-axis antiferromagnet (EA AFM) such as, for example, MnF_2. Among other things, it was shown that if the antiferromagnetism vector in equilibrium is perpendicular to the mechanically free surface of the AFM with completely free spins, the hybridization of the mechanisms of spin–spin exchange listed above leads to the formation of propagating nuclear spin oscillations of the formerly unknown type (viz., generalized surface NSW of the elasto-exchange type) near the crystal surface. This type of nuclear magnons is a two-partial spin wave. The type of localization of nuclear spin oscillations near the surface of the magnet varies smoothly from the quasi-surface to purely surface type depending on the magnitude of the wave vector $k_\perp$ in the plane of the crystal boundary. However, the entire analysis of the effect of the lattice on the Suhl–Nakamura exchange in the collinear phase of the EA AFM in Ref. 7 was carried out under the assumption of cylindrical symmetry of the magnetic system under investigation (the rotational axis was collinear to the easy axis of the AFM crystal). On the other hand, it was shown in Ref. 10 in the exchange-free (elastostatic) limit that a consistent inclusion of the effect of anisotropy of the magnetic system on the phonon mechanism of formation of NSW dispersion leads to previously unknown types of propagating exchange-free nuclear spin oscillations, viz., anisotropic bulk elastostatic NSW. This type of nuclear magnons did not exist in the crystal for $H=0$. Moreover, it was proved that the shape of the constant-frequency surface of elasto-exchange NSW of an unbounded magnet are in one-to-one correspon-

 © 1998 American Institute of Physics

dence with peculiarities of the bulk elasto-exchange nuclear spin dynamics of thin magnetic films. Under the conditions of hybridization of exchange and phonon mechanisms of formation of NSW dispersion, we can also expect the emergence of new peculiarities in the surface nuclear spin dynamics of an anisotropic magnet, but this problem has not been considered yet. This research aims at determining the conditions necessary for the formation of the formally unknown elasto-exchange types of surface NSW in a magnet, which are induced by magnetic anisotropy of the system.

The article consists of four sections. Section 1 contains general relations characterizing the dynamics of exchange-collinear AFM on the basis of consistent inclusion of interaction between the three subsystems of a real crystal: (1) the electron spin subsystem, (2) the nuclear spin subsystem, and (3) the lattice subsystem. The same section contains the formulation of the corresponding elasto-exchange boundary value problem, which makes it possible to analyze the surface nuclear spin dynamics of the magnetic medium under investigation in the phenomenological limit. The classification of possible types of elasto-exchange nuclear spin oscillations depending on the type of their spatial localization near the magnet surface is carried out in Sec. 2. In Sec. 3, the above boundary-value problem is solved, and the surface NSW of the elasto-exchange type induced by magnetic anisotropy of the medium is determined. The criterion is obtained in Sec. 4 can be used to determine the conditions for the existence of a generalized surface NSW of the elasto-exchange type in the vicinity of the mechanically free surface of an unbounded magnet can be determined on the basis of the results of calculations of the lattice effect on the NSW spectrum of the same magnet in the limit (1).

1. BASIC RELATIONS

By way of an example of magnetic medium, we consider a two-sublattice model ($\mathbf{M}_{1,2}(\mathbf{m}_{1,2})$ are the magnetizations of sublattices of the electron (nuclear) spin system, $|\mathbf{M}_1| = |\mathbf{M}_2| = M_0(|\mathbf{m}_1| = |\mathbf{m}_2| = m_0)$) of an easy-axis AFM ($0Z$ is the easy axis) in an external magnetic field $\mathbf{H} \perp 0Z$. Such a model is valid, for example, for an easy-axis AFM MnF_2 or an easy-plane AFM (XY is the easy plane) $CsMnF_3$ in an external magnetic field $\mathbf{H}$ perpendicular to the ''difficult'' axis. If the applied magnetic field H is small as compared to the intersublattice exchange interaction, we can neglect under conditions (1) (see above) the magnetic-dipole mechanism of the NSW formation in favor of the elastostatic mechanism. For the sake of simplicity and visualization of calculations, we shall assume that the magnetoelastic and elastic energies in the model under investigation are isotropic. As a result, the corresponding density of thermodynamic potential w in the model of an easy-axis AFM under consideration taking into account hyperfine, magnetoelastic, and nonuniform exchange interactions in terms of the ferromagnetism vectors ($\mathbf{m},\mathbf{M}$) and the antiferromagnetism vectors ($\mathbf{l},\mathbf{L}$) for $|\mathbf{M}| \ll |\mathbf{L}|; |\mathbf{m}| \ll |\mathbf{l}|$ can be presented in the form[7]

$$w = 2M_0^2 \left\{ \frac{1}{2}\,\delta \mathbf{M}^2 - \frac{1}{2}\,bL_z^2 + \frac{\alpha}{2}\left(\frac{\partial \mathbf{I}}{\partial x_i}\right)^2 + A\mathbf{Ll} - 2\mathbf{Mh} + \gamma L_i L_k u_{ik} \right\} + \frac{1}{2}\,\lambda u_{ii}^2 + \mu u_{ik}^2, \tag{2}$$

$$2M_0\mathbf{M} = \mathbf{M}_1 + \mathbf{M}_2; \quad 2M_0\mathbf{L} = \mathbf{M}_1 - \mathbf{M}_2;$$
$$2m_0\mathbf{m} = \mathbf{m}_1 + \mathbf{m}_2; \quad 2M_0\mathbf{l} = \mathbf{m}_1 - \mathbf{m}_2, \tag{3}$$

where δ, α, b, and γ are the constants of uniform exchange, nonuniform exchange, axial anisotropy, and magnetostriction respectively, λ and μ are the Lame coefficients, u_{ik} is the strain tensor, $M_0(m_0)$ the saturation magnetization of electron spin (nuclear spin) magnetic sublattice alone, and A the hyperfine interaction constant. Dynamic properties of the system under consideration can be described with the help of a coupled system of equations including the Landau–Lifshitz equations for the ferro- and antiferromagnetic vectors for the electron and nuclear spin systems and the equations of motion of a continuous medium for components of the displacement vector $\mathbf{u}$. Since our goal is to analyze the effect of the lattice on the surface dynamics of the magnetic medium under investigation, the above system of dynamic equations should be supplemented with corresponding boundary conditions. In the case of a mechanically free surface with the normal $\mathbf{n}$ and completely free spins, such a boundary-value problem can be written in the form[7]

$$\frac{\partial \tilde{\mathbf{L}}}{\partial \xi} = \frac{\partial \tilde{\mathbf{M}}}{\partial \xi} = 0; \quad \sigma_{ik} n_k = 0, \quad \xi = 0;$$
$$\tilde{\mathbf{L}}\tilde{\mathbf{M}} \to 0 \quad \text{for} \quad \xi \to -\infty, \tag{4}$$

where ξ is the coordinate along the normal $\mathbf{n}$ to the crystal surface, $\tilde{\mathbf{L}}(\tilde{\mathbf{M}})$ characterizes small oscillations of the vector $\mathbf{L}(\mathbf{M})$ near the equilibrium orientation, and σ_{ik} is the elastic stress tensor.

2. CLASSIFICATION OF POSSIBLE TYPES OF ELASTO-EXCHANGE NSW

If we henceforth assume, without loss of generality, that the applied magnetic field $\mathbf{H} \| 0X$ ($\mathbf{L} \| 0Z$ for $b > 0$), it follows from (2) and (3) that the characteristic equation for the elasto-exchange boundary-value problem (4) with an arbitrary orientation of the wave vector $\mathbf{k}$ can be presented in the form ($\hat{\Lambda}$ is the matrix of the Christoffel tensor, $\Lambda_{ik} = \tilde{c}_{iklm} k_l k_m$, $\omega_T^2 = g^2 2M_0 m_0 \delta A$)

$$\det|\Lambda_{ik}| = 0; \quad \omega_*^2 = \frac{\omega_n^2 \omega_T^2}{\omega_n^2 - \omega^2} + \omega^2; \quad i,k = 1-3;$$
$$\tilde{c}_{ii} = \lambda + 2\mu (i = 1-3); \quad \tilde{c}_{66} = 2\mu; \tag{5}$$
$$\tilde{c}_{12} = \tilde{c}_{23} = \tilde{c}_{13} = \lambda + \mu;$$
$$\tilde{c}_{55} = 2\mu\,\frac{\omega_0^2 + \omega_H^2 - \omega_*^2 + c^2k^2}{\omega_0^2 + \omega_H^2 + \omega_{me}^2 - \omega_*^2 + c^2k^2};$$
$$\tilde{c}_{44} = 2\mu\,\frac{\omega_0^2 - \omega_*^2 + c^2k^2}{\omega_0^2 + \omega_{me}^2 - \omega_*^2 + c^2k^2}. \tag{6}$$

Here $c^2=2M_0^2g^2\delta\alpha$ is the square of the velocity of propagation of the spin wave, $\omega_0^2=g^2 2M_0^2\delta b$; $\omega_H^2=g^2H^2$; ω_{me} is the magnetoelastic gap. It can be easily verified that expressions (5) and (6) describe the spectrum of linear electron-nuclear oscillations propagating in an EA AFM in the elastostatic approximation (1). We shall henceforth confine the analysis to only those geometries of NSW propagation in which the normal to the surface of the half-space coincides with a coordinate axis of the Cartesian system of coordinates chosen in (5), (6), and the lattice displacement vector **u** has only one nonzero component perpendicular to the plane of propagation of NSW. An analysis of relations (5) and (6) shows that in this case the characteristic equation for an EA AFM in $q^2\equiv(\mathbf{kn})^2$ can be quadratic for $\mathbf{k}\in XZ$ or $\mathbf{k}\in YZ$ and cubic for $\mathbf{k}\in XY$. Consequently, an elasto-exchange NSW propagating near the surface of the magnet is accordingly a two- or three-partial wave (for $\mathbf{k}\in XY$). Consequently, the structure of the amplitude (in particular, for a nonzero component of the lattice displacement vector **u**) can be presented in the form

$$u=\sum_j A_j \exp(-q_j\xi)\exp(i\omega t-i\mathbf{k}_\perp\cdot\mathbf{r}_\perp). \tag{7}$$

(A_j are certain constants).

It follows from (5) and (6) as well as from the results obtained in Ref. 8 that since the formation of an elasto-exchange NSW in the model of EA AFM under investigation is impossible for $H=0$ and $\mathbf{k}\in XY$; $\mathbf{u}\|0Z$, we shall analyze the effect of an external magnetic field on the NSW localization near the mechanically free surface of the magnet just for this case. We assume that the normal **n** to the surface of the magnet is directed along $\mathbf{u}\|0Z$ and coincides with one of the Cartesian axes of the coordinate system introduced above. It was mentioned above that the corresponding characteristic equation is bicubic, and hence its roots can be determined in analytical form. However, for the sake of simplicity and visualization of calculations, we consider here only the case when the applied magnetic field $\mathbf{H}\perp\mathbf{L}$ ($H\ll H_E$ is the intersublattice exchange field) satisfies the condition

$$\omega_H^2\gg\omega_0^2;\quad \omega_{me}^2. \tag{8}$$

This condition allows us to disregard the emergence of the antiferromagnetism vector (**L,l**) from the plane with the normal along **H**.[14] If we assume, without loss of generality, that the applied magnetic field is collinear to the axis $0X$, the characteristic equation (5), (6) under the condition (8) becomes biquadratic in q and assumes the following form for different orientations of the normal **n** to the interface ($\mathbf{k}\in XY$; $\tilde{\omega}_0^2\equiv\omega_0^2+c^2k_\perp^2$):

for $\mathbf{n}\|0Y$,

$$q^4-P_1q^2+P_2=0, \tag{9}$$

where

$$P_1=\frac{\tilde{\omega}_0^2+c^2k_\perp^2-\omega_*^2}{c^2};\quad P_2=\frac{\tilde{\omega}_0^2+\omega_{me}^2-\omega_*^2}{c^2}k_\perp^2;$$

for $\mathbf{n}\|0X$,

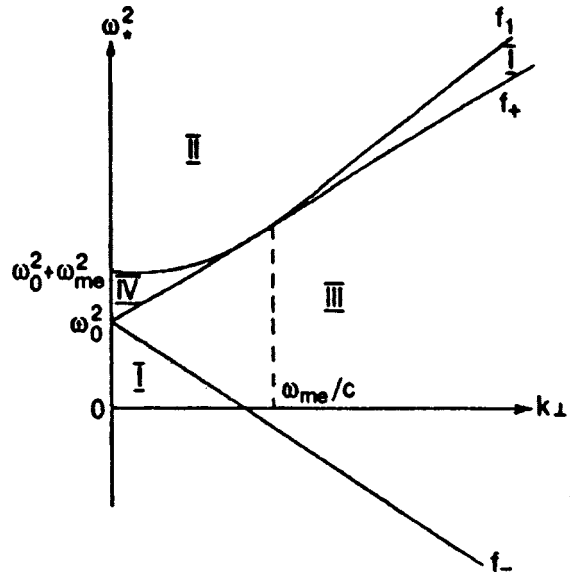

FIG. 1. Possible types of elasto-exchange NSW: $\mathbf{H}\|0X$, $\mathbf{L}\|0Z$, $\mathbf{k}\in XY$, $\mathbf{n}\|0Y$ (in the limit (8)) depending on frequency ω and wave number $\mathbf{k}_\perp$: $f_1=\tilde{\omega}_0^2+\omega_{me}^2$; $f_\pm=\omega_0^2\pm 2\omega_{me}ck_\perp$.

$$q^4-P_1q^2+P_2=0, \tag{10}$$

where

$$P_1=\frac{\tilde{\omega}_0^2+c^2k_\perp^2+\omega_{me}^2-\omega_*^2}{c^2};\quad P_2=\frac{\tilde{\omega}_0^2-\omega_*^2}{c^2}k_\perp^2.$$

If $q_{1,2}$ are the roots of the characteristic equation (9) or (10), we can use relations (7)–(10) to classify possible types of two-partial elasto-exchange NSW depending on the type of their spatial localization near the surface of the magnet. The results of analysis for $\mathbf{H}\|\mathbf{n}$ and $\mathbf{H}\perp\mathbf{n}$ are shown in Figs. 1 and 2 respectively. In these figures, regions I and II correspond to the surface NSW ($q_{1,2}^2>0$) or bulk NSW of the first type ($q_1^2<0$; $q_2^2>0$). Region III in Fig. 1 corresponds to generalized surface NSW ($\mathrm{Re}\,q_{1,2}^2\neq 0$; $\mathrm{Im}\,q_{1,2}^2\neq 0$), while bulk elasto-exchange NSW of the second type ($q_{1,2}^2<0$) are

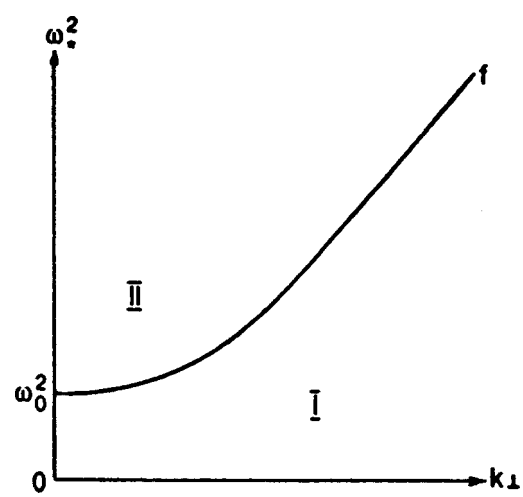

FIG. 2. Possible types of elasto-exchange NSW: $\mathbf{H}\|0X$, $\mathbf{L}\|0Z$, $\mathbf{k}\in XY$, $\mathbf{n}\|0X$ (in the limit (8)) depending on frequency ω and wave number $\mathbf{k}_\perp$: $f=\tilde{\omega}_0^2$.

observed for ω_* and $k_\perp$ from region IV in Fig. 1. Thus, the results of the above classification of possible types of propagating elasto-exchange NSW depending on the type of their spatial localization near the interface between magnetic and nonmagnetic media do not differ from the results of classification carried out in Ref. 7 for an EA AFM for $H=0$. However, for the geometry under consideration ($\mathbf{k}\in XY$, $\mathbf{u}\|0Z$), the types of elasto-exchange NSW listed above cannot exist if we do not take into account magnetic anisotropy (in the given case, induced by the field $\mathbf{H}\perp\mathbf{L}$) in the plane of propagation of the magnetic wave.

Using the results of the above classification of possible types of propagating elasto- exchange NSW, we can go over to the solution of the boundary-value problem.[4] The dispersion equation for a surface elasto-exchange NSW is determined from the condition of nontrivial solvability of (4) for amplitudes A_i from (7).

3. GENERALIZED SURFACE NUCLEAR SPIN WAVE

According to calculations, a propagating surface NSW of the elasto-exchange type can be formed only when $\mathbf{H}\perp\mathbf{n}$. The corresponding energy–momentum relation in approximation (1) can be obtained explicitly for an arbitrary value of the wave vector $k_\perp$:

$$\omega_*^2=N_1+[N_1^2-N_2]^{1/2};$$

$$N_1=\tilde{\omega}_0^2-c^2k_\perp^2/2;\quad N_2=\tilde{\omega}_0^4-c^2k_\perp^2(\tilde{\omega}_0^2+\omega_{me}^2). \tag{11}$$

The structure of the NSW under consideration is determined by expression (7) for $j=2$ taking into account (11) and the relations (see (9))

$$q_{1,2}^2=\frac{P_1}{2}+\left[\left(\frac{P_1}{2}\right)^2-P_2\right]^{1/2}. \tag{12}$$

It should be noted above all that this type of elasto-exchange NSW is an ''anisotropic'' wave since it is not observed in the absence of magnetic anisotropy in the plane of propagation of the wave ($H=0$). Taking into account the above classification, we can easily prove that for small wave vectors the NSW surface under consideration is a generalized ($\mathrm{Re}\, q_{1,2}^2\neq 0$; $\mathrm{Im}\, q_{1,2}^2\neq 0$) surface wave which is transformed into a two-partial surface NSW ($q_{1,2}^2>0$) when $k_\perp=k_*$ ($k_*=3\omega_{me}/2c$) (see Fig. 1).

An analysis shows that the presence of axial magnetic anisotropy with a constant b_s does not change qualitatively the type of dispersion of the anisotropy of the generalized surface NSW (11) (as compared to the above case with $b_s=0$), but affects significantly the type of its spatial localization near the free surface of the magnet in the range of small values of $|\mathbf{k}_\perp|$. According to calculations, the anisotropic elasto-exchange NSW in question for quite small wave number $k_\perp$ is a two- partial surface wave ($q_{1,2}^2>0$) whose energy–momentum relation for $k_\perp=k_{*-}(b_s)$ is smoothly transformed into the energy–momentum relation for a generalized surface NSW, and then into the energy–momentum relation for a two-partial surface NSW for $k_\perp=k_{*+}(b_s)$. In this case, the characteristic wave numbers $k_{*\pm}$ are connected with b_s through the relation

$$k_{*\pm}^2\mp\frac{\omega_{me}}{c}k_{*\pm}=\left\{\frac{b_s}{3}+\left[\left(\frac{b_s}{3}\right)^2+\frac{k_{*\pm}}{3}\right]^2\right\}^{1/2}. \tag{13}$$

It follows hence that in the case of completely free spins (i.e., for $b_s=0$), $k_{*-}=k_*=3\omega_{me}/2c$; $k_{*+}=0$. The energy–momentum relation of the generalized anisotropic surface NSW under investigation for $b_s\neq 0$ cannot be found in explicit form. Taking into account relation (12), we can write the energy-momentum relation in the form

$$q_1^2+q_2^2+q_1q_2=k_\perp^2+b_s(q_1+q_2). \tag{14}$$

For $b_s=0$, the root of (14) is determined by relation (11).

4. ANALYSIS OF THE SHAPE OF CONSTANT-FREQUENCY MAGNON SURFACE

It was proved in Ref. 10 that the shape of the constant-frequency surface for normal elasto-exchange nuclear spin oscillations of an unbounded magnet is in one-to- one correspondence with anomalies of the spectrum of bulk oscillations of a thin magnetic film made of the same material. It would certainly be interesting to establish a relation (on the basis of the relations obtained above) between the local geometry of a constant-frequency surface of normal spin oscillations and the formation of the corresponding generalized surface spin wave on the mechanically free surface of the magnet. It can easily be shown that the corresponding characteristic equation for $\mathbf{u}\perp\mathbf{k}$ and for given geometries of nuclear spin oscillations ($\mathbf{k}\in XZ$, $\mathbf{k}\in YZ$, or $\mathbf{k}\in XY$ in the case (8)) can be written in the form

$$\omega_*^2=\omega_0^2+\omega_{me}^2\frac{(\mathbf{k}\cdot\nu)^2}{\mathbf{k}^2}+c^2\mathbf{k}^2, \tag{15}$$

where ν is a unit vector along the direction of the ''difficult'' or middle magnetic axis ($\nu\|\mathbf{H}$ for $\mathbf{k}\in XY$ or $\mathbf{k}\in XZ$ for $\mathbf{H}\|0X$ or $\nu\|0Y$ for $\mathbf{k}\in YZ$). For $\omega=\mathrm{const}$, relation (15) determines the shape of the cross section of the relevant constant-frequency surface of a normal NSW in an unbounded antiferromagnet by the plane of propagation of the wave in the space of wave vectors $\mathbf{k}$. An analysis shows that for $|\mathbf{k}\cdot\nu|=|\mathbf{k}|$, the curve acquires segments with a negative curvature in the case when the following relation holds:

$$\omega_*^2\leqslant\omega_0^2+2\omega_{me}^2. \tag{16}$$

A comparison of the condition for the emergence of segments with a negative curvature on a constant-frequency surface in the spectrum of normal spin oscillations for an unbounded magnet with characteristic points on the plane of the parameters ω and $\mathbf{k}_\perp$ (see Fig. 1) readily shows that the equality sign in (16) corresponds to the point where the regions of bulk NSW of the first type ($q_1^2<0$, $q_2^2>0$) and the region of generalized surface NSW ($\mathrm{Re}\, q_{1,2}^2\neq 0$; $\mathrm{Im}\, q_{1,2}^2\neq 0$) merge:

$$k_\perp=\omega_{me}/c;\quad \omega_*^2=\omega_0^2+2\omega_{me}^2. \tag{17}$$

A comparison of relations (11)–(16) leads to the conclusion that the fulfillment of criterion (16) for a given direction of propagation of spin oscillations in the plane of the boundary is a sufficient condition for the formation of a general-

ized surface spin wave. Its energy–momentum relation is determined by formula (11) in the case when the surface of the magnet is mechanically free, and spins are not fixed. It can be easily proved that this criterion of the formation of a generalized surface spin wave also holds for other geometries of the problem, for example, for the geometry considered in Ref. 8: $\mathbf{L}\|\mathbf{n}\|0Z$, $\mathbf{k}_\perp\perp\mathbf{u}\perp\mathbf{n}$. It should be noted that the fact that the obtained criterion of the formation of generalized surface spin waves does not differ qualitatively from that proposed earlier by Kosevich and Syrkin[15–17] for the formation of a generalized surface elastic wave of the Rayleigh or Gulyaev–Blustein type also speaks in favor of the correctness of the given criterion. However, in the geometry under consideration ($\mathbf{n}\perp\mathbf{u}\perp\mathbf{k}_\perp$) and for the thermodynamic potential (2), none of the types of surface acoustic waves investigated in Refs. 15–17 is observed.

CONCLUSIONS

Thus, the results obtained here imply that

(1) the hybridization of the exchange and phonon mechanisms of the Suhl–Nakamura exchange in the nuclear spin subsystem of a magnetically ordered crystal leads to the formation of formerly unknown types of propagating generalized NSW in an anisotropic crystal;
(2) the type of spatial localization of this surface magnon depends considerably on the magnitude of the wave number $|\mathbf{k}_\perp|$ and on the surface magnetic anisotropy b_s:
(3) the directions of formation of curvature of a constant-frequency surface for normal elasto-exchange nuclear spin oscillations of an unbounded magnet are in one-to-one correspondence with the conditions of formation of generalized surface spin waves on the mechanically free surface of the magnet.

The author is deeply indebted to T. N. Tarasenko, E. P. Stefanovskii, and A. N. Bogdanov for the support of the idea of this research and for fruitful discussions.

*E-mail: bogdanov@host.dipt.donetsk.ua

[1] V. A. Tulin, Fiz. Nizk. Temp. **5**, 965 (1979) [Sov. J. Low Temp. Phys. **5**, 455 (1979)].
[2] A. V. Andrienko, V. I. Ozhogin, V. L. Safonov, and A. Yu. Yakubovskii, Usp. Fiz. Nauk **161**, 1 (1991) [Sov. Phys. Uspekhi **34**, 843 (1991)].
[3] P. G. de Gennes, P. A. Pincus, F. Hartmann-Boutron, and J. M. Winter, Phys. Rev. **129**, 1105 (1963).
[4] E. A. Turov and M. P. Petrov, *Nuclear Magnetic Resonance in Ferro- and Antiferromagnets* [in Russian], Nauka, Moscow (1969).
[5] A. R. King, V. Jaccarino, and S. M. Rezende, Phys. Rev. Lett. **37**, 533 (1976).
[6] T. G. Blocker, Phys. Rev. **154**, 446 (1967).
[7] E. P. Stefanovskii and S. V. Tarasenko, Fiz. Nizk. Temp. **19**, 63 (1993) [Low Temp. Phys. **19**, 45 (1993)].
[8] E. P. Stefanovskii and S. V. Tarasenko, Fiz. Nizk. Temp. **19**, 779 (1993) [Low Temp. Phys. **19**, 556 (1993)].
[9] S. V. Tarasenko, Fiz. Nizk. Temp. **21**, 1208 (1995) [Low Temp. Phys. **21**, 923 (1995)].
[10] S. V. Tarasenko, Fiz. Tverd. Tela (St. Petersburg) **37**, 2348 (1995) [Phys. Solid State **37**, 1285 (1995)].
[11] S. V. Tarasenko, Zh. Éksp. Teor. Phys. **110**, 1411 (1996) [JETP **83**, 778 (1996)].
[12] Yu. I. Sirotin and M. P. Shaskol'skaya, *Fundamentals of Crystal Physics* [in Russian], Nauka, Moscow (1979).
[13] E. A. Turov and V. G. Shavrov, Usp. Phys. Nauk **140**, 429 (1983) [Sov. Phys. Usp. **26**, 593 (1983)].
[14] V. I. Ozhogin and V. L. Preobrazhenskii, Usp. Phys. Nauk **155**, 593 (1988) [Sov. Phys. Usp. **31**, 713 (1988)].
[15] A. M. Kosevich, Yu. A. Kosevich, and E. S. Syrkin, Zh. Éksp. Teor. Fiz. **88**, 1089 (1985) [Sov. Phys. JETP **61**, 639 (1985)].
[16] Yu. A. Kosevich and E. S. Syrkin, Zh. Éksp. Teor. Fiz. **89**, 2221 (1985) [Sov. Phys. JETP **62**, 1282 (1985)].
[17] Yu. A. Kosevich and E. S. Syrkin, Fiz. Tverd. Tela (Leningrad) **28**, 248 (1986) [Sov. Phys. Solid State **28**, 134 (1986)].

Translated by R. S. Wadhwa

ELECTRONIC PROPERTIES OF METALS AND ALLOYS

Electron sound in aluminum. Electron–electron scattering

E. V. Bezuglyi,* N. G. Burma, A. L. Gaiduk, I. G. Kolobov, V. D. Fil',** and V. V. Khotkevich

B. Verkin Institute for Low Temperature Physics and Engineering, National Academy of Sciences of the Ukraine, 310164 Kharkov, Ukraine

H. van Kempen

Research Institute for Materials, University of Nijmegen, 6525, the Netherlands
(Submitted July 28, 1997; revised September 22, 1997)
Fiz. Nizk. Temp. **24**, 225–240 (March 1998)

The relaxation parameters of charge carriers in aluminum are measured by investigating the attenuation of electron sound and acoustic wave transfer under Doppler-shifted cyclotron resonance. It is shown that the electron–electron relaxation rate at spherical parts of the hole sheet of the Fermi surface is close to the results of the theory (A. Jaquier *et al.*, Phys. Rev. **B52**, 13005 (1995)) that takes into account the electron–electron interaction with the exchange of virtual phonons. At the same time, the experimental anisotropy of the electron–electron scattering is considerably smaller than the calculated value. A noticeable anisotropy of the electron–impurity collisions frequency in aluminum is discovered.
© *1998 American Institute of Physics.* [S1063-777X(98)00503-9]

INTRODUCTION

The temperature dependence of the bulk electron relaxation rate is determined by two processes: electron–electron ($e-e$) and electron–phonon (e–ph) collisions. At helium temperatures, the following dependences have been established reliably for the corresponding relaxation frequencies:

$$\nu_{ee}(T)=\alpha T^2, \quad \nu_{e\ \mathrm{ph}}(T)=\beta T^3.$$

The order-of magnitude estimate[1] for the ratio of the coefficients α and β has the form

$$\alpha/\beta \approx ms^2/k,$$

where m is the effective electron mass, s the velocity of sound, and k the Boltzmann's constant. For a standard simple metal ($m\approx m_0$, $s^2\simeq 10^{11}$ cm^2/s^2) $\alpha\sim\beta$, i.e., e–ph collisions prevail for $T>1-2$ K.

In general, the coefficients α and β depend on the direction of the electron wave vector **k**. The measurement of electron relaxation frequencies in a given metal, especially their dependence on the direction of **k**, is an important problem in the electron physics of metals since it is a good test for theoretical models of the electron relaxation rate developed in recent publications.

The measurement of β does not pose any difficulty: Any ballistic effects makes it possible to do that quite accurately. As a rule, the quantity being measured is the value of β averaged over a cyclotron orbit, although the methods allowing one to find $\beta(\mathbf{k})$ also exist.

The situation with $e-e$ collisions is more difficult. The coefficient α can be determined in two ways. The first method is obvious and involves measurements at low temperatures $T\leqslant 1-2$ K. The difficulties of this method are apparently associated with precision measurements of weakly varying quantities at presence of the background of scattering at impurities. Superconductivity can also be a deteriorating factor.

The other method is an analysis of effect insensitive to small-angle scattering typical for low-temperature e–ph collisions. The most known example is electrical resistance $\rho(T)$, although an unambiguous interpretation of experimental data which are results of averaging over the entire Fermi surface (FS) is also a nontrivial problem.

The history of studying the mechanisms of electron scattering is extremely rich: More than a dozen reviews and monographs have been devoted to this subject. The most interesting problem is the separation of the $e-e$ scattering. This was done comparatively easily for transition metals for which the values of α are larger than the values of β by several times. Reliable data were also obtained for metals of the alkali group. This problem is far from being solved completely for simple polyvalent metals; the situation has become slightly more clear in recent years for Al only.

Aluminum is one of the most interesting metals from the point of view of the electron theory since theoretical calculations taking into account the actual form of both the electron and phonon spectra can be carried out completely due to the relative simplicity of its FS. However, the experimental situation remained entangled almost as a detective story till recently. The contribution of $e-e$ collisions behaved as a fantom which now appeared and then vanished even in the same type of experiments. Quantitative results obtained in different experiments were extremely contradictory. The rea-

 © 1998 American Institute of Physics

sons behind such a state are quite trivial and boil down to an insufficient accuracy of measurements. The improvement of accuracy by two or more orders of magnitude, which has become possible due to revolutionary advances in digital technique, made it possible to tackle this problem at least partially.

Without going into the history of studying the $e-e$ scattering in Al, which is described in detail in several reviews (see, for example, Refs. 2 and 3), we shall describe the state-of-the-art in this field as we see it now.

(1) In 1981, the results of precision measurements of $\rho(T)$ were reported,[4] summing up the history of more than 15 years of investigations of transport properties of Al in zero magnetic field. It was found unambiguously that the quadratic contribution to $\rho(T)$ in Al prevails in the temperature interval above $T_c = 1.17$ K up to 4.2 K. As regards the e–ph contribution to $\rho(T)$, it was found that it obeys the Bloch law ($\rho_{e\,\mathrm{ph}}(T) = BT^5$) for $1.2\,\mathrm{K} < T < 2.2$ K, while near 4 K the temperature dependence becomes weaker, approaching T^3.

(2) In 1994, the contribution of $e-e$ collisions to the attenuation of the amplitude of rf size effect in Al was measured reliably for the first time.[5] The orbital-averaged values of α were measured for an orbit of the hole sheet of the FS as well as for two orbits belonging to the electron sheet of the FS. The value of α on the electron sheet proved to be 3–4 times larger than on the hole sheet.

(3) In 1995, a sort of final theoretical calculation of the electron relaxation rate in Al was reported.[6] In this publication, the coefficients α and β were presented as functions of the wave vector $\mathbf{k}$ on the FS. It was found that the function $\beta(\mathbf{k})$ is strongly anisotropic and attains its maximum values near the edges of the Brillouin zone (the anisotropy factor is ~ 20). The behavior of $\beta(\mathbf{k})$ is basically in accord with the available large body of experimental data. The theoretical anisotropy of $\alpha(\mathbf{k})$ also turned out to be significant (the anisotropy factor ~ 10) like the anisotropy of $\beta(\mathbf{k})$ as a result of inclusion of the $e-e$ interaction with the exchange of virtual phonons. The results of calculations correctly describe the difference in the rates of the $e-e$ relaxation on the hole and electron sheets.

It seems obvious, however, that the theory is much more advanced than the experimental studies: a comparison can be carried out only for three experimentally measured values of α averaged over the orbit[5] (the one orbit on the hole sheet and the two ones on the electron sheet) and for the coefficient of the quadratic contribution to $\rho(T)$.[4] On the whole, calculated values are 1.5–3 times as high as the measured ones. Such an agreement should be regarded as basically satisfactory and indicating undoubtedly the success of the theory. Nevertheless, the quantitative agreement between the theory and experiment has not been reached so far. For example, the result of averaging of the theoretical values of α over the relevant orbit on the main hole sheet of the FS is three times as high as the experimental value. Does this mean that all the calculated values of $\alpha(\mathbf{k})$ should be reduced by a factor of three while preserving the theoretical anisotropy, or is the latter absent or strongly smoothed?

In this research, we endeavor to remove this lag between experiments and the theory (at least partially) and to obtain data on the $e-e$ scattering at some characteristic points of the hole sheet on the FS of Al. We obtained the required information from an analysis of the temperature dependence of attenuation of electron sound.[7] It was found that the $e-e$ scattering rate in all spherical regions of the FS is close ($\sim 70\%$) to that calculated for the center of a hexagonal face of the hole sheet (point L). However, the experimentally observed anisotropy of α (anisotropy factor 2) turned out to be much smaller than the value calculated by Jaquier *et al.*[6]

1. EXPERIMENTAL TECHNIQUE

1.1. Measurements

Electron sound (ES) is a fast electron mode propagating in a metal at a velocity v_{ES} close to the Fermi velocity v_F and characterized by a linear energy–momentum relation. Electron sound is associated with lattice deformation and hence can be excited quite easily and detected with a help of piezoelectric transducers (the coupling coefficient $K \sim (s/v_F)^2$). Electron sound can be of various physical origin: (1) collective oscillations of the electron subsystem of the zero sound type, propagating in a two-component Fermi liquid[8] under the conditions $\omega/\nu \geqslant 1$ ($\omega/2\pi$ is the frequency of oscillations); (2) a damped concentration mode associated genetically with zero sound and existing for $\omega/\nu \leqslant 1$,[7,10] (the velocities of zero sound and concentration mode are close to the maximum Fermi velocity), and (3) purely ballistic transfer of elastic perturbation by nonequilibrium electrons from one sample face to another, i.e., a quasiwave[9] associated, as a rule, with a reference point on the FS. The origin of ES is not essential for the further analysis since for all the ES types listed above, the temperature dependence of damping is described by the simple exponential dependence

$$u_{ES} = K u_0 \exp(-\nu(T) L / v_{ES}), \tag{1}$$

where u_{ES} is elastic strain in the ES wave, u_0 the excitation amplitude, and L the sample thickness. Formula (1) reflects the fact that ES is excited directly on the sample surface. This statement is obvious for zero sound or a concentration wave since these oscillations, as well as an acoustic wave, are intrinsic modes of the metal, which are renormalized by the acousto-electron interaction. Being excited on the metal surface, these modes propagate further without interacting with one another. The fact that a quasiwave is excited essentially at the surface is less obvious, but theoretical calculations confirm this statement completely.[10] Physically, this is due to the fact that all perturbations of the electron distribution function in the bulk of the sample are self-averaged in view of a large difference between the Fermi velocity and the velocity of a sound.

The surface type of ES excitations is also responsible for the virtual independence of the transformation coefficient K in (1) of temperature. Thus, the logarithmic amplitude of ES

normalized to the time of flight contains direct information on the temperature evolution of the electron relaxation frequency.

Although formal theoretical calculations indicate that ES is formed by a small group of effective electrons in the range of low damping $\omega/\nu \geqslant 1$, small-angle scattering is ineffective in ES attenuation under actual experimental conditions. For example, the physical reasons behind the broadening of angular perturbation of the distribution function, leading to low efficiency of one-phonon scattering in the propagation of zero sound, are considered in Ref. 7. However, the general and probably main reason for the ineffectiveness of small-angle scattering is associated with the experimental geometry irrespective of the origin of ES. The diameters of the piezoelectric-transducers in our experiments as well as the distance travelled by ES are comparable with the ES wavelength or are even smaller than this value. The partial waves arriving along inclined trajectories at the observation point are slightly out of phase relative to the principal wave traversing the shortest distance from the emitting transducer to the receiving one, and make a comparable contribution to the ES signal. The size of the effective electron group is therefore determined not by the properties of the electron spectrum, but by the aperture of the system of piezoelectric transducers. It leads to a considerable broadening of the perturbation region of the distribution function. Thus, the departure of electrons from the ''hot'' regions of the momentum space due to scattering at phonons is of the diffusion type as in the case of transport experiments at low temperatures, and the effective frequency of the e–ph relaxation obeys the Bloch law. However, in contrast to $\rho(T)$, relaxation of the distribution function and not of the total momentum of the electron system is sufficient for ES attenuation, and hence normal collisions are as important as collisions involving U-processes.

The experiment[7] made with different metals (Ga, Al, Mo, and W) revealed the high efficiency of the method described above for separating the $e-e$ component of scattering. For example, $e-e$ collisions in Al make a decisive contribution to ES attenuation up to 10 K. According to formula (1), the ES attenuation length that virtually coincides with the mean free path for effective electrons is a directly measurable quantity. In order to compare these results with the data obtained in other experiments and with the calculated values, we must determine the relaxation frequency, i.e., measure independently the ES velocity in a given direction. Such measurements were made in Ref. 7 only for Ga. It is interesting to note that the value of $\alpha \simeq 1.6\times 10^7\ \mathrm{s}^{-1}\times \mathrm{K}^{-2}$ for Ga measured in Ref. 7 is comparable with the known maximum value $\alpha \simeq 2.5\times 10^7\ \mathrm{s}^{-1}\times \mathrm{K}^{-2}$ for Mo.[3] This means that transition metals are not distinguished by a strong $e-e$ scattering which can be quite significant in a simple nontransition metal also.

1.2. Sample preparation

Samples having a thickness of 3–4 mm and the required orientation were cut by the electric spark technique from Al single crystals prepared from high-purity material ensuring the ratio of resistivities at room and helium temperatures $RRR \simeq 4\times 10^4$. The error in the orientation relative to the crystallographic axes was $\pm 0.5°$. After lapping to make their surfaces plane-parallel, the samples were etched in diluted (40%) KOH, annealed in dry hydrogen for 0.5 h at $T = 500$ °C, 0.5 h at 450 °C, and slowly cooled (for 3–4 h) to room temperature. After this, the plane-parallel shape of the working surfaces, which was spoiled by etching, was restored by careful lapping with a fine ($\sim 5\ \mu$m) polishing powder. The latter operation was required since although the surface undulation ($\sim 2-5\ \mu$m) emerging during etching and undesirable in purely acoustic experiments is actually insignificant for ES with a wavelength ~ 1 cm. However, the deviations from planarity of the working surfaces in the measurements of the ES velocity (see below) were sources of considerable errors, which made us to sacrifice the quality of the surface which is inevitably deteriorated during polishing.

The averaged impurity relaxation frequency ν_0 in the samples was estimated by measuring the change in the velocity of sound at $T = 1.5$ K in a strong magnetic field ($\mathbf{q}\perp\mathbf{H}$, where $\mathbf{q}$ is the wave vector of sound) as compared to its value for $H = 0$. The required perpendicularity of $\mathbf{q}$ and $\mathbf{H}$ was attained at the symmetry point of the effect with small ($\sim s/v_F$) scanning of the angle between these vectors. According to Ref. 11 the change in the volocity of sound is defined by the formula

$$\frac{\Delta s}{s} = \left(\frac{\Delta s}{s}\right)_{\nu\to 0} \frac{\omega^2}{\omega^2+\nu^2},$$

from which the frequency $\nu_0 = (0.95\pm 0.1)\times 10^9\ \mathrm{s}^{-1}$ was determined from the measurement of $\Delta s/s$ at two frequencies (50 and 100 MHz).

In order to verify the matching between the obtained value of the impurity relaxation frequency and the known value of the residual resistance of the initial material, we can use the elementary Drude formula corresponding to the free electron approximation taking into account the effective mass renormalization constant λ:

$$\sigma = \frac{ne^2}{\nu_0 m_0(1+\lambda)}. \tag{2}$$

It is well known, however, that if we use in (2) the values of n and m_0 from the free electron model, the resistivity of Al turns out to be lower by approximately a factor of two.[12] In order to somehow take into account the actual electron structure of Al, we shall use the band value of its plasma frequency $\Omega_p = \sqrt{4\pi ne^2}/m = 1.88\times 10^{16}\ \mathrm{s}^{-1}$,[13] which gives for $\lambda = 0.4$ (as in Ref. 14) the value of $RRR \simeq (6.3\pm 0.6)\times 10^4$. The latter value is still 1.5 times larger than the actual one apparently in view of incomplete consideration of band effects.

2. PROPAGATION OF ES IN Al EXPERIMENTAL RESULTS

2.1. Measurement of ES velocities

The most complicated problem is the measurement of ES velocities. In order to find their values, it is necessary to measure the phase shift $\varphi(L)$ of the ES signal upon a change

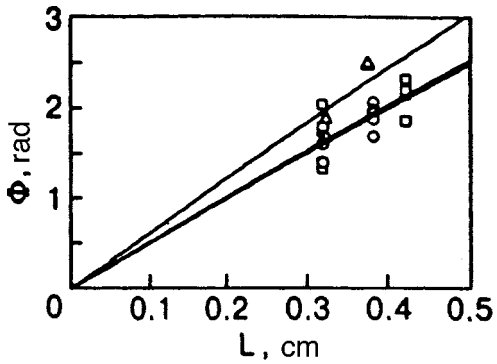

FIG. 1. The phase of the ES signal for various sample thicknesses and directions: $\mathbf{q}\|[111](\square)$, $\mathbf{q}\|[100](\triangle)$, $\mathbf{q}\|[110](\bigcirc)$; $f=100$ MHz.

in the sample thickness L. On one hand, the sample thickness must be at least 3 mm for a reliable separation of the ES signal from the leading edge of an acoustic pulse whose amplitude is four orders of magnitude larger than the amplitude of the signal under investigation. On the other hand, the impurity mean free path limits the maximum thickness of the sample to ~ 4 mm. Thus, the phase shift introduced by the sample upon a change of its thickness by 1 mm at an excitation frequency of 10^8 Hz and an ES velocity of $\sim 10^8$ cm/s amounted to ~ 0.5 rad and could be measured to a high degree of accuracy. The main source of errors was the regluing of piezotransducers to samples of different thickness. Piezoelectric elements were glued with a layer of silicon oil GKZh-94 of thickness $\sim 1.5-2$ μm. A ratio of acoustical impedances of the glue and the sample (as well as piezoelectric element and delay line) ~ 0.2. Neglecting the attenuation of sound in the glue, we can easily find the variation of phase shift introduced by glue layers upon a change in their thickness δl:

$$\delta\varphi=\left(1+\frac{2.5}{1+(2.5q_0l_0)^2}\right)q_0\delta l-2q_0\delta l,$$

where q_0 is the wave number for sound in the glue layer ($q_0\sim 2.5\times 10^3$ cm^{-1} for $\omega=2\pi\times 10^8$ s^{-1}). Thus, the random variation of the thickness l_0 of the glue layer by 0.5 μm generates a phase shift $\delta\varphi\sim 0.25$ rad comparable to the value to be measured.

The variation $\delta\varphi$ associated with the change in l_0 is also accompanied by the corresponding change in the amplitude of sound δA_0. It would be possible in principle to establish the correlation dependence $\delta\varphi(\delta A_0)$ and to correct the results of measurements. In actual practice, however, such a procedure cannot be carried out since the acoustic characteristics of the adhesive material are not known exactly, and the only way out is to make repeated measurements followed by the statistical analysis of the results. In order to narrow the confidence interval and to reduce the number of measurements the following additional condition was used: the straight lines approximating the dependence $\varphi(L)$ for different crystallographic directions must pass through the same point (the phase reference point) for $L=0$ (see Fig. 1). Since Al is virtually isotropic in its elastic properties, such a limitation is entirely substantiated. The slopes of approximating straight lines determine the corresponding ES velocities whose values are given in Table I for the principal crystallographic directions. For the comparison, the table also gives the Fermi velocities at corresponding reference points for the hole sheet of the FS,[14] with which our results coincide to within experimental errors. It should also be noted that the results of measurements of v_{ES} correctly reflect the relation between velocities from Ref. 14 for $\mathbf{q}\|[100]$ and $\mathbf{q}\|[111]$. Thus, the ES is associated with reference points of spherical region of the hole sheet of the FS at least for these orientations.

2.2. Temperature dependences of ES damping

The native experimental curves for the logarithmic amplitude of ES for the case of its propagation along the principle crystallographic axes are shown in Fig. 2 in the form of temperature dependences of the reciprocal length of attenuation. Plotting $\gamma=-\ln u_{ES}$ as a function of T^2 or constructing the dependence $\partial\gamma/\partial T^2$, we can easily prove that the main contribution to these dependences comes from the component quadratic in T. An example of such a construction is presented in Fig. 3 which shows that the coefficient $\alpha/v_{ES}\sim 0.05$.

It should be noted that the temperature dependences presented in Fig. 2 can be described equally well by a combination of the quadratic contribution of $e-e$ collisions with Bloch's law or with the cubic contribution corresponding to the efficiency of all collisions with phonons. In the latter case, the coefficient of T^3 must be determined by the constant β which is well known from other experiments (see, for example, Ref. 15). With such an interpretation, however, the values of $\beta\simeq(2-3)\times 10^5$ s^{-1}K^{-3} obtained from our data (see Fig. 2) are an order of magnitude smaller than the minimum values given in Ref. 15. We believe that this fact confirms a low efficiency of small-angle scattering in a propagating ES and justifies the representation of the $e-$ph contribution to ES attenuation in the form of Bloch's law.

TABLE I. Velocities of electron sound and Fermi velocities.

Direction $\mathbf{q}$	v_{ES}, 10^8 cm×s^{-1}	v_F, 10^8 cm×s^{-1}	L, cm	α_0/v_{ES}, cm^{-1}×K^{-2}	α_0, 10^6 s^{-1}×K^{-2}	$\alpha_{0\,\mathrm{calc}}$, 10^6 s^{-1}×K^{-2}	Θ, K $\beta_0=2.4\times 10^6$ s^{-1}×K^{-3}
$\mathbf{q}\|[111]$	1.24±0.2	1.38[14]	0.315	0.044±0.004	5.5	6.57[6]	190±5
			0.418	0.038±0.004	4.8		160±5
$\mathbf{q}\|[110]$	1.26±0.2	-	0.308	0.047±0.004	5.8	-	125±5
			0.380	0.042±0.004	5.2		145±5
$\mathbf{q}\|[100]$	1.03±0.2	1.28[14]	0.274	0.055±0.004	5.7	11.25[6]	105±5

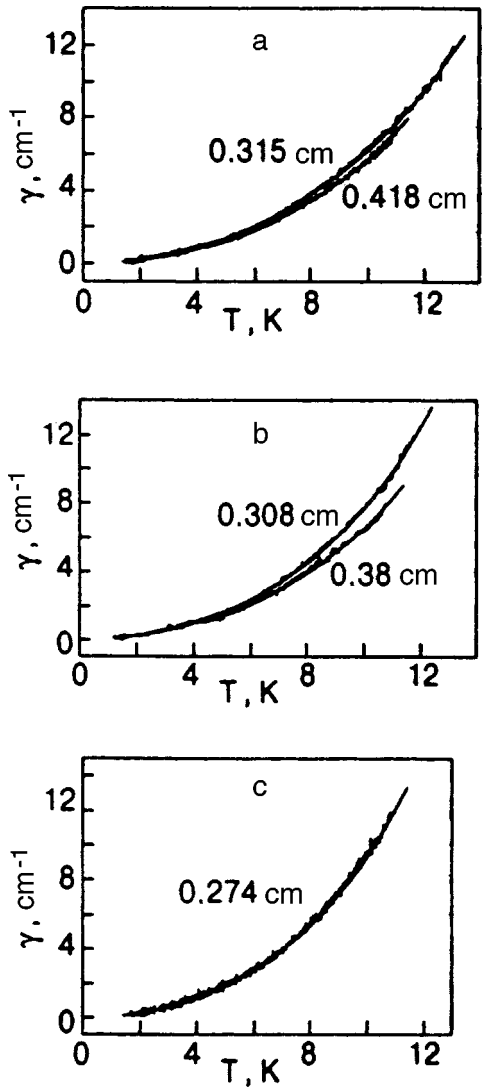

FIG. 2. Temperature variation of ES attenuation: $\mathbf{q}\|[111]$(a),$\mathbf{q}\|[110]$ $\times$(b),$\mathbf{q}\|[100]$(c), $f=54.3$ MHz. Smooth curves correspond to approximation according to (3).

In order to extract quantitative characteristics of $e-e$ and $e-$ph scattering from experimental dependences, we must take into account the energy dependence of the rates of both processes and carry out averaging in (1) with a weight function in the form of the derivative of the Fermi energy distribution at a given temperature (see, for example, Ref. 3). It is well known[16] that averaging over energy leads to an

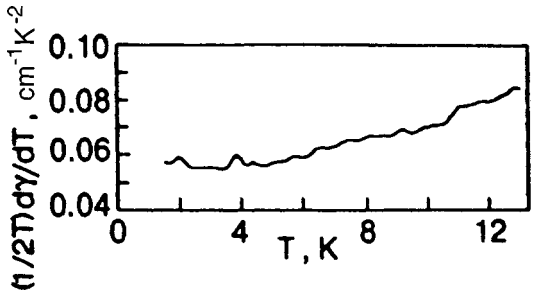

FIG. 3. Smoothed derivative $(1/2T)\partial\gamma/\partial T$:$\mathbf{q}\|[111]$,$L=0.315$ cm, $f=54.3$ MHz.

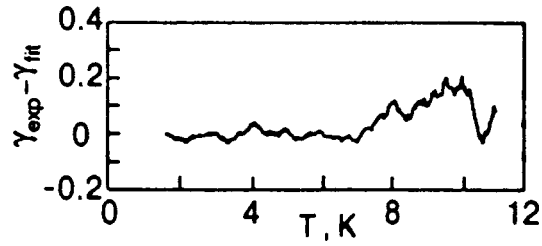

FIG. 4. Smoothed difference between the experimental recording and approximating curve, $\mathbf{q}\|[100]$.

increase in the constants α and β being measured at very low temperatures, when a decrease in the mean free path due to energy dispersion of relaxation frequencies is insignificant. In this case, $\alpha_{\rm eff}=(4/3)\alpha_0$, $\beta_{\rm eff}=(12/7)\beta_0$ in an experiment with significant small-angle scattering and $\beta_{\rm eff}=(80/31)\beta_0$ otherwise. The subscript ''0'' marks the values of the constants at the Fermi level. At an arbitrary temperature, we can assume that the coupling constant for electrons with elastic deformation is independent of energy and use the formulas for energy averaging given by Gasparov and Huguenin[3] in terms of directly measurable logarithmic amplitude normalized to the sample thickness:

$$\frac{\ln u_{ES}}{L}=\frac{1}{L}\ln\int_0^\infty\frac{\exp[-(\nu_{ee}(y)+\nu_{e\ \rm ph}(y))L/v_{ES}]}{2\cosh^2(y/2)}dy, \tag{3.1}$$

$$\nu_{ee}(y)=\alpha_0T^2(1+y^2/\pi^2), \tag{3.2}$$

$$\nu_{e\rm ph}(y)=\frac{\beta_0T^3}{7\zeta(3)}\left(\int_{\Theta/T}^\infty x^2\Phi(x,y)dx+\left(\frac{T}{\Theta}\right)^2\int_0^{\Theta/T}x^4\Phi(x,y)dx\right), \tag{3.3}$$

$$\Phi(x,y)=\frac{(e^y+1)^2}{\tanh(x/2)(e^{2y}+2e^y\cosh x+1)}. \tag{3.4}$$

Here x and y are the phonon and electron energies in temperature units and $\Phi(x,y)$ is the so-called population factor.[3] The interpolation relation (3c) takes into account a transition from low-efficiency small-angle scattering at $T\ll\Theta$ to the effective scattering at $T\geqslant\Theta$, where Θ/s is the characteristic size of the ''hot'' spot on the FS,[3] which is associated with ES. Expressions (3a)–(3c) contain the three parameters $(\alpha_0,\beta_0,\Theta)$ to be determined, whose values should be selected for the best description of experimental dependences. Running ahead, we note that the values of Θ obtained for minimum possible values of β_0[15] are at least an order of magnitude higher than the upper limit of the experimental temperature,[15] and the first term in (3c) makes practically no contribution; this reduces the description of $u_{ES}(T)$ to a two-parametric case. The deviation of the theoretical dependence (3) from a smoothed experimental dependence did not exceed 1–2% (Fig. 4). The results obtained for all the samples under investigation are summarized in Table I.

It should be noted first that variations of the logarithmic amplitude $u_{ES}(T)$ normalized to the sample thickness systematically deviated towards smaller values for samples with

a larger thickness. Qualitatively the same tendency is also observed in Eqs. (3) and is associated with a more rapid relaxation of electrons at a large distance from the Fermi level in a thick sample. However, this tendency is manifested weakly and does not explain experimental dependences. Two reasons can be proposed for a slower variation of $\ln u_{ES}(T)/L$ upon an increase in L: a decrease in the transformation coefficient with increasing temperature (the relative contribution of this process decreases with increasing L) and a relatively large contribution of partial waves arriving along inclined trajectories in a thinner sample. A decrease of such a contribution with increasing temperature is equivalent to the emergence of the $\Theta(T)$ dependence and also leads to a sharper variation of $\ln u_{ES}(T)/L$. This effect emerges due to limited size of transducers and can be taken into account by an additional averaging in (3) over the angle. However, it is hardly possible to carry out this procedure accurately in view of insufficient initial data (the more so since the change in numerical values of parameters for samples of different thickness does not exceed significantly the possible error). Nevertheless, we believe that the values of α_0 and β_0/Θ^2 obtained for thicker samples are closer to actual ones.

It was noted above that our data do not allow us to determine the values of β_0 and Θ separately; we can only find their ratio β_0/Θ^2. In order to obtain the values of Θ presented in Table I, we used the value of $\beta_0 \sim 2.4 \times 10^6\ \mathrm{s}^{-1}\times\mathrm{K}^{-3}$ measured in Ref. 15 near the points L and X at the Fermi level. The corresponding diameter of ''hot spots'' on the FS was about a half the characteristic size of spherical regions. Hence we can state that the ''hot spots'' associated with ES must be centered near the reference points belonging to the spherical regions of the hole sheet on the FS of Al, i.e., near the points L and X for $\mathbf{q}\|[111]$ and $[100]$ respectively. For $\mathbf{q}\|[110]$, these ''hot spots'' can be located only in spherical regions of hexagonal cups of the FS near the line UW. Such a conclusion correlates with the size of a ''hot spot'' which is maximum for $\mathbf{q}\|[111]$ and minimum for $\mathbf{q}\|[100]$. An analysis of the behavior of ES in a longitudinal magnetic field leads to the same conclusion: for $\mathbf{q}\|[111]$ or $\mathbf{q}\|[100]$, the application of a magnetic field up to 35 kOe does not change significantly the amplitude or velocity of ES since the magnetic field does not draw effective electrons from a ''hot spot.'' For $\mathbf{q}\|[110]$, the ES amplitude and velocity decrease sharply in a magnetic field, and the ES signal vanishes even for $H=300$ Oe due to the carrying away the effective electrons along trajectories from ''hot spots.''

Thus, the values of α_0 obtained by us also correspond to spherical regions of the FS, and we can compare them with the relevant calculated values $\alpha_{0\,\mathrm{calc}}$[6] given in Table I. The following aspects are worth noting.

(1) The experimental values of α_0 are close to the value calculated at the point L.

(2) The theoretically predicted difference between the $e-e$ relaxation rates at the points L and X (by a factor of 1.8) is apparently not confirmed. If we estimate the value of α_0 from the measured values of the ES velocities, there will be no difference between the values of α_0 at these points, and if we use the values of the Fermi velocities from Ref. 14 for estimates (the ES velocities are close to these values), the anisotropy in α_0 does not exceed 20%. It should also be noted that the orbit-averaged value of $\alpha_0 = 5.1\times 10^6\ \mathrm{s}^{-1}\times\mathrm{K}^{-2}$ on an orbit of the hole sheet of the FS investigated by Jaquier *et al.*[5] are in excellent agreement with our data. All these facts indicate that the actual anisotropy of α_0 is much smaller than predicted in Ref. 6.

It would be interesting to compare the obtained results (disregarding the anisotropy of α_0) with the resistivity data. Ribot *et al.*[4] obtained the coefficient $A_{\mathrm{exp}} = (2.7-3)\ \mathrm{f}\Omega\times\mathrm{mK}^{-2}$ for a quadratic contribution to $\rho(T) = AT^2$ in the temperature range $1.2\ \mathrm{K} < T < 2.2\ \mathrm{K}$. In order to obtain an independent estimate of $\rho_{ee}(T)$ from our data with the help of (2), we must use the low-temperature value of $\alpha_{\mathrm{eff}} = (4/3)\alpha_0 \simeq 7\times 10^6\ \mathrm{s}^{-1}\times\mathrm{K}^{-2}$. Taking into account the band value of the plasma frequency and the constant $\lambda = 0.4$, we obtain $A = 3.1\ \mathrm{f}\Omega\times\mathrm{mK}^{-2}$. Obviously, the agreement is apparent since only $e-e$ collisions involving U-processes lead to the relaxation of the total momentum of the system, which is responsible for electrical resistance, and the value of α_{eff} should be reduced by a factor of Δ. The estimated values of Δ vary from 0.2 to 0.8, and $\Delta = 0.4$ is regarded at present as the most feasible value.[2] On the other hand, formula (2) gives values of ρ smaller than actual values following from the RRR estimates by a factor of 1.5. The estimated value of A is generally close to the experimental one, but indeterminacy of these estimates is too large to make a conclusion about the presence or absence of anisotropy in the $e-e$ scattering.

As regards the $e-$ph contribution to electrical resistance, the spherical regions of the FS determine the behavior of $\rho(T)$ only in ''pure'' limit,[17] when the impurity relaxation can be neglected, i.e., for $T > 10$ K; in this case, $\beta_{\mathrm{eff}} = \beta_0$. Using the results obtained for the largest spherical region of the FS, i.e., for $\mathbf{q}\|[111]$, we can find the frequency of $e-$ph collisions[16]:

$$\nu_{e\ \mathrm{ph}} \approx \frac{\beta_0}{\Theta^2}\int_0^\infty x^4\Phi(x,0)\,dx = 96.44\,\frac{\beta_0}{\Theta^2}.$$

Hence we obtain from (2) for the coefficient B in Bloch's law at $\Theta = 175$ K the value $B = 3.4\times 10^{-3}\ \mathrm{f}\Omega\times\mathrm{mK}^{-5}$, which is approximately three times greater the experimental value $B = 1.2\times 10^{-3}\ \mathrm{f}\Omega\times\mathrm{mK}^{-5}$.[18] This is not surprising since the size of the diffusion region in the transport experiment is evidently larger than the size of the ''hot spot'' forming ES.

Thus, the results of investigations of the frequency of $e-e$ collisions in Al described above confirm, on one hand, the closeness of calculated and experimental values on the spherical regions of the FS, and on the other hand, cast a shadow of doubt on the existence of noticeable anisotropy in ν_{ee}.

In order to obtain a more definite answer to this question, we analyzed one more version of ES, viz., transfer of sound under Doppler-shifted cyclotron resonance (DSCR).[19]

3. ANALYSIS OF *e–e* SCATTERING BY THE METHOD OF ELECTRON TRANSFER OF SOUND UNDER DSCR

An acoustic signal transferred by electrons under the DSCR can also be regarded as an ES variety of the quasiwave type. For a certain value of a longitudinal magnetic field (parallel to **q**), we can find a group of electrons whose maximum displacement along the vector **q** over a cyclotron period is a multiple of the acoustic wavelength. At this instant, the attenuation and velocity of sound experience a sharp change, which is known as the magnetoacoustic resonance (or DSCR). Resonant electrons transfer the elastic field of an acoustic pulse with the Fermi velocity over a distance of the order of the mean free path, at which the field can be easily detected. Naturally, this ballistic effect can also be used for studying the temperature dependence of the electron relaxation rate.

This effect differs significantly from the phenomena discussed above in the inapplicability of the simple relation (1) for the DSCR transfer. Indeed, the transmission of the elastic field energy to resonant electrons takes place in the entire region of the sample occupied by the pulse, and a coherent transfer signal is similarly formed in the entire volume of the sample. As a result, the effect of pumping of the transfer field amplitude by the initial acoustic pulse during its lifetime in the sample is also significant.

The physical pattern of DSCR transport described here is quite complicated, and a complete theoretical analysis of the effect is required for obtaining quantitative information on the electron relaxation frequency from the experiments. Such an analysis will be carried out in the next section.

3.1. The theory of electron transport of an acoustic wave under DSCR

The effect of electron transport of a longitudinal acoustic wave packet (pulse) propagating in a metal along the z-axis is described by corrections to the solution of the wave equation for the elastic strain vector $\mathbf{u}=(0,0,u)$, i.e.,

$$-\frac{\partial^2 u}{\partial t^2}+s^2\frac{\partial^2 u}{\partial z^2}=F(z,t),\quad F(z,t)=\frac{1}{\rho}\frac{\partial}{\partial z}\langle\Lambda f(z,t)\rangle, \tag{4}$$

which are due to the electron force $F(z,t)$[11] exerted by nonequilibrium charge carriers on the crystal lattice outside the region of localization of the principal pulse. Here s is the velocity of sound in the adiabatic approximation, ρ the density of the metal, and $\Lambda=\Lambda_{zz}$ the longitudinal component of deformation potential. The angle brackets denote averaging over the Fermi surface. The nonequilibrium correction $f(\partial n_F/\partial\varepsilon)$ to the Fermi distribution function $n_F(\varepsilon)$ in a magnetic field directed along the acoustic wave vector **q** satisfies the kinetic equation

$$\frac{\partial f}{\partial t}+v_z\frac{\partial f}{\partial z}+\frac{\partial f}{\partial\tau}+\nu f+e\mathbf{E}\mathbf{v}=\Lambda\frac{\partial^2 u}{\partial z\partial t}, \tag{5}$$

where τ is the time of electron rotation in a cyclotron orbit and ν the collision frequency. In the general case, the system of equations (4) and (5) should be supplemented with Maxwell's equation for determining the self-consistent electric field **E** accompanying the formation of an acoustic wave. However, we will confine our further analysis only to the deformation mechanism of electron interaction with elastic vibrations since the account of the electric field only leads to a renormalization of the amplitude of the effect without changing the form of space and time distribution of the acoustic field we are interested in. Moreover, since the electron transport is accomplished by a small group of resonant charge carriers, and hence the electron force $F(z,t)$ is a small perturbation, we can neglect the contribution of the transferred acoustic field to the kinetic equation (5), and assume that the shape of the principal pulse in (5) is a preset function of the wave coordinate $\xi=z-st$:

$$u(z-st)=U(\xi)\exp(iq\xi), \tag{6}$$

where $U(\xi)$ is the envelope of the pulse, which varies smoothly over the acoustic wavelength, which coincides in the order of magnitude with the spatial period of the electron trajectory. Physically, this assumption corresponds to an analysis of space and time intervals over which the attenuation of the initiating pulse can be neglected.

The physical pattern of electron transport in a sample of a finite size $0<z<L$ comparable with the pulse length ξ_0 is complicated by the edge effects including the excitation of a quasiwave as well as an additional change in the amplitude of the effect upon the penetration of the pulse into the sample. In this connection, let us first consider the electron transport in an unbounded metal, confining our analysis to a time interval $0<t\ll t_0$ which is smaller than the time t_0 of attenuation of the principal pulse. The kinetic equation (5) in the accompanying reference frame, i.e.,

$$\frac{\partial f}{\partial t}+(v_z-s)\frac{\partial f}{\partial\xi}+\frac{\partial f}{\partial\tau}+\nu f=\omega q u(\xi)\Lambda(\tau), \tag{7}$$

in which we disregard the derivatives of the smooth envelope $U(\xi)$, should be supplemented with the boundary conditions that can be reduced to the condition of equilibrium of charge carriers flying from the bulk of the metal against the pulse localized on the interval $-\xi_0<\xi<0$:

$$f(v>0,\ \xi\leqslant-\xi_0)=f(v<0,\ \xi\geqslant 0)=0,\quad v=v_z-s. \tag{8}$$

The solution of the kinetic equation (7) in front of the principal pulse ($\xi>0$), which is obtained by the method of characteristics taking into account the boundary conditions (8), i.e.,

$$f(v>0,\ \xi>0)=\omega q\ \exp(-\nu\xi/v)\int_0^{\xi_0/v}d\tau_1 \times\exp(-\nu\tau_1)\Lambda(\tau-\tau_1-\xi/v)u(-v\tau_1) \tag{9}$$

has a clear physical meaning and describes the energy removal by electrons from the pulse over its entire length $-\xi_0<-v\tau_1<0$ taking into account the relaxation attenuation of the contribution of distant segments of the pulse (exponential in the integrand) and subsequent attenuation of the nonequilibrium distribution function upon an increase in the distance ξ from the pulse front.

The separation of the resonant contribution to (9) is carried out by the method of representation of the integral in (9)

in the form of the sum of integrals over the cyclotron periods T_H, which is known from the theory of magnetoacoustic resonance:

$$f(v>0,\ \xi>0)=\omega q\ \exp\left(-\frac{\nu\xi}{v}\right)\times\left(\int_0^{T_H}d\tau_1\ \exp(-\nu\tau_1-iqv\tau_1)\Lambda\times\left(\tau-\tau_1-\frac{\xi}{v}\right)\sum_{n=0}^{N-1}U(-v\tau_1-nT_Hv)\times\exp(-nT_H(\nu+iqv))+\int_{NT_H}^{\xi_0 v}d\tau_1\times\exp(-\nu\tau_1-iqv\tau_1)\Lambda\left(\tau-\tau_1-\frac{\xi}{v}\right)U(-v\tau_1)\right),\tag{10}$$

where N is the maximum number of periods of the electrons trajectory $D(p_z,H)=vT_H$ fitting into the pulse length. For $N\gg 1$, the last term in (10) is a small nonresonant correction and can be omitted. Neglecting also the weak relaxation damping in the first term ($\nu\tau_1\leqslant\nu T_H\ll 1$) as well as a small variation of the envelope ($U(-v\tau_1-nvT_H)\approx U(-nvT_H)$) over a cyclotron period, and substituting (10) into the expression for the electron force (4), we obtain

$$F(z,t)=F(\xi)=\frac{i\omega q^2}{\rho}\int\frac{m^*dp_z}{2\pi^2}\frac{\xi_0}{D(p_z)}\Psi_1(D(p_z),\xi)\times\Psi_2(D(p_z)),\tag{11}$$

$$\Psi_1(D,\xi)=\int_0^{T_H}d\tau\int_0^{T_H}d\tau_1\Lambda(\tau)\Lambda\left(\tau-\tau_1-\frac{\xi}{v}\right)=T_H\sum_m|\Lambda_m|^2\exp\left[2\pi im\frac{\xi}{D}\right]\int_0^1dx\times\exp[ix(2\pi m-qD)],\tag{12}$$

$$\Psi_2(D)=\frac{D}{\xi_0}\sum_{n=0}^{N-1}U(-nD)\exp[-n(\nu T_H+iqD)]=\sum_{k=-\infty}^{+\infty}\int_0^{\xi_0}\frac{dx}{\xi_0}U(-x)\exp\left(\frac{x}{D}(2\pi ik-iqD-\nu T_H)\right).\tag{13}$$

In Eq. (13), we have used the Poisson summation formula, and Λ_m are the harmonics in the Fourier expansion of the periodic function $\Lambda(\tau+T_H)=\Lambda(\tau)$:

$$\Lambda(\tau)=\sum_m\Lambda_m\exp(-im\Omega\tau),\quad\Omega=2\pi/T_H,\quad\Lambda_m=\Lambda^*_{-m}.\tag{14}$$

The function $\Psi_2(D)$ defined by (13) and containing integrals of a rapidly oscillating function is small ($\sim(D/\xi_0)U\ll U$) virtually for any p_z except the preferred values p_{zn} satisfying the resonance condition

$$qD_n=qD(p_{zn},H)=2\pi n,\quad n=1,2,...,\tag{15}$$

under which a resonant term of the order of U with $k=n$ is singled out in the sum (13). This term corresponds to electrons with an integral number of acoustic waves fitting into a period of the trajectory, its contribution to the electron force is proportional to the width of the resonant group and is also small in the general case. If, however, the resonance condition (15) holds for a certain value H_n of the magnetic field for a wide electron group, e.g., for a cross section with the extremal value of the period

$$qD(p_{z\ \mathrm{extr}},H_n)=2\pi n,\quad\frac{\partial D}{\partial p_z}(p_{z\ \mathrm{extr}})=0,\tag{16}$$

the electron force exhibits a sharp peak corresponding to resonant peaks of attenuation of sound in the DSCR theory and to an abrupt increase in the intensity of transfer in the case under investigation. Expanding the resonant terms in (12) and (13) in the vicinity of $p_{z\ \mathrm{extr}}$ and integrating with respect to p_z in (11), we obtain the value of electron force at the point of the nth resonance:

$$F_n=A_n\exp(iq\xi)\int_0^{\xi_0}\frac{d\xi'U(-\xi')}{\sqrt{\xi+\xi'}}\exp\left(-\frac{\nu}{v}(\xi+\xi')\right),$$

$$A_n=\frac{i\omega q^2|\Lambda_n|^2\exp(\pi i/4)}{2\pi^2\rho\sqrt{\pi nD_n''}}\sim\omega^2\frac{\omega q}{n\Omega}\left|\frac{\Lambda_n}{\varepsilon_F}\right|^2,\tag{17}$$

which indicates that resonant transfer forms a coherent acoustic field (''precursor'') with the frequency and wave vector of the initial pulse, extending over a distance of the order of a mean free path from the pulse front. Far away from resonance, the precursor field is small and incoherent (random).

In order to calculate the precursor field $u_n(\xi,t)$, we consider the wave equation (4) which has the following solution in the region $\xi>0$ in front of the pulse at the point of the nth resonance:

$$u_n(\xi,t)=-A_n\exp(iq\xi)\int_0^{\infty}dt_1(t-t_1)\exp(2i\omega t_1)\times\int_0^{\xi_0}d\xi'\frac{U(-\xi')}{\sqrt{\xi+\xi'+2st_1}}\exp\left(-\frac{\nu}{v}(\xi+\xi'+2st_1)\right)\approx\frac{A_nt}{2i\omega}\exp(iq\xi)\int_0^{\xi_0}d\xi'\frac{U(-\xi')}{\sqrt{\xi+\xi'}}\times\exp\left(-\frac{\nu}{v}(\xi+\xi')\right)\sim U\omega t\left|\frac{\Lambda_n}{\varepsilon_F}\right|^2\frac{\omega}{n\Omega}q\xi_0.\tag{18}$$

The linear increase of the precursor amplitude with time reflects continuous pumping of the acoustic field being transferred by nonequilibrium electrons removing energy from the pulse and is limited by attenuation which is not taken into

consideration.[1)] The presence of an additional (power) attenuation of the precursor described by the factor $1/\sqrt{\xi+\xi'}$ in the integrand is associated with dephasing of resonant electrons over large distances, and its shape can vary depending on the type of the cross section ensuring resonant transfer.

The solution of the problem on electron transfer of an acoustic pulse in a finite-length sample can be constructed similarly if we assume that the metal surface scatters charge carriers diffusely. In this case, the equilibrium condition (8) in which the role of ξ_0 is played by the current value st of the pulse length in the sample ($t=0$ is the instant when the pulse enters the sample) holds asymptotically accurately for a narrow resonant group of electrons we are interested in since f is the isotropic constant for reflected carriers determined from the electroneutrality condition and is negligibly small as compared to the resonant value of f formed after the passage of electrons through the pulse. The function $U(\xi)$ describing the pulse envelope vanishes abruptly at the sample surface $z=0$ containing the emitter; among other things, this leads to the excitation of a quasiwave, i.e., a long-wave ($q\approx\omega/v_z$) elastic field propagating at a velocity of the order of the Fermi velocity. The nonequilibrium correction to the distribution function calculated in analogy with (9), i.e.,

$$f(v>0,\ \xi>0)=\omega q\ \exp(-\nu\xi/v)\int_0^{T_0(z,t)} d\tau_1$$

$$\times\exp(-\nu\tau_1)\Lambda(\tau-\tau_1-\xi/v)u(-v\tau_1),$$

$$T_0(z,t)=\frac{z}{v_z}-\frac{\xi}{v}=\frac{s}{v}\left(t-\frac{z}{v_z}\right) \tag{19}$$

vanishes for $t<z/v_z$, reflecting the finiteness of the velocity of the precursor propagating from the pulse front. For the time we are interested in ($t\sim z/s\gg z/v_z$), the delay effect becomes insignificant, and the quantity t_0 can be replaced to within s/v_z by its approximate value $\xi_0(t)/v=st/v$. The expression for electron force at the resonance point coincides with (17) to the same accuracy, and the form of the precursor is described by the function

$$u_n(t_0)=\frac{A_n}{2i\omega}\exp(i\omega t_0)\int_0^{t_s-t_0} dt$$

$$\times(t_s-t_0-t)\ \frac{U(t)}{\sqrt{t_0+t}}\exp(-\chi(t_0+t)), \tag{20}$$

where we go over to the time representation for the convenience of comparison with experimental data (coordinates are normalized to the velocity of sound): $t_s=L/s$ is the acoustic delay time in the sample, t_0 the position of a reading strobe-pulse measured from the instant of arrival of the leading front of the main acoustic signal at the receiving end of the sample, and $\chi=\nu s/v_H$. Expression (20) differs from (18) in the nonlinear dependence of the amplitude boosting on t_0 due to a change in the length of the pulse entering the sample.

Concluding the section, we note that v_z was treated for the sake of brevity as independent of the position of an electrons on the orbit. The inclusion of this dependence only leads to the replacement of v by its average value $\overline{v}\equiv v_H$ on the resonant orbit.

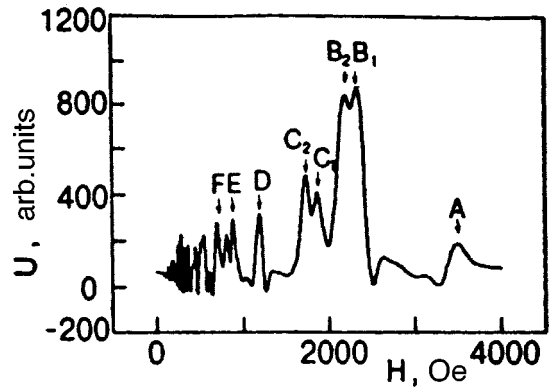

FIG. 5. Recorded signal of longitudinal acoustic field transfer; $\mathbf{q}\|H\|\Gamma U$, $f=54.3$ MHz. Resonant magnetic fields are marked.

3.2. DSCR transfer in Al for $\mathbf{q}\|\mathbf{H}\|\Gamma U$

In view of the aim of our experiments, we had to choose the sample orientation for which the ES signals discussed above are absent in a magnetic field, thus making interference impossible. This discards the directions [111] and [100], but suggests an analysis of the [110] direction. In such a geometry, however, the structure of DSCR transport is unproductive, and so we chose the orientation $\mathbf{q}\|\mathbf{H}\|\Gamma U$ for which we can expect the emergence of transport by electrons near the boundary cross section passing through the point U and corresponding to a two-loop orbit breakage into two circular orbits. This would allow us to determine the $e-e$ scattering frequency near the points U and W at which the calculated values of α are maximum.

The study of DSCR transport is technically the same as experiments with ES: the amplitude of the elastic field propagating through the sample prior to the arrival of the main acoustic signal is detected with the help of a strobing system. The recording of a DSCR transport signal in a sample with $\mathbf{q}\|\mathbf{H}\|\Gamma U$ at a frequency of 54.3 MHz is illustrated in Fig. 5. The main (marked) group of signals corresponds to resonances with $n=1$. The only possible exception is the signal E which can be attributed according to its position to resonances of group C for $n=2$, but differs in behavior from these resonances.

The absence of resonances with $n\neq1$ is apparently associated with the absence of wide regions of effective interaction of electrons with sound on resonant orbits, which are determined by the condition $\mathbf{q}\times\mathbf{v}_F=0$ (in all probability, this condition could be satisfied only on very narrow regions on the edges of the hole sheet on the FS). In this case, the amplitude of the nth resonance is determined by the square of the nth harmonic of deformation potential, whose value decreases rapidly with increasing n ($\Lambda_n\propto n^{-2}$) when the vector $\mathbf{q}$ lies in the symmetry plane, and when the deformation potential varies smoothly; this explains difficulties involved in observing higher resonances.

The magnitude of the resonant field $H_{\rm res}$ is determined by the following simple formula following from (16):

$$H_{\rm res}=\frac{qc}{2\pi e}\left(\frac{\partial S}{\partial p_H}\right)_{\rm extr}.$$

In order to identify resonances and (which is most important) to determine the velocity v_H of propagation of transfer signals, we carried out model calculations of $\partial S/\partial p_H$ and v_H.

3.3. Calculated differential characteristics of FS cross sections in Al for H‖Γ*U*

It should be noted that detailed information on a number of differential characteristics of the band structure is not available for a metal like Al, which has been investigated thoroughly in many respects. The existing data mainly pertain to high-symmetry points of the Brillouin zone (BZ) or to some high-symmetry lines. For example, there are practically no data on the behavior of the derivatives of the areas of FS cross sections in Al along the line ΓU of the BZ.

We calculated the band structure of Al by the method of pseudopotential (PP) using the highly effective PP model for Al proposed by Ashcroft[20] in the four-wave approximation. The computational error for $E_n(\mathbf{k})$ did not exceed 1 mRy. The cross-sectional areas $S(p_H)$ of the hole sheet of the FS in the second zone of Al were determined without using of any interpolation procedures associated with the computation of the band structure, which ultimately allowed us to minimize the error in the calculation of the derivatives $\partial S/\partial p_H$.

In the plane of the FS cross section (for a fixed value of p_H), the band structure was calculated directly at 1.6×10^5 points of the BZ forming a regular two-dimensional mesh. The values of $S(p_H)$ for the simply connected hole FS in the second zone were determined by calculating the mesh nodes with $E_2(\mathbf{k})>E_F$. The computational procedure for the derivatives $\partial S/\partial p_H$ was based on numerical differentiation of the cross-sectional areas of the FS with respect to the momentum in a given direction. It were used both of the simplest differentiation algorithms for computing derivatives with an adaptive step 0.01–0.0001 in the units of $2\pi/a$, and the representation of derivatives in terms of coefficients of the cubic spline constructed for the function $S(p_H)$.

The above parameters of the computational algorithm ensured a reliable reproduction of the nonmonotonic dependence of $\partial S/\partial p_H$, which suggests that the chosen model of the band structure of Al is the main source of systematic errors.

It should be noted that the computations carried out by us for the derivatives $\partial S/\partial p_H$ in the second zone in the approximation of an empty lattice demonstrates a qualitatively different pattern of extrema as compared to the PP method, and does not allow us to interpret experimental data adequately. At the same time, reasonable variations of the parameters of the computational algorithm in the PP approximation, including a shift of the Fermi level within 10 mRy from the value of $E_F=0.833$ Ry used by us do not lead to a considerable change in the differential characteristics of the band structure. Taking into account the relative error of less than 1% in determining the band effective masses attained here, the relative error in computation of drift velocities (except in the case stipulated below) can be estimated as 10 %.

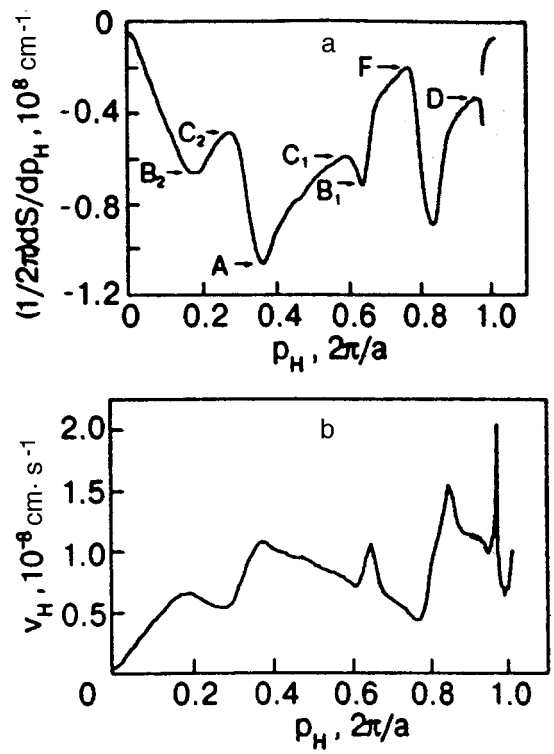

FIG. 6. Model dependence of the derivative of the cross-sectional area of the hole sheet of the FS for p_H varying along the ΓU direction. The arrows indicate the extrema corresponding to resonant fields in Fig. 5(a); the model dependence of the band drift velocity along the ΓU direction ($\mathbf{H}\|\Gamma U$) (b); a is the crystal structure constant.

Figures 6a and b show the calculated values of $\partial S/\partial p_H$ and v_H; the corresponding resonances are marked near extremal values of $\partial S/\partial p_H$. Numerical data characterizing the correspondence between the calculated and experimental values of $(\partial S/\partial p_H)_{\rm extr}$ are presented in Table II together with corresponding values of the drift velocity v_H.

It was noted above that certain difficulties are encountered in the classification of the E- resonance whose identification with the second harmonic of the C-resonance does not agree with our data. At the same time, it can be attributed to the boundary cross sections emerging on ''horns'' W of the hole sheet of the FS at the instant of splitting of two-loop

TABLE II. Calculated and experimental values of $(\partial S/\partial p_H)_{\rm extr}$ and drift velocities.

Resonance	$(S'/2\pi)_{\rm exp}$, Å^{-1}	$(S'/2\pi)_{\rm calc}$, Å^{-1}	$v_{H\ \rm zone}$, 10^8 cm×s^{-1}	$v_{H\ \rm zone}/(1+\lambda)$, 10^8 cm×s^{-1}
A	1.05	1.067	1.06	0.76
B_1	0.69	0.71	1.06	0.76
B_2	0.656	0.665	0.65	0.46
C_1	0.554	0.59	0.75	0.54
C_2	0.516	0.49	0.54	0.39
D	0.36	0.33–0.34	1.0–1.1	0.75
E	0.26	?	?	?
F	0.21	0.2	0.44	0.32

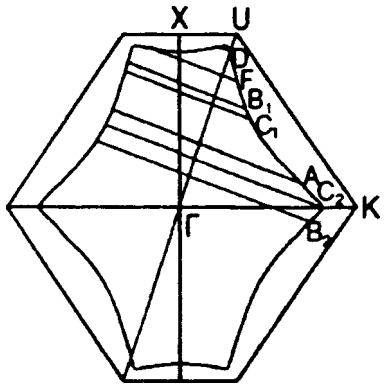

FIG. 7. Central cross section of the FS of Al by the [110] plane. The traces of resonant cross sections of the FS by the planes perpendicular to the ΓU direction are denoted by corresponding letters.

orbits. However, the error of calculations in the vicinity of such a ''topological transition'' increases significantly taking into account the divergence of $\partial S/\partial p_H$ as well as the cyclotron mass. This is apparently the reason behind a spike on the theoretical dependence $v_H(p_H)$ at the transition point, although the drift velocity should not have any singularity at this point according to physical considerations. For this reason, we shall not discuss here the behavior of the E-resonance and consider only the experimentally measured dependences.

Some resonances may belong to an electron sheet of the FS. We did not calculate $\partial S/\partial p_H$ on this sheet since the calculations of this kind are cumbersome due to multiconnectedness of such cross sections. It can be stated, however, that no extrema of $\partial S/\partial p_H$ are observed on the main tubes of the third electron band, which are successfully approximated by ellipsoids (naturally, we are interested only in $\partial S/\partial p_H$ for each simply connected cross section separately). The extrema can appear only in the regions of connection of the ellipsoids, in which the values of $(\partial S/\partial p_H)_{\text{extr}}$ are small. The ''fence'' of resonances in the region of weak fields apparently corresponds to these extrema.

On the whole, Table II demonstrates a good agreement between the calculated and experimental values of $(\partial S/\partial p_H)_{\text{extr}}$.

Figure 7 shows schematically the position of cross sections on the FS, that generate the resonances marked in Fig. 5. It can be seen that the most interesting is the D-resonance since the FS cross section corresponding to it lies near the points U and W.

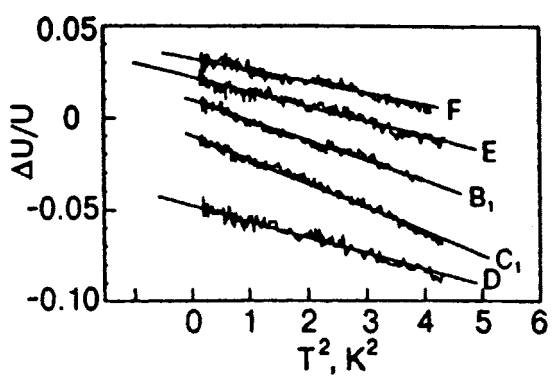

FIG. 8. Temperature variations of the amplitude of DSCR transfers for $t_0 = 0$. Straight lines correspond to approximation. Experimental curves are shifted arbitrarily one to another.

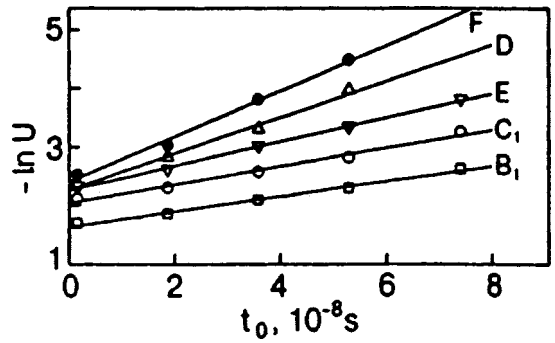

FIG. 9. Dependence of the logarithmic amplitude for DSCR transfers on the position of the strobe. Straight lines are approximations. The mutual arrangement of experimental points reflects the relative amplitude of signals.

3.4. Parameters of electron–impurity and *e–e* scattering

In order to obtain information on the parameters of $e-e$ scattering, we must get rid of the phonon contribution to the total relaxation frequency; for this reason, we confine our analysis to the temperature range $0.4\ \text{K} < T < 2\ \text{K}$. The temperature dependences of the relative changes in the amplitudes of ''precursors'' for the resonances B_1, C_1, D, E, and F at $t_0 = 0$ are shown in Fig. 8, which demonstrates that the law $\delta u/u = \tilde{\alpha} T^2$ holds well for all the resonances.

Since amplitude variations are small, we can derive an expression describing $\delta u/u$ by confining ourselves in (20) to the first term in the expansion in the small increment $\delta\nu$ of the relaxation frequency:

$$\frac{\delta u}{u} = \frac{\int_0^\infty (t_s - t) U(t) \chi_0 \sqrt{t} \exp(-\chi_0 t) dt}{\int_0^\infty (t_s - t) \dfrac{U(t)}{\sqrt{t}} \exp(-\chi_0 t) dt} \frac{\delta\nu}{\nu_0} \equiv S(\chi_0) \frac{\delta\nu}{\nu_0},$$

$$\chi_0 = \nu_0 s / v_H. \tag{21}$$

Thus, in order to find $\alpha = \tilde{\alpha} \nu_0 / S(\chi_0)$ for the known shape of the pulse $U(t)$, we must also measure the electron–impurity relaxation frequency ν_0.

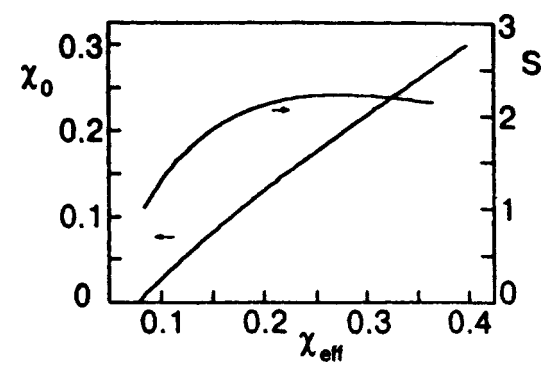

FIG. 10. Dependence of the coefficients χ_0 and S on χ_{eff} (see text).

TABLE III. Physical characteristics of investigated precursors.

Resonance	$\tilde{\alpha}$, K^{-2}	χ_{eff}, 10^8 s^{-1}	χ_0, 10^8 s^{-1}	$S(\chi_0)$	ν_0, 10^9 s^{-1}	α, 10^6 $s^{-1}\times K^{-2}$	α_0, 10^6 $s^{-1}\times K^{-2}$
B_1	0.0109	0.129	0.060	1.18	0.67	6.2	4.6 ± 0.4
C_1	0.0132	0.156	0.087	1.54	0.69	5.9	4.4 ± 0.4
D	0.00884	0.309	0.225	2.23	2.5	10	7.5 ± 0.8
E	0.0082	0.205	0.135	1.97	?	?	?
F	0.0065	0.387	0.29	2.17	1.37	4.1	3.1 ± 0.5

For this purpose, we measured the dependences of the amplitudes of the resonances in question on t_0 at $T=0.4$ K (Fig. 9). According to (20), for large values of the parameter χ_0, the logarithmic amplitude is a linear function of t_0 with a slope χ_0. This relation is nonlinear in the general case, but according to numerical calculations, it is correctly approximated by a linear dependence with an effective slope $\chi_{eff}(\chi_0)$ in the range $0<t_0<6\times10^{-8}$ s, where the transport field is detected reliably.

The functions $S(\chi_0)$ and $\chi_0(\chi_{eff})$ used for processing the results are shown in Fig. 10. It should be emphasized that these functions are not universal, but are determined by t_s (the sample thickness) and the shape of the exciting pulse. The subsequent procedure of processing of the results lies in the following: χ_{eff} is determined from the slopes of approximating curves in Fig. 9, the values of χ_0 and $S(\chi_0)$ are found from Fig. 10, the value of ν_0 is determined from the calculated value of v_H presented in Table II, and finally, Fig. 8 is used to find the values of α which in the given case are averaged over energy. The final results for the resonances under investigation are compiled in Table III.

Table III contains anything unexpected for the resonances B_1 and C_1 whose orbits mainly belong to spherical regions of the FS. The frequency ν_0 of impurity relaxation is close to the value 0.95×10^9 s^{-1} measured earlier and averaged over the entire FS. The values of the constant α are also virtually the same as those measured in Sec. 2 with the help of ES. The most unexpected result is apparently the anisotropy in ν_0: the impurity scattering frequencies for the resonances D and F are respectively four and two times the value of ν_0 for the resonances B_1 and C_1. At the same time, the value of α for the D resonance does not exceed the doubled value of α for the B_1 and C_1 resonances, although the electron orbits for the D resonance are so close to points of the type of U and W that we should expect an order of magnitude increase in the value of α according to the calculations made by Jaquier *et al.*[6]

Let us now consider the reliability of the results pertaining to the observed anisotropy of ν_0. The $u(t_0)$ dependences used to find the value of ν_0 are reproducible, and their measurements does not impose straight requirements to the accuracy of experiments. The corrections connecting χ_0 and χ_{eff} are significant only for small values of χ_{eff}; for large slopes, however (see Fig. 10), χ_{eff} approaches χ_0 irrespective of the shape of the pulse $U(t)$. The error in the estimation of ν_0 is also determined by the error in the calculation of v_H as well as by the used value of the electron–phonon renormalization constant $\lambda=0.4$, whose value apparently increases to 0.6 as we approach the points U and W.[15] In general, this can reduce the value of ν_0 by less than 20–25%. It should also be noted that the anisotropy in ν_0 was observed earlier in experiments on the de Haas–van Alphen effect in highly diluted Cu–Ni and Cu–Ge alloys.[21]

The estimates of the $e-e$ interaction parameter α are primarily based on the measurement of relative changes of the precursor's amplitude as a function of temperature (see Fig. 8). These dependences are also reproducible. The noise level is determined primarily not by the smallness of the amplitude of the transferred signal, but by the instability of the delay of a strobe-pulse with respect to an exciting rf pulse since the measurements are made on the exponentially descending edge of the transferred signal. For small χ_{eff}, the corrections change the values of ν_0 and $S(\chi_0)$ in the same direction so that the value of α virtually remains unchanged. For large χ_{eff}, the value of S is independent of χ_{eff} (see Fig. 10) (this is a reflection of the fact that the main transferred signal in the case of strong scattering arrives from a distance v_H/ν_0), and the dependence on t_s disappears. In this case, the estimates of α and ν_0 are virtually of the same accuracy.

In conclusion, let us formulate the main results. The temperature dependences of the amplitude of electron sound in Al are determined almost completely by electron–electron collisions up to 10–12 K in view of its extremely low sensitivity to small-angle scattering. The $e-e$ relaxation frequency determined from such measurements on spherical regions of the Fermi surface of Al is in good agreement with calculations.[6] The measurements of parameters of $e-e$ scattering from the data on the transfer of sound under DSCR have confirmed the estimates obtained for spherical regions of the FS. However, the considerable (an order of magnitude) increase in the frequency of $e-e$ collisions near corners and edges of the hole sheet of the Fermi surface predicted in the theory[6] was not confirmed experimentally the anisotropy factor does not exceed 2. A considerable increase is observed in the frequency of electron–impurity collisions near the points U and W of the Fermi surface for Al.

*E-mail: bezugly@ilt.kharkov.ua
**E-mail: fil@ilt.kharkov.ua

[1)]In our experiments, relaxation attenuation of ES is much stronger than the Landau absorption of an acoustic pulse, and the inclusion of the latter effect leads to insignificant corrections.

[1] A. A. Abrikosov, *Introduction to the Theory of Metals* [in Russian], Nauka, Moscow (1987).
[2] M. Kaveh and N. Wiser, Adv. Phys. **33**, 257 (1984).
[3] V. A. Gasparov and R. Huguenin, Adv. Phys. **42**, 393 (1993).
[4] J. H. I. M. Ribot, J. Bass, H. van Kempen *et al.*, Phys. Rev. B **23**, 532 (1981).

[5] A. Jaquier, P. A. Probst, R. Huguenin, and J. Pligs, J. Phys.: Condens. Matter **6**, 11081 (1994).
[6] A. Jaquier, R. Stubi, P. A. Probst *et al.*, Phys. Rev. B **51**, 13005 (1995).
[7] E. V. Bezuglyi, N. G. Burma, E. Yu. Deineka *et al.*, J. Low Temp. Phys. **91**, 179 (1993).
[8] S. Z. Dunin and E. P. Fetisov, Fiz. Tverd. Tela (Leningrad) **14**, 270 (1972) [Sov. Phys. Solid State **6,** 221 (1972)].
[9] M. I. Kaganov, Uspekhi Fiz. Nauk **145**, 507 (1985) [Sov. Phys. Usp. **28**, 257 (1985)].
[10] A. I. Kopeliovich and M. S. Churyukin, Fiz. Nizk. Temp. **19**, 176 (1993) [Low Temp. Phys. **19**, 125 (1993)].
[11] V. M. Kontorovich, in Conduction Electrons [in Russian], Nauka, Moscow (1985).
[12] Y. Fukai, Phys. Rev. **186**, 697 (1969).
[13] K. Schwartzman and W. E. Lawrence, Phys. Rev. B **48**, 14089 (1993).
[14] T. Wegehaupt and R. E. Doezema, Phys. Rev. B **16**, 2515 (1977).
[15] T. Wegehaupt and R. E. Doezema, Phys. Rev. B **18**, 742 (1978).
[16] V. F. Gantmakher and I. B. Levinson, *Scattering of Charge Carriers in Metals and Semiconductors* [in Russian], Nauka, Moscow (1984).
[17] A. I. Kopeliovich, Zh. Éksp. Teor. Fiz. **59**, 1273 (1970) [Sov. Phys. JETP **32**, 695 (1970); N. N. Bychkova and A. I. Kopeliovich, Fiz. Nizk. Temp. **3**, 458 (1977) [Sov. J. Low Temp. Phys. **3**, 221 (1977)].
[18] R. Reich, Proceedings of LT10, Vol. III, 371 (1966).
[19] N. G. Burma, V. D. Fil', and P. A. Bezuglyi, Pis'ma Zh. Éksp. Teor. Fiz. **28**, 216 (1978) [*sic*].
[20] N. W. Ashcroft, Philos. Mag. **8**, 2055 (1966).
[21] R. G. Pulsen, D. L. Raudles, and M. Springtord, J. Phys. F **4**, 981 (1974).

Translated by R. S. Wadhwa

Peculiarities of electronic properties of $\delta\langle$Sb$\rangle$ layers in epitaxial silicon. IV. Hopping conductivity and nonlinear effects

Vit. B. Krasovitsky and Yu. F. Komnik

*B. Verkin Institute for Low Temperature Physics and Engineering, National Academy of Sciences of the Ukraine, 310164 Kharkov, Ukraine**

O. A. Mironov

Institute of Radiophysics and Electronics, Academy of Sciences of the Ukraine, 310085 Kharkov

C. J. Emeleus and T. E. Whall

Department of Physics, University of Warwick, Coventry, CV4 7AL, UK
(Submitted September 5, 1997)
Fiz. Nizk. Temp. **24**, 241–249 (March 1998)

The temperature dependence of the kinetic electronic characteristics (conductivity, magnetoresistance, Hall e.m.f.) is studied in the temperature interval 3–50 K on epitaxial silicon crystals having a $\delta\langle$Sb$\rangle$ layer with sheet concentrations of Sb atoms 1×10^{13} and 5×10^{12} cm^{-2}. The shape of the current–voltage characteristics is determined at various temperatures. It is found that the low-temperature kinetic phenomena in these objects are governed by the hopping mechanism of conductivity. A variable range hopping conductivity is observed at sufficiently low temperatures (<10 K). The nonlinearity of the current–voltage characteristics is explained by the theory of non-Ohmic hopping conductivity in moderately strong electric fields. © *1998 American Institute of Physics.* [S1063-777X(98)00603-3]

INTRODUCTION

The electrical properties (conductivity, magnetoresistance, Hall e.m.f.) of $\delta\langle$Sb$\rangle$-layers in silicon obtained by molecular beam epitaxy have been studied in a wide temperature interval.[1–3] The delta layer is a conducting layer of atomic thickness formed by impurity atoms lying in the same crystallographic plane in the matrix of a semiconducting crystal. Electrons responsible for the δ-layer conductivity are located in a symmetric V-shaped potential well formed due to screening of the impurity atoms potential by electrons. Electrons in the potential well form a two-dimensional electron gas.

In contrast to the other types of two-dimensional electron systems (inversion layers, heterojunctions, etc.), δ-layers can be formed with any concentration of electrons. The kinetic characteristics of five samples with the following concentration N_D (in cm^{-2}) of antimony atoms in the δ-layer were studied by us[1] in a wide temperature interval (1.6–300 K): 3×10^{14} (sample A), 1×10^{14} (B), 3×10^{13} (C), 1×10^{13} (D) and 5×10^{12} cm^{-2} (E).[1)] All samples have an activation region of impurity carriers in which an exponential decrease in resistance with increasing temperature is observed. The temperatures above which an activation of impurity carriers to the conduction band of silicon is clearly manifested are $\sim$70 K (sample A), $\sim$60 K (B), $\sim$45 K (C), and $\sim$30 K (samples D and E). It was shown in Ref. 2 that at lower temperatures, the temperature and magnetic-field dependences of conductivity and Hall e.m.f. for samples A, B and C are described with a high degree of accuracy by quantum corrections to the conductivity associated with the interference effects of weak localization (WL) of electrons and electron–electron interaction (EEI) in a two-dimensional system. An analysis of these dependences leads to the temperature dependence of the time τ_φ of the electron phase relaxation which is treated as a manifestation of the electron–electron scattering in the δ-layer, as well as the spin–orbit interaction time τ_{so} and the electron–electron interaction parameter λ^D. A combined analysis of the interference effects and the electron-overheating effect in samples A, B, and C provides information about the temperature variation of the time τ_{ep} of electron–phonon relaxation.[3]

Properties of high-resistance samples D and E below 18 K were not discussed by us in Ref. 1 since their behavior does not correspond to the WL and EEI effects, but rather to the hopping mechanism of conductivity. In this work, we present the results of investigation of the behavior of conductivity of high-resistance silicon samples with a $\delta\langle$Sb$\rangle$ layer upon a change in temperature (in the helium region), as well as magnetic and electric fields. The obtained temperature dependences of resistance and current–voltage characteristics demonstrate the peculiarities of hopping mechanisms of conductivity in two-dimensional electron systems. The significant difference in the conductivity mechanisms in low- (A, B) and high-resistance samples (D, E) is illustrated by the dependence $R_\square(N_D)$ (curve *1*, Fig. 1) constructed for the entire investigated batch of samples on the basis of the data obtained by us earlier[1] and in the present work at a temperature 8 K. The sharp increase in the resistance at $N_D \leqslant 3\times10^{13}$ cm^{-2} is associated with the metal–insulator transition upon a decrease in the concentration of impurity atoms in the δ-layer. Such a transition occurs under conditions

 © 1998 American Institute of Physics

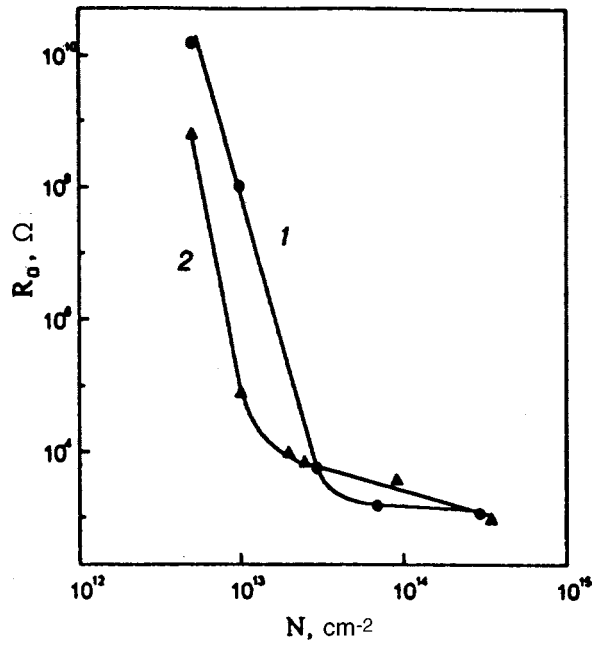

FIG. 1. Dependence of the resistance $R_\square$ on the sheet concentration N of impurity atoms in δ-layers in silicon for antimony (curve *1*) and boron[4] (curve *2*).

when the mean separation between ionized Sb atoms in the δ-layer ($\sim N_D^{-1/2}$) is larger than the Bohr radius a_B characterizing the dimensions of the electron wave function at the impurity atom. For the sake of comparison, Fig. 1 shows the dependence $R_\square(N_A)$ for δ-layers of boron, an acceptor impurity in silicon,[4] which was also measured at 8 K (curve *2*). In this case, the metal–insulator transition is observed for $N_A \sim 1\times 10^{13}$ cm^{-2}, i.e. for a lower concentration than for Sb, which is apparently due to a larger value of the effective Bohr's radius for boron. Thus, the high-resistance samples D and E with a $\delta\langle$Sb$\rangle$-layer are obviously on the insulator side of the metal–insulator transition.

2. MEASURING TECHNIQUE

The samples were single crystals of epitaxial silicon (of size $6\times 4\times 0.5$ mm) with a $\delta\langle$Sb$\rangle$-layer formed in the crystallographic plane (100) and having the shape of a double cross. The contact areas of current and potential leads at the crystal surface made it possible to connect the sample in the measuring circuit. Measurements of resistance, magnetoresistance, current–voltage characteristics, and Hall e.m.f. reported in the present work were made predominantly at temperatures below 20 K (down to 3 K for sample D). The temperature was stabilized to within 0.05 K.

In view of the large range of variation of sample resistance (10^3–10^{12} Ω), measurements were made in two regimes, viz., (a) by passing a fixed current (FC) through the sample for measurement of resistance below 10^8 Ω (measuring current $I=10^{-8}$ A), we measured either the voltage drop across the sample by the standard four-probe technique; or directly the resistance with the help of an ohmmeter; (b) by applying a fixed voltage (FV) across the sample having a resistance exceeding 10^8 Ω, in this case, we measured the current in the sample circuit which was determined only by the sample resistance that is several orders of magnitude higher than all the remaining resistances in the current circuit. The results of measurements made in the FC and FV regimes were ''joined'' in the vicinity of the value 10^8 Ω.

The investigated samples displayed transient processes whose origin remains unclear. It was found that after cooling of the sample from room temperature to helium temperatures, the first application of voltage (FV regime) across the sample results in the generation of a current whose value increases sharply by a factor of 2–3 after a few seconds, and then increases slowly over the next tens of minutes by an order of magnitude as compared with the initial value. If a switchover to the FC regime (ohmmeter) is made several times instantaneously, a monotonic decrease in the sample resistance is observed. Hence the applied voltage forms a new state of the sample which is characterized by a lower resistance. If the FC regime is preserved for a long time, the value of the sample resistance attained earlier in the FV regime will increase very slowly, tending to its initial value. Hence the electric measurements lead to a decrease in sample resistance, the magnitude of the decrease being the larger, the longer the time interval over which measurements are made, or the stronger the measuring current or the applied voltage. This circumstance was taken into consideration during measurements. For example, the temperature dependences of resistance were plotted from the results of measurements for a low applied voltage (<2 V). The resulting high-resistance state is reproduced in repeated cycles of measurements. Higher applied voltages as well as prolonged measuring cycles reveal low-resistance states of the samples, but the $R(T)$ dependences obtained in such cycles are functionally identical to the corresponding dependences for the high-resistance state of the samples. The current-voltage characteristics (IVC) were measured by varying discretely the applied voltage, while the duration of measurement of a complete IVC did not exceed two minutes, thus ruling out the influence of transient processes.

3. DISCUSSION OF EXPERIMENTAL RESULTS

3.1. Temperature variation of kinetic characteristics

Figure 2 shows the temperature dependences of the resistance R, the magnetoresistance $\Delta R_H = R(H) - R(0)$, and the reduced Hall e.m.f. $U_H/(Hj)$ (j is the current), measured on sample D in the temperature interval 10–50 K. For the sake of comparison, the logarithms of the quantities R, ΔR_H and $U_H/(Hj)$, plotted against the reciprocal temperature, are presented in relative units: all the curves are normalized to the corresponding values at $T=34.4$ K. It can be seen quite clearly that the dependences shown in the figure obey the same exponential dependence in the temperature interval 27–47 K. Below 27 K, the $R(T)$ dependence displays another (weaker) exponential region, while the quantities ΔR_H and $U_H/(Hj)$ decrease sharply upon a decrease in temperature after attaining their peak values at $T\approx 23$ K. The magnetic field dependences of the quantities ΔR_H and $U_H/(Hj)$, measured to the left and right of the peak at various temperatures, differ significantly (Fig. 3). A conventional power de-

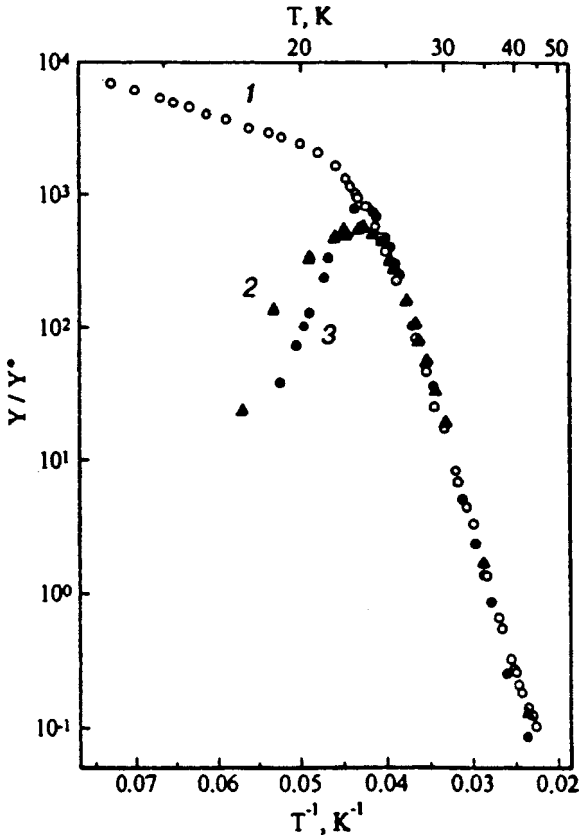

FIG. 2. Temperature dependence of resistance R (*1*), variation $\Delta R_H = R(H) - R(0)$ of resistance in a magnetic field ($H = 16$ kOe) (*2*), and the reduced Hall e.m.f. $U_H/(Hj)$ (*3*) for sample D with a concentration $N_D = 1 \times 10^{13}$ cm^{-2} of Sb atoms in the δ-layer. The curves are normalized to their corresponding values at $T = 34.4$ K.

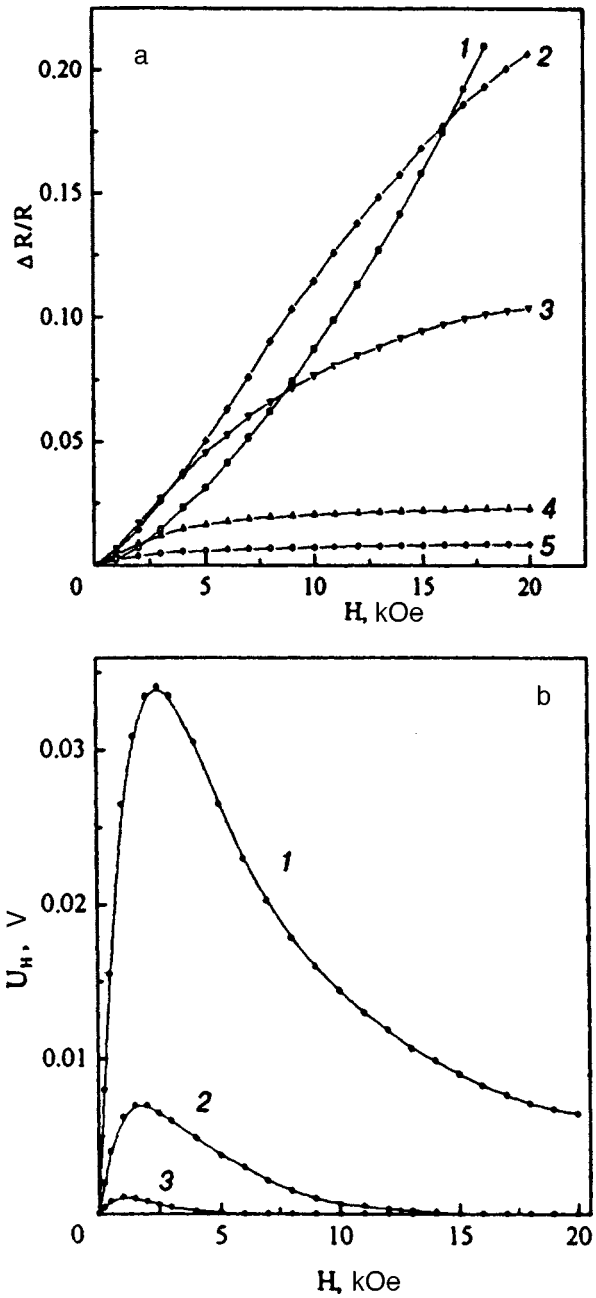

FIG. 3. Magnetic field dependences of relative variation $\Delta R/R_0$ of resistance (a) and Hall e.m.f. U_H (b) of sample D at various temperatures T, K: 27.25 (curve *1*), 25.25 (curve *2*), 23.15 (curve *3*), 20.4 (curve *4*), 18.8 (curve *5*) (a) and 20.4 (curve *1*), 18.8 (curve *2*), and 17.5 (curve *3*) (b).

pendence $\Delta R_H \sim H^n$ is observed to the right of the peak, where $n \sim 1.5$–2 (curve *1*, $n = 1.6$) and $U_H \sim H$. The dependences $\Delta R_H(H)$ tend to saturation to the left of the peak, and the amplitude of the magnetoresistance effect decreases rapidly (curves *3*–*5*), while the $U_H(H)$ dependences are in the form of curves with a peak followed by an asymptotic decrease to zero. The Hall e.m.f. also decreases rapidly upon a decrease in temperature. The low-temperature segment of the dependence $\log R(1/T)$ for the investigated samples is presented in Fig. 4.

The δ-layers of Sb in silicon used in this work are actually weakly doped weakly compensated n-type semiconductors of two-dimensional configuration. In the temperature interval 3–50 K studied by us, the current flow is mainly determined by two competing mechanisms of conductivity. The first mechanism, which dominates at higher temperatures, is associated with electrons in the conduction band that are in thermal equilibrium with electrons at the donor centers. The second mechanism, which is manifested at lower temperatures, is associated with electrons localized in the vicinity of impurities and having a weak overlapping of wave function tails. Under certain conditions, electrons may hop from donor to donor by tunneling without an activation transition to the conduction band. In spite of the fact that the electrons hopping over impurity levels have a very low mobility since it is associated with the interaction of impurities separated from each other by large distances, the impurity conduction begins to dominate at low temperatures due to ''freezing out'' of electrons in the conduction band. Consequently, the electrical conductivity assumes the form[5]

$$\rho^{-1}(T) = \rho_1^{-1} \exp(-\varepsilon_1/kT) + \rho_3^{-1} \exp(-\varepsilon_3/kT), \quad (1)$$

where the first term corresponds to band conductivity, and the second to hopping conductivity with a constant activation energy ε_3 whose origin is associated with the spread of impurity energy levels: an electron transition from one donor to another is possible only through absorption or emission of phonons. The constancy of the activation energy ε_3 upon a

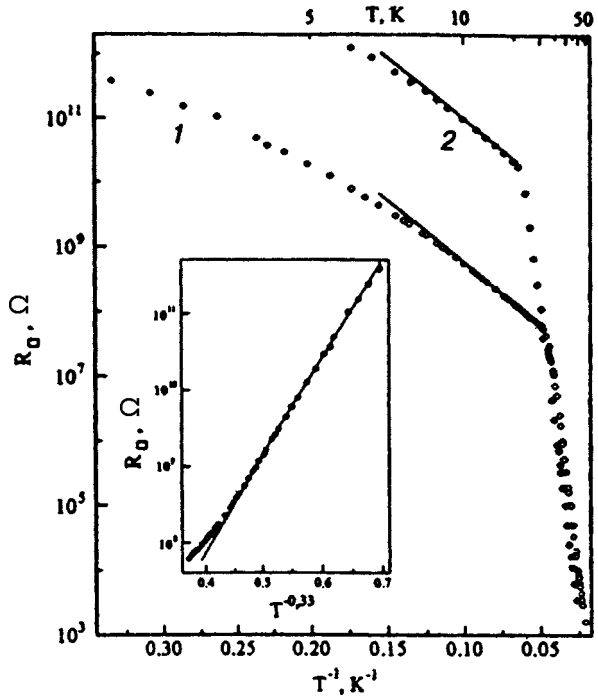

FIG. 4. Temperature dependence of the resistance of samples D (curve *1*) and E (curve *2*). The inset shows the low-temperature segment of the $R_\square(T)$ dependence for sample D.

decrease in temperature is determined by the inequality following from the coherence condition in the percolation theory[5]:

$$\varepsilon_{ij}/kT \ll 2r_{ij}/a, \tag{2}$$

where $\varepsilon_{ij}=(|\varepsilon_i-\varepsilon_F|+|\varepsilon_j-\varepsilon_F|+|\varepsilon_i-\varepsilon_j|)/2$; ε_i and ε_j are the energies of the donor ground states i and j, ε_F is the Fermi energy, and a is the radius of the state. For weak compensation, the mean value of ε_{ij} is essentially the activation energy ε_3, and r_{ij} acquires the meaning of mean separation between donor centers. However, at very low temperatures and in samples with impurity concentrations close to the insulator–metal transition, inequality (2) is violated. Consequently, the activation energy does not remain constant, but decreases upon a decrease in temperature according to a power law. The hopping conductivity with a decreasing activation energy (variable range hopping conductivity) is determined by states with energies in a narrow band in the vicinity of the Fermi level (Mott's law[6]):

$$\rho(T)=\rho_0 \exp(T_0/T)^{1/4}, \tag{3}$$

where $T_0=\beta/[kg(\varepsilon_F)a^3]$; $g(\varepsilon_F)$ is the density of states at the Fermi level, and $\beta=21.2$[5,7] is a numerical factor. For a two-dimensional system, Mott's law assumes the form[8]

$$\rho(T)=\rho_0 \exp(T_0'/T)^{1/3}, \tag{4}$$

where $T_0'=\beta'/[kg'(\varepsilon_F)a^2]$; $g'(\varepsilon_F)$ is the two-dimensional density of states at the Fermi level, and $\beta'=13.8$.[7]

A large number of publications[9–11] have been devoted to the experimental investigation of variable range hopping conductivity in real physical systems, viz., amorphous and crystalline semiconductors. These publications deal mainly with three-dimensional systems, and the results obtained in them are in satisfactory agreement with Mott's law (3).

A transition from activation conductivity to hopping conductivity upon a decrease in temperature in the investigated samples is confirmed by the existence of peaks on the dependences $\Delta R_H(T)$ and $U_H(T)$ (Fig. 2) at $T\approx 23$ K. A rapid decrease in ΔR_H and U_H below the temperature corresponding to the peak is associated with a decrease in the contribution to the overall current from the conduction band electrons having a much higher mobility than the hopping mobility. Measurement of U_H at lower temperatures, where the conductivity is determined only by the hopping mechanism, could provide valuable information about the Hall mobility and charge carrier concentration. Unfortunately, such measurements are hampered by a rapid decrease in ΔR_H and U_H, as well as the noises from the measuring instruments associated with the high sample resistance, and the anomalous form of the dependences $U_H(H)$ which, as was mentioned above, asymptotically tend to zero upon an increase in the magnetic field (Fig. 3b).

It can be seen clearly from Fig. 4 that the temperature dependence of the resistance of samples D and E at high temperatures is described by the first term in Eq. (1): $R=R_0 \exp(\varepsilon_1/kT)$. The energy ε_0 of the ground impurity state of Sb in silicon, which can be identified with the activation energy ε_1 and determined from experimental data with the help of Eq. (1), was found to be equal to 44 meV. Below ~20 K for sample D and ~16 K for sample E, the conductivity is described by the hopping mechanism. Let us study curve *1* in Fig. 4, which is essentially similar to curve *2* but measured over a wider temperature range. It can be seen that the dependence $R(T)$ straightens out in $\log R$ vs. T^{-1} coordinates in the temperature interval 11–20 K, while the experimental points below 11 K lie on a straight line in $\log R$ vs. $T^{-1/3}$ coordinates (see inset to Fig. 4). (Note that the straightening of the curve is much worse in $\log R$ vs. $T^{-1/4}$ coordinates.) Such a behavior of the temperature dependence of resistance upon a decrease in temperature corresponds to a transition from the hopping conductivity mechanism with a constant activation energy to variable range hopping conductivity (4) corresponding to Mott's law for a two-dimensional system. The activation energy ε_3, determined from the experimental data with the help of the second term $R=R_0 \exp(\varepsilon/kT)$ in Eq. (1), has the value 3.9 meV in the temperature interval 11–20 K. The experimentally obtained values of ε_3 and the separation $r_{ij}=N_D^{-1/2}$ lead to an estimate for the temperature at which relation (2) is violated, i.e., a transition to the conductivity type (4) takes place. The radius of the state $a=\hbar/(2m\varepsilon_0)^{1/2}$ for the given system has the value ≈19 Å. The equality of the right- and left-hand sides of the inequality (2) is attained at $T=13$ K, which is in quite good agreement with the experimental value ≈11 K.

3.2. Magnetoresistance

For the hopping conductivity mechanism, three-dimensional systems usually display an exponentially large positive magnetoresistance. The theory of this phenomenon

in strong magnetic fields was constructed by Shklovskii in Ref. 12, while weak magnetic fields were considered in Ref. 13. In his work,[12] Shklovskii used the ideas underlying the percolation theory in which the calculation of hopping resistance is reduced to finding the resistance of a three-dimensional random network whose elements correspond to the nearest impurity pairs. A strong magnetic field compresses the wave functions of impurity electrons in the transverse direction. The overlapping of exponential tails of electron wave functions at the adjoining impurities decreases, and hence the magnetoresistance must increase exponentially under the action of the magnetic field.

Unlike three-dimensional systems, the observed positive magnetoresistance in the $\delta\langle Sb\rangle$ layers in silicon in the hopping conductivity region is not exponentially large, but quite small and vanishing as the temperature is lowered below 18 K (Fig. 3). For example, we did not observe at 10 K any relative variation of sample resistance in a magnetic field 16 kOe to within 10^{-3}. Apparently, the smallness of the magnetoresistive effect is associated with two-dimensionality of the investigated objects, i.e., with two-dimensionality of the network reflecting the hopping conductivity process. In a real system, the impurity electron states are spread in the separation between the states and their energies. The decisive role in the conductivity of the network, especially in the two-dimensional case, is played by the key elements which create the most ''difficult'' hop. In this case, the role of variation of the overlapping of electron wave functions at adjoining impurities in a magnetic field becomes auxiliary in comparison to the contribution from the key elements of the network. The latter define a certain characteristic size L_0 of the critical subnetwork, whose concept plays an important role in describing the nonlinearity of current–voltage characteristics under conditions of hopping conductivity mechanism in moderately strong electric fields (see below).

3.3. Current–voltage characteristics

Figure 5 shows examples of IVC measured at various temperatures on the sample D. Note that all IVC are primary, i.e. correspond to the first electrical measurements on the sample after cooling. Repeated measurements of IVC at the same temperature after the voltage has dropped to zero give an IVC identical to the primary one, but with a higher current. For example, repeated IVC measurement at 14 K leads to a curve identical to the primary IVC measured at 16.6 K (Fig. 5), i.e., the current increases by nearly an order of magnitude as a result of repeated measurements.

For an electric field strength $E_B \approx 90$ V/cm, the IVC at 10 K reveal a sharp increase in current (a jump of several orders of magnitude). With increasing temperature, the voltage E_B at which the jump is initially observed is displaced towards lower values, and a blurring of the jump is observed on the voltage scale. For example, the blurring $\Delta E_B \approx 0.4$ V/cm at 10 K, while $\Delta E_B \approx 50$ V/cm at 20 K (Fig. 5). It should also be observed that the measured values of current become unstable in the voltage interval ΔU_B (the current ''jumps'' in this interval). At temperatures higher than 16 K, the IVC reveal another current jump of smaller amplitude, which is displaced towards lower voltages upon an increase in temperature (Fig. 5).

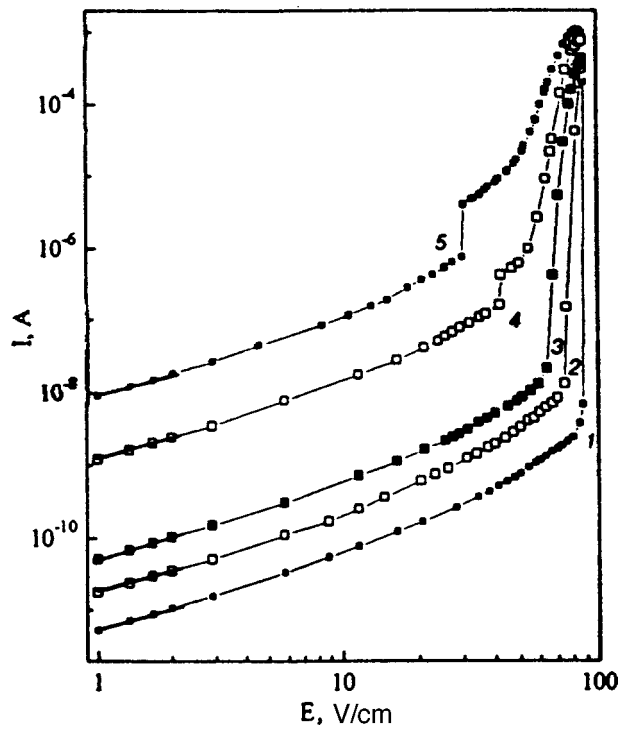

FIG. 5. Current–voltage characteristics for sample E at temperatures T (in K): 10 (curve *1*), 14 (curve *2*), 16.6 (curve *3*), 18.9 (curve *4*), and 20.4 (curve *5*).

Nonlinear current–voltage characteristics were observed by several authors in the temperature interval where the conductivity is of hopping type. The most suitable objects for investigations of nonlinear IVC are highly compensated and amorphous semiconductors. In these cases, the separation from the Fermi level to the edge of the nearest band is much larger than the binding energy of an isolated impurity, which hampers the ionization of impurities and allows investigations in a wide interval of electric fields in which nonohmic hopping conductivity can be observed, i.e., it can be assumed quite confidently that the observed nonlinearity is associated with the hopping mechanism of conductivity. At the same time, higher electric fields in weakly doped and weakly compensated semiconductors usually lead to a more rapid ionization of impurities (impurity breakdown), after which the conductivity is no longer of the hopping type. However, in the samples investigated in this work, the IVC nonlinearity begins to be manifested in such low electric fields that the electric field can be increased by almost two orders of magnitude before the onset of impurity breakdown. The temperature dependence of resistance measured at $E = 30$ V/cm, which is identical to the $R(T)$ dependence measured on the linear conductivity segment at $E = 1$ V/cm (Fig. 4), indicates that the nonlinearity observed in the entire range of applied electric fields (up to breakdown) is determined just by the hopping conductivity mechanism.

The theory of Mott's type hopping conductivity (3) in very strong electric fields $E > kT/ea$ constructed by Shklovskii[14] leads to IVC of the type

$$j(E) \propto \exp(-E_0/E)^{1/4}, \tag{5}$$

where $E_0 \approx kT_0/ea$. For moderately strong electric fields $E < kT/ea$, Hill[15] obtained an expression of the type

$$j(E) \propto \exp\{C(eEr(T)/kT)\} \approx \exp\{C(eEa/kT) \times (T_0/T)^{1/4}\}, \tag{6}$$

where $r(T) = a(T_0/T)^{1/4}$ (according to Shklovskii,[16] $(T_0/T)^{1/4} \equiv \xi_c$, where ξ_c is the percolation threshold), and C is a constant of the order of unity. Hill[15] considered a typical jump $r(T)$ and assumed that the voltage drop corresponding to this jump is $Er(T)$. The variation in the distribution function at the initial and final localized states was not taken into consideration. According to Shklovskii,[16] it weakens the effect of the electric field to a considerable extent. It was mentioned by Austin and Sayer[17] that system inhomogeneity plays an important role in the increase in nonohmicity, while Botger and Bryksin[18] pointed towards the need to take into account the rearrangement of current paths in a strong electric field.

The theory of nonohmic hopping conductivity in moderately strong electric fields starting right after the region where Ohm's law is observed and extending to $E \approx kT/ea$ was developed by Shklovskii.[16] Note that the quantitative analysis of the problem in his work is based on the percolation theory taking into account the change in the distribution function at the initial and final localized states. It was predicted that a departure from linearity occurs in the field

$$E_c = kT/eL_0, \tag{7}$$

which is much lower than in Ref. 15. The main idea behind Shklovskii's theory[16] is the introduction of the concept of the length L_0, which is much larger than the length $r(T)$ of a typical jump, namely, the characteristic dimension of the critical subnetwork $L_0 \approx r(T)\xi_c^{\nu} \approx a\xi_c^{1+\nu}$, where $\nu \approx 0.9$ is the correlation radius index (for two-dimensional case, numerical methods lead to the value $\nu \approx 1.3$).[5] This length plays an important role in the theory of physical phenomena in objects having a hopping conductivity.[19] The $j(E)$ dependence obtained by Shklovskii[16] for $E > E_c$ has the form

$$j(E,T) = \sigma(T)E_c \exp\{\mathrm{const}(eEL_0/kT)^{1/1+\nu}\}. \tag{8}$$

Here, $\sigma(T)$ is defined by one of the expressions (1), (3), or (4), while E_c is defined by the expression (7). Formula (7) for E_c and formula (8) are valid for hopping conductivity with a constant or decreasing activation energy, the only condition being that appropriate expressions must be used for quantities ξ_c and L_0.[19] Formula (8) is valid in the field interval $E_c < E < kT/ea$.

Formula (8) describes correctly the nonlinear part of the experimental IVC (Fig. 5). Figure 6 shows examples of computer fitting of dependence (8) to the nonlinear IVC segments (up to breakdown voltage) measured in sample E at 10 K and in sample D at 4.2 K. Condition (7) and the experimental value of $E_c \approx 2$ V/cm for sample E (Fig. 6). lead to the characteristic length $L_0 \approx 4.3 \times 10^{-4}$ cm. (For sample D, these quantities assume the values $E_c \approx 8$ V/cm and $L_0 \approx 4.5 \times 10^{-5}$ cm.) Further, using the obtained values of L_0, we can calculate the breakdown electric field strength E_B

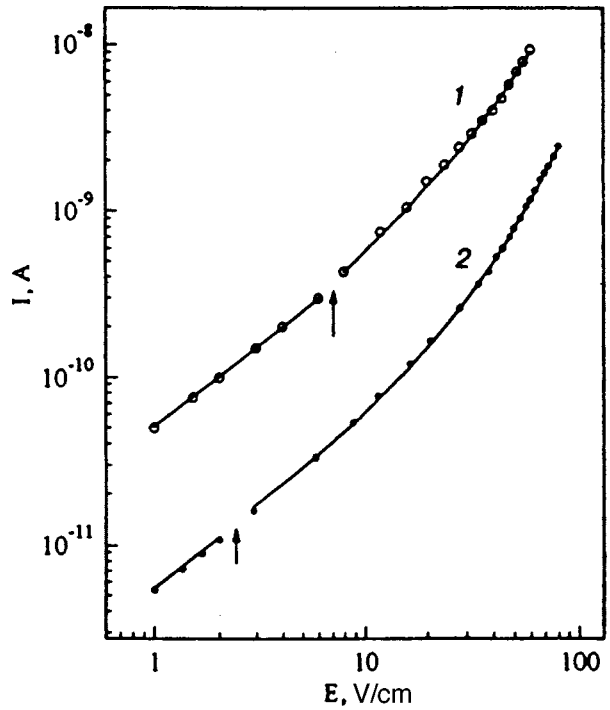

FIG. 6. Current–voltage characteristics (in bilogarithmic coordinates) for sample D at 4.2 K (curve *1*) and sample E at 10 K (curve *2*). The arrows indicate the fields E_c.

with the help of the equality $eE_BL_0 = \varepsilon_0$. The value $E_B \approx 100$ V/cm obtained in this way is close to the experimental value, and is only about 10% higher (Fig. 5). (The solution of the inverse problem, i.e., the evaluation of the quantity L_0 corresponding to the experimental value of E_B gives $L_0^B \approx 4.9 \times 10^{-4}$ cm.) On the other hand, the value of L_0 can be estimated from the temperature dependence of resistance, since, by definition, the approximate equality $L_0 \approx a\xi_c^2$ holds. Here, the percolation threshold ξ_c is equal to the exponent in (4), i.e., $\xi_c = (T_0'/T)^{1/3}$. For sample D at 10 K, the value of $\xi_c \approx 15$, which gives $L_0^T \approx 5.5 \times 10^{-5}$ cm (we have used the value $T_0' \approx 25 \times 10^3$ K determined from the experimental data shown in the inset to Fig. 4). Unfortunately, the experimental data for sample E in the low-temperature region are inadequate for determining ξ_c correctly. However, in view of the fact that $N^E < N^D$, we can use the typical value $\xi_c \approx 20-30$ for sample E (see Ref. 16). This gives $L_0^T \approx (1-2) \times 10^{-4}$ cm, which is in very good agreement with the values of L_0 and L_0^B determined above.

CONCLUSION

The low-temperature conductivity of δ-⟨Sb⟩ layers in silicon with a sheet concentration 1×10^{13} and 5×10^{12} cm^{-2} of antimony atoms is associated with the hopping conductivity mechanism with an activation energy ~ 3.9 meV, and at very low temperatures (<10 K), with variable-range hopping conductivity. In the latter case, two-dimensional electron systems are manifested quite clearly (Mott's law is obeyed for the two-dimensional case). The theory of nonohmic hopping conductivity in moderately strong electric fields[16] describes successfully the observed

nonlinearity in the IVC of the investigated objects and provides a good quantitative agreement of the characteristic fields E_c corresponding to the onset of nonlinearity, E_B corresponding to impurity breakdown, and the characteristic size L_0 of the critical percolation subnetwork of donor states over which hopping takes place.

This research was supported by the grant INTAS-93-1403-ext.

*E-mail: komnik@ilt.kharkov.ua

[1)]The samples were prepared by the Advanced Semiconductor Group, University of Warwick, Coventry, UK.

[1] V. Yu. Kashirin, Yu. F. Komnik, Vit. B. Krasovitskii *et al.*, Fiz. Nizk. Temp. **22**, 1166 (1996) [Low Temp. Phys. **22**, 891 (1996)].
[2] V. Yu. Kashirin, Yu. F. Komnik, O. A. Mironov *et al.*, Fiz. Nizk. Temp. **22**, 1174 (1996) [Low Temp. Phys. **22**, 906 (1996)].
[3] V. Yu. Kashirin, Yu. F. Komnik, A. S. Anopchenko *et al.*, Fiz. Nizk. Temp. **23**, 413 (1997) [Low Temp. Phys. **23**, 303 (1997)].
[4] N. L. Mattey, T. E. Whall, R. A. Kubiak *et al.*, Semicond. Sci. Technol. **7**, 604 (1992).
[5] B. I. Shklovskii and A. L. Efros, *Electronic Properties of Doped Semiconductors* [in Russian], Nauka, Moscow (1979).
[6] N. E. Mott, J. Non-Cryst. Solids **1**, 1 (1968).
[7] A. S. Skal and B. I. Shklovskii, Fiz. Tverd. Tela (Leningrad) **16**, 1820 (1974) [Sov. Phys. Solid State **16**, 1190 (1974)].
[8] W. Brenig, G. H. Dohler, and H. Heyszenau, Philos. Mag. **27**, 1093 (1973).
[9] R. M. Hill, Phys. Status Solidi A **34**, 601 (1976).
[10] R. M. Hill, Phys. Status Solidi A **35**, K29 (1976).
[11] A. G. Zabrodskii, Fiz. Tekh. Poluprovod. **11**, 595 (1977) [Sov. Phys. Semicond. **11**, 345 (1977)].
[12] B. I. Shklovskii, Zh. Éksp. Teor. Fiz. **61**, 2033 (1971) [Sov. Phys. JETP **34**, 1084 (1971)].
[13] B. I. Shklovskii, Fiz. Tekh. Poluprovod. **8**, 416 (1974) [Sov. Phys. Semicond. **8**, 268 (1974)].
[14] B. I. Shklovskii, Fiz. Tekh. Poluprovod. **6**, 2335 (1972) [Sov. Phys. Semicond. **6**, 1964 (1972)].
[15] R. M. Hill, Philos. Mag. **24**, 1307 (1971).
[16] B. I. Shklovskii, Fiz. Tekh. Poluprovod. **10**, 1440 (1976) [Sov. Phys. Semicond. **10**, 855 (1976)].
[17] I. G. Austin and M. Sayer, J. Phys. C **7**, 905 (1974).
[18] H. Botger and V. V. Bryksin, Phys. Status Solidi B **67**, 583 (1975); **68**, 285 (1975).
[19] B. I. Shklovskii and A. L. Efros, Usp. Fiz. Nauk **117**, 401 (1975) [Sov. Phys. Usp. **117**, 845 (1975)].

Translated by R. S. Wadhwa

Amplitude–frequency dependence of doppleron–phonon resonance

L. T. Tsymbal and A. N. Cherkasov

*A. Galkin Physicotechnical Institute, National Academy of Sciences of the Ukraine, 340114 Donetsk, Ukraine**

(Submitted September 5, 1997)
Fiz. Nizk. Temp. **24**, 250–261 (March 1998)

The amplitude-frequency dependence of the doppleron–phonon resonance (DPR) in tungsten is investigated experimentally and theoretically. The analysis is based on the general theoretical consideration of propagation and interaction of ultrasonic and electromagnetic modes in metals. It has been established that the weak doppleron–phonon interaction takes place in tungsten in the frequency range used (10–500 MHz). The complicated experimental amplitude–frequency dependence of DPR can be explained under the assumption of predominance of the induction mechanism of interaction between the electronic and ionic subsystems of the metal. It is found that under such an assumption, this dependence is of a general character and is not determined by the shape of the Fermi surface of the metal. © *1998 American Institute of Physics.* [S1063-777X(98)00703-8]

INTRODUCTION

Ultrasonic spectroscopy has become an informative method of studying collective excitations of the electron plasma in metals, especially specific excitations like dopplerons. A doppleron is a weakly attenuating electromagnetic mode existing due to Fermi degeneracy of the electron plasma.[1] The observation of doppleron–phonon resonance (DPR)[2] and subsequent magnetoacoustic investigations have considerably enriched our knowledge about the properties and peculiarities of doppleron spectra.[3–5] However, the problems associated with specific features of interaction of acoustic and electromagnetic modes in metals, which were formulated as a result of these and subsequent experimental investigations, have been studied insufficiently. Among other things, an important question arises in an analysis of essentially nonmonotonic experimental amplitude–frequency dependence of the DPR peak in tungsten. Is the observed dependence associated with the peculiarities of the electron energy spectrum, i.e., the shape of the Fermi surface (FS), or is it a specific feature of the doppleron–phonon interaction in general? The answer to this question forms the subject matter of this research.

We studied experimentally the frequency dependence of the amplitude of the absorption peak of a transverse acoustic wave caused by its interaction with the so-called G-doppleron in tungsten.[3,4] Tungsten is a compensated metal. For this reason, the G-peak of sound absorption is observed in tungsten in an external magnetic field in a wide frequency range. This basic feature of long-wave dopplerons in compensated metals considerably facilitates the solution of the problem formulated above.

In the general case, the DPR theory differs from the thoroughly developed theory of the helicon–phonon resonance (see, for example, the review in Ref. 6) only in view of the difference in the behavior of the doppleron and helicon spectra. However, this difference makes the theory of DPR much more complicated.

The DPR theory is considered in Ref. 4 and 7 for the aspect we are interested in. Medvedev *et al.*[7] constructed the DPR theory for the case of a strong interaction between dopplerons and phonons, the FS of a compensated metal and the deformation potential tensor being approximated by using simplified models. It should be emphasized that the correctness of application of the strong interaction limit, which is obviously observed for the helicon–phonon resonance in pure metals, requires a special verification in the case of DPR. It will be shown below that the models should also be chosen carefully since they determine the form of the frequency dependence of the DPR peak amplitude to a considerable extent.

Weak doppleron–phonon interaction was considered in Ref. 4. However, the analysis carried out by the authors of this publication was confined only to the absorption of sound in the local limit, and hence the deformation electron–phonon interaction was neglected. Consequently, the results obtained in Ref. 4 are valid only for the helicon–phonon resonance in ''dirty'' metals.

In this paper, we present a detailed theoretical analysis of the amplitude–frequency dependence of the G-peak of DPR obtained for tungsten. On one hand, this analysis takes into account the shape of the FS as well as peculiarities of spectra and attenuation of electron modes, and on the other hand, it is based on an estimate of the intensity of interaction between the electromagnetic and acoustic modes.

EXPERIMENTAL RESULTS

1. We used a pulse spectrometer which was a modified version of the spectrometer proposed by Galkin and Korolyuk.[8] Ultrasonic pulses were generated by piezotransducers made of lithium niobate and arranged parallel to one another. The absorption of transverse sound was measured in

 © 1998 American Institute of Physics

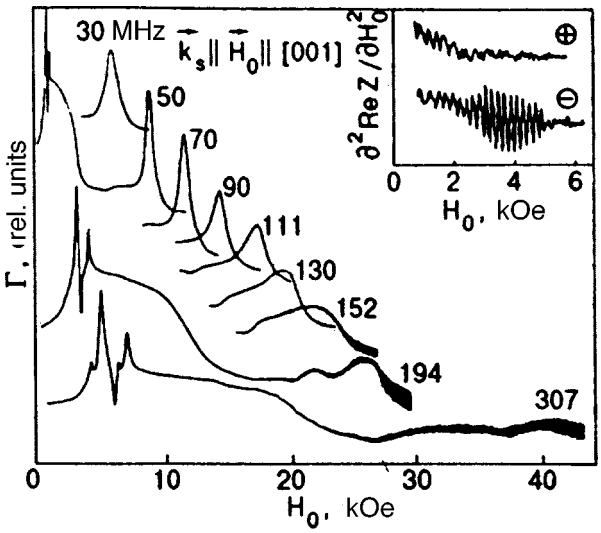

FIG. 1. Fragments of experimental dependences of the absorption coefficient for transverse ultrasound in tungsten for various frequencies of an ultrasonic wave ($\mathbf{k}_s \| \mathbf{H}_0 \| [001]$). The inset illustrates experimental recording of surface impedance in W.[4] The polarity of circular polarization of the exciting field is indicated in circles. Long-period oscillations in the "-" polarization are associated with the excitation of a G-doppleron.

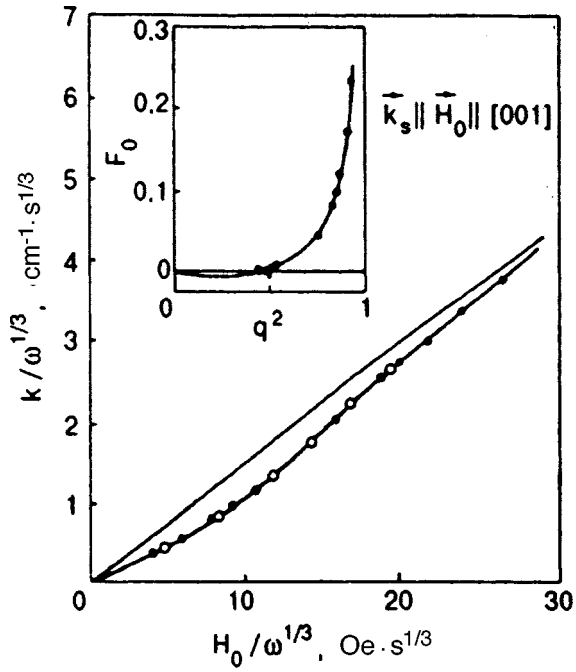

FIG. 2. Spectrum of a G-doppleron in W: our results (●), rf measurements data[4] (○). The curve describes the graphic solution of Eq. (9) with conductivity (21) (see the inset and Fig. 4). The inset shows nonlocal conductivity in W: experimental points (●) and the curve corresponding to function (21) ($F_0 = F_{\pm|\gamma=0}$).

the geometry $\mathbf{k}_s \| \mathbf{H}_0 \| [001]$ ($\mathbf{k}_s$ is the wave vector of sound) at a temperature 4.2 K and at frequencies $\omega/2\pi = 10-500$ MHz in an external magnetic field H_0 attaining values of 65 kOe. The error in the adjustment of $\mathbf{H}_0 \| [001]$ was $\sim 0.3°$.

The samples were cut from a tungsten single crystal with a resistivity ratio $\rho_{300\,\mathrm{K}}/\rho_{4.2\,\mathrm{K}} \simeq 1.5 \times 10^5$. The sample size along the [001] axis varied from 1 to 4 mm.

2. Figure 1 shows fragments of experimental dependences of absorption Γ of linearly polarized transverse sound on the magnetic field H_0. It should be noted that the value of Γ is generally not identical to the damping coefficient for sound since we disregarded the effects of ellipticity and rotation of the polarization plane of ultrasonic waves that occur on propagation of ultrasound in metals.[9] Nevertheless, it was found that if the sample thickness and the frequency of ultrasound are not large, and the intensity of the doppleron–phonon interaction is low, the attenuation of sound at resonance is determined to a high degree of accuracy by the amplitude of the DPR peak. These conditions were satisfied in our experiments. The correctness of such a statement can be easily verified in experiments by comparing the $\Gamma(H_0)$ dependences obtained for different number of passages of an ultrasonic wave through the sample.

3. The doppleron spectrum of the G-mode in tungsten we are interested in,[3,4] which was obtained from the resonance condition $k = k_s$ ($k_s = \omega/v_s$, $v_s = 2.88 \times 10^5$ cm/s being the velocity of ultrasound at helium temperature), is shown in Fig. 2. The coordinates $(k/\omega^{1/3}, H_0/\omega^{1/3})$ used by us and proposed for the first time in Ref. 10 are universal for weakly attenuating low-frequency modes since the corresponding spectral curves are defined uniquely for any values of the extrinsic parameters ω and H_0. In this respect, they differ advantageously from, say, the energy–momentum relations $\omega(k)$ ($H_0 = \mathrm{const}$) or $k(H_0)$ ($\omega = \mathrm{const}$). Figure 2 shows that the results of rf (see the inset to Fig. 1) and magnetoacoustic measurements are in good agreement although the latter make it possible to reconstruct the G-doppleron spectrum in a considerably wider range of $H_0/\omega^{1/3}$.

The amplitude–frequency dependence of the DPR peak is shown in Fig. 3. The characteristic feature of this dependence is that the peak amplitude first increases with frequency, and then decreases smoothly and monotonically. At high frequencies (>400 MHz), the peak becomes virtually

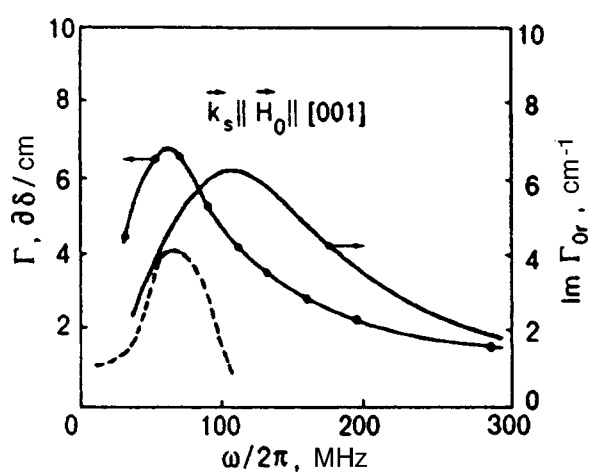

FIG. 3. Frequency dependence of the amplitude Γ of the G absorption peak for transverse sound in W (see Fig. 1). The dependence of Im Γ_{0r} is obtained by using formula (25) for a metal with conductivity (21). The dashed curve shows the amplitude–frequency dependence of doppleron oscillations in W, reduced to the ω-axis according to the algorithm $H_0 \to k \to \omega = kv_s$ (see Figs. 1 and 2).

indistinguishable against the background of quantum oscillations.

THEORY: MODEL AND METHODS

1. Equations of the theory of elasticity and Maxwell's equations supplemented with the constitutive relations form a complete system of equations describing elastic and electromagnetic oscillations in metals (see, for example, Refs. 11 and 12 and the reviews in Refs. 6 and 13). We shall confine our analysis to the interaction of plane monochromatic waves ($\mathbf{u}$, $\mathbf{E}\propto\exp(i\mathbf{kr}-i\omega t)$, $\mathbf{u}$ being the displacement vector of the lattice and $\mathbf{E}$ the electric field) in the geometry $\mathbf{k}\|\mathbf{H}_0\|\hat{\mathbf{z}}$ in a metal whose all the regions of the FS surface are axisymmetric about the axis $\hat{\mathbf{z}}$. In this case, the dispersion equation for interacting electromagnetic and acoustic waves with transverse circularly polarized components of oscillations ($\psi_\pm=\psi_x\pm i\psi_y$, $\psi=u,E$) can be written in the form

$$k^2-k_s^2=\frac{i\omega}{\rho v_s^2}\left(\frac{H_0}{c}\right)^2 \times\left\{\frac{[M\pm(k/m\omega_c)\langle\Lambda_\pm v_\pm^*\rangle][M\pm(k/m\omega_c)\langle\Lambda_\pm^* v_\pm\rangle]}{M-\sigma_\pm} -M+(k/m\omega_c)^2\langle\Lambda_\pm\Lambda_\pm^*\rangle\right\}\quad(\pm-\text{polarization}),\quad(1)$$

where ρ is the density of metal, $M=k^2c^2/4\pi i\omega$, $\omega_c=eH_0/mc$ is the cyclotron frequency, $\hat{\mathbf{\Lambda}}$ the deformation potential tensor ($\Lambda_\pm=\Lambda_{xz}\pm i\Lambda_{yz}$), $\mathbf{v}$ the electron velocity ($v_\pm=v_x\pm iv_y$); $\sigma_\pm=\langle v_\pm v_\pm^*\rangle$ the conductivity of metal, (*) indicates complex conjugation, and the angle brackets $\langle\psi_\pm\rangle$ (ψ is an arbitrary function) indicate integration over the FS in the momentum ($\mathbf{p}$) space:

$$\langle\psi_\pm\rangle=i\,\frac{2\pi e^2}{(2\pi\hbar)^3}\int_{(\mathrm{FS})}\frac{\psi_\pm|m|dp_z}{\omega+i\nu\pm\omega_c-kv_z}.\quad(2)$$

In Eq. (1), we have neglected the Tolman and Stewart effect, which is justified in the field and frequency range under investigation defined by the inequalities

$$\omega\lesssim\nu\ll\omega_c.\quad(3)$$

Here ν is the electron relaxation frequency.

The first term on the right-hand side of (1) is associated with the so-called field component of the force exerted by electrons on the lattice. This is the term determining the type of resonant interaction between electromagnetic and ultrasonic modes since zeros of its denominator are the roots of the equation

$$k^2c^2=4\pi i\omega\sigma_\pm\quad(\pm-\text{polarization}),\quad(4)$$

which is apparently the energy–momentum relation for electromagnetic waves in the absence of their interaction with sound. The other two terms are associated with the inductive and deformation components of this force.

2. Let us consider briefly the main features of the spectrum of weakly attenuating electromagnetic modes in noncompensated and compensated metals in the collisionless limit. We shall use in our analysis the model of an asymmetric FS of the ''corrugated cylinder'' type[14]:

$$S(p_z)=S_0+S_1\cos(\pi p_z/p_0),\quad |p_z|\leqslant p_0,\quad(5)$$

where $S(p_z)$ is the area of the FS cross section by the plane $p_z=\text{const}$, and S_0, $S_1\leqslant S_0$, and p_0 are the model parameters. This model is quite simple, but it reflects the main physical peculiarities of actual FS. The conductivity can be calculated by using the relations $v_\pm v_\pm^*=S(p_z)/\pi m^2$, $v_z=-(\partial S/\partial p_z)/2\pi m$ and assuming that $|m|$ and $\nu=\text{const}$ for all charge carriers.

For a noncompensated metal with an electron FS ($\omega_c>0$) (5), we obtain from (2)

$$\sigma_\pm=\pm i(Nec/H_0)[(1\pm i\gamma)^2-(kv_e/\omega_c)^2]^{-1/2}.\quad(6)$$

Here $\gamma=(\nu-i\omega)/\omega_c$; $v_e=|(\partial S/\partial p_z)/2\pi m|_{\max}$ is the maximum drift velocity of electrons along $\mathbf{H}_0\|\hat{\mathbf{z}}$, and N is the electron concentration defined as

$$N=\frac{2}{(2\pi\hbar)^3}\int_{(\mathrm{FS})}S(p_z)dp_z.\quad(7)$$

An analysis of the dispersion equation (4) and of the nature of its roots becomes more visual if we introduce the dimensionless parameters

$$q=kv_e/\omega_c,\quad \xi^3=\omega_c^3c^2/\omega_p^2wv_e^2,\quad(8)$$

write (4) and (6) in the form

$$\mp q^2\xi^3=F_\pm(q)\quad(\pm-\text{polarization})\quad(9)$$

and solve (9) graphically in the limit $\gamma\to0$.[14] In formulas (8) and (9), $\omega_p=(4\pi Ne^2/m)^{1/2}$ is the plasma frequency and

$$F_\pm(q)=[(1\pm i\gamma)^2-q^2]^{-1/2}\quad(10)$$

is a nonlocal factor in the conductivity (6) ($\sigma_\pm=\pm i(Nec/H_0)F_\pm$).

Curve *1* in Fig. 4 illustrates the graphic solution of Eqs. (9) and (10) in the limit $\gamma\to0$ in the ''-'' polarization. It can be seen that the dispersion equation has either two real-values solutions, viz. the helicon ($\mathscr{G}$) and doppleron (D_1) solutions (straight line *c*), or no solutions at all (straight line *a*) depending on the value of $\xi\propto H_0/\omega^{1/3}$. The threshold value[14] of $\xi_m=(27/4)^{1/6}$ (straight line *b*) separates these regions of solutions. The spectra of electromagnetic modes corresponding to the obtained real-valued solutions are shown in Fig. 5 (curve *1*).

Analyzing the spectrum of electromagnetic modes in a compensated metal with equal concentrations of electrons and holes ($N_e=N_h=N$), we can use a simple two- band model. We approximate the electron and hole FS by two ''corrugated cylinders'' (5) of the same volume, assuming that $S_1=0(v_z=0)$ for the hole surface. It can be seen from (2) that such an assumption is equivalent to the inclusion of the hole contribution to the conductivity in the local ($k\to0$) limit. In this case, we have

$$F_\pm(q)=F_\pm^e+F_\pm^n=[(1\pm i\gamma)^2-q^2]^{-1/2}-(1\mp i\gamma)^{-1}.\quad(11)$$

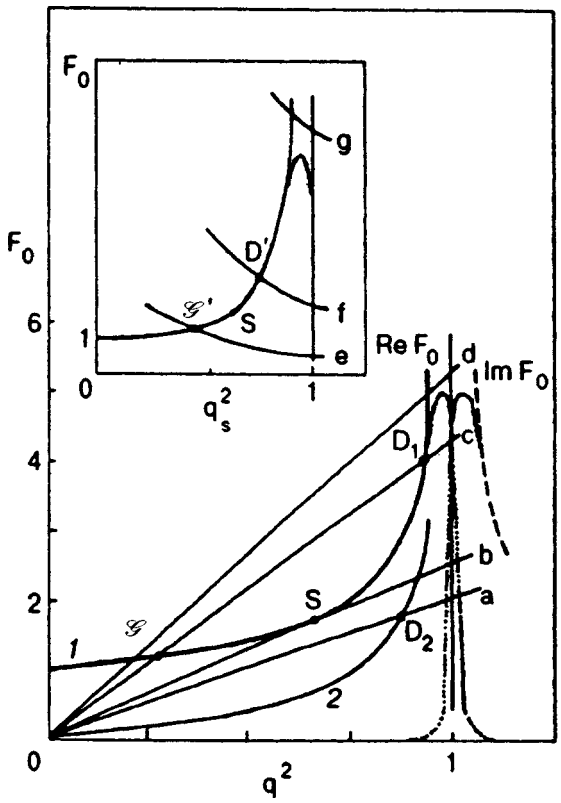

FIG. 4. Graphic solutions of the dispersion equation (9) with conductivity (10) (curve *1* for a noncompensated metal) and (11) (curve *2* for a compensated metal) for $\gamma\to 0; F_0=F_{\pm|\gamma=0}$. The straight lines a, b, c, and d is the left-hand side of (9) in the ''-'' polarization for successively increasing values of $\xi\propto H_0/\omega^{1/3}$: $\mathscr{G}$ stands for the helicon solution and D_1 and D_2 for doppleron solutions. The inset illustrated the graphic solution of Eq. (19) with conductivity (10) ($q=q_s$). The curves e, f, and g correspond to the left-hand side of (19) in the ''-'' polarization for successively increasing values of $\Omega\propto\omega$. The dotted curves correspond to the function F_- (10) for $\gamma\neq 0$. The curves are of qualitative nature.

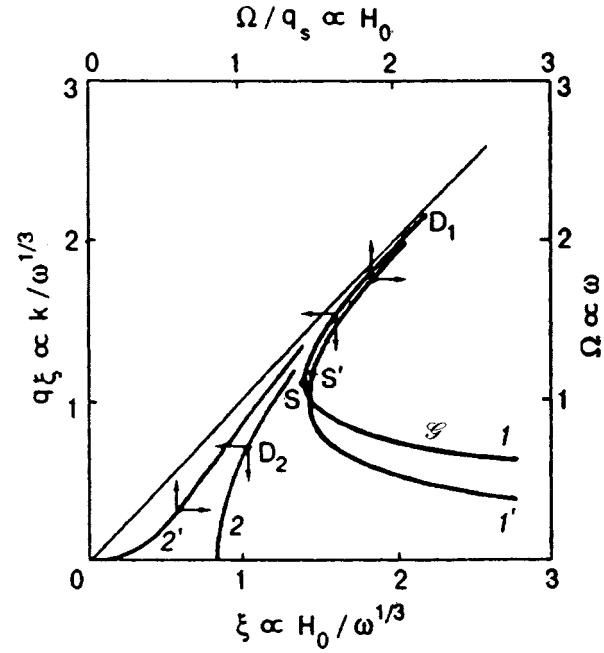

FIG. 5. Spectrum of electromagnetic modes in a noncompensated (curve *1*) and compensated (curve *2*) metal. The dependence of the resonant field H_0 on the ultrasonic frequency at helicon– and doppleron–phonon resonances in a noncompensated metal (curve $1'$); at DPR in a compensated metal (curve $2'$) (see Fig. 4). Arrows on the curves indicate the relevant coordinate axes.

Here we take into consideration the sign of cyclotron masses, putting $\omega_{ce}=\omega_{ch}=\omega_c>0$. Here and below, the subscripts ''e'' and ''h'' mark the electron and hole parameters respectively.

The graphic solution of Eqs. (9) and (11) in the limit $\gamma\to 0$ in the ''-'' polarization is illustrated by curve *2* in Fig. 4. It can be seen that as a result of compensation, the range of the doppleron solution (point D_2) has changed ($\xi_m=0.5^{1/3}, q^2<1$), while the helicon solution degenerates into zero. The spectrum of the D_2-doppleron is shown by curve 2 in Fig. 5.

The obtained spectra of electromagnetic modes have two characteristic features. First, it is a threshold for their existence on the ξ-scale from below. It should be noted that this feature is generally not essential for dopplerons and is a result of the choice of the FS model. This is illustrated, for example, by the thresholdless doppleron spectrum in Fig. 2. The other characteristic feature of doppleron spectra is their asymptotic behavior: $q^2\to 1$ for $\xi\to\infty$. This peculiarity makes it possible to determine experimentally the differential characteristics of resonant FS cross sections. Usually, the condition $q^2=1$, which is the equation of the straight line in Fig. 5, is used to find

$$R_{\text{extr}}=\frac{1}{2\pi\hbar}\left|\frac{\partial S}{\partial p_H}\right|_{\text{extr}}=\frac{e}{c\hbar}\,\frac{H_0/\omega^{1/3}}{k/\omega^{1/3}}. \tag{12}$$

3. Let us now analyze the role of collisions in the attenuation of electromagnetic modes in metals. According to Fig. 4, the doppleron solutions of the dispersion equation exist since the conductivity has a singularity at the point $q^2=1$ due to nonlocal effects associated with the Doppler-shifted cyclotron resonance (DSCR). For $q^2>1$, the function $F_\pm(q)$ is complex-valued even in the absence of collisions ($\gamma\to 0$) due to collisionless attenuation of electromagnetic waves as a result of DSCR. The inclusion of collisions leads to blurring of the absorption edge. The function $F_\pm(q)$ becomes complex-valued for $q^2<1$, and dopplerons and helicons attenuate as a result. We assume that the following inequalities hold: $\gamma\ll 1, |q''/q'|\ll 1$ ($q=q'+iq''$). Using expression (2) for the conductivity $\langle v_\pm v_\pm^*\rangle$, we obtain after simple transformation of (9) the approximate equations describing the spectrum and attenuation of electromagnetic modes:

$$\mp q'^2\xi^3\cong F_0'(q'), \tag{13}$$

$$2q'q''\cong\frac{F_\pm''(q')}{\mp\xi^3-\partial F_0/\partial(q'^2)}, \tag{14}$$

$$F_\pm''(q')=F_0''(q')\mp\frac{\nu}{\omega_c}\left[F_0'(q')+2q'^2\,\frac{\partial F_0}{\partial(q'^2)}\right]. \tag{15}$$

Here and below, $F_0=F_{\pm|\gamma=0}$ ($F_0=F_0'+iF_0''$). Relations (13)–(15) have been derived in the general case and are valid as long as the initial inequalities hold.

For large values of $\xi > \xi_m$, $\partial F_0/\partial(q'^2) \gg \xi^3, q' \approx 1$ for the doppleron mode (see Fig. 4), and we obtain from (14) the doppleron damping coefficient $k''_D \simeq l^{-1}$, where $l = \nu/v_e$ is the mean free path for resonant electrons.[1] The minus sign appears due to the fact that the group and phase velocities of dopplerons have opposite directions in the given models.[14] Near the doppleron threshold, $\xi^3 \approx \partial F_0/\partial(q'^2)$, and attenuation becomes much stronger.[1,4,10] It should be noted that although this attenuation appears due to the inclusion of electron collisions, it is collisionless according to its physical meaning. As a matter of fact, for $q^2 < 1$ there are no charge carriers for which the DSCR condition $kv_z = \omega_c$ holds. Nevertheless, the energy absorbed by electrons drifting in the field of the wave has a finite (nonzero) value just in view of the finiteness of the mean free path. It is this energy that is lost by electrons as a result of collisions.

Let us now consider the role of collisions from a somewhat different point of view. For $\nu \neq 0$, the function $F_\pm$ is complex: $F_\pm = F'_\pm + iF''_\pm$. Transforming Eq. (10), we obtain

$$F'_\pm(x) = F''_\pm(-x) = \left[\frac{(x^2+4y^2)^{1/2}+x}{2(x^2+4y^2)}\right]^{1/2}, \tag{16}$$

where $x = (1 \pm \omega/\omega_c)^2 - (\nu/\omega_c)^2 - q^2 \cong 1 - q^2$; $y = \mp(\nu/\omega_c) \times (1 \pm \omega/\omega_c) \cong \mp \nu/\omega_c$.

The inclusion of collisions leads to the finiteness of the functions $F'_\pm$ and $F''_\pm$ in the vicinity of the point $q^2 = 1$, which have peaks at the points $x = x_{m1} = (2/\sqrt{3})y$ and $x = x_{m2} = -(2/\sqrt{3})y$ respectively. At these points, we have

$$F'_{\pm\max} = |F''_{\pm\max}| = \frac{3^{3/4}}{4|y|^{1/2}} \cong 0.57\left(\frac{\omega_c}{\nu}\right)^{1/2}. \tag{17}$$

The dotted curves in Fig. 4 describe qualitatively the form of functions (16).

In pure metals in relatively strong fields (3), the value of $|x_{m1}| = |x_{m2}|$ is small. Consequently, for $x^2 \gg 4y^2$ we have

$$F'_\pm \cong F_0(q), \quad F''_\pm \cong \mp \frac{\nu}{\omega_c} F_0^3(q), \tag{18}$$

in a fairly wide range of $q^2 < 1$. For example, in a noncompensated metal with conductivity (10), exactly these functions appear in Eqs. (13) and (14) ($q = q'$). However, the difference in functions defined by relations (16) and (18) becomes significant in the immediate vicinity of the point $q^2 = 1$. It may appear at first glance that Eq. (13) has no purely real-valued doppleron solution for large values of ξ. Figure 4 shows the graphic solution of Eq. (9) with F'_- (16) on the right-hand side in the case when the straight line d intersects the curve F'_- at a single point $\mathscr{G}$. Such a situation is possible for large values of ξ since the left-hand side of (9) is proportional to ξ^3, while $F'_{-\max} \propto \xi^{1/6}$ ($\omega = \text{const}$). It is important, however, that such a solution is incorrect. Indeed, if collisions are taken into account in the solution of Eq. (9), we must also take into consideration the attenuation of a doppleron due to collisions. This was done in the course of direct derivation of Eqs. (13) and (14). In this case, we have $x \approx 1 - q'^2$ and $y \approx (\nu/\omega_c) + q'q''$ in (16) with the "-" polarization. Taking into account such a correction, the value of y decreases with increasing ξ in accordance with (14) ($y \to 0$ for $\xi \to \infty$), while the value of $F'_{-\pm\max}$ increases. As a result, the function F'_- (16) virtually coincides with the function F_0 ($q \approx q'$) in the vicinity of the doppleron solution D_1 as before for any large value of ξ. Equations (13) and (14) remain valid, and the range of a nearly real-valued solution D_1 is not bounded in ξ from above. The only exception is the neighborhood of the point $\xi \approx \xi_m$ in which the doppleron spectrum is distorted in view of enhancement of attenuation.

4. Using the results obtained above, we can analyze the correlation of field dependences of the amplitude of doppleron oscillations and the damping coefficient for the doppleron mode. In accordance with (14), the damping coefficient for dopplerons decreases with increasing ξ, attaining a finite value ($k''_D \to l^{-1}$). At first glance, this result contradicts the experimentally observed dependences of the amplitude of doppleron oscillations of surface impedance on H_0. A typical example of such oscillations is shown in the inset to Fig. 1. It can be seen that the amplitude of oscillations decreases abruptly with increasing H_0. In this case, however, the form of the amplitude–field dependence of doppleron oscillations in strong fields is determined not by the increase in the damping coefficient for dopplerons, but by specific features of the experimental method used. As a matter of fact, as soon as we go over to the solution of a specific problem of excitation of electromagnetic waves in a metal plate, the well-known boundary problem arises.[17] It is extremely difficult to obtain the solution of the boundary-value problem in the general case since it depends not only on the extrinsic parameters, but also on the type of conductivity and the nature of reflection of electrons by the surface. Nevertheless, this solution can be found in the case of simple models of the FS and the sample surface. For example, in a relatively pure metal ($l \gg d$, where d is the sample thickness) with conductivity (10) (doppleron D_1; see Fig. 4), the amplitude of doppleron oscillations for specular reflection of electrons at the surface in strong fields ($\xi \gg 1$, $\omega = \text{const}$) is proportional to $\omega^3/\nu\omega_c^7$,[14] and hence must decrease. It should be noted that the decrease in the amplitude of doppleron oscillations with increasing H_0 can be explained by a typical feature of the solution of the boundary-value problem, which is associated with the asymptotic behavior of doppleron spectra ($q^2 \to 1$ for $\xi \to \infty$) and hence does not depend on the choice of the model of the FS of the metal.

5. Let us now consider briefly some aspects of interaction of ultrasonic and electromagnetic modes, which are associated with peculiarities of the spectra of the latter modes. Resonant interaction is obviously possible at degeneracy points for the modes, i.e., for $k = k_s$ (k is the wave vector of the electromagnetic mode). Substituting $k = k_s$ into (9) and putting $\gamma = 0$, we obtain the following equation describing the position of resonant points on the ω, H_0 plane:

$$\mp \Omega^2/q_s = F_0(q_s), \quad (\pm - \text{polarization}). \tag{19}$$

Here $\Omega = \omega/\omega_0$; $\omega_0^2 = \omega_p^2 v_s^3/c^2 v_e$; $q_s = q|_{k=k_s}$.

The inset to Fig 4 shows the graphic solution of Eq. (19) with conductivity (10) in the "-" polarization for various values of Ω. The point $\mathscr{G}'$ corresponds to the helicon–phonon resonance ($\Omega^4 < \Omega_m^4 = 2$), while the point D' corre-

sponds to the DPR ($\Omega > \Omega_m$). Figure 5 shows the solutions of Eq. (19) ($\Omega \propto \omega; \Omega/q_s \propto H_0$) for a noncompensated metal with conductivity (10) (curve *1′*) and a compensated metal with conductivity (11) (curve *2′*).

Let us obtain numerical estimates by using typical values of parameters of a metal:

$$N = 10^{22}\ \text{cm}^{-3}, \quad v_s = 3\times 10^5\ \text{cm/s}, \quad R^e_{\text{extr}} = 1\ \text{Å}^{-1}. \tag{20}$$

Here $R^e_{\text{extr}} = (m/\hbar)v_e$ is the maximum value of R for electrons (see (12)). For parameters (20), $\Omega = 1$ for $\omega/2\pi = 460$ MHz and $\Omega/q_s = 1$ for $H_0 = 63$ kOe. It can be seen from Fig. 5 that DPR and helicon–phonon resonance can be observed in a noncompensated metal only in relatively strong fields $H_0 \geqslant 90$ kOe. It is probably for this reason that the resonant field was attained in magnetoacoustic experiments on helicon–phonon resonance only for indium.[15] Conversely, a considerable segment of curve 2′ for a compensated metal lies in the range of frequencies and fields easily attainable in experiments. It should also be noted that in contrast to a noncompensated metal, the range of the real-valued solution of Eq. (19) for a compensated metal is not bounded on the H_0 scale from below at all. For this reason, compensated metals are preferred objects of investigation of ultrasonic and electromagnetic modes in metals.

6. Let us now analyze the experimental results obtained by us. Earlier,[3,4] we analyzed qualitatively the form of doppleron spectra in tungsten by using a simplified two-band model of the FS. In the present case, however, an exact model of the FS is required for an adequate description of not only the G-doppleron spectrum, but also the amplitude–field dependence of the DPR. For small q^2, the main nonlocal contribution to conductivity comes from charge carriers localized near the cross sections of the electron ''jack'' with $R^e_{\text{extr}} \sim 1\ \text{Å}^{-1}$ and the A cross section of the hole octahedron with $R^h_{\text{extr}} = 0.495\ \text{Å}^{-1}$.[4] For this reason, we assume that the FS is formed by the two (electron and hole) ''corrugated cylinders'' (5) with charge carrier concentrations $\alpha_e N$ and $\alpha_h N$ ($\alpha_e, \alpha_h < 1$) respectively. The contribution from the remaining charge carriers will be taken into account in the local limit. The function $F_\pm$ for such a FS has the form

$$F_\pm(q) = F^e_\pm + F^h_\pm = \frac{\alpha_e}{[(1\pm i\gamma)^2 - q^2]^{1/2}} + \frac{1-\alpha_e}{1\pm i\gamma} - \frac{\alpha_h}{[(1\mp i\gamma)^2 - \alpha^2 q^2]^{1/2}} - \frac{1-\alpha_h}{1\mp i\gamma}. \tag{21}$$

Here $\alpha = R^h_{\text{extr}}/R^e_{\text{extr}}$.

The inset to Fig. 2 shows the function F_0 (21) calculated for $\alpha_e = 0.1$, $\alpha_h = 0.6$, $R^e_{\text{extr}} = 1.04\ \text{Å}^{-1}$, $R^h_{\text{extr}} = 0.495\ \text{Å}^{-1}$, as well as the spectrum obtained as the result of graphic solution of Eqs. (9) and (21) for $N = 0.767\times 10^{22}\ \text{cm}^{-3}$. The value of N was obtained by us from the data on the size and cross sections of hole sheets of the FS for tungsten presented in Ref. 16. It can be seen that the calculated curves are in good agreement with experimental dependences, indicating satisfactory fitting of FS parameters. It should be noted that the function F_0 changes its sign for $q^2 \simeq 0.42$, which determines the thresholdless form of the G-doppleron spectrum.

Let us now calculate the amplitude–frequency dependence of the G-peak of the DPR. It was noted above that the type of resonant interaction between electromagnetic and ultrasonic modes is determined by the first term on the right-hand side of (1). Hence the two other terms can be omitted. We shall seek the ''acoustic'' solution of Eq. (1) in the form $k = k_s + \Delta k_s$, assuming that $|\Delta k_s| \ll k_s$. In the case of weak interaction between dopplerons and sound, in the first approximation we can put $k = k_s$ on the right-hand side of (1). In this case, the damping coefficient for sound is defined as

$$\text{Im}(\Delta k_s) \cong \text{Im}(\beta\Gamma_0), \tag{22}$$

$$\Gamma_0 = \frac{1}{2}\frac{Nm}{\rho}\frac{v_e\omega_c}{v_s^2}\frac{\Omega/q_s}{\Omega^2/q_s \pm F_\pm(q_s)}, \tag{23}$$

$$\beta = [M \pm (k/m\omega_c)\langle \Lambda_\pm v^*_\pm\rangle][M \pm (k/m\omega_c) \times \langle \Lambda^*_\pm v_\pm\rangle]/(Nec/H_0)^2|_{k=k_s}. \tag{24}$$

Such a simplified method of solution of the dispersion equation for coupled ultrasonic and electromagnetic waves in metals was successfully used, for example, in an analysis of one-particle interaction of electrons with sound, which is associated with DSCR.[18] However, the correctness of this method in the case of resonant interaction of ultrasonic and collective electromagnetic modes should be substantiated.

The resonance peak of sound absorption is due to the presence of a denominator in the expression for the coefficient Γ_0 (23) singled out by us. The resonant singularity described by the dependence $\Gamma''_0(H_0) = \text{Im}\,\Gamma_0$ is manifested in the form of a peak of the quasi-Lorentzian type. The magnitude of the field corresponding to the peak of Γ''_0 virtually coincides with the value determined by Eq. (19). Consequently, the real part of the denominator in (23) vanishes at resonance, and the peak amplitude is given by

$$\Gamma''_{0r} \cong \frac{1}{2}\frac{Nm}{\rho}\frac{v_e\omega_c}{v_s^2}\frac{\Omega/q_s}{F''_-(q_s)}\bigg|_{q_{sr}}, \tag{25}$$

where q_{sr} is the value of q_s at resonance.

The experimentally observed DPR peak at relatively low frequencies is described qualitatively by the dependence $\Gamma''_0(H_0)$. Consequently, the dimensionless coefficient β (24) for tungsten does not affect the form of this dependence radically. However, the frequency dependence of the coefficient β remains unclear. We shall consider briefly this problem later. Here we confine ourselves to the calculation of the frequency dependence of the quantity Γ''_0 at the peak: Γ''_{0r}. Such a dependence obtained for the model of tungsten used by us is shown in Fig. 3. The mean free path $l = v_e/\nu$ of resonant electrons was assumed to be equal to 0.5 mm.

Let us now obtain the criterion for the validity of the weak interaction between electrons and sound. For the sake of simplicity, we confine our analysis to the DPR in a noncompensated metal with conductivity (10). In the first approximation, $\text{Im}\,\Delta k_s \propto (F''_-)^{-1}$ at resonance or, in accordance with (17), $\text{Im}\,\Delta k_s \propto [(\nu/\omega_c)F_0^3]^{-1}$. Substituting into (22) the obtained solution $q = q' + iq''$, where $q' \approx q_s$, $q'' = \text{Im}(\Delta k_s)/(\omega_c/v_e)$ we obtain in the second approximation $\text{Im}(\Delta k_s) \propto [(\nu/\omega_c + q'q'')F_0^3]^{-1}$. Obviously, we can confine our-

selves to the first approximation (22) if the inequality $\nu/\omega_c \gg q'q''$ holds. In accordance with (14), $|q'_D q''_D| \geqslant \nu/\omega_c$ for a doppleron wave in the absence of interaction. Consequently, this inequality at resonance ($|k'_D| \approx k_s$) can be written in the form

$$k''_D \gg \mathrm{Im}(\Delta k_s), \tag{26}$$

where $k''_D \geqslant l^{-1}$ is the damping coefficient for dopplerons in the absence of interaction, and $\mathrm{Im}(\Delta k_s)$ the damping coefficient for sound at resonance, calculated by formula (22). Criterion (26) has a simple physical meaning. As a matter of fact, resonant contributions to the attenuation of ultrasonic and doppleron waves are equal in magnitude. Consequently, the condition of weak coupling between dopplerons and sound is the smallness of doppleron damping associated with the DPR as compared with the ''background'' damping. For a typical value of the electron mean free path $l = 0.5$ mm and in accordance with (14), the background damping of dopplerons (in the absence of interaction) amounts to $k''_D > 20\ \mathrm{cm}^{-1}$. Figure 3 shows that the values of Γ obtained by us here are much smaller than this value. Hence we can draw the conclusion that the weak coupling approximation used by us is correct. Concluding the section, we note that criterion (26) can be obtained without specifying the form of the function $F_\pm(q)$ described by relation (2).

THEORETICAL ANALYSIS OF AMPLITUDE–FREQUENCY DEPENDENCE OF DPR

1. Analyzing the asymptotic behavior of the amplitude of the DPR peak for $\omega \to \infty$, it is natural to compare it with the dependence of the doppleron damping coefficient k''_D on the quantity ξ considered above. These dependences can be compared since the graphic solution of Eq. (19) shows (see insets to Figs. 4 and 2) that $q_{sr} \to 1$ as $\omega \to \infty$, and hence $\xi \propto \omega^{2/3} \to \infty$ also. It is obvious, however, that the expected correlation is not observed (even qualitatively). With increasing ω, attenuation of a doppleron in the resonant field becomes weaker ($k''_D \to l^{-1}$; see (14)), and the efficiency of interaction should increase. On the contrary, the amplitude of the DPR peak decreases also. The calculated dependence $\Gamma''_{0r}(\omega)$ (see Fig. 3) behaves similarly. In this connection, let us analyze the structure of expressions (14) and (25).

It follows from (14) and (25) that the quantities k''_D and Γ''_{0r} correlate with respect to the parameter ν as expected: $(k''_D \propto \nu, \Gamma''_{0r} \propto \nu^{-1}) \to \Gamma''_{0r} \propto k''^{-1}_D$, i.e., the amplitude of the DPR peak decreases upon an increase in doppleron damping associated with an increase in ν, and vice versa. On the other hand, the asymptotic behavior of k''_D in (14) is associated with the compensation of an increase in the value of F''_- in the numerator at resonance for $\omega \to \infty$ by the corresponding increase in the derivative $\partial F_0/\partial(q^2)$ in the denominator. This is not observed in (25), which ultimately explains a decrease in the value of Γ''_{0r} with increasing ω.

Let us consider in greater detail the dependence $\Gamma''_{0r}(\omega)$ in a compensated metal in two limiting cases without specifying the form of the function $F_\pm$. For the sake of definiteness, we assume that the ''long-wave'' doppleron solution exists in the ''-'' polarization and is due to singularity of $F_\pm$ at the point $q^2 = 1$. Using expression (14) for F''_-, we can write (25) in the form

$$\Gamma''_{0r} \propto \frac{\omega_c^2}{\Sigma_{i=e,h} |F'^{\,i}_0 + 2q_s^2 \partial F'^{\,i}_0/\partial(q_s^2)|_{q_{sr}}}. \tag{27}$$

The modulus in the denominator of (27) reflects the fact that the contributions of electrons and holes to the dissipative component of conductivity have the same sign.

A. The limit $\omega \to 0$. Taking into account the presence of the inversion center and using (2), we can easily prove that the expansions

$$\begin{aligned} F'^{\,e}_0 &= 1 + b_1 q^2 + b_2 q^4 + \dots\ ; \\ F'^{\,h}_0 &= -1 - c_1 q^2 - c_2 q^4 - \dots\ , \end{aligned} \tag{28}$$

where $b_1, b_2, \dots$ and $c_1, c_2, \dots$ are positive constants, are valid for a compensated metal. If the function F'_0 does not change its sign for $q^2 < 1$ ($F'_0 = F'^{\,e}_0 + F'^{\,h}_0 > 0$) and the following relations hold:

$$\begin{aligned} &(b_1 - c_1) = 0, \dots, (b_{n-1} - c_{n-1}) = 0, \\ &(b_n - c_n) > 0 \quad (n \geqslant 1), \end{aligned} \tag{29}$$

it follows from the graphic solution of Eq. (19) that $q_{sr} \to 0$ in the limit under investigation. In the expansion of the function F'_0, we can confine ourselves to the first nonzero term ($F'_0 \cong (b_n - c_n) q_s^{2n}$), and obtain from (19) $\omega_c \propto \omega^{(2n-1)/(2n+1)}$. Since the limiting value of the denominator in (27) is equal to two, at low frequencies we have

$$\Gamma''_{0r} \propto \omega^{2(2n-1)/(2n+1)} \quad (n \geqslant 1). \tag{30}$$

In particular, $n = 1$ and $\gamma''_{0r} \propto \omega^{2/3}$ for a metal with conductivity (11).

If the first nonzero difference in (28) is $(b_n - c_n) < 0 (n \geqslant 1)$, the function F'_0 changes its sign at a certain point $q_0^2 < 1$ since $F'_0 \to +\infty$ for $q^2 \to 1$ (see, for example, Fig. 2). Obviously, in this case we have at resonance $q_{sr}^2 \to q_0^2$ in the limit $\omega \to 0$, i.e., $\omega_c \propto \omega$. The limiting value of the denominator in (27) is finite, and relation (27) leads to the dependence $\Gamma''_{0r} \propto \omega^2$, which coincides with (30) for $n \to \infty$ as expected.

B. The limit $\omega \to \infty$. In this limit, $q_{sr} \to 1$, and the function F'_0 increases unlimitedly. It is obvious, however, that the nonlocal contribution $F'^{\,e}_{0r}$ of the resonant group of electrons dominates in conductivity at high frequencies. This is illustrated by the function (21) ($q = q_{sr}$) in which the first term on the right-hand side dominates at high frequencies. Consequently, we can neglect the contributions from remaining charge carriers and write (14) and (27) in the form

$$\Omega^2 \cong F'^{\,e}_{0r}, \tag{31}$$

$$\Gamma''_{0r} \propto \frac{\omega_c^2}{|\partial F'^{\,e}_{0r}/\partial(q_s^2)|_{q_{sr}}}, \tag{32}$$

considering that $2q_s^2 \partial F'^{\,e}_{0r}/\partial(q_s^2) \gg F'^{\,e}_{0r}(q_s^2 = q_{sr}^2 \to 1)$.

Falk *et al.*[14] give a ''hierarchy'' of singularities on the basis of an analysis of the function $S(p_z)$ at the points at which the derivative $|\partial S/\partial p_z|$ has an extremum (see, for ex-

ample, (5)). Such singular points should be supplemented with points at which the derivative has a discontinuity. The FS cross sections corresponding to these points as well as the groups of charge carriers localized in the vicinity of such points are referred to as resonant. The existence of such cross sections is a purely geometric property of real FS, leading to the emergence of singularities in the conductivity, which can be of the logarithmic ($F_0' \propto \ln(1-q^2)$) or power ($F_0' \propto \times(1-q^2)^{-m}, m>0$) type. If the resonant cross sectional area $S_r \neq 0$, we have $1/2 \leqslant m \leqslant 1$. If, however, $S_r = 0$ (reference point), we have $1/3 \leqslant m \leqslant 1$. In the case of a power-type singularity in (32), $\partial F_{0r}'^{e}/\partial(q_s^2) \propto F_{0r}'^{e(m+1)/m}$ and we obtain $\Gamma_{0r}'' \propto \omega^{-2/m}$ on account of (31). Consequently, in the limit $\omega \to \infty$, the value of Γ_{0r}'' always decreases, the decrease having the lowest rate for $m=1$. Such a singularity in conductivity ($F_0 = (1-q^2)^{-1}$) is observed if we have a layer of orbits for which $\partial S/\partial p_z = \text{const}$. An example of this kind is a physically unfeasible model of FS of the type of a ''parabolic lens.'' [7,14] For the FS model (5) used by us, conductivity (10) has a root singularity ($m=1/2$), and $\Gamma_{0r}'' \propto \omega^4$. If the singularity is logarithmic, the derivative $\partial F_{0r}'^{e}/\partial(q_s^2)$ can be presented in the form of an expression containing the exponential function $\exp F_{0r}'^{e}$. As a result, this expression at high frequencies will contain all powers of ω^2 ($\exp x = 1 + x + x^2 + \ldots$), and the decrease of Γ_{0r}' with increasing ω will be ''faster'' than in the case of a power singularity.

Summarizing the results described in A and B, we can draw the first and most important conclusion: for compensated metals with any form of conductivity, the quantity Γ_{0r}'' (25) defining the amplitude of the DPR peak under weak doppleron–phonon interaction (26) always increases at first with frequency, attains its peak value, and then decreases monotonically. The specific asymptotic form of Γ_{0r}'' is determined by the shape of the curve $F_{\pm}'(q)$, and hence by peculiarities of the actual FS of the metal.

2. An analysis of the amplitude–frequency dependence of DPR was limited to the calculation of the quantity Γ_{0r}''. However, this dependence can be changed radically by taking into account the coefficient β (24) which depends on frequency both explicitly and implicitly. The complexity of the problem of such an inclusion is illustrated by Grishin *et al.*[18] we considered a simplified model of a metal with a single group of charge carriers, whose deformation potential tensor ($\Lambda_{\alpha\beta} = \lambda_0 m(v_\alpha v_\beta - v^2 \delta_{\alpha\beta}/3)$; $\lambda_0 = \text{const}$) corresponds to an isotropic energy–momentum relation. These authors used the transformation $\beta\Gamma_0 \to \beta^* \Gamma_0 + \Gamma_0^*$; as a result, the expression for the coefficient β^* we are interested in does not contain singular terms any longer, and the term Γ_0^* is of nonresonant type. In our notation, the expression for β^* has the form

$$\beta^* = (\lambda_1 \Omega^2/q_s \mp \lambda_2)^2. \tag{33}$$

Here $\lambda_1 = 1 - \lambda_0(1 \pm i\gamma)$, $\lambda_2 = \lambda_0$.

It can be seen from (33) that the form of the frequency dependence of β^* can be different even for such a simple model. In the given case, it is determined by the deformation potential constant λ_0 which is a characteristic of an electrons about which the information is scarce. For example, the coefficient β^* depends on frequency weakly for $\lambda_0 \simeq 1$ in a wide frequency range defined by the inequality $\Omega^2/q_s < \lambda_0/|1-\lambda_0|$.

The expression for β^* becomes multiparametric and is complicated considerably for a metal with several groups of charge carriers, e.g., for a compensated metal. Medvedev *et al.*[19] analyzed DPR in a compensated metal, which was approximated by an extremely simplified model. Among other things, it was assumed (which is very important) that $\lambda_0 = \text{const}$ for all charge carriers. For such a model, $\lambda_2 = 0$ in (33), and $\beta^* \propto \omega^4$ for $\lambda_0 \neq 1$ at high frequencies. As a result, the expression for the sound absorption coefficient at resonance has the asymptotic form $\text{Im}(\Delta k_s'') \propto \omega$, which differs radically from that obtained in our experiment ($\Gamma \to 0$ for $\omega \to \infty$).

The above qualitative analysis of the expression for coefficient β and a comparison of amplitude–frequency dependences $\Gamma(\omega)$ and $\Gamma_{0r}''(\omega)$ lead to the following conclusions. First, the frequency dependence of the amplitude of the DPR peak in tungsten is mainly determined by relation (25), and the coefficient β (to be more precise, β^*) weakly depends on frequency. The weak frequency dependence (33) of the coefficient β^* observed by Grishin *et al.*[18] indicates that the inductive interaction between the electron and ion subsystems dominates over the deformation interaction. Although Grishin *et al.*[18] confined their analysis to a special case of a noncompensated metal with a single group of charge carriers, a physical analysis of the nature of the interaction indicates that this conclusion is of general nature. The statement concerning the weak frequency dependence of β^* naturally requires a more rigorous analysis. Second, the FS model used by us apparently does not describe the actual FS exactly. As a result, the peaks on the curves $\Gamma(\omega)$ and $\Gamma_{0r}''(\omega)$ are shifted relative to each other, and the theoretical curve decreases with increasing ω at a noticeably lower rate. These discrepancies do not cast a shadow of doubt on the correctness of qualitative conclusions. Probably, the model proposed in Ref. 20 provides a more adequate description of the Fs. In this model, the conductivity has a logarithmic singularity leading (see above) to a ''stronger'' frequency dependence of Γ_{0r}''.

3. The amplitude–frequency dependences $\Gamma(\omega)$ and $\Gamma_{0r}''(\omega)$ resemble qualitatively the amplitude–field dependence of doppleron oscillations (see the inset to Fig. 1). In Fig. 3, this dependence is reduced to the ω axis according to the algorithm $H_0 \to k \to \omega = k v_s$ based on the identity of the doppleron spectra (see Fig. 2) obtained from magnetoacoustic and rf measurements. It is obvious, however, that this similarity is not connected directly with the physics of the effects under investigation. It was noted above that the form of the amplitude–field dependence of doppleron oscillations is determined by singularities of the solution of the boundary-value problem. This dependence correlates with $\Gamma_{0r}''(\omega)$ to a certain extent. As a matter of fact, in the case when an electromagnetic wave is incident on the metal boundary, the amplitude of the transmitted wave is determined by the integral whose integrand has the same denominator as on the right-hand side of (23).[14,17] Such a structure of the integral leads to a decrease in the wave amplitude

upon an increase in the function F' in strong fields at points corresponding to the doppleron solutions of the dispersion equation (9) and coinciding with zeros of the denominator of the integrand. On the other hand, the increase in F' is accompanied by an increase in F'' in (25). As a result, the value of Γ''_{0r} as the amplitude of doppleron oscillations decreases in a resonance field in the limit $\omega \to \infty$.

4. While deriving the ''acoustic'' solution (1), we neglected attenuation of sound on the right-hand side putting $k = k_s$. Such a method of solution of Eq. (1) is quite correct since we assume that doppleron in tungsten weakly interacts with sound, the inequality (26) serving as a criterion of the intensity of this interaction. In this case, however, the finiteness of the function $F'_{\pm}$ associated with inclusion of collisions will be manifested in Eq. (19) with $F_{\pm}(q_s)$ on the right-hand side (in contrast to Eq. (9) for large values of ξ). As a result, the situation takes place when the curves $F'_{-}(q_s)$ and Ω^2/q_s do not intersect at high frequencies (curve g in Fig. 4) and the real component of the denominator in (23) does not vanish. This obviously does not mean at all that DPR is not manifested. However, the frequency asymptotic form of the DPR peak amplitude can change. Such a situation emerges for the FS model (21) of tungsten used by us at relatively high frequencies $\omega/2\pi > 500$ MHz, and hence was not investigated by us.

CONCLUSIONS

In this research, we have studied experimentally and explained theoretically the amplitude–frequency dependence of DPR in tungsten.

A graphic analysis of the dispersion equation has been used for constructing the spectra of weakly attenuating electromagnetic modes in compensated and noncompensated metals in the collisionless limit. The influence of collisions on the attenuation of these modes has been analyzed. The dependences of the external magnetic field at the doppleron–phonon and helicon–phonon resonances on the ultrasonic wave frequency have been constructed. The proposed model of the FS in tungsten correctly describes the spectrum of the doppleron mode under investigation. Subsequent analysis based on this theoretical investigation of the problem led to the following conclusions.

(1) In the case of tungsten, a simplified method of the solution of equation for coupled electromagnetic and acoustic modes is possible. This statement is based on an analysis of the obtained experimental results demonstrating that G-dopplerons weakly interact with sound in tungsten.

(2) The form of the amplitude–frequency dependence of DPR is determined to a considerable extent by the coefficient β (24) (to be more precise, β^* (33)). It is found that this coefficient in tungsten depends weakly on the frequency of sound. This conclusion actually indicates that the inductive mechanism of interaction between the electron and ion subsystems dominates over the deformation mechanism in tungsten.

(3) Under the conditions of dominating inductive mechanism of interaction between the two subsystems of the metal, the amplitude of the DPR peak first increases with frequency, attains the peak value, and then decreases monotonically irrespective of the shape of the FS. The results of calculation of the amplitude–frequency dependence of DPR in tungsten are in good qualitative agreement with experimental data.

This research was supported by the Ukrainian Foundation of Fundamental Research, project No. 2.4/211.

*E-mail: tsymbal@host.dipt.donetsk.ua

[1] V. G. Skobov, in *Waves and Interactions in Solid State Plasmas* by P. Platzman and P. Wolff (Suppl.), Academic Press, New York (1975).
[2] L. T. Tsymbal and T. F. Butenko, Solid State Commun. **13**, 633 (1973).
[3] A. A. Galkin, L. T. Tsymbal, T. F. Butenko *et al.*, Phys. Lett. **67A**, 207 (1978).
[4] T. F. Butenko, V. T. Vitchinkin, A. A. Galkin *et al.*, Zh. Éksp. Teor. Fiz. **78**, 1811 (1980) [Sov. Phys. JETP **51**, 909 (1980)].
[5] D. E. Zherebchevskii and L. T. Tsymbal, Fiz. Nizk. Temp. **11**, 98 (1985) [Sov. J. Low Temp. Phys. **11**, 53 (185)].
[6] J. Metrsching, Phys. Status Solidi **14**, 3 (1966); **37**, 465 (1970).
[7] S. V. Medvedev, V. G. Skobov, L. M. Fisher, and V. A. Yudin, Zh. Éksp. Teor. Fiz. **69**, 2267 (1975) [Sov. Phys. JETP **42**, 1152 (1975)].
[8] A. A. Galkin and A. P. Korolyuk, Pribory Tekhn. Éksp. No. 6, 99 (1960).
[9] K. B. Vlasov and B. N. Filippov, Fiz. Met. Metalloved. **17**, 152 (1964).
[10] V. P. Naberezhnikh, D. E. Zherebchevskii, L. T. Tsymbal, and T. M. Yeryomenko, Solid State Commun. **11**, 1529 (1972).
[11] V. G. Skobov and E. A. Kaner, Zh. Éksp. Teor. Fiz. **46**, 273 (1964) [Sov. Phys. JETP **19**, 189 (1964)].
[12] V. M. Kontorovich, Zh. Eksp. Teor. Fiz. **45**, 1638 (1963); **59**, 2116 (1970); **61**, 1181 (1971); [Sov. Phys. JETP **18**, 1125 (1963); **32**, 1146 (1970); **34**, 630 (1971)].
[13] V. M. Kontorovich, Usp. Fiz. Nauk **142**, 265 (1984) [Sov. Phys. Usp. **27**, 134 (1984)].
[14] D. S. Falk, B. Gerson, and J. F. Carolan, Phys. Rev. B **1**, 406 (1970).
[15] V. U. Gudkov, Solid State Commun. **44**, 229 (1982).
[16] J. B. Ketterson, D. D. Koelling, J. C. Shaw, and R. Windmiller, Phys. Rev. B **11**, 1447 (1975).
[17] G. H. Reuter and E. H. Sondheimer, Proceedings Roy. Soc. **195**, 130 (1948).
[18] A. M. Grishin, V. G. Skobov, L. M. Fisher, and A. S. Chernov, Pis'ma Zh. Éksp. Teor. Fiz. **35**, 370 (1982) [JETP Lett. **35**, 455 (1982)].
[19] S. V. Medvedev, V. G. Skobov, L. M. Fisher, and V. A. Yudin, Zh. Éksp. Teor. Fiz. **69**, 2267 (1975) [Sov. Phys. JETP **42**, 1152 (1975)].
[20] A. N. Cherkasov, Ph.D. Thesis, Donetsk (1983).

Translated by R. S. Wadhwa

LOW-DIMENSIONAL AND DISORDERED SYSTEMS

Effect of boson peak on low-temperature electron spin–lattice relaxation in amorphous materials

N. P. Giorgadze and L. Zh. Zakharov

Institute of Physics, Georgian Academy of Sciences, 380077 Tbilisi, Georgia
(Submitted September 30, 1997)
Fiz. Nizk. Temp. **24**, 262–265 (March 1998)

The effect of a boson peak (BP) on the low-temperature electron spin–lattice relaxation in amorphous materials is investigated. It is shown that the contribution of the boson peak to one-phonon relaxation for EPR frequencies within the boson peak width dominates over the Debye contribution, and the field dependence of relaxation rate changes qualitatively, while the temperature dependence remains unchanged. © *1998 American Institute of Physics.* [S1063-777X(98)00803-2]

It is well known[1] that the density of vibrational states in amorphous materials (glasses) is characterized by a low-temperature peak corresponding to vibrational excitations obeying the Bose statistics. The frequency ω_m corresponding to the maximum density of states at the peak varies (for different materials) from 4×10^{11} s^{-1} to 20×10^{11} s^{-1}, while the maximum density of states at the peak exceeds the Debye density of states at the same frequency ω_m by a factor of 2–10. The existence of a boson peak (BP) is confirmed in experiments on Raman scattering and neutron scattering. Its existence in the density of vibrational states affects significantly the physical properties (heat capacity and thermal conductivity) of amorphous materials in the temperature range 3–15 K.

The boson peak must also naturally affect considerably the electron spin–lattice relaxation (ESLR) for which phonon mechanisms are obviously of primary importance (including the case of amorphous materials). To our knowledge, Lebanidze *et al.*[2] were the first to pay attention to this circumstance. They considered a two-quantum process of electron spin–lattice relaxation (of the Raman type) under the conditions when vibrational excitations pertaining to the BP play an active part in the relaxation process. These authors obtained an expression for relaxation rate which was used for estimating the temperature dependence of this rate as proportional to T_L^5 (T_L is the lattice temperature). It should be noted that the expression derived in Ref. 2 presumes that the EPR frequency is smaller than ω_m. It is remarkable, however, that the frequency interval embraced by the peak partly overlaps with the EPR frequency range $(10^{10}-10^{11})$ s^{-1}. Consequently, we can expect that the two-quantum relaxation mechanism associated with the BP is suppressed considerably for high EPR frequencies (especially for frequencies $\sim\omega_m$) since the number of pairs of vibrational excitations pertaining to the BP and participating in an act of energy exchange between the electron spin system and the lattice is extremely small in this case.

Simultaneously, we must expect that the rate of one-quantum mechanism of spin–lattice relaxation involving in the present case the vibrational excitations with an excess density of states will be considerably enhanced. This communication is devoted to a quantitative analysis of this problem.

We confine our analysis to the case when the spin $S=1/2$ and assume that the time of establishment of intrinsic equilibrium in the spin system is much shorter than the characteristic time scales of spin–lattice relaxation. Further, we assume that the parameter $\hbar\omega_s/k_BT_L$ is arbitrary, while the parameter $\hbar\omega_d/k_BT_L\ll1$ (ω_s is the EPR frequency and ω_d the frequency of the electron spin in the local field determined by the dipole–dipole interaction of electron spins). Finally, we assume that the thermal equilibrium of the spin system with the thermostat is violated by resonance interaction. Under these conditions, we can consider that the relaxation of electron polarization is independent of the energy relaxation of spin–spin interaction (assuming that the secular component of the latter interaction continues to be the source of randomization) and proceed from the Hamiltonian of a coupled spin–phonon system presented in Ref. 3:

$$H=H_S+H_L+H_{SL}, \tag{1}$$

where

$$H_s=\hbar\omega_s\sum_j S_j^z, \tag{2}$$

is the Zeeman energy of the electron spin system,

$$H_L=\hbar\sum_{\mathbf{q}}\omega_{\mathbf{q}}a_{\mathbf{q}}^+a_{\mathbf{q}} \tag{3}$$

the Hamiltonian of phonons (lattice),

$$H_{SL}=\frac{i\hbar}{2}\sum_{\mathbf{q}}\sum_j\frac{1}{N^{1/2}}(g_{\mathbf{q}}^+S_j^-+g_{\mathbf{q}}^-S_j^+)(\exp i\mathbf{q}r_j(a_{\mathbf{q}}-a_{-\mathbf{q}}^+)) \tag{4}$$

 © 1998 American Institute of Physics

the Hamiltonian of the spin–phonon interaction, $\mathbf{q}$ and $\omega_{\mathbf{q}} = qc$ are the wave vector and the phonon frequency, c is the velocity of sound, $a_{\mathbf{q}}^{+}$ and $a_{\mathbf{q}}^{-}$ are the creation and annihilation operators for a phonon with the wave vector $\mathbf{q}$, N is the number of atoms in the sample, $\mathbf{r}$ the radius vector of the jth spin, and $g_{\mathbf{q}}^{\alpha}$ the spin–phonon interaction constant. In this case,

$$g_{\mathbf{q}}^{+} = \omega_s \left(\frac{\omega_{\mathbf{q}}}{4\Omega_1} \right)^{1/2}$$

for the Kramers magnetic ions and

$$g_{\mathbf{q}}^{+} = \left(\frac{\omega_{\mathbf{q}} \Omega_2}{4} \right)^{1/2}$$

for non-Kramers magnetic ions (Ω_1 and Ω_2 are constants having the dimensions of frequency), and the relation $(g_{\mathbf{q}}^{-})^* = g_{-\mathbf{q}}^{+}$ holds.

The electron spin–lattice relaxation can now be considered as a process of stabilization of thermal equilibrium at the kinetic stage of evolution in a quasi-equilibrium system consisting of a Zeeman reservoir of electron spins and the lattice (thermostat). Using the method of a nonequilibrium statistical operator[4] for describing this process, we obtain after simple calculations the well-known equations for the rate of variation of relaxing electron polarization $P_S = -\mathrm{th}(\hbar\omega_s/2k_B T_s)$ (T_s is the Zeeman spin-temperature):

$$\frac{dP_S}{dt} = -\frac{(P_S - P_{SL})}{T_{SL}}, \tag{5}$$

where the relaxation rate is defined as

$$\frac{1}{T_{SL}} = \frac{4\pi}{|P_{SL}|N} \sum_{\mathbf{q}} |g_{\mathbf{q}}^{-}|^2 \delta(\omega_s - \omega_{\mathbf{q}}), \tag{6}$$

and P_{SL} is the electron polarization at the lattice temperature.

A transition to the continual description in terms of phonon is carried out by conventional replacement of summation by integration:

$$\sum_{\mathbf{q}} (\ldots) \to \int \frac{d\Omega_{\mathbf{q}}}{4\pi} \int d\omega G(\omega)(\ldots),$$

where (in contrast to ordinary materials) the density of states is defined by[1]

$$G(\omega) = \frac{9N\omega^2}{\omega_D^3} \left\{ 1 + \mu \frac{\omega_m^2}{\omega^2} \exp\left[-\left(\frac{\ln \omega/\omega_m}{\sqrt{2}\sigma} \right)^2 \right] \right\}, \tag{7}$$

$\omega_D = (6\pi^2 c^3/a^3)^{1/3}$ is the Debye frequency, a the lattice parameter, μ the coefficient assuming values from 2 to 10 for different materials and characterizing the BP width, and the parameter $\sigma \simeq 0.48$. The first term in this expression is the conventional Debye density of states, while the second term is the contribution of vibrational excitations localized in the vicinity of the frequency ω_m to the density of states, the width of the corresponding region being

$$\gamma = 2\omega_m \sinh \sigma\sqrt{2\ln 2} = 1.2\omega_m.$$

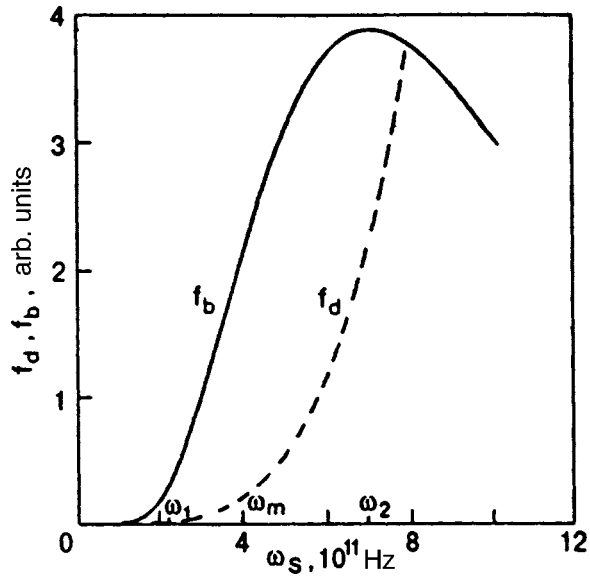

FIG. 1. Relaxation rates $f_b = 1/(T_{SL}^{BP})(2\times10^{-20}\Omega_1)/9\pi$ (solid curve) and $f_d = 1/(T_{SL}^{D})(2\times10^{-20}\Omega_1)/9\pi$ (dashed curve) as functions of the EPR frequency (constant magnetic field); $\omega_1 = \omega_m \exp(-\sigma\sqrt{2\ln 2}) \simeq 2.3\times10^{11}$ Hz and $\omega_2 = \omega_m \exp(\sigma\sqrt{2\ln 2}) \simeq 7\times10^{11}$ Hz are the frequencies corresponding of the BP half-widths. The difference $\gamma = \omega_2 - \omega_1 = 4.7\times10^{11}$ Hz is the boson peak width.

Using the above-mentioned transformation and expression (6) for the required rate of electron spin–lattice relaxation, we obtain

$$\frac{1}{T_{SL}} = \frac{1}{T_{SL}^{D}} + \frac{1}{T_{SL}^{BP}}, \tag{8}$$

where

$$\frac{1}{T_{SL}^{D}} = \frac{18\pi\omega_s^2}{\omega_D^3 |P_{SL}|} g^2(\omega_s) \tag{9}$$

is the Debye relaxation rate,

$$\frac{1}{T_{SL}^{BP}} = \frac{18\pi\mu\omega_m^2}{\omega_D^3 |P_{SL}|} g^2(\omega_s) \exp\left[-\frac{\ln(\omega_s/\omega_m)}{\sqrt{2}\sigma} \right]^2 \tag{10}$$

the contribution to the relaxation rate from the BP, and

$$g^2(\omega_S) = \int \frac{d\Omega_{\mathbf{q}}}{4\pi} |g_{\mathbf{q}}^{+}|^2.$$

Let us analyze the obtained results.

It should be noted above all that (in accordance with (9) and (10)) the contribution of the BP to the one-phonon relaxation for large values of μ and for EPR frequencies lying within the BP dominates over the Debye contribution, and hence the type of one-phonon relaxation is determined just by this contribution. Naturally, the presence of a BP does not affect the temperature dependence of relaxation rate which has the form $1/T_{SL} \propto \coth(\hbar\omega_s/k_B T_L)$ (as in the Debye case). However, the field dependence changes qualitatively. This is illustrated graphically in Fig. 1 depicting the field dependence of the relaxation rates $1/T_{SL}^{D}$ and $1/T_{SL}^{BP}$ for Kramers magnetic ions in a sample with $\omega_D \sim 10^{13}$ Hz and $\omega_m \sim 4\times10^{11}$ Hz at $T = 3$ K and $\mu = 10$.

It is also important that the general increase in relaxation rate must lead to the expansion of the temperature range in which the one-quantum mechanism of ESLR dominates over the Raman two-quantum mechanism.

It should also be noted that glasses with a moderate position of the peak ($T_m=(\hbar\omega_m/k_B)\sim 3-5$ K) and with the maximum possible value of μ are the most suitable materials for studying the effect of the BP on the one-phonon electron relaxation. Indeed, in this case the two-quantum relaxation mechanism associated with the BP, as well as the Raman mechanism, is obviously ineffective (at least at temperatures $T_L \leqslant T_m$), and the typical features of the one-quantum relaxation mechanism associated with the BP are manifested most clearly.

In conclusion, the authors express their gratitude to K. I. Sigua who made computer calculations for plotting curves in Fig. 1.

This research was made possible owing to Grant No. 2.12 of the Georgian Academy of Science.

[1] V. K. Malinovskii, V. I. Novikov, and A. P. Sokolov, Usp. Fiz. Nauk **163**, 119 (1993) [*sic*].
[2] A. A. Lebanidze, T. L. Buishvili, and G. R. Kakabadze, Biofizika, **42**, 811 (1997).
[3] R. J. Elliot and J. B. Parkinson, Proc. Phys. Soc. **92**, 1024 (1967); R. Kh. Sabirov, Fiz. Nizk. Temp. **16**, 1338 (1990) [Sov. J. Low Temp. Phys. **16**, 765 (1990)].
[4] D. N. Zubarev, *Nonequilibrium Statistical Thermodynamics* [in Russian], Nauka, Moscow (1997).

Translated by R. S. Wadhwa

LOW-TEMPERATURE PHYSICS OF PLASTICITY AND STRENGTH

Superconducting properties and structure of vanadium after cryogenic deformation

V. K. Aksenov, N. A. Chernyak, O. I. Volchok, A. V. Mats, and Ya. D. Starodubov

National Science Center ''Kharkov Physicotechnical Institute'', 310108 Kharkov, Ukraine
(Submitted June 4, 1997; revised September 22, 1997)
Fiz. Nizk. Temp. **24**, 266–271 (March 1998)

The effect of low temperature (77 K) deformation by drawing (80%) on the superconducting properties and structure of vanadium is studied. The structural elements (fragment boundaries) responsible for the observed changes of critical parameters are isolated. The electron-phonon coupling constant and the electron mean free path undergo most significant changes in these regions of rotational deformation localization, which have a high density of defects and are powerful sources of internal stresses. The dislocation density at the fragment boundaries is estimated. © *1998 American Institute of Physics.* [S1063-777X(98)00903-7]

This paper is written in commemoration of the 70th anniversary of the National Science Center ''Kharkov Physicotechnical Institute''

1. INTRODUCTION

According to the prevailing concepts, the change in the superconducting properties of metals subjected to plastic deformation is associated with the level of defects and the nature of the structural state formed as a result of deformation. This problem has been studied theoretically and experimentally for quite some time, and the maximum progress has been attained for the cases when the structure of the materials is characterized by a uniform distribution of dislocations, a weakly disoriented cellular structure, and the presence of twin interlayers (see, for example, Refs. 1 and 2). The situation was found to be quite different in the studies of the influence of the fragmented structure, one of the most frequently encountered types of structural state, on the properties of superconductors. As a rule, the emergence of such a structure is associated with the growth of large plastic deformations and leads to the fragmentation of the material into a large number of highly disoriented microregions (fragments). Several authors assume that significant changes in the properties of the superconducting state are associated with the onset of rotational plasticity.[3,4] However, the interpretation of the experimental results is greatly hampered due to the absence of suitable models explaining the entire complexity and diversity of this phenomenon. We believe that the separation of contributions from individual elements of fragmented structure in the variation of the superconducting parameters would be an important step towards the solution of this problem and the construction of models conforming to the experimental results.

Earlier, we studied the effect of large plastic deformation by drawing at 77 and 300 K on the magnetic properties of vanadium at 4.2 K.[4] In order to interpret the observed variations, it was proposed by us that one of the main factors responsible for the observed effects is the strength of fragment boundaries which depends primarily on the disorientation angle, the number density of defects, and the level of nonuniform internal stresses caused by them. The strength of boundaries increases significantly as a result of cryogenic deformation, which enables us to study the nature of the phenomenon. In the present paper, which is a continuation of our earlier publication describing the effect of fragmentation on the superconducting properties of vanadium,[4] we endeavor to describe the results of new experimental studies whose analysis makes it possible to isolate the contribution from individual elements of the fragmented structure to the variation of superconducting characteristics of the metal taking into account the internal stress fields.

2. EXPERIMENTAL TECHNIQUE

In the present work, we study the connection between the variations of the lower critical field H_{c_1}, the thermodynamic field H_c, and the upper critical field H_{c_2}, as well as the superconducting transition temperature T_c, the resistivity ρ_n, and the emergence of inhomogeneous dislocation structures as a result of large plastic deformations. As in our earlier work,[4] we chose 99.88% pure vanadium obtained by electron-beam melting as the object of our investigations. Cylindrical bars were first subjected to recrystallization annealing at a temperature of 1300 K in a vacuum of 1.3×10^{-5} Pa for three hours. Subsequent deformation by drawing at 77 K was carried out on a special device.[5] As the deformation attained the level $\varepsilon=80\%$, samples of wire having a diameter 1.2 mm and a length 12 mm were cut. A structural state of the samples identical to the initial (recrystallized) state was created by repeated annealing.

In order to plot the field dependences of magnetization $M(H)$ for vanadium at 4.2 K, we used a special magnetometer capable of recording the dependence $M(H)$ under a con-

 © 1998 American Institute of Physics

TABLE I. Characteristics of vanadium in different structural states.

State	T_c, K	H_{c1}, Oe	H_{c2}, Oe	$\rho_n \cdot 10^8$, $\Omega\cdot$m
Initial	4.88	90	1660	3.78
Deformed $\varepsilon=80\%$, $T=77$ K	4.98	80	2660	4.18

tinuous variation of the magnetic field. The sample axis was at right angles to the magnetic field. The technique for magnetic measurements was described in detail in our earlier publications.[6,7] With the exception of H_c corresponding to the deformed state, the values of the critical fields at 4.2 K were determined by using the standard technique for processing the $M(H)$ dependences.[8,9] The estimate for the value H_c of the deformed state is presented below. The superconducting transition curves were recorded by the usual resistive technique, and the error in determining T_c was 0.001 K. The structural state was studied by transmission electron microscopy on longitudinal sections of the samples. Note that all investigations in the initial state and in the state deformed by drawing were carried out on the same sample after removing a surface layer of thickness $\simeq 10$ μm.

In our calculations, we used the quantity ρ_D, the contribution to ρ_n from a unit length of the dislocation line. This quantity was determined in supplementary experiments by measuring the increment in ρ_n at 5 K as a result of an increase in the mean dislocation density N registered by an electron microscope after relatively small deformations. It was found that $\rho_D \simeq 1\times 10^{-24}\Omega\cdot\mathrm{m}^3$.

3. DISCUSSION OF RESULTS

Table I shows the characteristics of vanadium in various structural states. It can be seen that deformation leads to a decrease in the value of H_{c_1} and an increase in the values of H_{c_2}, T_c and ρ_n, the variation in the value of H_{c_2} being the most significant. While the magnetization of the initial sample is described by a typical hysteresis curve, the nature of magnetization changes significantly as a result of deformation, and a peak effect is observed (Fig. 1).

The initial structural state of vanadium is characterized by a low dislocation density $N \simeq 10^{12}$ m^{-2}, and polygonal

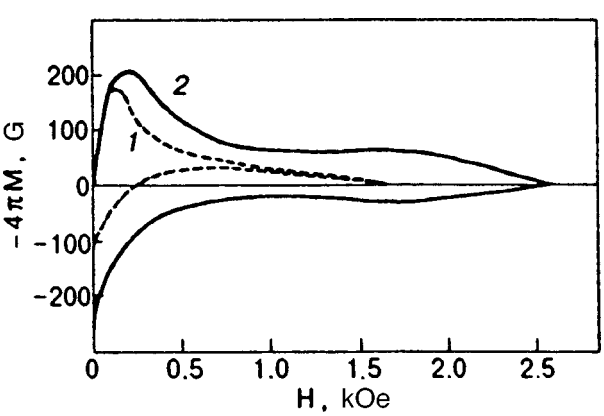

FIG. 1. Magnetization curves for vanadium samples: initial state (curve *1*) and after deformation by drawing (80%) at 77 K (curve *2*).

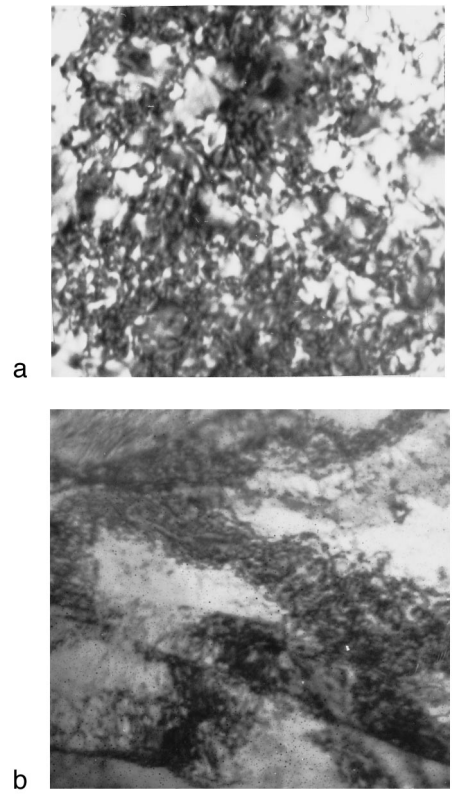

FIG. 2. Vanadium structure after drawing (77 K, $\varepsilon \simeq 80\%$): a—core ($\times$80 000); b—periphery of the sample ($\times$40 000).

structure is practically not observed. The grain boundaries are in equilibrium state and do not cause any internal stresses. Low-temperature deformation leads to the formation of a macroscopically heterogeneous structure over the sample cross section due to different conditions of plastic flow in the core and over the periphery of the bar during drawing. Microhardness measurements show that the ratio of the corresponding regions of the cross section after deformation is about 5:1. The core is characterized by a morphologically homogeneous distribution of dislocations with $N \approx 1.4 \times 10^{15}$ m^{-2} (Fig. 2a), and fragments stretched along the direction of drawing are encountered rarely. On the other hand, the periphery abounds in fragmented structure and the fragments are also stretched along the direction of drawing (Fig. 2b). In the region of bulk fragmentation, the density of dislocations uniformly distributed in the fragments is $N \approx 2.6\times 10^{15}$ m^{-2}, the average size of fragments is $d \approx 3.0 \times 10^{-7}$ m, and the fragments may be disoriented by up to 15°. The fine structure of fragment boundaries is not resolved, which is apparently due to a very high density of defects at the boundaries, and the presence of internally stress fields in them. This leads to a significant blurring and overlapping of the regions of diffractional contrast between dislocations. Note that strong variations of diffractional contrast and a large number of flexural contours observed frequently in the fragments point towards the existence of quite large and nonuniform internal stresses caused by interfaces. Twinning is not observed after deformation.

Let us compare and analyze the obtained results. It

should be remarked at the very outset that a more detailed analysis of the reasons behind observed effects requires a knowledge of not only the characteristics presented in Table I, but also several other theoretical parameters characterizing the superconducting state of the initial and the deformed samples. These parameters are calculated on the basis of the BCS theory and the Ginzburg–Landau theory.[10,11]

Let us consider the properties of the initial state and define its generalized parameter:

$$\kappa_1 = \frac{1}{\sqrt{2}} \frac{H_{c1}}{H_c}. \tag{1}$$

An analysis of the magnetization curve shows that $H_c \approx 290$ Oe, which gives $\kappa_1 \approx 4.1$. In order to estimate the ''purity'' of the superconductor under investigation and to select a criterion for correctly determining the variation of κ_1 in the deformed state, we calculate the Sommerfeld constant γ. For this purpose, we use the temperature dependence $H_c(T)/H_c(0)$[12] to estimate the value of $H_c(0) \approx 1.24$ kOe. Using familiar relations,[10,11] we can obtain from here the constant $\gamma = 1.1 \times 10^3$ J/(m$^3 \cdot$K^2) and the BCS coherence length ξ_0. The value of $\xi_0 \cong 5.35 \times 10^{-8}$ m was obtained from a comparison of the characteristics T_c and γ for vanadium which was also analyzed by us in Ref. 12. Having calculated the mean free path $l = 9.3 \times 10^{-9}$ m from the relation $\rho_n l = 3.5 \times 10^{-16} \Omega \cdot \mathrm{m}^2$,[12] we obtain the impurity parameter $\alpha = 0.882 \xi_0 / l \approx 5.1$. This means that the metal under investigation is a quite ''dirty'' superconductor.

Let us now consider the possible reasons behind the variation of superconducting properties of a metal as a result of deformation. In the first approximation, these variations may be caused by an increase in the dislocation density in the regions of their uniform distribution (core and the regions inside the fragments), fragment boundaries and macroscopic internal stresses. The latter emerge as a result of any variation in sample shape and must be taken into consideration while estimating the effect of the structural factor on the critical parameters. In the case studied by us, tensile stresses dominate at the periphery, while compressive stresses abound in the core region.[13] For the sake of simplicity, we shall consider the maximum possible effect of these stresses on superconducting characteristics. While evaluating the critical parameters in the core of the sample, we shall assume that the effect of compressive stresses on the chosen volume is similar to the effect of hydrostatic pressure. Considering that fragments are strongly stretched in the peripheral regions, we shall confine ourselves to the case when a trial fragment mainly undergoes an axial elongation. According to Rybin *et al.*,[14] the internal stress field distribution in the fragments is quasiuniform in this case, except in the boundary regions which have a characteristic linear size $\approx 0.05d$.

Let us estimate the most probable variations in the critical parameters in the regions with a uniform dislocation distribution. According to Zaitsev's model[15] and our experimental data,[3] the dislocation part of the growth in T_c satisfies the approximate equality

$$\Delta T_c(N) \cong \frac{\pi}{18} \left(\frac{s_\perp}{s_\parallel} \right)^4 \frac{E_F^2 m s}{\hbar k_B G} N, \tag{2}$$

where $s_\perp$ and $s_\parallel$ are the transverse and longitudinal sound velocities, E_F is the Fermi energy, m the electron mass at the Fermi surface, s the velocity of sound, G the shear modulus, $\hbar$ the Planck constant, and k_B the Boltzmann constant. Substituting into (2) the values $s = 6 \times 10^3$ m/s, $G = 4.65 \times 10^{10}$ Pa,[16] $E_F = 0.76$ [17] $m \approx m^* \approx 2m_0$ (m^* is the effective cyclotron mass and m_0 the electron mass),[18] and assuming that $s_\perp / s_\parallel$ has the value ~ 0.67 typical of a metal, we obtain

$$\Delta T_c(N) \approx 0.15 \times 10^{-16} N \tag{3}$$

(ΔT_c is in kelvins). It is well known[19] that for a uniform distribution of dislocations, the stress level can be defined with the help of the expression

$$\sigma = \sigma_0 + \alpha G b N^{1/2}, \tag{4}$$

where σ_0 is the yield stress in the initial state, b the modulus of the Burgers vector, and α is a constant. The values $\sigma_0 = 250$ MPa and $\alpha = 0.3$ are obtained from mechanical testing, while Fidel[20] gives the value $b = 2.63 \times 10^{-10}$ m. This gives $\sigma = 8.4 \times 10^{-3} G$. In the first approximation, we shall consider elastic stress fields as the additional additive contribution to the overall increase in the value of T_c. Using formula (3) and the value $dT_c/dp = 0.62 \times 10^{-5}$ K/bar,[21] we find that $\Delta T_c / T_c \approx 0.8\%$, which is smaller than the experimentally observed increase in the value of T_c.

For the relative deviation of H_{c2}, we obtain from Eq. (1)

$$\frac{\Delta H_{c2}}{H_{c2}} = \frac{\Delta k_1}{k_1} + \frac{\Delta H_c}{H_c}. \tag{5}$$

Since vanadium which was the object of our investigations is a very ''dirty'' superconductor and κ_1 is defined in the vicinity of T_c, we obtain

$$\Delta \kappa_1 \approx 2.37 \times 10^6 \gamma^{1/2} \Delta \rho_n. \tag{6}$$

In subsequent calculations, we can disregard the small increase in γ associated with an increase in T_c. The dislocation contribution to the increase in the electrical resistance is estimated from the relation $\Delta \rho_n \approx N \rho_D$. Nearly the same increase in electrical resistance is caused by the point-type scatterers accumulated as a result of deformation.[22] Further, we consider that the scale of effects associated with the connection between H_{c2} and elastic stresses is mainly determined for $T \sim T_c$ by the quantity $dH_c/dp \approx 1.85 \times 10^{-3}$ Oe/bar.[23] In this case we obtain from Eq. (5) the value $\Delta H_{c2}/H_{c2} \approx 8\%$, which is also much lower than the experimentally determined variation of H_{c2} in vanadium after low-temperature deformation.

A practically similar result is obtained from analogous calculations for the quasiuniform core region of the fragment, since a certain increase in the critical parameters associated with an increase in the dislocation density will be compensated by the competing effect of tensile stresses.

Thus, the analysis carried out by us shows that even the maximum possible values of T_c and H_{c2} in regions with a uniform dislocation distribution are smaller than the experimentally recorded values, which can be naturally associated

with the fragment boundaries that are narrow unrelaxed zones of localization for rotational deformation.

According to the prevailing concepts, the main variations in the critical characteristics of vanadium observed after deformation are caused by an enhancement of the electron-phonon interaction and a decrease in the electron mean free path. Using McMillan's formula[24] and assuming[25] that an equal increase in the value of T_c is accompanied by an insignificant decrease in the Debye temperature, we obtain the value $\Delta\lambda/\lambda \approx 1.5\%$ for the relative increase in the electron-phonon interaction constant. This value is close to the estimates for the increase in λ at the regions of plastic deformation localization.[1]

Let us now evaluate the parameter κ_1 and the characteristic electrical resistance ρ_b of the boundary by using the experimental values of H_{c2} and T_c and disregarding possible distortions of the dependence $H_c(T)/H_c(0)$ introduced by the stress field. Considering that the increase in γ as a result of deformation of vanadium correlates with the increase in T_c,[25] and using relations from the Fetter-Hohenberg theory,[11] we obtain $H_c(0) \approx 1.27$ kOe, $H_c \approx 330$ Oe, and $\kappa_1 \approx 5.8$. This gives the required value of $\rho_b \approx 5.88 \times 10^{-8} \Omega \times$m. Since the measuring current flows through the circuit element with a resistance lower than ρ_b, we find that $\rho_b > \rho_n$. Naturally, the electron mean free path in the deformation localization region is smaller than in the surrounding volume.

The value of ρ_b can be used to calculate approximately the dislocation density at deformation boundaries. Assuming that scattering at the cores of individual dislocations is a dominating factor, we obtain $N \approx 2 \times 10^{16}$ m^{-2} from the relation $\rho_b = \rho_n + N\rho_D$. This value of the dislocation density is an order of magnitude larger than at the core of the fragment.

CONCLUSION

Thus, an analysis of the experimental data allows us to differentiate the contribution from individual elements of the fragmented structure to the variation of the critical parameters of deformed vanadium. The dominating contribution is made by boundaries of fragments that are unrelaxed zones of localization of rotational plasticity and are regions of high density of crystal structure defects as well as powerful sources of internal stress fields. The variations of superconducting characteristics observed at fragment boundaries are associated with the combined effect of an increase in the electron-phonon interaction constant and a decrease in the electron mean free path in such structural formations. The dislocation density at fragment boundaries causing a disorientation of about 15° may attain values up to $\approx 2 \times 10^{16}$ m^{-2}.

This research was supported by the Soros International Research Foundation (Grant No. U9Z000).

[1] V. I. Sokolenko and Ya. D. Starodubov, Fiz. Nizk. Temp. **19**, 951 (1993) [Low Temp. Phys. **19**, 675 (1993)].
[2] D. Dew-Hughes and M. J. Witcomb, Philos. Mag. **26**, 73 (1972).
[3] V. K. Aksenov, V. I. Sokolenko, and Ya. D. Starodubov, Fiz. Nizk. Temp. **19**, 1083 (1993) [Low Temp. Phys. **19**, 768 (1993)].
[4] V. K. Aksenov, N. A. Chernyak, O. I. Volchok, and Ya. D. Starodubov, Fiz. Nizk. Temp. **22**, 583 (1996) [Low Temp. Phys. **22**, 449 (1996)].
[5] O. I. Volchok, I. M. Neklyudov, Ya. D. Starodubov, and B. P. Chernyi, Metalloved. i Term. Obrabotka Metallov **12**, 28 (1993).
[6] B. G. Lazarev, L. S. Lazareva, V. A. Poltavets, and S. I. Goridov, in Vopr. Atom. Nauki i Tekh., Ser. Fund. i Prikl. Sverkhprovod. Issue 3(9), 45 (1979).
[7] N. A. Chernyak, B. K. Pryadkin, M. A. Tikhonovskii, and M. M. Oleksienko, in Vopr. Atom. Nauki i Tekh., Ser. Fund. i Prikl. Sverkhprovod. Issue 7(7), 11 (1989).
[8] J. E. Evetts and J. M. A. Wade, J. Phys. Chem. Solids **31**, 973 (1970).
[9] L. W. Dubeck, D. R. Aston, and F. Rothmarf, J. Appl. Phys. **41**, 1593 (1970).
[10] T. P. Orlando, E. J. McNiff, S. Foner, and M. R. Beasley, Phys. Rev. B **19**, 4545 (1979).
[11] A. L. Fetter and P. S. Hohenberg, in *Superconductivity*, Vol. 2 (Ed. by R. D. Parks and Marcell Dekker) New York (1969), p. 817.
[12] R. Radebaugh and P. H. Keesom, Phys. Rev. **149**, 217 (1966).
[13] R. P. Gromov, *Theory of Processing by Pressure* [in Russian], Metallurgiya, Moscow (1967).
[14] V. V. Rybin, Yu. M. Zolotarevskii, and I. M. Zhukovskii, Fiz. Met. Metalloved. **1**, 5 (1990).
[15] R. O. Zaitsev, Zh. Éksp. Teor. Fiz. **54**, 1445 (1968) [Sov. Phys. JETP **27**, 775 (1968)].
[16] K. A. Gschneider, Jr., Solid State Phys. **16**, 275 (1964).
[17] D. A. Papaconstantopoulos, J. R. Anderson, and J. M. McCaffrey, Phys. Rev. B **5**, 1214 (1972).
[18] R. A. Phillips, Phys. Lett. **36A**, 361 (1971).
[19] R. W. Honeycombe, *The Plastic Deformation of Metals*, Edward Arnoed Ltd. (1968).
[20] G. Fidel, *Dislocations* [Russian translation], Mir, Moscow (1967).
[21] N. F. Smith, J. Phys. F **2**, 292 (1972).
[22] I. A. Gindin, Ya. D. Starodubov, and V. K. Aksenov, Metallofizika **2**, 49 (1980).
[23] G. K. White, Cryogenics **2**, 292 (1962).
[24] W. L. McMillan, Phys. Rev. **167**, 331 (1968).
[25] R. Kuntzler, Phys. Lett. **104A**, 221 (1984).

Translated by R. S. Wadhwa

Nanostructure of superconducting Nb–Ti alloys

B. G. Lazarev, V. A. Ksenofontov, I. M. Mikhailovskii, and O. A. Velikodnaya

National Science Center ''Kharkov Physicotechnical Institute,'' 310108 Kharkov, Ukraine
(Submitted August 21, 1997; revised October 22, 1997)
Fiz. Nizk. Temp. **24**, 272–277 (March 1998)

The paper reports on the results of high-resolution field emission microscopy technique and its application for a qualitative analysis of the local chemical composition of superconducting Nb–Ti alloys. Previous investigations based on field ion microscopy revealed that a superconducting wire made of Nb–60 at. %Ti alloy contains thin and extended regions with a composition close to Nb, which form current-carrying paths with a density 4×10^{10} cm^{-2}. The formation of such zones is associated with rising diffusion occurring during thermal treatment and correlates with high critical currents. The development of the high-resolution field emission microscopy has made it possible to refine considerably in the present work the distribution of precipitated components and the configuration of the current-carrying system. The obtained results confirm that high current-carrying properties of Nb–Ti alloys are due to the presence of phases with a composition close to pure Nb precipitated as a result of thermomechanical treatment and forming a three-dimensional lattice of inclusions. © *1998 American Institute of Physics.* [S1063-777X(98)01003-2]

INTRODUCTION

The origin of a heterophase structure formed in deformed superconducting Nb-based alloys (Nb–Ti and Nb–Zr) during uphill diffusion, which was discovered and analyzed quantitatively in the theoretical work by Konobeevskii (see Ref. 1, p. 399) was discussed consistently in a series of our earlier publications over a long time. The concepts of current-carrying structure and the magnitude of the critical current in superconducting alloys are associated with the parameters of this structure. The evolution of the concentration of components in an alloy deformed during thermal treatment can be described by the equation

$$\partial c/\partial t = D_1 \partial^2 c/\partial x^2 - D_2 \partial^2 \varepsilon/\partial x^2, \tag{1}$$

in which the diffusion coefficient D_2 associated with the stress gradient is larger than the ordinary diffusion coefficient D_1 in Fick's equation by several orders of magnitude and is negative, and ε stands for strain.

For this reason, ''the diffusion occurring in a solid solution in the presence of a nonuniformly stressed state due to the second term in the equation leads not to levelling out of concentrations, but to the separation of components.'' [1] In other words, in our case of deformation by drawing a wire made of a superconducting alloy, diffusion leads to the formation of a well-developed thin and extended current-carrying Nb system in the alloy matrix. This structure was discovered by us by using various methods;[2–4] and its existence was demonstrated most convincingly in Refs. 3 and 4 on the basis of field ion microscopy in a Nb–60 at. %Ti alloy. It is expedient for subsequent analysis to consider here some of the results described in these publications.

Figure 1 shows a typical ion-microscopic pattern of a tip made of a thin wire subjected to final (optimal) thermal treatment at 400 °C for two hours. Light contrast spots correspond to precipitated phase rich in Nb. Statistical treatment of 1000 microphotographs of the samples led to a histogram of the relative transverse size distribution of precipitates (Fig. 2) with a peak corresponding to a diameter of 10–40 Å and a density of precipitates of $(4\pm1)\cdot10^{10}$ cm^{-2}. The experimental technique also allowed us to trace the evolution of the structure upon an increase in the annealing temperature from 200 to 550 °C and to compare it with the critical current variation with a peak at 400 °C. This corresponded to an increase in the size of precipitates to the optimal values, coagulation, and a decrease in their number. This information was used for obtaining quantitative results concerning the origin of high current-carrying structure of the material, i.e., typical sizes of the elements of this structure, their density, and the total cross-sectional area. In our opinion, such parameters are universal for all superconducting materials with high values of J_c and H_{c2}.

It should be noted that the methods developed by us showed graphically the ''filamentary'' extended precipitates of the nanometer size, which have the same crystal lattice (bcc) as the matrix and hence cannot be distinguished by an electron microscope. This remark is significant since (until recently) numerous publications[5–7] devoted to the synthesis of Nb-alloy-based superconducting materials with a high critical current density contain results obtained by using high-resolution electron microscopes, which are confined to a quantitative but essentially auxiliary tracking of the evolution of titanium precipitation without associating it with the formation of the basic Nb system during phase separation.

In our opinion, such experiments which disregard the main mechanism of rising diffusion do not provide much information on the origin of high critical currents in alloys.

A considerable advance in these studies was made when the quantitative distribution of Nb and Ti was determined in precipitates of phases found earlier (see Fig. 1). An atomic-

 © 1998 American Institute of Physics

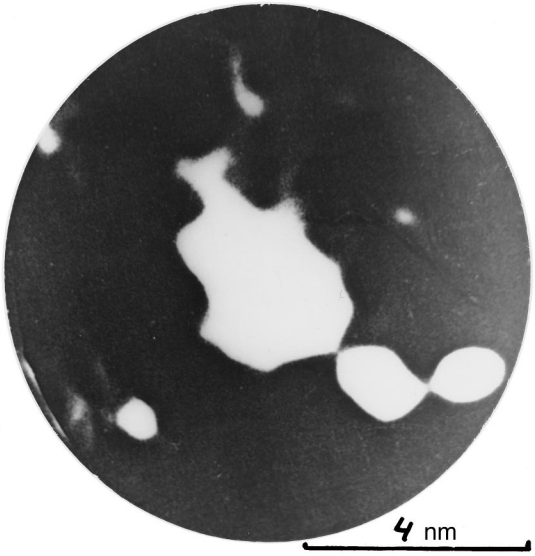

FIG. 1. Field ion-microscopic image of a Nb–Ti alloy.

scale analysis of the heterophase structure ensuring high critical current densities for superconducting alloys was carried out by using the methods of field (electron and ion) emission microscopy and mass spectrometry with a considerably reduced area (1×1 nm) and with a high resolution in phase concentration.

EXPERIMENTAL TECHNIQUE

Measurements were made on a two-chamber field emission microscope in which the samples were cooled to 21 K.[9] Image was formed by using hydrogen gas under a pressure of 10^{-4}–10^{-3} Pa. The microscope was evacuated by cryogenic pumps to a residual gas pressure of 10^{-7} Pa in the working chamber of the microscope.

In order to use the microscope in the field and electron modes, a constant positive voltage of 5–22 kV, and a varying voltage of amplitude 6–25 kV, and frequency 50 Hz was supplied to needle-shaped samples of diameter 20–140 nm. The application of a constant voltage ensured the operation of the microscope in the ion mode. The total voltage was of the pulse type. The ratio of the amplitudes of positive and negative voltages supplied to the sample varied from 7 to 12. The amplitude of negative voltage pulses of duration $(2-3)\times10^{-3}$ s was sufficient for creating on the sample surface a field strength corresponding to an electron current density of $10-10^3$ A/cm^2. In order to reduce the intensity of ionic bombardment of the surface during the removal of the field electron current, we used a microchannel amplifier of image brightness.

The local chemical composition was determined by using the field ion microscope with an atom probe allowing us to identify the chemical nature of individual atoms on the sample surface being evaporated. The operation principle of the instrument is similar to that described in Ref. 8. Evaporation of ions subjected to mass-spectroscopic analysis was implemented by a pulse generator with the front steepness of 20 ns and a pulse duration of 50 ns at a level of 0.7 the amplitude. The voltage pulse amplitude was varied smoothly from 1 to 15 kV. Evaporation occurred under the effect of the total voltage (a constant voltage of 5–20 kV required for the formation of the field ion voltage and a pulsed voltage). The signals generated by individual ions after the flight through the drift chamber were detected by a secondary electron multiplier, amplified by a wide-band amplifier, and fed to the input of the timer and the counting instrument.

For some samples, measurements were made in a vacuum of 10^{-4}–10^{-5} Pa. The surfaces of the samples were partly coated by residual gases in spite of the presence of a shielding positive electric field.[8] In order to reduce the errors of mass-spectroscopic analysis, we operated in a kinetic mode[9] realized with the help of a pulse pair generator. The first of high-voltage pulses was desorbing, while the second pulse was analyzing. The pause between the pulses varied from 10^{-5} to 10^{-4} s. The indicator block operated in the delay mode with a time-of-flight delay for desorbed ions, and detected only the spectrum of ions evaporated by the analyzing pulse. Experiments proved that a pause between pulses of 10^{-5} s is sufficient for ensuring a virtually absolute purity of the sample surface during the analysis. The exposure of the samples in the residual gas in this case varies from 10^{-6} to 10^{-5} Langmuir units, which corresponds to standard mass-spectrometric studies in ultrahigh vacuum.

The material of investigation was the same multiple-strand wire (1045 strands) made of Nb–60 at. %Ti superconducting alloy as that used in Ref. 4 and subjected to optimal thermal treatment at 400 °C for two hours. The diameter of superconducting strands was 15 μm. Prior to the preparation of sharp-tipped samples for emission microscopic experiments, the copper matrix was etched in nitric acid. This was followed by electrochemical polishing of filaments in the electrolyte $HNO_3(9)+HF(1)$ in a direct current of 4–8 A at 15 °C. Such a regime of polishing made it possible to avoid preferential etching of precipitates in the alloy.

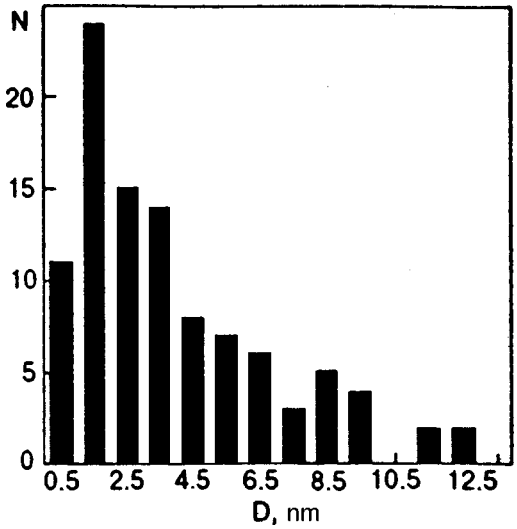

FIG. 2. Size distribution of precipitates enriched by Nb, constructed on the basis of ion-microscopy data.

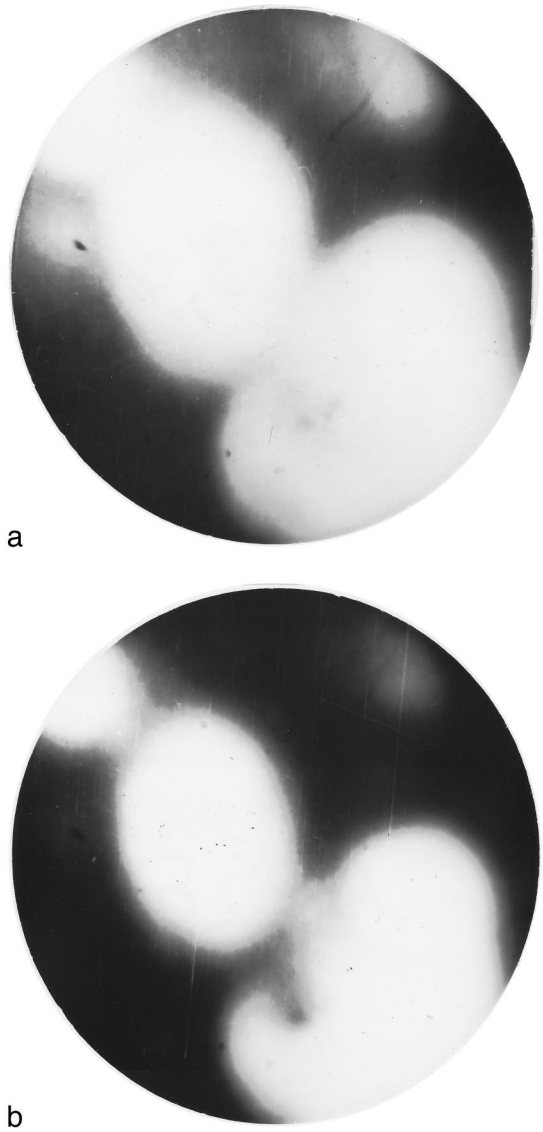

FIG. 3. Field electron-microscopic images of Nb–Ti alloy samples before (a) and after (b) field evaporation to a depth of 150 nm.

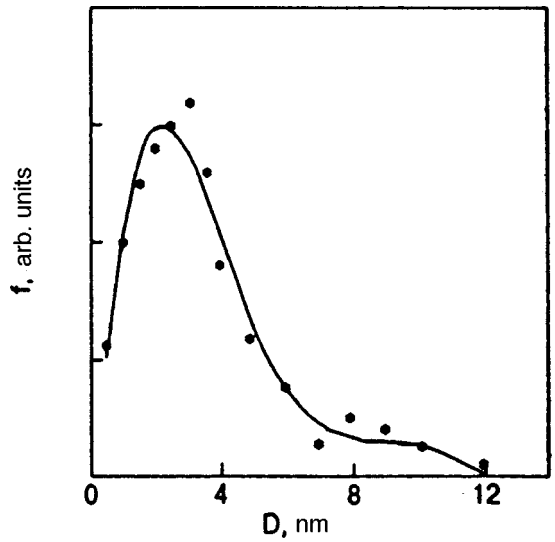

FIG. 4. Distribution of filamentary precipitates enriched by Nb over averaged diameters of cross section.

DISCUSSION OF RESULTS

Figures 1 and 3a and 3b show typical ionic and electronic images of Nb–Ti alloys respectively. Under the conditions of electron emission, large-scale contrast heterogeneities were observed on the surfaces of samples polished during low-temperature field evaporation in ultrahigh vacuum: regions with enhanced emissivity separated by distances of 5–30 nm could be singled out (see Fig. 3). The surface density of such regions, which was obtained as a result of treatment of 1000 microphotographs of various sample cross sections, amounted to $(6.0\pm2.0)\times10^{10}$ cm^{-2}. As in Ref. 4, an increase in the working voltage reduces the emission contrast. Some regions enriched with Ti and having the minimum emissivity were not processed on microphotographs. The electron-microscopic images presented in Fig. 3a and 3b were obtained at different stages of field evaporation. The microphotograph b was obtained after evaporation to a depth $\sim$150 nm. A comparison of microphotographs corresponding to different stages of processing of surface layers over their thickness shows that the position of most regions with an enhanced emissivity remains unchanged, indicating that precipitates singled out in the electron mode are stretched along the axis of the sample, and hence along the wire. Most of these precipitates has a nearly axisymmetric cross section, and their distribution correlates with the distribution of ion-microscopic contrast observed under stimulated field evaporation (see Fig. 1).

The use of a microanalyzer makes it possible to determine the average concentration of elements in cylindrical regions of diameter 1 nm and length 10–20 nm, analyzed during field evaporation. Before measurements, the sample was oriented so that the center of a brightly emitting region coincided with the probing aperture of the microanalyzer. Thus, the obtained results usually pertained to the central regions of precipitates enriched with Nb to within 1.5–2.0 nm. The maximum Nb concentration was 80 at. %. The niobium concentration decreased with increasing distance from the axis of the precipitate (in the course of field emission). Thus, the application of the combined method of field emission ion–electron microscopy provided a detailed information on the spatial distribution of elements in the alloy.

Considering that the electron work functions for niobium and titanium are approximately equal, while the energies of evaporation differ considerably,[8] we can conclude that brightly emitting regions correspond to the emergence of precipitates with a higher energy of field evaporation (enriched with Nb)[4] at the surface. Figure 4 shows the distribution of such precipitates over diameters of cross sections. Most filaments in the precipitate have a diameter ranging from 1.5 to 4.5 nm. The peak of the distribution lies near 2.5 nm. A comparison with the results presented in Ref. 4 shows that the sizes of precipitates obtained by the method of preferred field evaporation[8] are slightly underestimated. The microscopic images of Nb-enriched precipitates, which were obtained in one-chamber microscopes, have a comparatively high emission contrast. A possible reason behind this phe-

nomena is associated with processes of evaporation of Nb-enriched phases stimulated by residual gases and occurring under a relatively low vacuum typical of one-chamber microscopes. This effect is suppressed in two-chamber field emission microscopes used by us due to ultrahigh-vacuum conditions in the working chamber.

Precipitate phases are distributed nonuniformly over the sample cross section. The density of precipitates of the Nb-enriched phase varied from 3 to 20%; the calculated averaged value taking into account the difference in the probabilities of concentration values was 4.5%.

The methods of field electron microscopy of samples formed preliminarily by field evaporation allows us to determine the local energy of field evaporation and use it to calculate the concentration of elements. For example, the deviation of the Nb concentration C_{Nb} from the mean value $\overline{C}_{\mathrm{Nb}}$ can be determined from the relation

$$C_{\mathrm{Nb}}=\overline{C}_{\mathrm{Nb}}+(dQ/dC_{\mathrm{Nb}})^{-1}(Q-\overline{Q}), \tag{2}$$

where Q and $\overline{Q}$ are the local and mean values of field evaporation energy. In order to determine the value of Q, we can use the image force model[8] of field evaporation in the form of n-fold ionized atoms:

$$Q=(ne)^{3/2}F_i^{1/2}, \tag{3}$$

where F_i is the local value of electric field strength for activationless evaporation and e the electron charge. The average electric field strength $\overline{F_i}$ was determined from the field corresponding to the best image in hydrogen ions (22 V/nm).[8] The average value of the field strength for evaporation of the Nb–Ti alloy (40 at. %Nb) proved to be equal to 35 V/nm, the strength for evaporation of pure Nb was 40 V/nm, and $dQ/dC_{\mathrm{Nb}}=4.4\times10^{-2}$ eV/at. %. An analysis of the low-temperature evaporation spectra for the alloy on a field emission microanalyzer proved that more than 80% of Nb atom evaporate in the form of doubly charged ions ($n=2$).

Variations of the field strength F were determined from the displacement of constant brightness contours of field electron image (constant electron current density j_e) upon a change in the amplitude of negative pulses of high voltage. It follows directly from the Fowler–Nordheim relation[10] for the electron field emission in narrow field strength intervals that

$$dj_e/j_e=\kappa dF/F, \tag{4}$$

where κ is the electron emission field sensitivity, which varies in our experiments in the interval $15<\kappa<20$.

The high field sensitivity of electron emission has made it possible to determine (to within ~1 nm) the configuration of contours characterized by a constant evaporation field strength, and hence the evaporation energy and chemical composition.

Figure 5 shows the dependence of the Nb concentration on the distance from the precipitation center. It can be seen from the figure that the atomic concentration of niobium changes by 60 at. % over a segment of 3 nm width. The maximum value of concentration gradient (30 at. %/nm) is attained at a distance of 1.5 nm from the precipitation center.

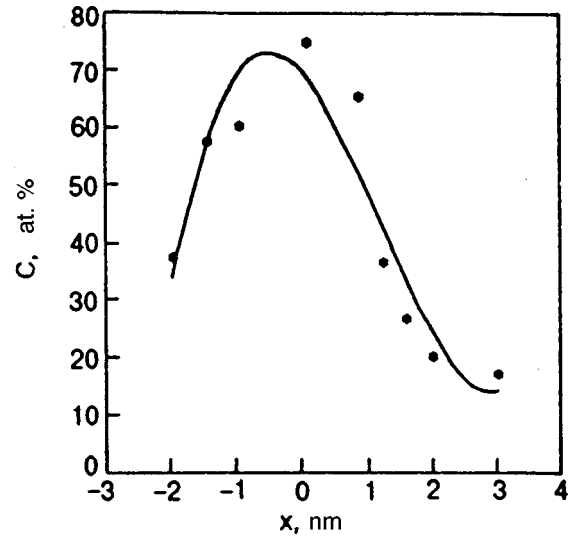

FIG. 5. Nb concentration as a function of the distance to the center of the precipitate.

CONCLUSION

In our previous works involving the application of the ion field microscopy in a superconducting wire made of the Nb–60 at. %Ti alloy, we detected thin (1–4 nm) extended (>100 nm) precipitates with a composition close to niobium and corresponding, according to modern concepts, to relevant current-carrying paths. Their formation was naturally associated with uphill diffusion occurring during thermal treatment after a strong plastic deformation and correlated with critical currents. The development of the high-resolution method of field emission microscopy in the present research resulted in a significant quantitative refinement of the form of distribution of precipitating components, i.e., in the construction of a map for the distribution of component concentrations over the conductor cross section. These results not only confirmed the pattern obtained by using the ion field microscopy, but also improved considerably the developed concepts concerning the nature of current-carrying capacity of superconducting alloys and allowed us to correct the technology of preparing superconducting materials.

This research was partly supported by the International Science Foundation.

[1] Ya. S. Umanskii, B. N. Finkelshtein, M. E. Blanter *et al.*, *Physical Foundations of Metal Science* [in Russian], Metallurgizdat, Moscow (1955).
[2] B. G. Lazarev, V. K. Khorenko, L. A. Kornienko *et al.*, Zh. Éksp. Teor. Fiz. **54**, 2068 (1963) [*sic*].
[3] R. I. Garber, B. G. Lazarev, L. S. Lazareva *et al.*, Zh. Éksp. Teor. Fiz. **63**, 1359 (1972) [Sov. Phys. JETP **36**, 718 (1972)].
[4] B. G. Lazarev, R. I. Garber, Zh. I. Dranova *et al.*, *Questions of Atomic Science and Technology, Ser. Fundamental and Applied Superconductivity* No. 1(5), 20 (1977).
[5] P. J. Lee and D. C. Larbalestier, Acta Metall. **35**, 2523 (1987).

[6] O. V. Chernyj, G. F. Tikhinskij, G. E. Storozhilov *et al.*, Supercond. Sci. Technol. **4**, 318 (1991).

[7] D. C. Larbalestier and P. J. Lee, *Paper TPEOI Presented at the 1995 Particle Accelerator Conference*, TPEOI (1995).

[8] M. Miller and G. Smith, *Atom Probe Microanalysis*, Mat. Res. Soc., Pittsburgh (1989).

[9] I. M. Mikhaĭlovskii, Zh. I. Dranova, V. A. Ksenofontov, and V. B. Kul'ko, Zh. Éksp. Teor. Fiz. **76**, 1309 (1979) [Sov. Phys. JETP **49**, 664 (1979)].

[10] A. Modinos, *Field, Thermionic and Secondary Electron Emission Spectroscopy*, Plenum Press, New York–London (1994).

Translated by R. S. Wadhwa

SHORT NOTES

Effect of impurities and external fields on second-harmonic generation in ceramics $YBa_2Cu_3O_{7-\delta}$ exposed to laser radiation

Ya. O. Dovhyj, I. V. Kityk, R. V. Lutciv, and S. Z. Malynych

I. Franko State University, 290602 L'vov, Ukraine
(Submitted July 14, 1997)
Fiz. Nizk. Temp. **24**, 278–280 (March 1998)

A single-mode picosecond YAG-Nd^{3+} laser ($P=30$ MW, $\lambda=1.06$ μm) is used to measure the reflected second-harmonic generation (SHG) in cerium-doped $YBa_2Cu_3O_{7-\delta}$ ceramics at low temperatures. An enhancement of the SHG signal is observed in the vicinity of T_c. Concentration variations of the effect are associated with the splitting near the van Hove singularities. The SHG signal is found to depend on the magnitude and direction of the external magnetic field. © *1998 American Institute of Physics.* [S1063-777X(98)01103-7]

The second-harmonic generation (SHG) was observed earlier in the centrally symmetric (space group $D_{2\mathbf{h}}^{17}$) HTS ceramics $YBa_2Cu_3O_{7-\delta}$.[1–4] In crystals having a center of inversion, nonlinear optical effects described by tensors of rank three are forbidden in the dipole approximation, since all components of the quadratic nonlinear optical susceptibility tensor are identically equal to zero in them. In this case, the SHG effect can emerge as a result of quadratic quadrupole polarization, or under the action of a constant external electric field.[5] However, this restriction on SHG in the dipole approximation may be removed in centrally symmetric media if the quadratic dipole polarization $P^{(2)}(2\omega)$ at the sample surface is taken into consideration. The existence of an interface leads to a lowering of symmetry and to the disappearance of the center of inversion in the symmetry group of the surface layer even for isotropic materials.[5] An analogous effect was also observed in semiconductors, e.g., in the system $SiO_2\backslash Si(111)$.[6]

The restriction on SHG can also be removed under a certain magnetic ordering. For example, SHG is observed in the antiferromagnetic tetragonal phase of $YBa_2Cu_3O_{7-\delta}$ owing to the existence of a magnetic structure associated with the ordering of copper ions Cu^{2+} with a spin $S=1/2$. This structure is described by ferro- and antiferromagnetism vectors (L_α, $\alpha=1,2,3$). The generation of second harmonic was also observed in the superconducting phase of $YBa_2Cu_3O_{7-\delta}$.[2,3,7] It was shown by Akhmanov *et al.*[2] that quadratic polarization is of dipole type.

A striking feature of the SHG signal is its significant temperature dependence. The signal sort of ''perceives'' the approach of the transition to the superconducting state.[7]

In this communication, we describe the results of investigations of the the ceramic $Y_{1-x}Ce_xBa_2Cu_3O_{7-\delta}$ ($x=0$; 0.05, 0.1, 0.2, 0.4). The ceramic was synthesized by solid-

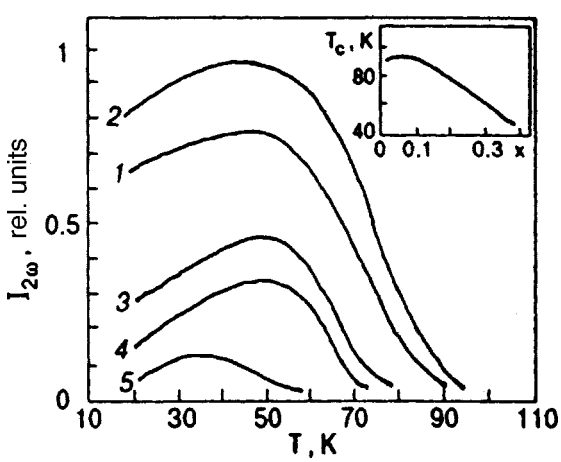

FIG. 1. Temperature dependence of the RSHG signal in doped ceramics: $YBa_2Cu_3O_{7-\delta}$ (*1*); $Y_{1-x}Ce_xBa_2Cu_3O_{7-\delta}$, $x=0.05$ (*2*); $Y_{1-x}Ce_xBa_2Cu_3O_{7-\delta}$, $x=0{,}1$ (*3*); $Y_{1-x}Ce_xBa_2Cu_3O_{7-\delta}$, $x=0{,}2$ (*4*); $YBa_{2-x}Ce_xCu_3O_{7-\delta}$, $x=0{,}4$ (*5*) The inset shows the dependence of the superconducting transition temperature on the extent of doping.

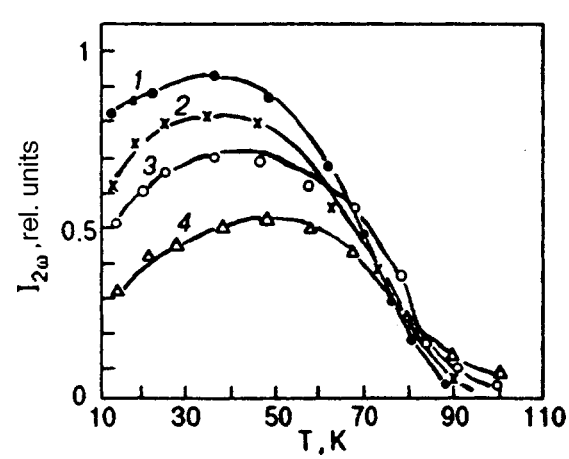

FIG. 2. Temperature dependence of the RSHG signal in the ceramic $YBa_2Cu_3O_{7-\delta}$ in an external electric field: $E=0$ (curve *1*); 2×10^4 V/m (curve *2*); 4×10^6 V/m (curve *3*), and 5×10^7 V/m (curve *4*).

 © 1998 American Institute of Physics

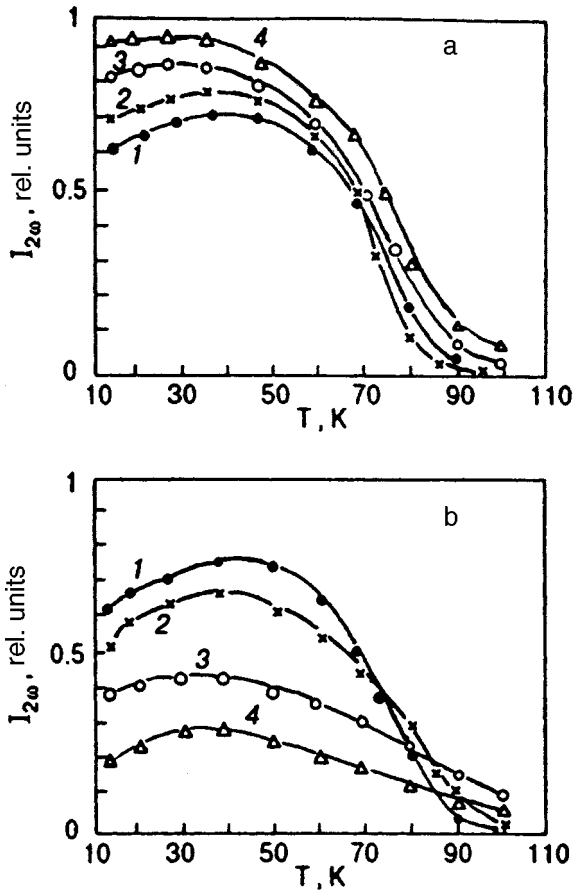

FIG. 3. Temperature dependence of the RSHG signal in the ceramic $YBa_2Cu_3O_{7-\delta}$ in an external magnetic field H parallel (a) and perpendicular to the sample surface (b): $H=0$ (curve *1*); $H=2$ (curve *2*); $H=5$ (curve *3*); and $H=8$ kOe (curve *4*).

phase reactions in oxygen flow at a temperature 1010 K from a mixture of components Y_2O_3, $BaCO_3$ and CuO with a doping of CeO_2 in stoichiometric proportions.

An unfocused beam of single-mode picosecond YAG-Nd^{3+} laser ($P=30$ MW, $\lambda=1.06$ μm) was used to excite the SHG. The angle of incidence was varied from 2 to 48° relative to the normal to the surface. The SHG signal was separated from the fundamental frequency radiation with the help of a monochromator ZMR-12 and was registered by a photomultiplier FEU-79. Measurements were made in the single-pulse mode with a pulse repetition frequency of 12 Hz. Samples were placed in a helium cryostat. The temperature was varied smoothly in the interval between 4.2 and 300 K with the help of the system *UTREKS*.

It was shown by us earlier[8] that the highest-intensity reflected SHG (RSHG) was observed by doping the ceramic $YBa_2Cu_3O_{7-\delta}$ with cerium. As the temperature is lowered and the superconducting transition is approached, the RSHG signal undergoes a characteristic enhancement. The correlation between the RSHG intensity and the superconducting transition temperature T_c is shown clearly in Fig. 1 for various samples. The effect is probably associated with local symmetry violation or with noncentral modulation. The latter may be due to superconducting pairing emerging in the vicinity of van Hove singularities owing to the Jahn–Teller band effect, and having a close connection with the emergence of phonon anharmonism.[9] In $YBa_2Cu_3O_{7-\delta}$ crystals, structural modulation may appear in oxygen-deficient planes.

The temperature dependences of the RSHG signal for an undoped ceramic in external electric and magnetic fields are shown in Figs. 2 and 3. The application of a magnetic field parallel to the sample surface enhances the effect, while a field applied at right angles to the sample surface suppresses the signal at a frequency 2ω. This is in qualitative agreement with the results obtained by Lyubchanskii[10] who explained the SHG effect by taking into account the nonuniform magnetoelectric effect associated with the presence of domain boundaries.

Thus, the nonlinear optics methods can be used for contactless diagnostics of high-temperature superconductors. A conclusive explanation of the SHG effects for these materials will probably provide an understanding of the very mechanism of high-temperature superconductivity.

[1] S. V. Borisov, I. L. Lyubchanskii, and V. L. Sobolev, Fiz. Tverd. Tela (Leningrad) **31**, 158 (1989) [*sic*].
[2] S. A. Akhmanov, S. V. Govorkov, N. I. Koroteev *et al.*, Izv. Akad. Nauk SSSR **53**, 762 (1989) [*sic*].
[3] J. K. Rice, S. W. McCaluey, A. P. Baronawski *et al.*, Phys. Rev. B **47**, 6086 (1993).
[4] V. V. Rumyantsev and V. T. Shunyakov, Izv. Ros. Akad. Nauk, Ser. Fiz. **56**, 178 (1992) [*sic*].
[5] I. R. Shen, *Principles of Nonlinear Optics* [in Russian], Nauka, Moscow (1989).
[6] F. Ito and H. Hirayama, Phys. Rev. B **50**, 11208 (1994).
[7] Ya. O. Dovhyj, I. V. Kityk, R. V. Lutciv, and S. Z. Malynych, in Proceedings of Int. School Conference ''Solid State Physics: Fundamentals and Applications,'' Uzhgorod, Sept. 18–26, 1995.
[8] Ya. O. Dovhyj, I. V. Kityk, R. V. Lutciv, and S. Z. Malynych, in Proceedings of I Int. Conference ''HTS Materials Science,'' Kharkov, April 5–9, 1993.
[9] R. S. Markiewicz, J. Phys. Chem. Solids **52**, 1363 (1991).
[10] I. L. Lyubchanskii, Fiz. Tverd. Tela (St. Petersburg) **37**, 1812 (1995) [Phys. Solid State **37**, 987 (1995)].

Translated by R. S. Wadhwa

LETTERS TO THE EDITOR

Light-induced optical absorption in the garnet $Ca_3Mn_2Ge_3O_{12}$

V. A. Bedarev and S. L. Gnatchenko

*B. Verkin Institute for Low Temperature Physics and Engineering, National Academy of Sciences of Ukraine, Lenin ave. 47, 310164, Kharkov, Ukraine**

R. A. Rupp

*Vienna University, A-1090 Vienna, Strudlhofgasse 4, Austria***

B. Sugg

University of Osnabrueck, D-49069 Osnabrueck, Barbarastrasse 7, Germany
(Submitted November 18, 1997)
Fiz. Nizk. Temp. **24**, 281–283 (March 1998)

Light-induced change in the optical absorption of the garnet $Ca_3Mn_2Ge_3O_{12}$ has been found. The magnitude of the light-induced optical absorption does not depend on the polarization state of the exciting illumination. The effect persists for a long time at low temperatures and can be attributed to light-induced generation or redistribution of Mn^{4+} ions in the crystal. © *1998 American Institute of Physics.* [S1063-777X(98)01203-1]

Photoinduced effects occurring in dielectric crystals, in particular, in yttrium iron garnet, may be classified according to whether they depend on the polarization state of the exciting light or not. Different physical mechanisms are responsible for the first and second type of photoinduced effects.[1]

Until now, only photoinduced effects depending on the polarization state of the exciting irradiation were reported for the garnet $Ca_3Mn_2Ge_3O_{12}$. Illumination with linearly polarized light changes the optical anisotropy[2–5] and influences the process of magnetization reversal of the sublattices induced in the antiferromagnetic state by a magnetic field.[6,7]

In the present paper we report the results of an experimental observation of a photoinduced effect in calcium manganese germanium garnet (CaMnGeG), which is independent of the polarization state, namely, light-induced optical absorption (LIOA).

The effect of illumination on the optical absorption of CaMnGeG was studied with use of an optical double-beam setup. The beam of the He-Ne laser with the wavelength $\lambda = 633$ nm and a power of several milliwatts was split into two beams. The sample was irradiated by the first beam, which served at the same time as a transmission probe, while the second beam passed by the sample. Each beam was chopped alternatingly with a frequency of about 170 Hz by means of a mechanical modulator and hit the photocathode of a photoelectric multiplier. At the beginning, the intensity of the second beam was adjusted to the same intensity as one of the beams that passed through the sample. As the transmission of the sample changed under illumination, the intensity of the first beam also changed and an alternating electric signal appeared at the photoelectric multiplier. This signal is proportional to the change in the transmission of the sample. It was measured by means of a lock-in amplifier.

The sample, a plate of thickness $d \approx 130$ μm, was cut from a single crystal of CaMnGeG, which was polished mechanically and annealed at a temperature of approximately 1 000 °C to relax the internal stresses which appeared during polishing. At the temperature $T \approx 520$ K a twin domain structure arises in CaMnGeG because of a Jahn-Teller phase transition from the cubic to the tetragonal state.[8–10] Therefore, a thermal treatment[9] is needed to increase the average size of the domains in the sample to approximately 1 mm^2. A special sample holder with a diaphragm was used to select a single-domain region of the sample. The measured beam passed through a domain in which the tetragonal c axis was perpendicular to the plate; i.e., the measurements of the LIOA were carried out for a sample cut perpendicularly to the tetragonal axis. The sample was immersed into a helium cryostat in a vacuum.

The light-induced variation in the transmission of CaMnGeG was measured as a function of the illumination time. The curves which were measured at several temperatures are shown in Fig. 1, where ΔI is the change in intensity of the transmitted light as a result of the illumination of the crystal, and I is the intensity of the transmitted light measured at the beginning of the illumination of the sample. The measurements show that illumination increases the optical absorption of CaMnGeG.

As the optical absorption of CaMnGeG increases with increasing temperature, too,[11] it is necessary to separate the genuine LIOA from the increase in the optical absorption due to heating of the sample under illumination. For this purpose the change in the temperature of the sample under illumination was determined from the known temperature dependence of the linear birefringence,[9] using a domain with

 © 1998 American Institute of Physics

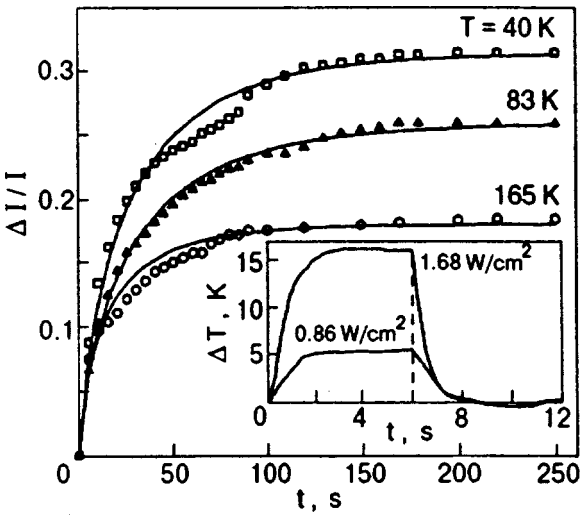

FIG. 1. Change of the optical transmission as a function of the time of illumination measured for the garnet $Ca_3Mn_2Ge_3O_{12}$ at temperatures $T = 40$, 83, and 165 K ($I = 0.16$ W/cm^2, $\lambda = 633$ nm, $d \approx 130$ mm). The inset shows the time dependences of the temperature change of the sample at $I = 0.86$ and 1.68 W/cm^2.

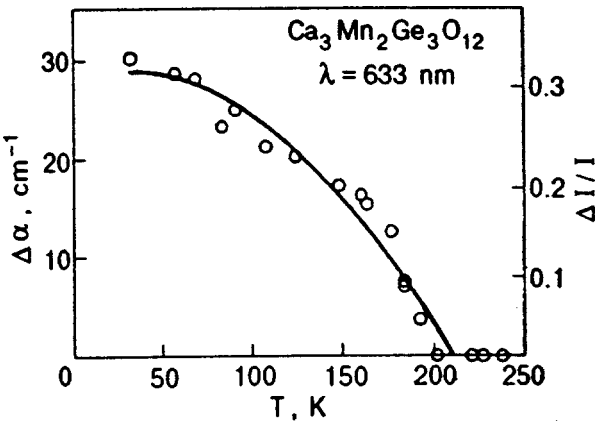

FIG. 2. Temperature dependence of the saturation value of the light-induced optical absorption for the garnet $Ca_3Mn_2Ge_3O_{12}$.

the c axis in the plane of the sample. The measurements were carried out at an initial temperature of the sample (before illumination) of $T = 200$ K, because there is no photoinduced linear birefringence above a temperature of 180 K (Refs. 2–5). The time dependences of the sample temperature are shown in the inset in Fig. 1 for heating of the sample during illumination and for cooling after the illumination is switched off. The curves were measured for an intensity of 1.68 and 0.86 W/cm^2, respectively. As can be seen from a comparison of the dependences shown in Fig. 1 and in the inset in Fig. 1, the time constants for heating and thermal relaxation are much smaller than the time constants for induction and relaxation of LIOA. Measurements of the change in birefringence as a result of illumination at low temperatures allow us to conclude that the time constants for heating and thermal relaxation remain approximately the same, and that heating of the sample by light increases insignificantly. The large difference between the two processes allows us to separate them unambiguously. Furthermore, the measurements of LIOA were carried out at a much lower intensity, 0.16 W/cm^2. In this case the increase in the temperature of the sample under illumination was less than 1 K and the change in the optical absorption caused by heating of the sample was not essential.

As can be seen from Fig. 1, the saturation value of the LIOA depends on temperature. The temperature dependence of the light-induced change of the transmission of CaMnGeG, measured after reaching saturation, is shown in Fig. 2. The light-induced change in the optical absorption coefficient was calculated using the relation

$$\Delta\alpha = -[\ln(1 - \Delta I/I)]/d$$

and is also plotted in Fig. 2 as a function of temperature. The change in the absorption coefficient under illumination reaches a value of about 30 cm^{-1} at a low temperature but decreases with increasing temperature. LIOA is not observed above $T = 200$ K. It should be noted that the photoinduced linear birefringence in CaMnGeG disappears at $T = 180$ K (Refs. 2–5).

The saturation value of the LIOA is approximately the same for illumination of the crystal with linearly and circularly polarized light as well as unpolarized light. Hence, the magnitude of the LIOA does not depend on the polarization of the inducing light.

The most probable cause for the change in the optical absorption of CaMnGeG under illumination is the generation of Mn^{4+} ions due to optically induced transfer of electrons from Mn^{3+} ions to traps (photodoping). In accordance with Refs. 12 and 13, Mn^{4+} ions can be located in the octahadral positions in CaMnGeG. The local octahedral oxygen surrounding of the Mn^{4+} ion in $Ca_3Mn_2Ge_3O_{12}$ differs from that of the Mn^{3+} ion, because the Mn^{4+} ion has an orbitally nondegenerate ground state, and because it is not a Jahn-Teller ion. Local distortions and stresses of crystal lattices should accompany an appearing of Mn^{4+} ions in CaMnGeG. The Mn^{4+} ions placed within the changed oxygen octahedra in the lattice of CaMnGeG can be the light-induced absorption centers, which are responsible for the increase of absorption. It is known that Mn^{4+} ions in the octahedral position of the garnet lattice (e.g., in the garnet $Ca_3Ga_2Ge_3O_{12}$:Mn) have absorption bands in the visible range of the optical spectra.[14] The optical absorption can also increase due to charge transfer transitions between Mn^{3+} and Mn^{4+} ions.

A further conceivable mechanism is the change in the optical absorption of CaMnGeG by light-induced redistribution among already existing Mn^{4+} in the crystal. A similar model was proposed for the explanation of LIOA in the garnet $Y_3Fe_5O_{12}$.[15,16] The photoinduced change of the optical absorption in this garnet was interpreted in terms of different properties of Fe^{2+} and Fe^{4+} ions at the sites that are near and far from an impurity ion or a vacancy. The compensation for the electrical charge of the Mn^{4+} ions is accomplished by vacancies of Ge^{4+} ions in the crystal.[12,13] If it is assumed that the optical properties of Mn^{4+} ions differ at the sites that are near and far from Ge vacancies, then the optical absorption of CaMnGeG can change as a result of the light-induced

redistribution of these ions between the sites near and far from the vacancies.

We wish to thank Dr. J.-M. Desvignes (CNRS Laboratoire de Physique des Solides, Meudon-Bellevue, France) for providing $Ca_3Mn_2Ge_3O_{12}$ single crystals. This work was supported in part by the Volkswagen-Stiftung I/70980.

*E-mail: gnatchenko@ilt.kharkov.ua
**E-mail: rrupp@pap.univie.ac.at

[1] V. F. Kovalenko and E. L. Nagaev, Usp. Fiz. Nauk **148**, 561 (1986) [Sov. Phys. Usp. **29**, 297 (1986)].
[2] S. L. Gnatchenko, V. V. Eremenko, S. V. Sofroneev, and N. F. Kharchenko, Pis'ma Zh. Éksp. Teor. Fiz. **38**, 198 (1983) [JETP Lett. **38**, 233 (1983)].
[3] S. L. Gnatchenko, N. F. Kharchenko, V. A. Bedarev, V. V. Eremenko, M. Artinian, J.-M. Desvignes, and H. Le Gall, Fiz. Nizk. Temp **15**, 627 (1989) [Sov. J. Low Temp. Phys. **15**, 353 (1989)].
[4] V. A. Bedarev and S. L. Gnatchenko, Fiz. Nizk. Temp **20**, 124 (1994) [Low Temp. Phys. **20**, 100 (1994)].
[5] B. Sugg, S. L. Gnatchenko, and R. A. Rupp, J. Opt. Soc. Am. B **13**, 2670 (1996).
[6] N. F. Kharchenko and V. A. Bedarev, Piz'ma Zh. Éksp. Teor. Fiz **56**, 360 (1992) [JETP Lett. **56**, 345 (1992)].
[7] N. F. Kharchenko and V. A. Bedarev, Fiz. Nizk. Temp. **19**, 72 (1993) [Low Temp. Phys. **19**, 52 (1993)].
[8] Z. A. Kazei, P. Novak, and V. I. Sokolov, Zh. Éksp. Teor. Fiz. **83**, 1483 (1982) [Sov. Phys. JETP **56**, 854 (1982)].
[9] S. L. Gnatchenko, V. V. Eremenko, S. V. Sofroneev, N. F. Kharchenko, J.-M. Desvignes, P. Feldmann, and H. Le Gall, Zh. Éksp. Teor. Fiz. **90** 179 (1986) [Sov. Phys. JETP **63**, 102 (1986)].
[10] W. Graeff, J. Kub, and K. Wieteska, Phys. Status Solidi A **126**, 477 (1991).
[11] B. Sugg, S. L. Gnatchenko, B. Faust, and R. A. Rupp, Appl. Phys. Lett. **67**, 766 (1995).
[12] A. E. Nosenko, V. A. Padlyak, and V. V. Kravchishin, Fiz. Tverd. Tela **27**, 3455 (1985) [Sov. Phys. Solid State **27**, 2083 (1985)].
[13] V. A. Padlyak and A. E. Nosenko, Fiz. Tverd. Tela **30**, 1788 (1988) [Sov. Phys. Solid State **30**, 1027 (1988)].
[14] A. E. Nosenko, A. P. Abramov, L. V. Kostyk, A. I. Bily, and V. V. Kravchishin, Opt. Spectrosc. **61**, 1037 (1986).
[15] E. M. Georgy, J. E. Dillon, and J. P. Remeika, J. Appl. Phys. **42**, 1454 (1971).
[16] K. Hisatake, I. Matsubara, K. Maeda, H. Yasuoka, H. Mazaki, and K. Vematsu, J. Magn. Magn. Mater. **140–144**, 2127 (1995).

This article was published in English in the original Russian journal. It was edited by S. J. Amoretty.

CHRONICLE

2nd International Conference on Cryocrystals and Quantum Crystals (CRYOCRYSTALS'97) (Wroclaw, Poland; Sept. 7–12, 1997)

E. S. Syrkin

*B. Verkin Institute for Low Temperature Physics and Engineering, National Academy of Sciences of the Ukraine, 310164 Kharkov, Ukraine**

(Submitted October 21, 1997)
Fiz. Nizk. Temp. **24**, 284–287 (March 1998)

[S1063-777X(98)01303-6]

The 2nd International Conference on Cryocrystals and Quantum Crystals (CRYOCRYSTALS'97) was held from September 7 to 12, 1997 in Polanica-Zdroj near the city of Wroclaw, Poland. The conference was organized by the Institute of Low Temperatures and Structural Transformations, Polish Academy of Sciences, and the Institute of Physical and Theoretical Chemistry of the Wroclaw Technical University in collaboration with the Polish Physical Society.

The term ''cryocrystals,'' which was introduced by the famous Ukrainian physicist Academician Antonina Fedorovna Prikhot'ko in the early sixties, is widely used at present in the world literature to represent a special group of solids including atomic and molecular quantum crystals (^{3}He, ^{4}He, H_2, D_2, CH_4), solidified inert gases (Ne, Ar, Kr, Xe), as well as simplest molecular crystals (N_2, CO, O_2, CO_2, N_2O, etc.). The introduction of a common term to emphasize the close similarity between the physical properties of such objects turned out to be extremely fruitful.

The first International Conference ''CRYOCRYSTALS'95'' was held in 1995 in Alma-Aty (Kazakhstan). The conference proceedings were published in the journal ''Low Temperature Physics'' (No. 2, Vol. 22) in 1996. This conference was a continuation of the tradition of conferences on the physics of cryocrystals held regularly in the former Soviet Union since 1979. Eight such conferences were held before this (Viljandi, Estonia, 1979; Kharkov, Ukraine, 1981; Donetsk, Ukraine, 1983 and 1985; Odessa, Ukraine, 1987; Alma-Aty, Kazakhstan, 1989; and Donetsk, Ukraine, 1991 and 1993).

Thus, the conference held in Poland was in fact the tenth (Jubilee) conference in the series. Considerable attention was paid in the materials of the conference not only to the traditional $3D$ objects, but also to various problems of $2D$ cryocrystals, the structure and properties of microcrystallites, spectroscopy of cryocrystals, matrix isolation in cryocrystals, molecular cryocrystals under high and ultrahigh pressures, atoms and ions in cryocrystals, technological applications, etc.

Forty six oral communications were presented at the conference in addition to about fifty papers displayed at poster sections.

The following works were presented at the 2nd International Conference ''CRYOCRYSTALS'97:''

INVITED LECTURES

1. Russell J. Hemley (Geophysical Laboratory and Center for High-Pressure Research, Carnegie Institution of Washington, 5251 Broad Branch Rd., NW, Washington, DC 20015-1305, USA; e-mail: hemley@gl.ciw.edu) ''Hydrogen atoms at ultrahigh pressures: H_2, H_2O, and low-z compounds.''

2. Jon H. Eggert, Eran Karmon, Alexander Goncharov, Russell J. Hemley, Ho-kwang Mao (Department of Physics, Colorado School of Mines Golden, CO 8041, USA; e-mail: jeggert@state.mines.edu) ''High-pressure hydrogen results on ortho-para conversion.''

3. A. B. Harris (University of Pennsylvania, Philadelphia, USA; e-mail: harris@physics.upenn.edu), H. Meyer (Duke University, e-mail: hm@phy.duke.edu) ''NMR in solid deuterium: a review.''

4. Tetsuo Miyazaki (Department of Applied Chemistry, School Engineering, Nagoya University, Furo-cho, Chikusa-ku, Nagoya 464-01, Japan; e-mail: miyamiya@apchem.nagoya-u.ac.jp), Takayuki Kumada (Japan Atomic Energy Research Institute), Naoki Kitagawa (Nagoya University), Kenji Komaguchi, and Yasuyuki Aratono (Japan Atomic Energy Research Institute) ''Quantum tunneling of D(H) atoms and H_2^- anions in solid hydrogen.''

5. Paul Leiderer (Fakultät für Physik, Universität Konstanz, D-78434 Konstanz, Germany; e-mail: paul.leiderer@uni-konstanz.de) ''On the Van der Waals-interaction in cryocrystals.''

6. J. A. Schouten (Van der Waals-Zeeman Institute, University of Amsterdam, Valckenierstraat 67, 1018 XE Amsterdam, The Netherlands; e-mail: schouten@phys.uva.nl) ''Disorder in N_2 and the mixed solid N_2-Ar; experiment and computer simulations.''

7. Robert O. Pohl (Cornell University, Department of Physics, Ithaca NY, USA; e-mail: pohl@msc.cornell.edu) ''Elastic properties of films of water ice and noble gases.''

8. A. van der Avoird (Institute of Theoretical Chemistry, University of Nijmegen, Nijmegen, The Netherlands; e-mail:

 © 1998 American Institute of Physics

avda@theochem.kun.nl) ''Dynamics of CO molecules trapped in solid C_{60}: theory, infrared and NMR spectra.''

9. V. G. Manzhelii, M. I. Bagatskii, I. Ya. Minchina, and N. A. Aleksandrovskii (B. Verkin Institute for Low Temperature Physics and Engineering, National Academy of Sciences of Ukraine, 47, Lenin Ave., 310164, Kharkov, Ukraine; e-mail: manzhelii@ilt.kharkov.ua) ''Thermodynamic properties of molecular orientational glasses with indirect interaction.''

10. F. J. Bermejo, A. de Bernabe, and J. L. Martinez (Consejo Superior de Investigationes Cientificas, Serrano 123, E-28006, Madrid, Spain; e-mail: embermejo@iem.csic.es), S. F. Cox (ISIS Pulsed Muon Facility, Rutherford Appleton Laboratory, Chilton, Didcot, Oxon, OX11 OQX and Department of Physics & Astronomy, University College London, Gower St., London WC1E 6BT, UK) ''Magnetic dynamics in condensed molecular oxygen: an overview of recent results.''

11. F. Dunstetter (Marie-Noelle de Noirfontaine, Ecole Polytechnique, Laboratoire des Solides Irradies, 91128 PALAISEAU; e-mail: mndn@hp1sesi.polytechnique.fr) ''Molecular dynamics simulation of the plastic phase of oxygen. Comparison with diffuse neutron scattering.''

12. Hector E. Lorenzana, William J. Evans, and Magnus Lipp (Lawrence Livermore National Laboratory Livermore, CA 94551, USA; e-mail: hector.lorenzana@quickmail.llnl.gov) ''Properties of nitrogen and carbon monoxide at high pressures.''

13. G. Frossati (Kamerlingh Onnes Laboratory, Leiden University, Nieuwsteeg, 18, NE 2311 VZ, Leiden, The Netherlands; e-mail: giorgio@qv3pluto.leidenuniv.nl) ''Polarization of ^{3}He, D_2 and (eventually) ^{129}Xe using low temperatures and high magnetic fields.''

14. V. G. Storchak (Russian Science Center ''Kurchatov Institute,'' Kurchatov square, 1, Moscow, 123182, Russia; e-mail: storchak@chen.net.kiae.su; mussr@triumf.ca), J. H. Brewer (Canadian Institute for Advanced Research and Department of Physics, University of British Columbia, Vancouver, B. C., Canada V6T 2A3; e-mail: msr@triumf.ca), S. F. J. Cox (Rutherford Appleton Laboratory, Chilton, Oxfordshire OX11 OQX, UK; e-mail: sfrjc@isise.rl.ac.uk) ''Quantum diffusion in cryocrystals studied by muon spin relaxation.''

15. Richard D. Etters (Colorado State University, Fort Collins, Colorado 80523, USA; e-mail: etters@alamar.colostate.edu), Bogdan Kuchta (Institute of Physical and Theoretical Chemistry, Technical University of Wroclaw, Poland; e-mail: kuchta@kchf.ch.pwr.wroc.pl) ''The character of melting for simple molecules deposited on graphite.''

16. J. D. Close, F. Federmann, K. Hoffman, and N. Quaas (Max Planck Institut für Strömungsforschung, Bunsenstra[dS]e, 10, D-37073 Göttingen, Germany; e-mail: jclose@gwdg.de) ''Helium droplets: a nanoscale cryostat for synthesis of advanced materials, high resolution spectroscopy, and studies of quantized vorticity.''

17. N. S. Sullivan and Kiho Kim (Department of Physics, University of Florida, Gainesville, FL 32611-8440, USA; e-mail: sullivan@phys.ufl.edu ''New phases for the orientational ordering of quantum rotors: H_2 on hexagonal BN.''

18. Henri Dubost (Laboratoire de Photophysique Moléculaire CNRS Batiment 210-Université de Paris-Sud-91405 ORSAY CEDEX, France; ''Picosecond to minute molecular vibration dynamics in cryosolids.''

19. G. Zimmerer (University of Hamburg, 11. Institute of Experimental Physics, Luruper Chaussee 149, D-22761 Hamburg, Germany; e-mail: zimmerer@vxdesy.desy.de) ''Hot photo-carriers, excitons, desorption, and surface diffusion in rare gas solids.''

20. K. S. Song (Department of Physics, University of Ottawa, Ottawa, Ontario, Canada K1N6N5; e-mail: song@joule.physics.uottawa.ca) ''Exciton self-trapping and lattice defect creation in rare gas solids and other insulations.''

21. M. Le Cointe-Buron, M. H. Lémee-Cailleau, and H. Cailleau (Groupe Matiere Condensée et Materiaux, UMR 6626 CNRS-Univ. Rennes 1, Rennes, France; e-mail: lecointe@univ-rennes1.fr; mhlemee@univ-rennes1.fr; cailleau@univ-rennes1.fr), T. Luty (Institute of Physical and Theoretical Chemistry, Technical University Wroclaw, Poland; e-mail: luty@kchf.ch.pwr.wroc.pl) ''Condensation of self-trapped charge-transfer excitations and interplay between quantum and thermal effects at the neutral-to-ionic transition.''

SELECTED LECTURES

1. Hitose Nagara and Kazutaka Nagao (Osaka University, Department of Material Physics, Faculty of Engineering Science, Toyonaka, Osaka 560, Japan; e-mail: nagara@mp.es.osaka-u.ac.jp; nagao @hbar.mp.es.osaka-u.ac.jp) ''Vibrons and phonons in solid hydrogen at megabar pressures.''

2. Valeri Shevtsov (Russia Research Center ''Kurchatov Institute,'' 123182 Moscow, Russia; e-mail: vash@orc.ru), Pekka Malmi, Eero Ylinen, and Matti Punkkinen (Wihuri Physical Laboratory, University of Turku, FIN20014, Turku, Finland; e-mail: matpun@utu.fi) ''The conversion and diffusion of ortho-H_2 molecules in solid hydrogen.''

3. Takamasa Momose (Division of Chemistry, Graduate School of Science, Kyoto University, Kyoto 606.01, Japan; e-mail: momose@kuchem.kyoto-u.ac.jp) ''Impurity molecules in parahydrogen crystal; high resolution infrared spectroscopy.''

4. V. B. Kokshenev (Department of Physics, State University of Minas Gerais (UFMG), ICEx, C. P. 702, CEP 30161-970, MG, Brazil; e-mail: valery @oraculo.lcc.ufmg.br) ''Intrinsic-field cooperative freezing into the orientational glass phase in solid hydrogen. Theory and experiment.''

5. Alfred Huller (Institute für Theoretische Physik 1, Universität Erlangen, Staudtstr. 7B, D-91058 Erlangen, Germany; e-mail: alfred.hueller@physik.uni-erlangen.de) ''Quantum mechanical simulations of molecular rotations in crystals at finite temperatures.''

6. K. Knorr (Technische Physik, Universität des Saarlandes, Saarbrücken, Germany; e-mail: knorr@rz.uni-sb.de)

''Phase diagrams and structures of monolayers of C_2F_6 and some related molecules physisorbed on graphite.''

7. Yu. A. Freiman and S. Tretyak (B. Verkin Institute for Low Temperature Physics and Engineering, 47 Lenin Ave., 310164, Kharkov, Ukraine; e-mail: freiman@ilt.kharkov.ua), Andrzej Jezowski (W. Trzebiatowski Institute for Low Temperatures and Structural Research Polish Acad. Sci., P. O. Box 937, 50-590 Wroclaw-2, Poland; e-mail: anje@int.pan.wroc.pl) ''On theory of the phase transitions in solid hydrogen under pressure. Reentrant behavior and critical points.''

8. A. A. Solodovnik and M. A. Strzhemechny (B. Verkin Institute for Low Temperature Physics and Engineering, 47 Lenin Ave., 310164, Kharkov, Ukraine; e-mail: strzhemechny@ilt.kharkov.ua) ''CO_2-Ar alloys: structure and orientational order.''

9. C. Seyfert, H. Sinn, and E. Burkel (FB PHYSIK, Universität Rostock, August-Bebel-Str., 55, 18055 Rostock, Germany; e-mail: seyfert@desy.de; sinn@desy.de; burkel@villa.physik1.uni-rostock.de), D. A. Arms and R. O. Simmons (Department of Physics, University of Illinois, Urbana-Champaign, IL 61801, USA; e-mail: dohnarms@aps.anl.gov; ros@uiuc.edu) ''First determination of the phonon dispersion relation in hcp helium-3.''

10. N. Mikhin, V. Shvarts, and E. Rudavskii (B. Verkin Institute for Low Temperature Physics and Engineering, National Academy of Sciences, 47 Lenin Ave., 310164 Kharkov, Ukraine; e-mail: mikhin@ilt.kharkov.ua) ''Growth kinetics of bcc ^{3}He phase in separating hcp ^{3}He-^{4}He mixture.''

11. Horst Wiechert (Institut für Physik, Johannes Gutenberg-Universität, D-55099 Mainz, Germany; e-mail: wiechert@mzdmza.zdv.uni-mainz.de) ''Ordering and phase transitions in deiterium monolayers physisorbed on krypton preplated graphite.''

12. E. B. Gordon (Institute of Energy Problems of Chemical Physics, Russian Academy of Sciences, 142432, Chernogolovka, Moscow Region, Russia; e-mail: gordon@binep.ac.ru) ''Impurity nanosuspension in liquid helium.''

13. G. Weiss and K. Eschenroder (Universität Karlsruhe, Physikalisches Institut, Germany; e-mail: georg.weiss@phys.uni-karlsruhe.de; klaus.escheroeder @phys.uni-karlsruhe.de), J. Classen and S. Hunklinger (Universität Heidelberg, Institut für Angewandte Physik, Germany; e-mail: classen@urz.uni-heidelberg.de; hunklinger@urz.uni-heidelberg.de) ''Ultrasonic measurements on quench-condensed noble gas films.''

14. L. P. Mezhov-Deglin, A. A. Levchenko, and A. B. Trusov (Laboratory of Quantum Crystals, Institute of Solid State Physics, RAS 142432, Chernogolovka, Moscow distr., Russia; e-mail: mezhov@issp.ac.ru) ''Charges and vacancies in hcp crystals of p-H_2, D_2, and ^{4}He.''

15. M. Bienfait and J. M. Gay (CRMSC@-CNRS, Case 901, Campus de Luminy, 132288 Marseille, France; e-mail: beinfait@crmc2.univ-mrs.fr), P. Zeppenfeld (Johannes-Kepler-Universität, Inst. für Physik, A-4040 Linz, Austria; e-mail: zeppenfeld@exphys.uni-linz.ac.at), O. E. Vilches (Department of Physics, University of Washington, Seattle, WA 98195-1560, USA; e-mail: vilches @dirac.phys.washington.edu), I. Mirebeau (Laboratoire Leon Brillouin, CEA Saclay, 91191 Gif-sur-Yvette, France; H. J. Lauter (Institute Laue-Langevin, B. P. 156, 38042 Grenoble, France) ''Isotopic ordering in adsorbed hydrogen single layers.''

16. E. V. Savchenko (B. Verkin Institute for Low Temperature Physics and Engineering, 47 Lenin Ave., 310164, Kharkov, Ukraine; e-mail: savchenko@ilt.kharkov.ua), N. Caspary, A. Lammers, and V. E. Bondybey (Institut für Physikalishe und Theoretische Chemie der TU Munchen Lichtenbergstrasse 4, 85747 Garching, Germany) ''Spectroscopy of ionic centers in solid Xe.''

17. R. A. Zhitnikov and Yu. A. Dmitriev (A. F. Ioffe Physico-Technical Institute, 26 Politekhnicheskaya, 194021, St. Petersburg, Russia; e-mail: zhitnikov @mares.ioffe.rssi.ru; dmitriev@mares.ioffe.rssi.ru) ''Interaction of trapped excited metastable atoms with Ne, Ar, Kr, and Xe noble-gas cryocrystals.''

18. L. Ulivi (Instituto di Elettronica Quantistica, CNR, Firenze, Italy; e-mail: ulivi@mail-box.ieq.fi.cnr.it), R. Bini (LENS, Laboratorio di Spettroscopie Non-Lineari, Firenze, Italy; Laboratorio di Spettroscopie Molecolare, Dipart. di Chimica, Universita di Firenze, Italy; e-mail: bini@chim.unifi.it), H. J. Lodl (Laboratorio di Spettroscopie Molecolare, Dipart. di Chimica, Universita di Firenze, Italy; Fachbereich Physik, Universität Kaizerlautern, Germany; e-mail: jodl@rhrk.uni-kl.de), P. Loubeyre, R. LeToullec, and F. Datchi (Physique des Milieeux Consensee, Universite P. et M. Curie, Paris, France; e-mail: paul.loubeyre @pmc.jussieu.fr) ''Infrared absorption spectra of $Ar(H_2)_2$ at low temperature.''

19. M. Suzuki, M. Katsuragawa, R. S. D. Sihombing, J. Z. Li, and K. Hakuta (Division of Natural Sciences, Department of Applied Physics and Chemistry, Institute for Laser Science, Institute of Electro-Communications 1-5-1 Chofugaoka, Chofu, Tokyo 182, Japan; e-mail: suzuki@phys.uec.ac.jp) ''Solid hydrogen for nonlinear optics.''

ORAL CONTRIBUTIONS

1. E. A. Grigoriantz and M. J. Clouter (Physic Department, Memorial University of Newfoundland, St. John's, NF, Canada; e-mail: geamun@kelvin.physics.mun.ca; clouter@kelvin.physics.mun.ca) ''Elastic constants of CH_4 by Brillouin spectroscopy.''

2. K. Damde and H. J. Jodl (University of Kaizerslautern, Department of Physics, Erwin-Schrodinger-Strase, 67663 Kaizerslautern, Germany; e-mail: damde@rhrk.uni-kl.de; jodl@physik.uni-kl.de) ''Mixtures of N_2:O_2 at high pressure and low temperature.''

3. E. S. Yakub (Odessa State Medical University, Odessa, Ukraine; e-mail: yakub@unive.odessa.ua) ''Short-range intermolecular interaction and phase transitions with rearrangement of chemical bonds in solid nitrogen.''

4. M. E. Kooi and J. A. Schouten (University of Amsterdam, Van der Waals-Zeeman Institute, Amsterdam,

The Netherlands; e-mail: ekooi@phys.uva.nl; schouten@phys.uva.nl) ''Raman spectra and phase behavior of the mixed solid N_2-Ar at high pressure.''

5. Jorgen Schou, Birgitte Thestrup, Winne Svendsen, Bjarne Stenum, and Ole Ellegard (OFD, Riso National Laboratory, DK-4000 Roskidle, Denmark; e-mail: j.schou@risoe.dk), R. Pedrys and B. Warczak (Institute of Physics, Jagiellonian University, PL-30 059 Krakow, Poland; e-mail: ufpedrys@cyf-kr.edu.pl) ''Sputtering of surfaces of the solid hydrogens by electrons and ions.''

6. M. Selg (Institute of Physics, Tartu, Estonia) and V. Hizhnyakov (University of Tartu, Estonia) ''Relaxation jumps and hot luminescence of excitons in rare gas crystals.''

Lively discussion of the topics covered in oral contributions was also continued at poster sections. We shall not list the titles of the fifty papers presented at the poster sections since we believe that the titles of the oral papers give a fairly good idea about the most important problems in the topics of cryocrystals and quantum crystals. Most of the papers presented at the conference will be published in one of the issues of the Journal of Low Temperature Physics.

In conclusion, it would be appropriate to mention that the conference was very well organized and conducted.

*E-mail: syrkin@ilt.kharkov.ua

Translated by R. S. Wadhwa